2007

Exploring the quark-gluon content of hadrons: from mesons to nuclear matters

Hrayr Hamlet Matevosyan
Louisiana State University and Agricultural and Mechanical College

EXPLORING THE QUARK-GLUON CONTENT OF HADRONS: FROM MESONS TO NUCLEAR MATTER

A Dissertation

Submitted to the Graduate Faculty of the
Louisiana State University and
Agricultural and Mechanical College
in partial fulfillment of the
requirements for the degree of
Doctor of Philosophy

in

The Department of Physics and Astronomy

by
Hrayr Hamlet Matevosyan
B.Sc. Yerevan State University, 2001
M.Sc. Yerevan State University, 2003
August, 2007

Dedication

To my mother Roza Saribekyan and to my late father Dr. Hamlet Matevosyan for their love and support. To my beautiful nieces Anna and Maria Matevosyan for all the joy and inspiration they brought.

Acknowledgments

I would like to begin by acknowledging my adviser Dr. Jerry P. Draayer, who presented me with several opportunities to advance my career in the direction that most interested me. Not only did he make it possible for me to start my doctoral program at LSU, he also proposed that I conducted my research at Jefferson Lab, where I had the unique prospect of interacting with many world-class physicists acquiring a very broad perspective of both theoretical and experimental hadronic physics. His support and guidance during the course of my studies at LSU and research at JLab are invaluable to me.

I would also like to thank my scientific adviser at JLab Dr. Anthony W. Thomas for presenting me the opportunity to conduct research in a variety of areas with many collaborators, which allowed me to learn new and exciting subjects. Being very liberal and erudite, he encouraged me to explore new subjects and expand my knowledge in the subjects which most interest me. His very measured, wise advice and encouragement helped me to make the right decisions and maintain a positive attitude throughout my graduate studies.

During my graduate studies I have been privileged to work with collaborators such as: Drs. Gerald A. Miller, Peter C. Tandy, Pierre A. Guichon, Jirina Rikovska-Stone and Nicolae G. Sandulescu. I want to thank Drs. Anatoly V. Radyushkin and Jose Goity at JLab for many stimulating and fruitful discussions. I would like to also acknowledge Dr. George S. Pogosyan and the late Dr. Vladimir V. Papoyan, who played an important role in my progress through their continuous support at the Joint Institute of Nuclear Research in Dubna, Russia. I would like to also thank my high school teachers, especially Nairi Sedrakyan, Dr. Arthur Davdyan and Dr. Gagik V. Grigorian for their dedicated work in seeding the love of math and physics in me and all of the other numerous pupils that became very successful in their careers.

The example set by my parents both in academic excellence and moral purity served as a criterion I have always tried to live and work by. My choice of an academic career came as a natural extension of my studies, which was always encouraged by them. My late father, Dr. Hamlet H. Matevosyan and my uncle Dr. Norair H. Arakelian were my role models. My mother Roza A. Saribekyan, being a high-school math teacher, always expected the best academic results, while being a very loving and supportive parent. My brother Dr. Norayr H. Matevosyan and his wife Dr. Julija V. Matevosyan have always been most supportive in challenging times.

I would like to thank all my friends that I met in US who helped to make the time spent here enjoyable, Mher Aghasyan, Gagik Gavalian, Aram Teymurazyan, Hovhannes Baghdasaryan, Joseph (Jivan) Santoro, Armen Khachatryan, Nerses Gevorgyan, Hovanes Egiyan, Heghine Seraydaryan and many others. I wish to specially mention Joseph Santoro, Ross Young and Susan Brown for their invaluable feedback and assistance in writing my dissertation.

My study opportunities was made possible through the financial support of the Department of Physics and Astronomy, Thomas Jefferson National Accelerator Facility, Southeastern Universities Research Association (SURA) and the Graduate School of Louisiana State University for which I am appreciative.

Table of Contents

Abstract

Even though Quantum Chromodynamics (QCD) was formulated over three decades ago, it poses enormous challenges for describing the properties of hadrons from the underlying quark-gluon degrees of freedom. Moreover, the problem of describing the nuclear force from its quark-gluon origin is still open. While a direct solution of QCD to describe the hadrons and nuclear force is not possible at this time, we explore a variety of developed approaches ranging from phenomenology to first principle calculations at one or other level of approximation in linking the nuclear force to QCD.

The Dyson Schwinger formulation (DSE) of coupled integral equations for the QCD Green's functions allows a non-perturbative approach to describe hadronic properties, starting from the level of QCD n-point functions. A significant approximation in this method is the employment of a finite truncation of the system of DSEs, that might distort the physical picture. In this work we explore the effects of including a more complete truncation of the quark-gluon vertex function on the resulting solutions for the quark 2-point functions as well as the pseudoscalar and vector meson masses. The exploration showed strong indications of possibly large contributions from the explicit inclusion of the gluon 3- and 4-point functions that are omitted in this and previous analyses. We then explore the possibility of extrapolating state of the art lattice QCD calculations of nucleon form factors to the physical regime using phenomenological models of nucleon structure.

Finally, we further developed the Quark Meson Coupling model for describing atomic nuclei and nuclear matter, where the quark-gluon structure of nucleons is modeled by the MIT bag model and the nucleon many body interaction is mediated by the exchange of scalar and vector mesons. This approach allows us to formulate a fully relativistic theory, which can be expanded in the nonrelativistic limit to reproduce the well known phenomenological Skyrme-type interaction density functional, thus providing a direct link to well modeled nuclear forces. Moreover, it allows for a derivation of the equation of state for cold uniform dense nuclear matter for application to calculations of the properties of neutron stars.

Chapter 1

Introduction

Ever since the birth of human civilization, we have pondered over how "things are made" and what "things are made of". Even in ancient times people were concerned over this question, as the atomic theory of the structure of matter was first proposed in the fifth century BC by the Greek philosophers Democritus and Lecippus. The proof of their theory came only in the nineteenth century, after many advances in our knowledge and technology, especially Rutherford's famous gold foil experiment. This question in some sense constitutes human curiosity, being more or less universal. For example, even one of the very popular contemporary TV shows on the "Discovery" channel is named "How It's Made". The exploration of this problem drove science and technology forward, and is currently the main motivation for cutting edge, large-scale scientific experiments such as those conducted at the Thomas Jefferson National Accelerator facility, Fermi National Accelerator Laboratory, etc. The Large Hadron Collider will be soon operational, opening new horizons on our understanding of the physics of the most elementary particles known to us. History has shown that even though the direct benefits of these explorations are not always clear, they come in unexpected ways and enable us to create unimaginable benefits, provided the knowledge is applied with great care.

According to our present understanding, the most elementary particles involved in the strong interaction are the quarks and gluons, which make up the large variety of discovered hadrons. A distinguishing property of the quarks is the color quantum number and the anticolor for the antiquarks. Currently we believe that the number of the colors are three as entailed by a local $SU(3)$ gauge symmetry, but an assumption of a large number of colors is useful in some applications. This quantum number can only be changed by exchange of a gluon, naïvely carrying both color and anticolor quantum numbers. A peculiar feature of the quarks, the so-called confinement phenomenon, is that they are always bound into hadrons, making up only colorless configurations, i.e. configurations where every color is present in equal proportions, or a quark and antiquark cancel each other's colors. The universal theory of the strong interaction is widely believed to be Quantum Chromodynamics (QCD), which is the $SU(3)$ local gauge theory of the strong interaction [1], [2]. Even though QCD is often referred as the "perfect theory", it poses enormous challenges for describing the properties of hadrons from the underlying quark-gluon degrees of

freedom. The non-Abelian nature of QCD implies a self-interaction of the gauge field, which manifests itself in an extremely non trivial structure of the QCD vacuum, as illustrated in the Fig. 1.1. This makes the effective coupling constant of the theory dependent on the momentum transfer, becoming large at the momentum scale of most of the hadronic states. Thus, a perturbative expansion in the coupling constant is rendered useless in describing physical processes, as in any approximation all orders of the expansion contribute with comparable strength. Novel methods and approaches to solving the problem, like Lattice QCD (LQCD), have been developed for solving this problem, with various degrees of success and many obstacles are yet to be overcome.

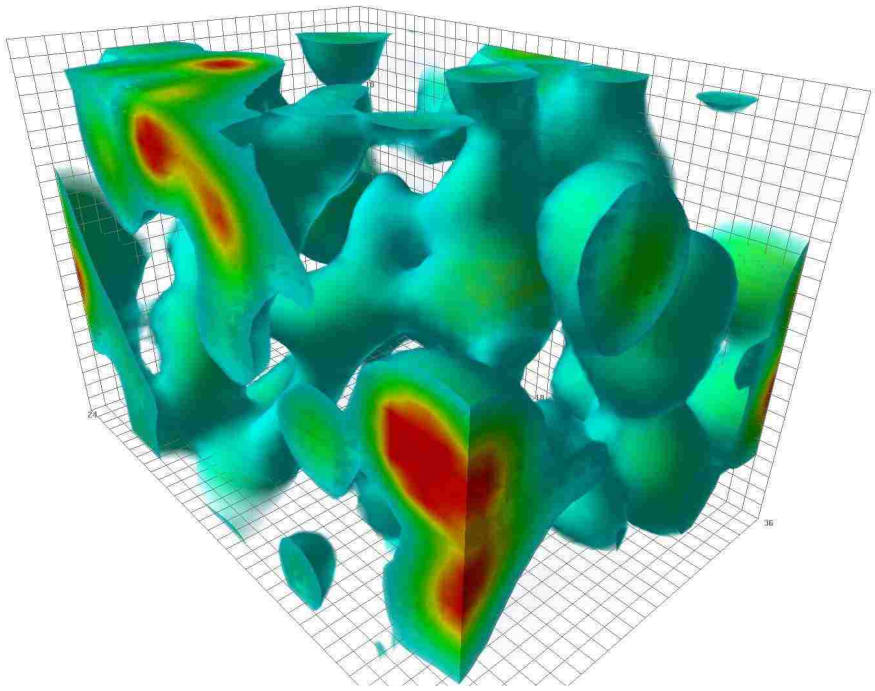

Figure 1.1: The vacuum action density of QCD gauge field as calculated in Lattice QCD. The red color reflects a higher value and the blue a lower value of the action density, which is similar to the energy density of the field. This plot is courtesy of Dr. Derek Leinweber [3].

The more general question of whether one can find an *ab-initio* description of the nuclear force is still open. The interaction of nucleons binding them into atomic nuclei is mediated by the strong force, where the electroweak interaction plays a secondary role with exactly calculable small corrections. Some of the phenomenological aspects of this force, like the spin dependence and saturation have long been extracted from experiment and many models based on this phenomenology with a good description of the properties of the known nuclei close to the beta stability valley have been created. On the other hand, many questions like the density dependence of the nuclear force, the role of strangeness at high densities and the behavior of the nuclear force in neutron rich nuclei are not very well known yet. Moreover, a

direct derivation of the force from QCD itself has yet to be provided. This situation is comprehensible in the light of our previous discussion of the properties of QCD in the regime of low energies. However, any advances in understanding hadrons without fully describing atomic nuclei will be incomplete to state the least. Thus the solution of this problem is essential for further validation of both QCD and the methods employed for its solution, as well as our understanding of nuclear physics. In this work we outline a possible scenario for connecting the nuclear force with its QCD origin. Development of the methods and models for solving QCD at the hadronic level will play a central role in this work.

The first approach that we will study and develop will be the framework of QCD Dyson Schwinger Equations (DSE) and their application to hadronic physics. DSEs are the equations governing the QCD Green's functions, derived directly from the QCD Lagrangian, where employment of a particular gauge enables significant advances in analytic treatment [4], [5]. While the full system of the DSEs is an infinite tower of coupled QCD n-point functions, employment of finite truncations of this system have proven to be very successful in describing the low-order n-point functions and several hadronic observables ([6], [7] and references therein). A widely employed truncation scheme in describing various quantities is the so-called "Ladder-Rainbow" approximation for solving the quark DSE and constructing equations for the bound state hadrons, where the quark-gluon vertex is taken to be bare. Exploration of the accuracy of this approximation thus far has included only certain infinite classes of diagrams in Refs. [8], [9], where phenomenological inclusion of the three gluon dressing with the previous class of diagrams was explored in Ref. [10]. In Chapters 2 and 3 we will build successively more sophisticated models for the dressed quark-gluon vertex and explore the effect of including the more realistic vertex function on the calculated quark two-point function and meson masses.

As we have already mentioned, QCD in the low energy region does not have a small parameter that can be used in an expansion. Gerard 't Hooft proposed to use the inverse of the number of the colors, $1/N_c$, as such an expansion parameter, where the number of the colors is assumed to be very large for the expansion to be convergent [11]. This model proved to be a very useful analytical tool for obtaining exact results in QCD-like theories and hadron phenomenology [12], [13], [14]. The shortcoming of the current formulation of the Feynman rules for the $1/N_c$ expansion is that they are accurate only in the leading order of the expansion, which is usually the order considered. In our explorations of the quark-gluon vertex diagrams, we came across some diagrams contributing at the next-to-leading order in the $1/N_c$ expansion, thus we needed a more complete rules for the expansion to examine their relative strength in this limit. We have formulated a complete set of Feynman rules in Chapter 3, that allow one to calculate the expansion coefficients exactly.

While Lattice QCD has achieved very significant results in recent years [15], [16], [17], there are still large obstacles in the path of solving QCD with physical hadrons in this method. The LQCD approach employes finite space-time discretization (lattice) for calculating the QCD vacuum gauge field configurations and expectation values for observables on the background of the gauge field. The discretization then introduces two scales into the problem, one being the lattice spacing and the

other being the length of the lattice sides in each direction. The existence of these scales means that the momentum in the LQCD is discretized, with the minimum allowed momentum being set by the inverse of the lattice length and the maximum by the inverse of the lattice spacing with the usual cyclic boundary conditions set on the lattice. An additional restriction is imposed by the capability of modern computers, as the volume of the numerical calculations grows as some inverse power of the quark masses used, thus presently only unphysically high masses are used in calculations of the physical observables. A necessary connection to the physical mass scale must be provided before comparing the results to the experiment.

The recent Lattice QCD calculated nucleon electromagnetic form factors of the Ref. [18] have attracted significant attention in the light of recent experimental discoveries. The nucleon electric and magnetic form factors reflect the distribution of charge and magnetization inside the nucleon, thus providing invaluable information on the dynamical structure created by the quarks and gluons. Until recently, the experimental measurements of the ratio of the electric to magnetic form factors of the proton utilizing the Rosenbluth separation method showed constant behavior versus the momentum transfer squared [19]. This result was anticipated in the very high momentum transfer region, where a perturbative expansion of QCD is possible and one can rely on the dimensional scaling arguments of Ref. [20], but wasn't rigorously justified in the low momentum transfer region. Several experiments in Jefferson Laboratory (JLab) used the method of measuring the polarization transfer to the struck nucleon (Refs. [21], [22]) and showed a steep decline of the ratio as the momentum transfer square exceeded 1 GeV^2, strongly disagreeing with the previous measurements. While several arguments exist explaining the discrepancy between the measurements with two different methods, that generally involve large contributions from two photon exchange [23], a direct guidance from the LQCD calculations can be very helpful. In Chapter 4 we employ a specific method of using phenomenological models of nucleon structure for extrapolating the LQCD calculated form factors in both quark mass and the momentum transfer region. Let's note that latter is necessary as the possible values of momenta on the lattice are discrete and limited, as explained above. We choose to employ two distinct models that provide a good fit to the experimental data, but differ in the phenomenological ideas of nucleon structure behind them, namely the Light Front Cloudy Bag Model (LFCBM) of Refs. [24], [25], [26] and a modern version of the Vector Meson Dominance (VMD) model of Ref. [27], where successful description of LQCD data will serve as an additional measure of reliability of the models.

After exploring several methods and models for solving for the hadronic properties from QCD, in Chapter 5 our work culminates in meeting our initial goal of connecting the nuclear force to QCD. A first principle calculation of the properties of the nuclear force is still unaffordable, thus we resort to the phenomenological modeling that proved to work very well for hadrons. Here we further develop the Quark Meson Coupling (QMC) model (see Refs. [28], [29], [30]) for describing atomic nuclei and nuclear matter, where the quark-gluon structure of nucleons is modeled by the MIT bag model and the nucleon many body interaction is mediated by the exchange of scalar and vector mesons. We derive a refined formalism for QMC,

where we lift the tight constrain of small values of the scalar field imposed in the previous formulations. Through our research into QCD dynamics, we argue that this approach has intimate connections to QCD and is one of the very few prospects we have to solve this problem. In fact, this approach allows us to formulate a fully relativistic theory, which can be expanded in the nonrelativistic limit to reproduce the well known phenomenological Skyrme-type interaction density functional, thus providing a link directly to well modeled nuclear forces. Moreover, it allows for a derivation of the equation of state for cold uniform dense nuclear matter for application to calculations of the properties of neutron stars. This discussion concludes our work, as we meet our goals and examine the results. We give our concluding remarks in Chapter 6.

Chapter 2

Dyson-Schwinger Equations and Hadronic Physics

2.1 Overview

At present Quantum Chromodynamics is believed to be the fundamental theory of the strong interaction. Even though it was formulated more than thirty years ago, it still presents enormous challenges in describing the bound states (hadrons) of its quanta, quarks and gluons, as solutions of the theory. Moreover, the puzzle of confinement, namely the fact that quarks and gluons are *only* observed bound in hadrons, has still not been solved. In contrast with QED, QCD has a running coupling constant which becomes large at the energy scale corresponding to hadrons, making a perturbative expansion impossible. This non-perturbative nature of QCD requires the employment of new approaches, such as Lattice QCD (LQCD), Effective Field Theories (EFT), AdS/CFT Correspondence and Dyson-Schwinger Equations (DSE) in order to allow for a solution. All of the approaches that are currently known have their limitations and shortcomings, due to both technical difficulties and matter of principal. For example, Lattice QCD calculations, among other restrictions, are performed at unphysically high quark masses to make them affordable with the present large-scale supercomputing clusters. Thus all of the above mentioned approaches should complement each other in piecing together the physical picture from the information that becomes available as advances in each field are made. For example, EFT is being widely used to extrapolate the LQCD results to the physical masses, while in DSE, Lattice calculated QCD Green's functions are used to constrain the parameters of the models.

In recent years there has been significant progress in the study of the spectrum of hadrons and their non-perturbative structure and form factors through DSE approaches that are manifestly covariant, and which accommodate both dynamical chiral symmetry breaking (DCSB) and quark confinement [6]. Covariance provides efficient and unambiguous access to form factors [31–33]. Consistency with chiral symmetry and its spontaneous breaking is obviously crucial to prevent the pseudoscalars from artificially influencing the difficult task of describing and modeling

the infrared dynamics; this is a role better left to other hadronic states that are not so dominated by chiral symmetry. The associated concept of a constituent quark mass is important and it is often implemented in models as a constant mass appearing in the propagator, however this idealization runs into trouble for higher lying states where the sum of the constituent masses is below the hadron mass. This difficulty is marginally evident with the ρ, but it is inescapable by the time one has reached the ground state axial vector mesons (e.g., a_1, b_1 mesons) [34].

In reality, solutions of the QCD equation of motion for the quark propagator (quark Dyson-Schwinger equation) give a momentum-dependent quark mass function. Model calculations, mostly in Landau gauge, typically yield a mass function that evolves from the current mass value at ultraviolet spacelike momenta to a value some 0.4 GeV larger in the deep infrared [35]. The propagator is a gauge-dependent object and the gauge dependence of this phenomenon has not been fully explored. In the chiral limit, such an enhancement is DCSB. At finite current mass, models also strongly suggest that the enhancement is the same mechanism as DCSB which has an important influence over the low-lying hadron spectrum. In the chiral limit, the scalar term of the quark self-energy, which shows most of the momentum dependence, plays a dual role as the dominant invariant amplitude of the chiral pion Bethe-Salpeter equation (BSE) amplitude at low momenta [36]. In any process where the spatial extent of the pion plays an important role, the running of the quark mass function is likewise crucial to an efficient symmetry-preserving description. Otherwise a theoretical model is fighting symmetries. An example is provided by the pion charge form factor above the chiral symmetry breaking scale, i.e., $Q^2 > m_\rho$. It is this large value of the dressed quark mass function at low spacelike momentum that leads, in model solutions of the quark DSE, to $|p^2| \neq M^2(p^2)$ within a significant domain of timelike momenta where these models can be trusted. For example, this is sufficient to prevent spurious $q\bar{q}$ production thresholds in light quark hadrons below about 2 GeV [34].

The task of maintaining manifest covariance, DCSB, a running quark mass function and an explicit substructure in terms of confined quarks is often met by models defined as truncations of the DSEs of QCD [5, 6, 37]. For practical reasons the equations must be truncated to decouple arbitrarily high order n-point functions from the set of low order n-point functions used to construct observables. A common truncation scheme is the rainbow-ladder truncation. Here the one-loop gluon dressing of the quark (with bare gluon-quark vertices) is used self-consistently to generate the quark propagator. In general the kernel, K, of the Bethe-Salpeter equation is given in terms of the quark self-energy, Σ, by a functional relation dictated by chiral symmetry [38]. This preserves the Ward-Takahashi identity for the color singlet axial vector vertex and ensures that chiral pseudoscalars will remain massless, independent of model details. With a rainbow self-energy, this relation yields the ladder BSE kernel. To go beyond this level, one needs to realize that the exact quark self-energy is given by the same structure except that one of the gluon-quark vertices is fully dressed. It is the vertex dressing that generates the terms in K beyond the ladder level. This is the topic we are concerned with in this chapter.

The ladder BSE for meson bound states is an integral equation with a one-loop kernel structure that must allow for the spinor structure of propagators and the meson amplitudes. With the four-dimensional space-time that one must use to maintain manifest covariance, and with dynamically generated quark propagators that one must use to preserve the Ward-Takahashi identities of chiral symmetry, the numerical task is large. Any scheme for corrections to the ladder truncation will in general add the complexity of multiple loop Feynman diagrams involving amplitudes that are only known after solution. For practical reasons the studies that have been able to investigate hadron states beyond ladder-rainbow (LR) truncation in recent years [8–10,39] have exploited the simplifications following from use of the Munczek-Nemirovsky (MN) model [40]. In this case the basic element is a delta function that restricts the exchanged (or gluon) momentum to zero. It reduces both the quark DSE and the meson BSE to algebraic equations with only one parameter, a strength set by m_ρ.

This simplified kernel has no support in the ultraviolet and one must be wary of its use for related physics. Bound state masses are relatively safe in this regard; even heavy quark states that sample short distance or large momenta are safe due to the large quark mass scale present. Even with the MN model, the DSE solutions for the quark propagators have the correct power law behavior, and they continuously connect to the current quark mass, in the ultraviolet, apart from log corrections. The dominant qualitative features of DSE solutions of realistic models are preserved in the MN model: large infrared strength giving DCSB and the (confining) absence of a mass pole. Our analysis is not intended to provide a serious representation of experimental data; rather we aim at some understanding, even if it is quite qualitative, of the relative importance of classes of higher-order diagrams for the BSE kernel for bound states. Because of the inherent complexity brought by the use of a momentum distribution as a kernel, there is little information available in the literature on this topic. To obtain such information, we feel the price paid by dispensing with a clear connection to perturbative QCD is worthwhile in the initial stages.

There are studies of vertex corrections and the relevance of the ladder-rainbow truncation of the BSE that have utilized the convenience of purely scalar field theories (see Ref. [41]) or scalar QED (see Ref. [42]). In a non-Abelian context, a first study of the correction to ladder-rainbow truncation for pseudoscalar and vector mesons and scalar and axial vector diquark correlations was made in Ref. [8] where a one-gluon exchange dressing of the quark-gluon vertex was implemented. Subsequently [9], it was realized that the algebraic structure allowed a recursive implementation of the ladder series of diagrams for the quark-gluon vertex as well as an implementation of the corresponding series of diagrams for the chiral symmetry-preserving BSE kernel. As far as we are aware, this was the first solution of a BSE equation for bound states of colored quarks and gluons in which the kernel contained the effects from an infinite number of loops. In these works the chiral pseudoscalars remained massless independent of the model parameter and m_ρ received corrections of order 10% from ladder dressing of the vertex. The influence of vertex dressing upon the quark propagator was also studied.

There is very little in the way of guidance from realistic non-perturbative non-Abelian models of the infrared structure of the quark-gluon vertex. It has often been assumed, e.g., see Ref. [43], that a reasonable beginning is the Ball-Chiu [44] or Curtis-Pennington [45] Abelian Ansatz times the appropriate color matrix. These Abelian descriptions of the momentum dependence satisfy the Abelian vector Ward-Takahashi identity, and their use makes the implicit assumption that this might be a good enough approximation to the corresponding identity for QCD, namely the Slavnov-Taylor identity for the color octet vertex [46]. The use of an explicit ladder sum for the gluon vertex provides easy access to the chiral symmetry preserving BSE kernel and receives some motivation from the fact that a ladder-summed photon-fermion vertex combines with the rainbow approximation for the fermion propagator to preserve the Ward-Takahashi identity for that vertex.

However, when initial results from lattice-QCD simulations of the gluon-quark vertex became available [47,48], it was realized [49] that the color algebra generated by any ladder sum for this vertex gives a magnitude and strength for the dominant amplitude at zero gluon momentum that is qualitatively and quantitatively incompatible with the lattice data and incompatible with the leading ultraviolet behavior of the one-loop QCD Slavnov-Taylor identity. The infrared vertex model developed in Ref. [49] made an extension of the fact that the one-loop QCD color structure introduced by the three-gluon coupling repairs the deficiency of a purely ladder structure. The color structure of the ladder class of diagrams produces a weak repulsive vertex, while the color structure of the three-gluon coupling contribution produces an attractive contribution that is enhanced by a factor of $-N_c^2$ at the purely one-loop level.

These observations from Ref. [49] were blended with the algebraic features afforded by the MN model to re-examine the relation between vertex dressing, the chiral symmetry-preserving BSE kernel, and the resulting meson spectrum and diquark correlations [10]. This approach introduced one extra parameter (besides the gluon 2-point function strength and the quark current mass)—an effective net color factor fitted to lattice-QCD data on the gluon-quark vertex. The net attraction in the vertex, driven by the explicitly non-Abelian 3-gluon coupling, had a marked effect: the ladder-rainbow truncation made m_ρ 30% too high compared to the solution from the completely summed vertex. In other words, the attraction produced by summed vertex dressing in a non-Abelian context is more important than previously thought. However in that approach, the structure of the vertex is such that the coupling of any internal gluon line to a quark is itself bare. This is not self-consistent and one can question what effect this omitted infinite sub-class of vertex dressing and BSE kernel contributions may have upon the hadron spectrum.

In the present chapter we extend the analysis of Ref. [10] by the incorporation of a wider class of vertex dressing diagrams. We allow the coupling of any internal gluon line to a quark to be described by the dressed vertex at an order consistent with a given total order in the final vertex. In the limit of the vertex summed to all orders, this becomes the use of the self-consistent quark-gluon vertex at every internal location in a diagram. We borrow from previous work the use of the MN model of the 2-point gluon function to generate an algebraic structure and we again

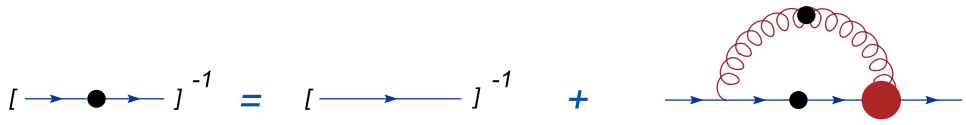

Figure 2.1: The GAP equation for the dressed quark 2-point function. The black circle denotes that the corresponding propagator is fully dressed and the red circle denotes the fully dressed quark-gluon vertex function.

incorporate the important non-Abelian three-gluon coupling through the device of an effective net color factor refitted to the lattice data for the vertex. We use the infinite series of diagrams for the BSE kernel generated from the chiral symmetry-preserving relation to the quark self-energy and investigate the resulting spectrum of pseudoscalar and vector mesons.

2.2 The Quark GAP Equation and the Ladder-Rainbow Truncation

The Dyson-Schwinger equation for the dressed quark propagator or the GAP equation is

$$S(p)^{-1} = Z_2\, S_0^{-1}(p) + C_{\rm F}\, Z_1 \int_q^{\Lambda} g^2 D_{\mu\nu}(p-q)\, \gamma_\mu S(q) \Gamma_\nu(q,p), \tag{2.1}$$

where $S_0^{-1}(p) = i\not{p} + m_{bm}$, m_{bm} is the bare current quark mass, $Z_2(\mu^2, \Lambda^2)$ is the quark wave function renormalization constant, and $Z_1(\mu^2, \Lambda^2)$ is the vertex renormalization constant. The general form for $S(p)^{-1}$ is

$$S(p)^{-1} = i\not{p}\, A(p^2, \mu^2) + B(p^2, \mu^2) \tag{2.2}$$

and the renormalization condition at scale $p^2 = \mu^2$ is $S(p)^{-1} \to i\not{p} + m(\mu)$ where $m(\mu)$ is the renormalized current quark mass. The GAP equation is diagrammatically depicted in Fig. 2.1.

It is clear that in order to solve this equation, we need both the dressed gluon propagator and the dressed quark-gluon vertex. The Dyson-Schwinger equations for these Green's functions involve higher order n-point functions. For example, the DSE for the gluon propagator involves the dressed 3 and 4 gluon vertices, the dressed ghost-gluon vertex, etc. To solve these equations a certain truncation scheme should be employed to express the higher n-point functions through the lower ones, guided by chiral symmetry, gauge invariance and other fundamental symmetries of QCD. The truncation closes the set of integral equations which can then be solved simultaneously to produce the considered Green's functions.

One of the most explored and widely used truncation schemes is the so called "Ladder-Rainbow" (LR) truncation. In this truncation the dressed quark-gluon

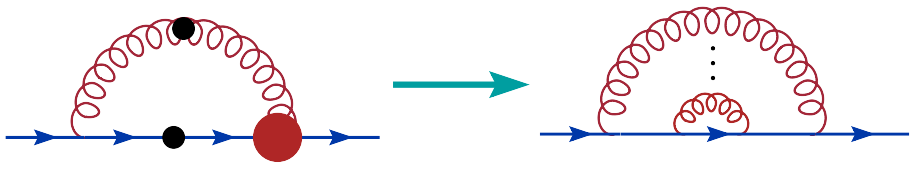

Figure 2.2: The "Rainbow" truncation of the quark self-energy term in the GAP equation.

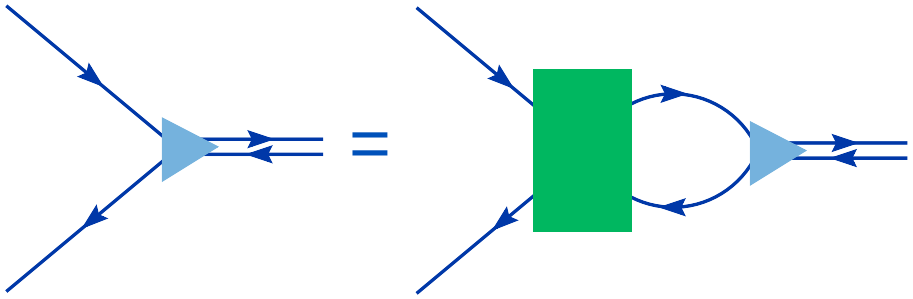

Figure 2.3: The homogeneous Bethe-Salpeter equation for the quark-antiquark scattering amplitude.

vertex, $\Gamma_\nu(q,p)$, in the quark self-energy term in Eq. (2.1) is set simply to its bare value, γ_ν, and a model gluon propagator is employed to absorb the effects of both vertex and gluon dressing. The corresponding "Rainbow"-dressed self-energy term is depicted schematically in Fig. 2.2.

Probably the easiest physical observables that can be calculated in this approach are the meson properties using the relativistic two-body Bethe-Salpeter equations (BSE) for quark-antiquark scattering amplitudes. The renormalized homogeneous Bethe-Salpeter equation for the quark-antiquark channel, denoted by M, can be compactly expressed as

$$[\Gamma_M(k;P)]_{EF} = \int_q^\Lambda [K(k,q;P)]^{GH}_{EF}\,[\chi_M(q;P)]_{GH}\,, \tag{2.3}$$

where $\Gamma_M(k;P)$ is the meson Bethe-Salpeter amplitude (BSA), k is the relative momentum of the quark-antiquark pair and P is their total momentum. E,...,H represent color, flavor and spinor indices and the BS wavefunction is

$$\chi_M(k;P) = S(k_+)\Gamma_M(k;P)S(k_-), \tag{2.4}$$

where $k_\pm = k \pm \frac{P}{2}$, and K is the amputated quark-antiquark scattering kernel. The BSE of Eq. (2.3) is diagrammatically depicted in Fig. 2.3.

The scattering kernel K describes the interaction between the quark and the anti-quark and should be constructed to best reproduce it. The "Ladder" approximation for the K is formulated by simply replacing it with a one dressed gluon

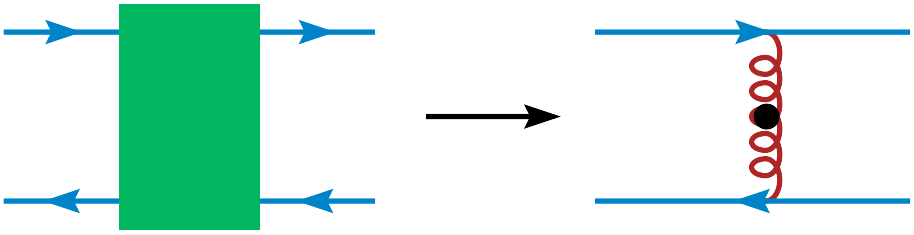

Figure 2.4: The "Ladder" approximation for the BSE scattering kernel.

exchange between the pair, where the gluon couples to the quarks by a bare quark-gluon vertex. Diagrammatically it can be seen in Fig. 2.4.

The "Rainbow" approximation to the GAP equation self-energy and "Ladder" approximation to the BSE scattering kernel constitute the "Ladder-Rainbow" approximation. While this approximation is seemingly very crude, it preserves the chiral symmetry of QCD by satisfying the axial-vector Ward-Takahashi identity. Thus the solutions of the BSE in the pseudoscalar channel, with quark 2-point functions as solutions of the GAP equation, ensure that the resulting meson is a Goldstone boson.

In 't Hooft's model of $1+1$ dimensional QCD, in the leading order $1/N_c$ expansion, the LR truncation is exact [11], [12], [14]. In this oversimplified model of QCD that has only one time and one space dimension, the light-cone choice for the gauge fixing , $A^+ = A_- = 0$, simplifies the Lagrangian density, eliminating the 3 and 4 gluon couplings. QCD at small momentum scale doesn't have small parameters for perturbative expansion. This means that in calculations of any observable one must calculate all the diagrams with infinite number of loops. 't Hooft has proposed to use the inverse of the number of colors, $1/N_c$, as such a small parameter, assuming N_c to be so large that the expansion will be sensible. The hope is that the expansion will give qualitative results that will hold even for the $N_c = 3$. The $1/N_c$ expansion will be described in more detail in the next chapter. The interesting result of this model is that in leading order of the expansion only the "Rainbow" type diagrams contribute to the quark self-energy term and only "Ladder" type diagrams to the quark-antiquark interaction. This further encourages the exploration of the LR truncation scheme.

Even with LR truncation, in practice the GAP equation is solved with a model dressed gluon two point function. This approach proves to be productive in both reducing the numerical task of solving coupled quark and gluon DSEs as well as allowing us to introduce some phenomenology to compensate for the shortcomings of the truncation. This scheme has been used to successfully describe the experimental observables such as meson masses, decay widths and form factors (see, for example, Refs. [50], [51], [52], [53]) as well as baryon properties [33]. With all its success, the LR truncation has its shortcomings. For example, it yields bound diquark states, contradicting all observations of no colored bound states. It also gives an inadequate description of scalar mesons, etc [8].

The LR truncation is a non-perturbative truncation of the theory, which is believed to be a good representation of the full theory. In order to test this hypothesis, we need to study the theory with more complete truncation and explore how the calculated observables change. The task of maintaining manifest covariance, DCSB, a running quark mass function and an explicit substructure in terms of confined quarks is often met by models defined as truncations of the DSEs of QCD [5, 6, 37]. For practical reasons, the equations must be truncated to decouple arbitrarily high order n-point functions from the set of low order n-point functions used to construct observables. A common truncation scheme is the rainbow-ladder truncation. Here the one-loop gluon dressing of the quark (with bare gluon-quark vertices) is used self-consistently to generate the quark propagator. In general, the kernel K of the Bethe-Salpeter equation is given in terms of the quark self-energy, Σ, by a functional relation dictated by chiral symmetry [38]. This preserves the Ward-Takahashi identity for the color singlet axial vector vertex and ensures that chiral pseudoscalars will remain massless, independent of model details. With a rainbow self-energy, this relation yields the ladder BSE kernel. To go beyond this level, one needs to realize that the exact quark self-energy is given by the same structure, except that one of the gluon-quark vertices is fully dressed. It is the vertex dressing that generates the terms in K beyond ladder level. The first steps in this direction were taken by considering the ladder-summed vertex [8], [9], [10].

2.3 The Ladder-Summed Vertex and Its Consequences

In order to continue our description of the subject we briefly describe the framework for the calculations. We employ Landau gauge and a Euclidean metric, with: $\{\gamma_\mu, \gamma_\nu\} = 2\delta_{\mu\nu}$; $\gamma_\mu^\dagger = \gamma_\mu$; and $a{\cdot}b = \sum_{i=1}^4 a_i b_i$. The dressed quark-gluon vertex for gluon momentum k and quark momentum p can be written $ig\,t^c\,\Gamma_\sigma(p+k,p)$, where $t^c = \lambda^c/2$ and λ^c is an SU(3) color matrix. In general, $\Gamma_\sigma(p+k,p)$ has 12 independent invariant amplitudes. We are particularly concerned in this work with the vertex at $k = 0$, in which case the general form is

$$\Gamma_\sigma(p) = \alpha_1(p^2)\gamma_\sigma + \alpha_2(p^2)\not{p}p_\sigma - \alpha_3(p^2)ip_\sigma + \alpha_4(p^2)i\gamma_\sigma\not{p} \tag{2.5}$$

where $\alpha_i(p^2)$ are invariant amplitudes. In the model studies of Refs. [9] and [10] that we build upon, one finds $\alpha_4 = 0$, which will also be the case here.

As we shall discuss later, we wish to utilize the functional relation that enables the BSE kernel to be generated from the quark self-energy so that chiral symmetry is preserved. This requires the vertex to be represented in terms of a set of explicit Feynman diagrams. Some exact results are known for the vertex at 1-loop order in QCD [54]. In Landau gauge and to $\mathcal{O}(g^2)$, i.e., to 1-loop, the amplitude Γ_σ is given by

$$\Gamma_\sigma^{(1)}(p+k,p) = Z_1\gamma_\sigma + \Gamma_\sigma^{\rm A}(p+k,p) + \Gamma_\sigma^{\rm NA}(p+k,p), \tag{2.6}$$

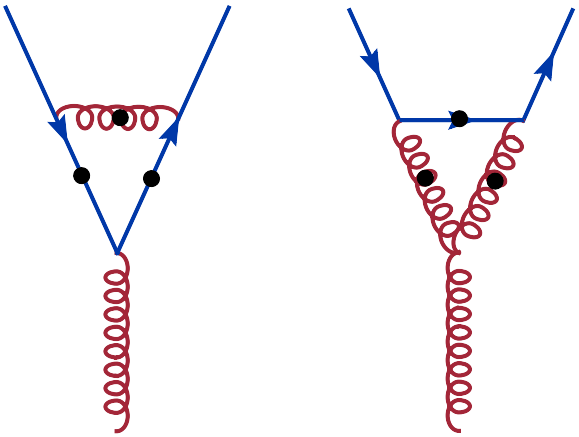

(a) $-\frac{1}{2N_c}$ (b) $\frac{N_c}{2}$

Figure 2.5: The $\mathcal{O}(g^2)$ contributions to the quark-gluon vertex. The color factor of the vertex dressed with 2-point gluon function a) is N_c^2 times smaller than the vertex dressed with 3-point gluon function b). The corresponding color factors are shown next to the labels of the diagrams.

with

$$\Gamma^{\rm A}_\sigma(p+k,p) = -(C_{\rm F} - \frac{C_{\rm A}}{2}) \int_q^\Lambda g^2 D_{\mu\nu}(p-q)\gamma_\mu S_0(q+k)\gamma_\sigma S_0(q)\gamma_\nu, \tag{2.7}$$

and

$$\Gamma^{\rm NA}_\sigma(p+k,p) = -\frac{C_{\rm A}}{2} \int_q^\Lambda g^2 \gamma_\mu S_0(p-q)\gamma_\nu D_{\mu\mu'}(q+k) i\Gamma^{3g}_{\mu'\nu'\sigma}(q+k,q) D_{\nu'\nu}(q), \tag{2.8}$$

where $\int_q^\Lambda = \int^\Lambda d^4q/(2\pi)^4$ denotes a loop integral regularized in a translationally-invariant manner at mass-scale Λ. Here $Z_1(\mu^2,\Lambda^2)$ is the vertex renormalization constant to ensure $\Gamma_\sigma = \gamma_\sigma$ at renormalization scale μ. The following quantities are bare: the three-gluon vertex $ig\, f^{\rm abc}\, \Gamma^{3g}_{\mu\nu\sigma}(q+k,q)$, the quark propagator $S_0(p)$, and the gluon propagator $D_{\mu\nu}(q) = T_{\mu\nu}(q) D_0(q^2)$, where $T_{\mu\nu}(q)$ is the transverse projector. The next order terms in Eq. (2.6) are $\mathcal{O}(g^3)$: the contribution involving the four-gluon vertex, and $\mathcal{O}(g^4)$: contributions from crossed-box and two-rung gluon ladder diagrams, and 1-loop dressing of the triple-gluon vertex, etc. The corresponding Feynman diagrams are depicted in Fig. 2.5.

The color factors in Eqs. (2.7)and (2.8) are given by

$$t^a t^b t^a = (C_{\rm F} - \frac{C_{\rm A}}{2}) t^b = -\frac{1}{2N_c} t^b$$
$$t^a f^{abc} t^b = \frac{C_{\rm A}}{2} i t^c = \frac{N_c}{2} i t^c$$
$$t^a t^a = C_{\rm F} \mathbf{1_c} = \frac{(N_c^2-1)}{2N_c} \mathbf{1_c}. \tag{2.9}$$

In contrast, for the color singlet vector vertex, i.e. for the strong dressing of the quark-photon vertex, one has the one-loop Abelian result

$$\tilde{\Gamma}^{(1)}_\sigma(p+k,p) = \tilde{Z}_1 \gamma_\sigma - C_{\rm F} \int_q^\Lambda g^2 D_{\mu\nu}(p-q) \gamma_\mu S_0(q+k) \gamma_\sigma \, S_0(q) \gamma_\nu. \tag{2.10}$$

To motivate the approximate vertex used in the present study, we note that the local color SU(3) gauge invariance of the QCD action gives the Slavnov-Taylor identity [46] for the gluon vertex

$$k_\mu i\Gamma_\mu(p+k,p) = G(k^2) \left\{ [1 - B(p,k)] \, S(p+k)^{-1} - S(p)^{-1} \, [1 - B(p,k)] \right\}, \tag{2.11}$$

which relates the divergence of the vertex to the quark propagator $S(p)$, the dressing function $G(k^2)$ of the ghost propagator $-G(k^2)/k^2$, and the ghost-quark scattering kernel $B(p,k)$, all consistently renormalized. Even though there is no explicit ghost content evident in the 1-loop vertex Eq. (2.6), it does satisfy this identity at one-loop order [54].

Prior to the recent appearance of quenched lattice-QCD data [47,48], there had been little information available on the infrared structure of the gluon-quark vertex. The two $\mathcal{O}(g^2)$ diagrams of Eq. (2.6) cannot be expected to be adequate there. A common assumption [43] has been to adopt an Abelian vertex Ansatz, such as the Ball-Chiu [44] or Curtis-Pennington [45] forms and attach the appropriate color matrix. In the case of an Abelian U(1) gauge theory, the counterpart to Eq. (2.11) is the Ward-Takahashi identity (WTI)

$$k_\mu \, i\tilde{\Gamma}_\mu(p+k,p) = S(p+k)^{-1} - S(p)^{-1}. \tag{2.12}$$

At $k = 0$, the Abelian vertex $\tilde{\Gamma}_\mu$ has the same general form as given earlier in Eq. (2.5). The Ward identity $\tilde{\Gamma}_\sigma(p) = -i\partial S(p)^{-1}/\partial p_\sigma$ yields: $\tilde{\alpha}_1 = A(p^2)$, $\tilde{\alpha}_2 = 2\,A'(p^2)$, and $\tilde{\alpha}_3 = 2\,B'(p^2)$, where $f' = \partial f(p^2)/\partial p^2$. However, even if the Abelian Ansatz, $ig\,t^c\,\tilde{\Gamma}_\sigma(p)$, were to be adopted for the gluon vertex, it would not help in the present context because we need a representation in terms of an explicit set of Feynman diagrams for the resulting self-energy, in order to determine the symmetry-preserving BSE kernel.

In Ref. [9] a study was made of a ladder summation Ansatz for the gluon vertex based on just the Abelian-like gluon exchange diagram of Eq. (2.7); the

symmetry-preserving BSE kernel was generated and used to explore meson and diquark masses. The vertex was generated by iterative and recursive techniques and, after convergence, is equivalent to solution of the integral equation

$$\Gamma_\sigma(p+k,p) = Z_1\gamma_\sigma - (C_{\rm F} - \frac{C_{\rm A}}{2}) \int_q^\Lambda g^2 D_{\mu\nu}(p-q)\gamma_\mu S(q+k)\Gamma_\sigma(q+k,q)S(q)\gamma_\nu. \quad (2.13)$$

Here, at any order of iteration, the quark propagator is calculated by using the same vertex in the gap equation, Eq. (2.1). Is this ladder sum a good approximation to the gluon-quark vertex, particularly in the infrared? The quenched lattice-QCD data indicates that the answer is no. The lattice data clearly gives $\alpha_1(p^2) > 1$ for all available p^2 and the infrared limit appears to be $\alpha_1(0) \gtrsim 2.2$. The ladder summation based on Eq. (2.13) gives $\alpha_1(p^2) < 1$, with infrared limit $\alpha_1(0) \approx 0.94$. The 1-loop QCD analysis indicates that in the ultraviolet $\alpha_1(p^2)$ approaches unity from above [54], while the recent model vertex [49], based on a non-perturbative extension of the two 1-loop diagrams from Eq. (2.6), yields $\alpha_1(p^2) > 1$ for all p^2, and agrees quite well with the lattice data.

The reason for the discrepancy mentioned above can be seen from the color factors associated with the two 1-loop diagrams, Eq. (2.7) and Eq. (2.8), which are the leading terms in the ultraviolet region. The ladder sum in Eq. (2.13) is built on the least significant of the two diagrams. The color factor of the omitted 3-gluon term is N_c^2 times that of the term retained. The relative contribution to the Slavnov-Taylor identity, Eq. (2.11), from that term is of the same order at 1-loop. More generally, as discussed in Ref. [10], if $G(k^2)(1 - B(p,k)) > 0$ persists into the non-perturbative region, one can expect $\alpha_1(p^2) > 1$. One can also expect to obtain the wrong sign for $\alpha_1(p^2) - 1$ if a model kernel has the wrong sign. This is the case with the Abelian-like ladder sum, Eq. (2.13). Note that in an Abelian $U(1)$ gauge theory, e.g., the photon-quark vertex, $\tilde{\alpha}_1(p^2) = A(p^2) > 1$. An Abelian Ansatz for this amplitude of the gluon-quark vertex might be quite reasonable, but it cannot be simulated by an explicit ladder sum because the color algebra prevents it. In analogy with the photon-quark vertex, where $\tilde{\alpha}_1(p^2) > 1$ is correlated with the spectral density being positive definite as the timelike region is approached, the gluon-quark vertex dressing has been referred to as an attractive effect in the infrared spacelike region [10]. (Of course, for the gluon vertex there should be no color octet bound states and no positive spectral density in the timelike region.) The 3-gluon coupling is a strong source of the attraction at low spacelike p^2. It is N_c^2 times larger than the small repulsive effect of gluon exchange.

The model for $D_{\mu\nu}$ that we employ in this work, described in Section III, allows us to focus on zero gluon momentum. In this case, as discussed and utilized in Ref. [49], the two pQCD 1-loop diagrams for the vertex, Eq. (2.7) and Eq. (2.8), are both closely related to the momentum derivative of the corresponding quark self-energy, apart from the differing color factors. The resulting dependence upon the single quark momentum variable is similar for each diagram. Both are 1-loop integrals projected onto the same Dirac structures. We adopt the approach of Ref. [10] to the vertex for our algebraic study. The approach is defined by taking the momen-

tum dependence to be similar even in the infrared and with dressed propagators. Thus we combine the two terms and write Eq. (2.6) as

$$\Gamma^{(1)}_\sigma(p+k,p) \approx Z_1\gamma_\sigma - \mathcal{C}C_{\rm F}\int_q^\Lambda g^2 D_{\mu\nu}(p-q)\gamma_\mu S_0(q+k)\gamma_\sigma S_0(q)\gamma_\nu, \qquad (2.14)$$

with $\mathcal{C}$ being an effective color factor to be determined by a fit to lattice-QCD data for the vertex. If the momentum dependence of the two combined terms from Eq. (2.6) were identical, then we see that $\mathcal{C} = 1$. This is equivalent to the Abelian limit. If one were to omit the 3-gluon term altogether, as in the iterative study in Ref. [9], then $\mathcal{C} = (C_{\rm F} - \frac{C_{\rm A}}{2})\,{C_{\rm F}}^{-1}$, which for $N_c = 3$, gives $\mathcal{C} = -1/8$. One expects that the non-Abelian term is necessary for an effective model and thus that $0 < \mathcal{C} < 1$.

This vertex Ansatz allows us to avoid making a model for the dressed 3-gluon vertex for which there is little in the way of reliable information. It is the hope that the fit of $\mathcal{C}$ to lattice data will effectively compensate for these deficiencies. Our aim is not the vertex itself but a study of the relative importance of classes of diagrams for the BSE kernel for meson masses. This vertex Ansatz allows an algebraic approach to the BSE meson masses that is quite illustrative of new qualitative information.

From Eq. (2.14), non-perturbative summation equivalent to the integral equation

$$\Gamma_\sigma(p+k,p) = Z_1\gamma_\sigma - \mathcal{C}C_{\rm F}\int_q^\Lambda g^2 D_{\mu\nu}(p-q)\gamma_\mu S(q+k)\Gamma_\sigma(q+k,q)S(q)\gamma_\nu, \quad (2.15)$$

is a natural suggestion. This was studied in Ref. [10], with $S(q)$ being the self-consistent solution of the quark DSE, Eq. (2.1), containing the same dressed vertex. A fit to the lattice-QCD data for the vertex gave $\mathcal{C} = 0.51$, a value that confirms that attraction by a mechanism outside the scope of iterated gluon exchange is present.

An iterative representation is useful: $\Gamma_\mu = \sum_{i=0}\Gamma^i_\mu$, where $\Gamma^0_\mu = Z_1\,\gamma_\mu$, and i labels the number of internal gluon lines. The contribution with $i+1$ internal gluon lines is obtained from the i^{th} contribution by adding one gluon ladder. This is schematically depicted in Fig. 2.6.

2.4 Self-Consistent Quark-Gluon Vertex

2.4.1 A Wider Class of Quark-Gluon Vertex Dressing

In this section we propose to include self-consistent dressing of all internal vertices in the the ladder-summed dressing scheme for the quark-gluon vertex. The enlarged class of dressing diagrams considered here is obtained iteratively as depicted in Fig. 2.7. The contribution with i internal gluon lines is generated from three contributions having a smaller number of gluon lines by adding one gluon ladder with dressed vertices. If the number of gluon lines in the three vertex contributions are denoted j, k and l, then summation is made over j, k and l such that $j+k+l+1 = i$.

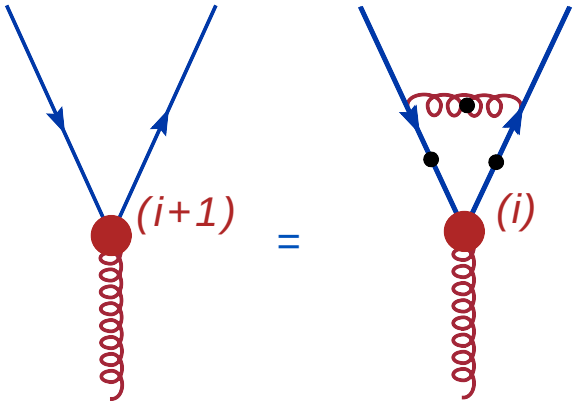

Figure 2.6: The iterative relation for successive terms in the ladder-summed vertex. Here the large filled circles denote the dressed quark-gluon vertex, the numbers in the parenthesis denote the numbers of gluon lines contributing to the particular vertices and the small filled circles denote that the propagators are fully dressed. Note that an important non-Abelian term is approximately accounted for by the effective color factor $\mathcal{C}$, as described in the text.

Again, $\Gamma_\mu = \sum_{i=0} \Gamma^i_\mu$. The iterative scheme is described by

$$\Gamma^i_\mu(p+k,p) = \\ -\mathcal{C}C_{\rm F} \sum_{\substack{j,k,l \\ i=j+k+l+1}} \int_q^\Lambda g^2 D_{\sigma\nu}(p-q)\Gamma^j_\sigma(p+k,q+k)S(q+k)\Gamma^l_\mu(q+k,q)S(q)\Gamma^k_\nu(q,p), \tag{2.16}$$

for $i \geq 1$.

If the iteration is carried to all orders, the equivalent integral equation is

$$\Gamma_\mu(p+k,p) = Z_1\gamma_\mu \\ -\mathcal{C}C_{\rm F}\int_q^\Lambda g^2 D_{\sigma\nu}(p-q)\Gamma_\sigma(p+k,q+k)S(q+k)\Gamma_\mu(q+k,q)S(q)\Gamma_\nu(q,p). \tag{2.17}$$

If the iteration is stopped to produce all vertex functions with up to n internal two point gluon lines, our improved scheme takes into account $1 + n(n+1)(n+2)/6$ diagrams. The corresponding ladder-summed vertex at that order contains a subset of $(n+1)$ of these diagrams.

In Fig. 2.8 we use low order diagrams to illustrate the more general class of dressing terms included this way. Note that the included diagrams are restricted to planar diagrams. The contribution from crossed gluon lines in Fig. 2.8d is not included. All diagrams of the ladder sum used in Ref. [10], such as Fig. 2.8a, are included, where the new element here is the self-consistent dressing of the internal vertices illustrated by Fig. 2.8b and Fig. 2.8c.

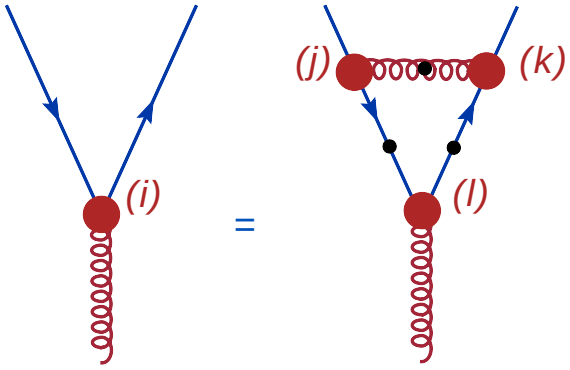

Figure 2.7: The iterative relation for the enlarged class of dressing diagrams considered in this work. Here the large filled circles denote the dressed quark-gluon vertex, the numbers in the parenthesis denote the numbers of gluon lines contributing to the particular vertices (with $j+k+l+1 \equiv i$) and the small filled circles denote that the propagators are fully dressed. The vertex contribution with i internal gluon lines is obtained from vertex contributions with less gluon lines. Note that an important effect of the non-Abelian 3-gluon coupling is approximately accounted for by the effective color factor $\mathcal{C}$, as described in the text.

2.4.2 Symmetry-Preserving Bethe-Salpeter Kernel

Chiral symmetry is one of the very important symmetries of the QCD Lagrangian, where an arbitrary rotation of quark colors at every point in space-time leaves the physical observables unchanged. Thus preserving this symmetry in deriving the BSE scattering kernel in a particular truncation scheme allows for a realistic description of mesons. A general prescription exists for expressing the chiral-symmetry preserving BSE kernel K as a functional of the quark self-energy, Σ, [38]. This preserves the Ward-Takahashi identity for the color singlet axial vector vertex and ensures that chiral pseudoscalars will remain massless, independent of model details.

In a flavor non-singlet channel, and with equal mass quarks, the axial-vector Ward-Takahashi identity is

$$-iP_\mu \Gamma^5_\mu(p+P,p) = S(p+P)^{-1}\gamma_5 + \gamma_5 S(p)^{-1} - 2m(\mu)\Gamma^5(p+P,p), \qquad (2.18)$$

where we have factored out the explicit flavor matrix. The color-singlet quantities Γ^5_μ and Γ^5 are the axial-vector vertex and the pseudoscalar vertex, respectively, and P is the total momentum. The amplitude $\Gamma^5_\mu(p+P,p)$ has a pseudoscalar meson pole. A consequence is that the meson BSE (2.3) for the (dominant) γ_5 amplitude at $P^2 = 0$ is equivalent to the chiral limit quark DSE for $B(p^2)$ and a non-zero value for the latter (DCSB) necessarily produces a massless pseudoscalar bound state [36].

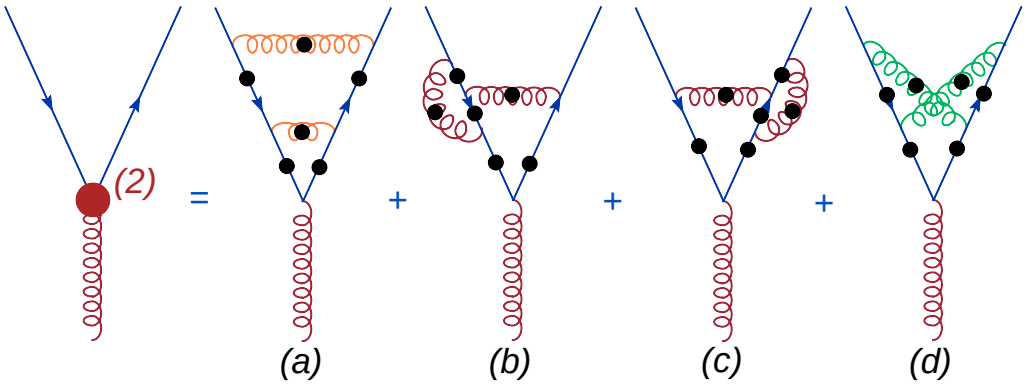

Figure 2.8: Vertex diagrams at $\mathcal{O}(g^5)$. Here the large red circle denotes the 2-nd order dressed quark-gluon vertex function (2 in the parenthesis denotes the number of gluon lines contributing to the vertex) and the small black circles on the propagators denote that the propagators are fully dressed. Previous work included the ladder structure typified by part (a). The enlarged class of dressing diagrams implemented in this work includes parts (b) and (c) as well. Non-planar diagrams such as part (d) are not accommodated by the present approach. We use an effective color factor to accommodate a major non-Abelian effect from the 3-gluon coupling as described in the text.

The general relation between the BSE kernel, K, and the quark self-energy, Σ, can be expressed through the functional derivative [38]

$$K(x',y';x,y) = -\frac{\delta}{\delta S(x,y)}\Sigma(x',y'). \tag{2.19}$$

It is to be understood that this procedure is defined in the presence of a bilocal external source for $\bar{q}q$ and thus S and Σ are not translationally invariant until the source is set to zero after the differentiation. An appropriate formulation is the Cornwall-Jackiw-Tomboulis effective action [55]. In this context, the above coordinate space formulation ensures the correct number of independent space-time variables will be manifest. Fourier transformation of that 4-point function to momentum representation produces $K(p,q;P)$ having the correct momentum flow appropriate to the BSE kernel for total momentum P.

The constructive scheme of Ref. [8] is an example of this relation as applied order by order to a Feynman diagram expansion for $\Sigma(p)$. An internal quark propagator $S(q)$ is removed and the momentum flow is adjusted to account for injection of momentum P at that point. The number of such contributions coming from one self-energy diagram is the number of internal quark propagators. Hence the rainbow self-energy generates the ladder BSE kernel. A 2-loop self-energy diagram (i.e., from 1-loop vertex dressing) generates 3 terms for the BSE kernel. One can confirm that the axial-vector Ward-Takahashi identity is preserved. Similarly, the vector Ward-Takahashi identity is also preserved.

To be more specific, with the discrete indices made explicit, we consider

$$K_{EF}^{GH} = -\frac{\delta \Sigma_{EF}}{\delta S_{GH}}, \tag{2.20}$$

with the self-energy given by the second term on the RHS of Eq. (2.1). After a decomposition

$$\Sigma(k) = \sum_{n=0}^{\infty} \Sigma^n(k), \tag{2.21}$$

according to the number n of gluon kernels in the vertex defined by

$$\Sigma^n(k) = C_{\rm F} \int_q^\Lambda g^2 D_{\mu\nu}(k-q)\gamma_\mu \, S(q) \Gamma^n_\nu(q,k), \tag{2.22}$$

for $n \geq 1$, with

$$\Sigma^0(k) = m_{bm} + C_{\rm F} \int_q^\Lambda g^2 D_{\mu\nu}(k-q)\gamma_\mu S(q) \gamma_\nu, \tag{2.23}$$

The order n contribution to the BSE kernel is

$$\begin{aligned}[K^n(k,q;P)]^{GH}_{EF} = & -C_{\rm F} g^2 D_{\mu\nu}(k-q) \left[\gamma_\mu\right]_{EG} \left[\Gamma^n_\nu(q_-,k_-)\right]_{HF} \\ & - C_{\rm F} \int_l^\Lambda g^2 D_{\mu\nu}(k-l) \left[\gamma_\mu S(l_+)\right]_{EL} \frac{\delta}{\delta S_{GH}(q_\pm)} \left[\Gamma^n_\nu(l_-,k_-)\right]_{LF}. \end{aligned} \tag{2.24}$$

This format is the same as used in Refs. [9] and [10], except that here the content of Γ^n_ν is more extensive. With a bare vertex, the first term of Eq. (2.24) produces the ladder kernel and the second term is zero. With a vertex up to 1-loop ($n = 1$), the first term of Eq. (2.24) produces the ladder term plus a 1-loop correction to one vertex, while the second term produces two terms: a 1-loop correction to the other vertex and a non-planar term corresponding to crossed gluon lines. These three corrections to the ladder kernel have the same structure as the kernels shown in parts (b), (c), and (d) of Fig. 2.8. At higher order, $n > 1$, the BSE kernel produced in the present work departs from that considered in Ref. [10].

After substitution of Eq. (2.24) into the BSE Eq. (2.3), and with a change of variables, the meson BSE becomes

$$\Gamma_M(k;P) = -C_{\rm F} \int_q^\Lambda g^2 D_{\mu\nu}(k-q)\gamma_\mu \left[\chi_M(q;P)\Gamma_\nu(q_-,k_-) + S(q_+)\Lambda_{M\nu}(q,k;P)\right], \tag{2.25}$$

where we denote by $\Lambda_{M\nu}$ the summation to all orders of the functional derivative of the vertex as indicated in Eq. (2.24). In particular,

$$\Lambda_{M\nu}(q,k;P) = \sum_{n=0}^{\infty} \Lambda^n_{M\nu}(q,k;P), \tag{2.26}$$

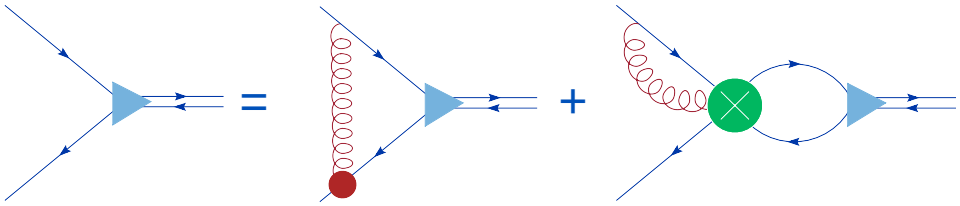

Figure 2.9: Kernel decomposition. The filled triangles represent the meson BSAs, the filled circle represents the dressed quark-gluon vertex and the crossed circle represents the Λ function.

with

$$[\Lambda^n_{M\nu}(q,k;P)]_{LF} = \int_l^\Lambda \frac{\delta}{\delta S_{GH}(l_\pm)} [\Gamma^n_\nu(q_-,k_-)]_{LF} [\chi_M(l;P)]_{GH} \,. \tag{2.27}$$

The vertex iteration given in Eq. (2.16) produces the recurrence formula for the $\Lambda^n_{M\nu}$

$$\begin{aligned}
\Lambda^n_{M\nu}(q,k;P) = -\mathcal{C}C_{\rm F} \sum_{\substack{j,k,h \\ n=j+k+h+1}} \\
\Big[\int_t^\Lambda g^2 D_{\rho\sigma}(q-t)\Gamma^j_\rho(q_+,t_+)\chi_M(t;P)\Gamma^k_\nu(t_-,t_-+k-q) \\
S(t_-+k-q)\Gamma^h_\sigma(t_-+k-q,k_-) \\
+\int_t^\Lambda g^2 D_{\rho\sigma}(k-t)\Gamma^j_\rho(q_+,t_++q-k)S(t_++q-k) \\
\Gamma^k_\nu(t_++q-k,t_+)\chi_M(t;P)\Gamma^h_\sigma(t_-,k_-) \\
+\int_t^\Lambda g^2 D_{\rho\sigma}(q-t)\Lambda^j_{M\rho}(q,t;P)S(t_-)\Gamma^k_\nu(t_-,t_-+k-q) \\
S(t_-+k-q)\Gamma^h_\sigma(t_-+k-q,k_-) \\
+\int_t^\Lambda g^2 D_{\rho\sigma}(q-t)\Gamma^j_\rho(q_+,t_+)S(t_+)\Lambda^k_{M\nu}(t,t+k-q;P) \\
S(t_-+k-q)\Gamma^h_\sigma(t_-+k-q,k_-) \\
+\int_t^\Lambda g^2 D_{\rho\sigma}(q-t)\Gamma^j_\rho(q_+,t_+)S(t_+)\Gamma^k_\nu(t_+,t_++k-q) \\
S(t_++k-q)\Lambda^h_{M\sigma}(t+k-q,k;P)\Big]
\end{aligned} \tag{2.28}$$

where $\Lambda^0_{M\nu}(q,k;P) = 0$.

The structure of the $q\bar{q}$ BS kernel produced by Eq. (2.25) and Eq. (2.28) is schematically depicted in Figs. 2.9 and 2.10. With a general interaction kernel, $g^2 D_{\rho\sigma}$, it is exceedingly difficult to implement this formal recurrence relation to

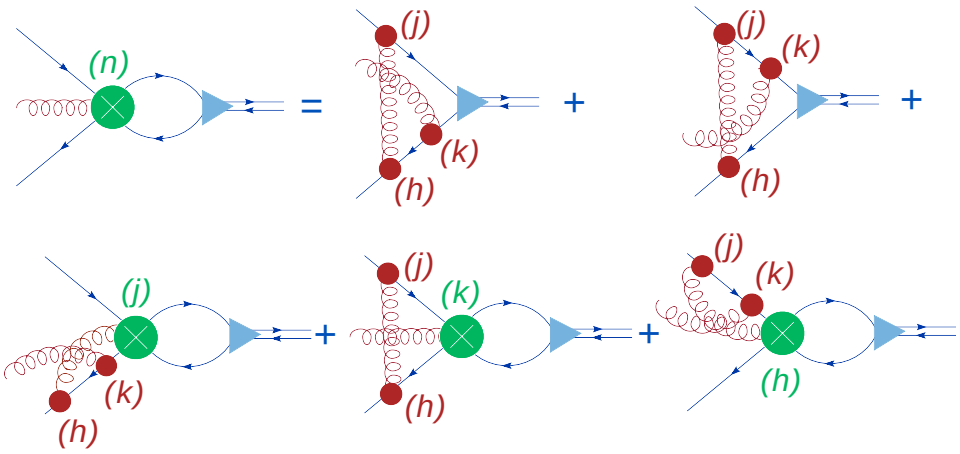

Figure 2.10: Λ function decomposition. The filled triangles represent the meson BSAs, the filled circles represent the dressed quark-gluon vertex functions and the crossed circles represent the Λ functions. The numbers in the parenthesis denote the numbers of gluon lines contributing to the particular functions.

obtain a BS kernel because of overlapping multiple integrals that compound rapidly with increasing order.

2.5 Algebraic Analysis

The ladder BSE for meson bound states is an integral equation with a one-loop kernel structure that must allow for the spinor structure of propagators and the meson amplitudes. With the four-dimensional space-time that one must use to maintain manifest covariance, and with dynamically generated quark propagators that one must use to preserve the Ward-Takahashi identities of chiral symmetry, the numerical task is large. Any scheme for corrections to the ladder truncation will in general add the complexity of multiple loop Feynman diagrams involving amplitudes that are only known after solution. For practical reasons the studies that have been able to investigate hadron states beyond ladder-rainbow (LR) truncation in recent years [8–10,39] have exploited the simplifications following from use of the Munczek-Nemirovsky (MN) model [40]. In this case, the basic element is a delta function that restricts the exchanged (or gluon) momentum to zero. It reduces both the quark DSE and the meson BSE to algebraic equations. There is only one parameter which is a strength set by m_ρ.

This simplified kernel has no support in the ultraviolet and one must be wary of its use for related physics. Bound state masses are relatively safe in this regard, even heavy quark states that sample short distance or large momenta due to the large quark mass scale present. Even with the MN model, the DSE solutions for the quark propagators have the correct power law behavior, and they continuously connect to the current quark mass, in the ultraviolet, apart from log corrections.

The dominant qualitative features of the DSE solutions of a realistic model are preserved in the MN model: large infrared strength giving DCSB and the (confining) absence of a mass pole. Our analysis is not aimed to provide a serious representation of experimental data; rather we aim for a deeper understanding of the relative importance of classes of higher-order diagrams for the BSE kernel for bound states. Because of the inherent complexity brought by use of a momentum distribution as a kernel, there is little information available in the literature on this topic. To obtain such information, we feel the price paid by dispensing with a clear connection to perturbative QCD is worthwhile in the initial stages.

2.5.1 The Interaction Model

In the ultraviolet, the kernel of the quark DSE, Eq. (2.1), takes the form

$$Z_1\gamma_\mu g^2 D_{\mu\nu}(k)\Gamma_\nu(q,p) \to 4\pi\alpha(k^2)\gamma_\mu D^{\rm free}_{\mu\nu}(k)\gamma_\nu, \tag{2.29}$$

where $k = p - q$, and $\alpha(k^2)$ is the renormalized strong running coupling, which has absorbed the renormalization constants of the quark and gluon propagators and the vertex. The ladder-rainbow truncations that have been phenomenologically successful in recent years for light quark hadrons adopt the form of Eq. (2.29) for all k^2 by replacing $\alpha(k^2)$ by $\alpha_{\rm eff}(k^2)$, which contains the correct 1-loop QCD ultraviolet form and a parameterized infrared behavior fitted to one or more chiral observables, such as $\langle\bar{q}q\rangle^0_\mu$. In this sense, such an $\alpha_{\rm eff}(k^2)$ contains those infrared effects of the dressed vertex $\Gamma_\nu(q,p)$ that can be mapped into a single effective amplitude corresponding to γ_ν for chiral quarks. Such a kernel does not have the explicit dependence upon quark mass that would occur if the vertex dressing were to be generated by an explicit Feynman diagram structure. In particular, one expects the vertex dressing to decrease with increasing quark mass. The effective ladder-rainbow kernel appropriate to heavy quark hadrons should have less infrared strength from dressing than is the case for light quark hadrons.

We use an explicit (but approximate) diagrammatic description of the dressed vertex $\Gamma_\nu(q,p)$, and to facilitate the analysis we make the replacement $4\pi\alpha_{\rm eff}(k^2)/k^2$ $\to (2\pi)^4\mathcal{G}^2\delta^4(k)$. This is the Munczek-Nemirovsky Ansatz [40] for the interaction kernel. The parameter $\mathcal{G}^2$ is a measure of the integrated kernel strength, and we expect this to be less than what would be necessary in ladder-rainbow format because of the infrared structure provided explicitly by the model vertex $\Gamma_\mu(q,p)$. The equations of the previous sections convert to model form by the replacement

$$g^2 D_{\mu\nu}(k) \to \left(\delta_{\mu\nu} - \frac{k_\mu k_\nu}{k^2}\right)(2\pi)^4\mathcal{G}^2\delta^4(k), \tag{2.30}$$

where we choose Landau gauge. It is the combination of Eq. (2.30) and the model vertex that is the DSE kernel. Comparisons of Eq. (2.30) with information about the dressed gluon 2-point function are incomplete. The resulting DSEs for the quark propagator and gluon-quark vertex are ultraviolet finite, thus the renormalization

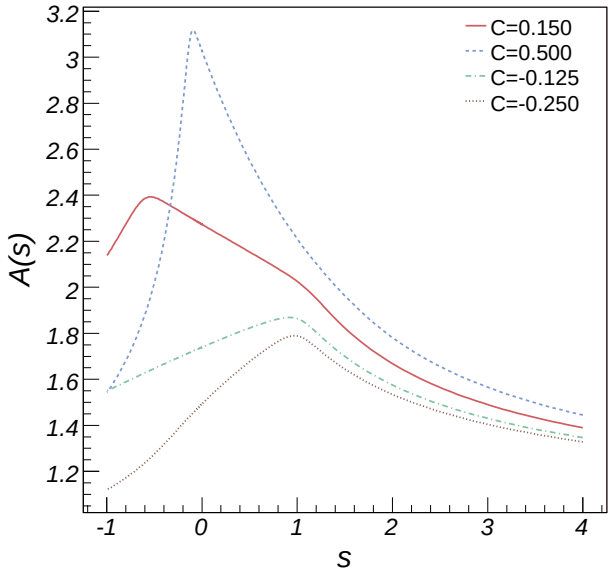

Figure 2.11: Quark propagator amplitude $A(s)$ versus Euclidean $s = p^2$. We use the interaction mass scale $\mathcal{G} = 1$ GeV and the current mass is $m = 0.0183\ \mathcal{G} = 18.3$ MeV. $\mathcal{C}$ dependence calculated with converged summation of vertex dressing, for $\mathcal{C} = 0.15$ (solid curve), $\mathcal{C} = 0.5$ (dashed curve), $\mathcal{C} = -0.125$ (dot-dashed curve) and $\mathcal{C} = -0.25$(dotted curve).

constants are unity: $Z_1 = Z_2 = 1$, and there is no distinction between bare and renormalized quark current mass. We set $m_{bm} = m(\mu) = m$.

2.5.2 The Algebraic Vertex and Quark Propagator

With this kernel, the vertex integral equation Eq. (2.17) determines solutions for $k = 0$ and we define $\Gamma_\mu(p, p) \equiv \Gamma_\mu(p)$. Eq. (2.17) reduces to the algebraic form

$$\Gamma_\mu(p) = \gamma_\mu - \mathcal{C}\mathcal{G}^2\Gamma_\sigma(p)S(p)\Gamma_\mu(p)S(p)\Gamma_\sigma(p)\ . \tag{2.31}$$

In obtaining this form, we have used $3C_{\rm F}/4 = 1$, where the extra factor of $3/4$ arises from the transverse projector. The general form of the vertex is:

$$\Gamma_\mu(p) = \alpha_1(p^2)\gamma_\mu + \alpha_2(p^2)\not{p}p_\mu - \alpha_3(p^2)ip_\mu + \alpha_4(p^2)i\gamma_\mu\not{p} \tag{2.32}$$

where $\alpha_i(p^2)$ are invariant amplitudes. From Eq. (2.31) we find $\alpha_4 = 0$, as was the case for the related models in Refs. [9] and [10].

The vertex is a sum over contributions with exactly n internal effective gluon kernels according to

$$\Gamma_\mu(p) = \sum_{n=0}^{\infty}\Gamma_\mu^n(p), \tag{2.33}$$

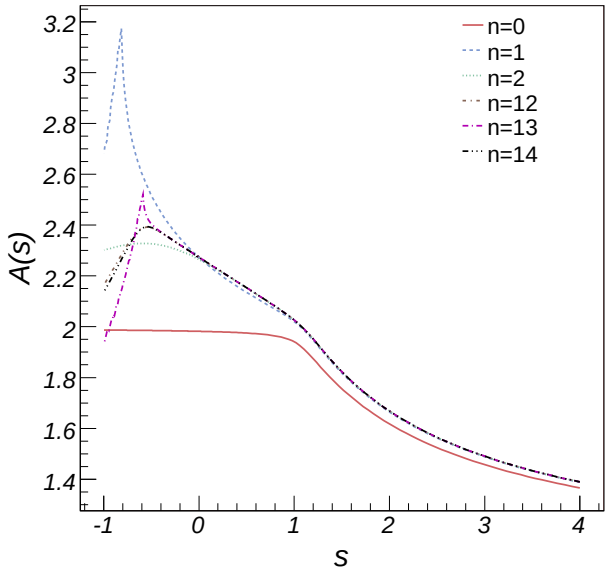

Figure 2.12: Quark propagator amplitude $A(s)$ versus Euclidean $s = p^2$. We use the interaction mass scale $\mathcal{G} = 1$ GeV and the current mass is $m = 0.0183$ $\mathcal{G} = 18.3$ MeV. We show the influence of vertex dressing to order n as described in the text. For $\mathcal{C} = 0.15$, $n = 0$ yields the solid curve and the result is the ladder-rainbow truncation. The other curves are $n = 1$ (long dashed curve, 1-loop vertex), $n = 2$ (dotted curve, 2-loop vertex), $n = 12$ (dot - short dashed curve), $n = 13$ (dot - long dashed curve) and $n = 14$ (dot dot dot - dashed curve) order of dressing for the quark gluon vertex.

with the general contribution given by the recursive relation

$$\Gamma^n_\mu(p) = -\mathcal{C}\mathcal{G}^2 \sum_{\substack{j,k,l \\ n=j+k+l+1}} \Gamma^j_\nu(p) S(p) \Gamma^k_\mu(p) S(p) \Gamma^l_\nu(p), \tag{2.34}$$

where $\Gamma^0_\mu(p) = \gamma_\mu$. Substitution of the form $S(p)^{-1} = i\not{p}A(p^2) + B(p^2)$ into Eq.(2.34) gives $\Gamma^n_\mu(p^2)$ in terms of the functions $A(p^2)$ and $B(p^2)$. These latter functions must be solved simultaneously with the vertex at the given order. The algebraic form of the gap equation for the propagator is

$$S(p)^{-1} = i\not{p} + m + \mathcal{G}^2 \gamma_\mu S(p) \Gamma_\mu(p), \tag{2.35}$$

where again the transverse projector and the color factor combine to yield $3C_{\rm F}/4 = 1$. After projection onto the two Dirac amplitudes we have

$$A(p^2) = 1 - \mathcal{G}^2 \frac{i}{4} tr \left[\frac{\not{p}}{p^2} \gamma_\mu S(p)\, \Gamma_\mu(p) \right], \tag{2.36}$$

$$B(p^2) = m + \mathcal{G}^2 \frac{1}{4} tr \left[\gamma_\mu\, S(p)\, \Gamma_\mu(p) \right]. \tag{2.37}$$

Equations (2.34), (2.36) and (2.37) are solved simultaneously at a specified order n of vertex dressing.

In the case where one is limited to a strict ladder summation for the vertex with bare internal vertices, closed form expressions for the vertex amplitudes α_i in terms of A and B are obtainable [9, 10]. With the enlarged class of dressing considered here, corresponding closed form expressions have not been obtained. However numerical evaluation is sufficient for the vertex and propagator amplitudes. A numerical treatment of the BSE kernel must be made in any case. Numerical solution of the simultaneous algebraic equations for the vertex and propagator is carried out here using the algebraic and numerical tools of *Mathematica* [56] with the assistance of the *FeynCalc* package used for computer-algebraic evaluation of the Dirac algebra [57].

The model parameter $\mathcal{C}$ for the vertex is determined by a fit to selected global features of quenched lattice-QCD data for the quark propagator [58] and the quark-gluon vertex [47]. This data is available for both quantities at current quark mass $m = \bar{m} = 60$ MeV. This is the same data as used to fit the same parameter $\mathcal{C}$ in Ref. [10]. A different result will therefore reflect the wider class of vertex dressing herein. To facilitate comparison we also eliminate the role of the interaction strength mass scale parameter, $\mathcal{G}$, in this step by dealing with dimensionless quantities. $\mathcal{G}$ will later be fixed by requiring that m_ρ be reproduced.

The lattice-QCD data for the quark propagator indicates that $Z_{qu}(0) \equiv 1/A_{qu}(0) \approx 0.7$ and $M_{qu}(0) \equiv B(0)/A(0) \approx 0.42$ GeV. Following Ref. [10] the lattice data for both the propagator and the vertex in the infrared is characterized by the set of

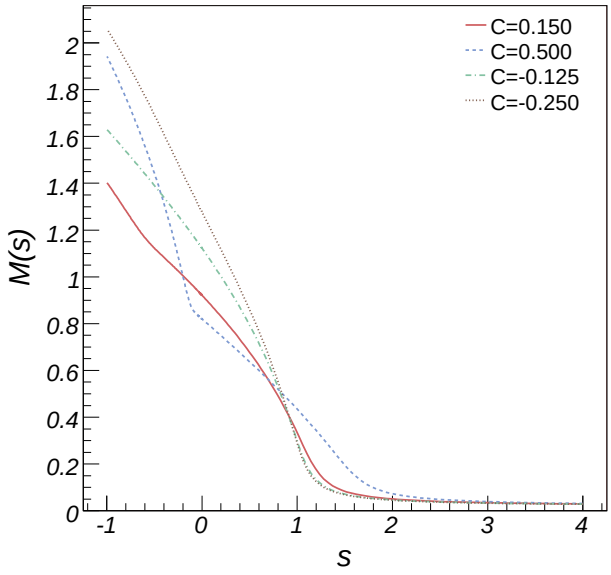

Figure 2.13: Quark mass function $M(s)$ versus Euclidean $s = p^2$. We use the interaction mass scale $\mathcal{G} = 1$ GeV and the current mass is $m = 0.0183\ \mathcal{G} = 18.3$ MeV. $\mathcal{C}$ dependence calculated with converged summation of vertex dressing, for $\mathcal{C} = 0.15$ (solid curve), $\mathcal{C} = 0.5$ (dashed curve), $\mathcal{C} = -0.125$ (dot-dashed curve) and $\mathcal{C} = -0.25$(dotted curve).

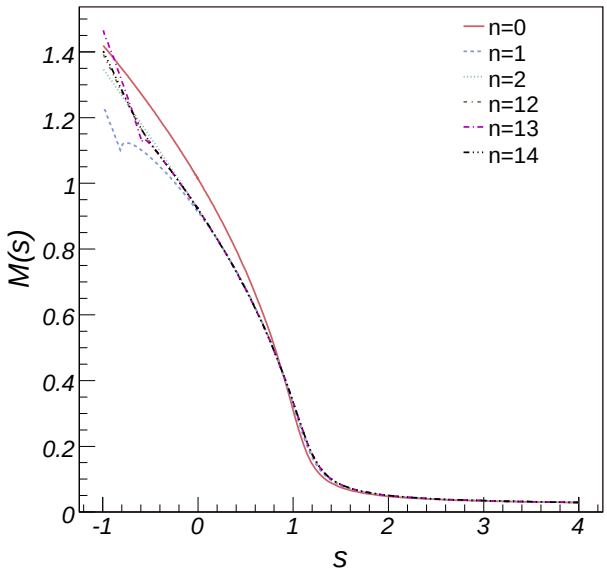

Figure 2.14: Quark mass function $M(s)$ versus Euclidean $s = p^2$. We use the interaction mass scale $\mathcal{G} = 1$ GeV and the current mass is $m = 0.0183\ \mathcal{G} = 18.3$ MeV. We show the influence of vertex dressing to order n as described in the text. For $\mathcal{C} = 0.15$, $n = 0$ yields the solid curve and the result is the ladder-rainbow truncation. The other curves are $n = 1$ (long dashed curve, 1-loop vertex), $n = 2$ (dotted curve, 2-loop vertex), $n = 12$ (dot - short dashed curve), $n = 13$ (dot - long dashed curve) and $n = 14$ (dot dot dot - dashed curve) order of dressing for the quark gluon vertex.

four dimensionless quantities evaluated at $p^2 = 0$:

$$A(0, m_{60}) = 1.4 \tag{2.38}$$

$$\alpha_1(0, m_{60}) = 2.1 \tag{2.39}$$

$$-M(0, m_{60})^2 \alpha_2(0, m_{60}) = 7.1 \tag{2.40}$$

$$-M(0, m_{60}) \alpha_3(0, m_{60}) = 1.0, \tag{2.41}$$

where $m_{60} = \bar{m}/M_{qu}(0)$. The best fit to these quantities gives $\mathcal{C} = 0.34$ with an average relative error of $\bar{r} = 24$ % and standard deviation $\sigma_r = 70$ %. The quality of fit is about the same as in Ref. [10], and changes $\Delta\mathcal{C} \approx \pm 0.2$ are not significant in this regard. For example, $\mathcal{C} = 0.15$ leads to $\bar{r} = 39$ % and $\sigma_r = 72$ %. We will use $\mathcal{C} = 0.15$ because the resulting vertex at timelike p^2 is more convergent with respect to increasing order of dressing. The value of $\mathcal{C}$ being significantly greater than the strict ladder sum limit, $\mathcal{C} = -1/8$, we see that the attraction provided by the 3-gluon coupling is important for the vertex. However, the amount of attraction that must be provided in this phenomenological way in the present work is less than what was required in Ref. [10] to fit the same lattice quantities. In that work, $\mathcal{C} = 0.51$ was found necessary. We attribute this difference to the fact that a wider class of self-consistent dressing diagrams is included in the present approach. Attraction is provided by every vertex that is internal in the sense of Fig. 2.7.

In Figs. 2.11 and 2.12 we present the results for our calculations of $A(p^2)$ for different values of $\mathcal{C}$ and different orders of quark-gluon vertex dressing. We set $\mathcal{G} = 1$ GeV, so all dimensionful quantities are measured in units of $\mathcal{G}$. The current mass is $m_q = 0.0183\,\mathcal{G}$. One can see from Fig. 2.11 that $\mathcal{C}$ has a major impact on the behavior of $A(s)$, especially in the timelike region. Fig. 2.12 shows that with $n = 14$ as the order of dressing of the quark-gluon vertex, we achieved convergence of the quark propagator function $A(p^2)$ for $p^2 > -\mathcal{G}^2$. The same is true for the function $B(p^2)$. The relative measure of the convergence of the quark propagator functions with n is the convergence of the meson masses calculated using the solutions for the propagators. It will be shown later on that our calculations of m_π and m_ρ have converged to better than 1% for $n = 14$. For heavier current quarks, the convergence region for the solutions of $A(p^2)$ and $B(p^2)$ extends deeper into the time-like region of p^2, which allows for convergent calculations of heavier meson masses.

In Figs. 2.13 and 2.14 we present the results for our calculations of $M(p^2) = B(p^2)/A(p^2)$ for different values of $\mathcal{C}$ and different orders of quark-gluon vertex dressing. Again these calculations have $\mathcal{G} = 1$ GeV, so all dimensionful quantities are measured in units of $\mathcal{G}$. The vertex parameter $\mathcal{C}$ has a modest impact on the behavior of $M(s)$.

Figures 2.15, 2.16 and 2.17 display the results for the vertex amplitudes $\alpha_i(s)$ corresponding to different orders of vertex dressing. Successive orders after 1-loop ($n = 1$) serve to enhance the infrared strength for $s < 1$. The convergence with n is monotonic, in contrast to the convergence of the BSE kernel that is generated from this vertex, as discussed later.

The quark condensate in the present model is given by

$$\langle\bar{q}q\rangle^0 = -\frac{3}{4\pi^2}\int_0^{s_0} ds s \frac{B_0(s)}{s\,A_0^2(s)+B_0^2(s)}, \tag{2.42}$$

in terms of the chiral limit quark propagator amplitudes. There is no renormalization necessary because there is a spacelike s_0 for which $B_0(s>s_0)=0$. Because of the underrepresentation of the ultraviolet strength of the interaction in this model, the condensate is characteristically too low. In particular, we find

$$-\langle\bar{q}q\rangle^0_{\mathcal{C}=0.15} = (0.2146\ \mathcal{G})^3 = (0.1266\ \text{GeV})^3 \tag{2.43}$$

with $\mathcal{G}=0.59$ GeV. The rainbow-ladder result ($\mathcal{C}=0$) is $-\langle\bar{q}q\rangle^0_{\rm LR} = \mathcal{G}^3/(10\pi^2) = (0.1277\ \text{GeV})^3$. Thus one can see that the vertex dressing decreases the condensate slightly. In more detail, we have

$$\frac{\langle\bar{q}q\rangle^0_{\rm LR}}{\langle\bar{q}q\rangle^0_{\mathcal{C}=0.15}} = 1.03, \tag{2.44}$$

which indicates that the ladder-rainbow truncation overestimates the condensate by 3% compared to the more completely dressed vertex considered here. The previous study [10] with a more restricted class of vertex dressing diagrams found that the ladder-rainbow truncation was 18% too low.

2.5.3 The Algebraic Bethe-Salpeter Kernel for Mesons

Substitution of the model interaction kernel Eq. (2.30) into the meson BSE, Eq. (2.25), produces the algebraic form

$$\Gamma_M(k;P) = -\mathcal{G}^2\gamma_\mu\left\{\chi_M(k;P)\Gamma_\mu(k_-) + S(k_+)\Lambda_{M\mu}(k;P)\right\}. \tag{2.45}$$

The previous general recurrence relation Eq. (2.28) for the general term of $\Lambda_{M\nu} = \sum_{n=0}^{\infty}\Lambda^n_{M\nu}$ now has the algebraic form

$$\Lambda^n_{M\nu}(k;P) = -\mathcal{C}\mathcal{G}^2 \sum_{\substack{j,k,h\\ n=j+k+h+1}} \tag{2.46}$$
$$\left[\Gamma^j_\rho(k_+)\chi_M(k;P)\Gamma^k_\nu(k_-)\,S(k_-)\Gamma^h_\rho(k_-) + \Gamma^j_\rho(k_+)S(k_+)\Gamma^k_\nu(k)\chi_M(k;P)\Gamma^h_\rho(k_-)\right.$$
$$+\Lambda^j_{M\rho}(k;P)S(k_-)\Gamma^k_\nu(k_-)S(k_-)\Gamma^h_\sigma(k_-) + \Gamma^j_\rho(k_+)S(q_+)\Lambda^k_{M\nu}(k;P)S(k_-)\Gamma^h_\rho(k_-)$$
$$\left.+\Gamma^j_\rho(k_+)S(k_+)\Gamma^k_\nu(k_+)S(k_+)\Lambda^h_{M\sigma}(k;P)\right].$$

If we work at a given order, n, of vertex dressing, then the quark propagator, the dressed vertex, and the BSE kernel can be constructed recursively. By construction, chiral symmetry is preserved and the chiral pseudoscalar states are massless, independent of model parameters. Because of the algebraic structure, in which the

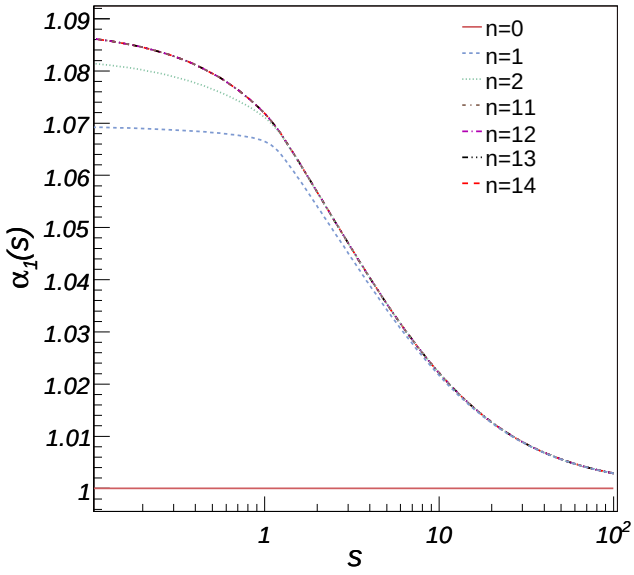

Figure 2.15: Gluon-quark vertex amplitude $\alpha_1(s)$ versus Euclidean $s = p^2$, for $\mathcal{C} = 0.15$. We use the interaction mass scale $\mathcal{G} = 1$ GeV and the current mass is $m = 0.0183\ \mathcal{G} = 18.3$ MeV. $n = 0$ (solid curve) results from the bare vertex and is the ladder-rainbow truncation. The other curves are $n = 1$ (short dashed curve, 1-loop vertex dressing), $n = 2$ (dotted curve), $n = 11$ (dot - short dashed curve), $n = 12$ (dot - long dashed curve), $n = 13$ (dot dot dot - dashed curve) and $n = 14$ (long dashed curve).

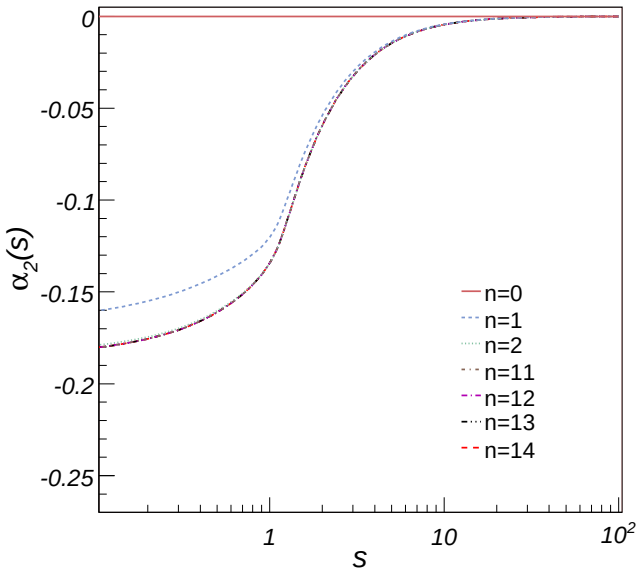

Figure 2.16: Gluon-quark vertex amplitude $\alpha_2(s)$ versus Euclidean $s = p^2$, for $\mathcal{C} = 0.15$. We use the interaction mass scale $\mathcal{G} = 1$ GeV and the current mass is $m = 0.0183\ \mathcal{G} = 18.3$ MeV. $n = 0$ (solid curve) results from the bare vertex and is the ladder-rainbow truncation. The other curves are $n = 1$ (short dashed curve, 1-loop vertex dressing), $n = 2$ (dotted curve), $n = 11$ (dot - short dashed curve), $n = 12$ (dot - long dashed curve), $n = 13$ (dot dot dot - dashed curve) and $n = 14$ (long dashed curve).

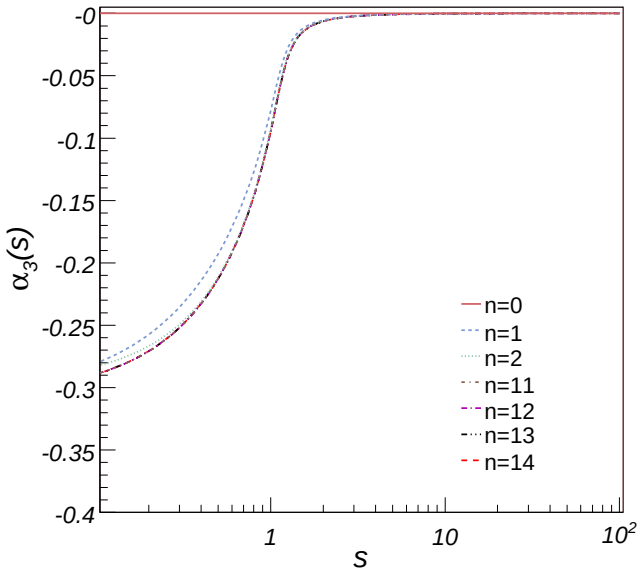

Figure 2.17: Gluon-quark vertex amplitude $\alpha_3(s)$ versus Euclidean $s = p^2$, for $\mathcal{C} = 0.15$. We use the interaction mass scale $\mathcal{G} = 1$ GeV and the current mass is $m = 0.0183\ \mathcal{G} = 18.3$ MeV. $n = 0$ (solid curve) results from the bare vertex and is the ladder-rainbow truncation. The other curves are $n = 1$ (short dashed curve, 1-loop vertex dressing), $n = 2$ (dotted curve), $n = 11$ (dot - short dashed curve), $n = 12$ (dot - long dashed curve), $n = 13$ (dot dot dot - dashed curve) and $n = 14$ (long dashed curve).

BS amplitude $\Gamma_M(k;P)$ appears on both sides of Eq. (2.45) with the same $q\bar{q}$ relative momentum k, a physical solution where $P^2 = -M_M^2$ is independent of k is defined only at $k = 0$. That is, the quark and antiquark have momenta ηP and $(1-\eta)P$. (Here we consider only equal mass quarks and thus have chosen $\eta = 1/2$.) The Munczek-Nemirovsky model interaction does not allow momentum transfer to quarks. This is a restriction present in all hadron studies made within this model. We define $\Gamma_M(P) = \Gamma_M(k=0;P)$, after which the form in which we solve the BSE is

$$\Gamma_M(P) = -\mathcal{G}^2\,\gamma_\mu S(\frac{P}{2})\left\{\Gamma_M(P)\,S(-\frac{P}{2})\,\Gamma_\mu(-\frac{P}{2}) + \Lambda_{M\mu}(0;P)\right\}. \tag{2.47}$$

2.6 Meson Masses and Results

The general form of a meson BS amplitude can be written as

$$\Gamma_M(k;P) = \sum_i \mathcal{K}^i(k;P)\,f_M^i(k^2, k\cdot P; P^2), \tag{2.48}$$

where the $\mathcal{K}^i(k;P)$ are a complete set of independent covariants constructed from Dirac matrices and momenta that transform in a manner specified by the quantum numbers of the meson under consideration. The $f_M^i(k^2, k\cdot P; P^2)$ are the corresponding invariant amplitudes. (We do not show explicitly the color singlet unit matrix.) The model BSE under consideration here, Eq. (2.47), has relative momentum $k = 0$, and the set of covariants is reduced considerably. We have

$$\Gamma_M(P) = \sum_{i=1}^{N} \mathcal{K}^i(P) f_M^i(P^2) \tag{2.49}$$

and it is convenient to develop a set of projection operators $\mathcal{P}_j$ that allow us to isolate each amplitude according to

$$f_M^j = Tr_D\left[\mathcal{P}_j \Gamma_M\right]. \tag{2.50}$$

Then projection of the BSE, Eq. (2.47), yields the eigenvalue equation

$$f(P^2) = \mathcal{H}(P^2)\,f(P^2), \tag{2.51}$$

where $f = (f_M^1, f_M^2 \cdots)$ is a vector of invariant amplitudes and the matrix $\mathcal{H}(P^2)$ is an $N \times N$ representation of the kernel.

The mass, M_M, of the lowest bound state is obtained from the highest negative value of P^2 for which

$$\det\left[\mathcal{H}(P^2) - I\right]_{P^2+M_M^2=0} = 0. \tag{2.52}$$

This method, namely the solution of the characteristic polynomial for Eq. (2.51), has also been followed in earlier work of this type [9, 10].

2.6.1 The Pion

The general form of the π Bethe-Salpeter amplitude requires four covariants and is

$$\Gamma_\pi(k;P) = \gamma_5\,[i\,f_\pi^1 + \not{P}\,f_\pi^2 + \not{k}\,k\cdot P\,f_\pi^3 + \sigma_{\mu\nu}k_\mu P_\nu\,f_\pi^4], \tag{2.53}$$

in terms of amplitudes $f_\pi^i(k^2, k\cdot P; P^2)$. We do not show flavor dependence since we treat we treat u-quarks and d-quarks the same in all other respects. In the present case only two covariants survive and we have

$$\Gamma_\pi(P) = \gamma_5\,[if_\pi^1(P^2) + \not{P} f_\pi^2(P^2)]. \tag{2.54}$$

Convenient projection operators in this case are

$$\mathcal{P}_1 = -\frac{i}{4}\gamma_5, \quad \mathcal{P}_2 = \frac{1}{4P^2}\not{P}\gamma_5. \tag{2.55}$$

2.6.2 The Rho

The general form of the ρ Bethe-Salpeter amplitude requires eight transverse covariants and the corresponding amplitudes. Specific choices that have been found convenient in earlier work are given in Refs. [34, 59]. In the present case, the most general form is simply

$$\Gamma_{\rho\,\mu}(P) = \left(\delta_{\mu\nu} - \frac{P_\mu P_\nu}{P^2}\right)\,\gamma_\nu f_\rho^1(P^2) + \sigma_{\mu\nu}P_\nu f_\rho^2(P^2). \tag{2.56}$$

Again a unit color matrix is understood and we treat u-quarks and d-quarks as the same. Convenient projection operators that isolate the amplitudes are

$$\mathcal{P}_1 = \frac{1}{12}\gamma_\mu, \quad \mathcal{P}_2 = \frac{1}{12P^2}\sigma_{\mu\nu}P_\nu. \tag{2.57}$$

2.6.3 Vertex Dressing for Light Quarks

There are a total of three parameters: $\mathcal{C} = 0.15$, which has already been set by the quenched lattice data for the quark propagator and the gluon-quark vertex, while the experimental m_π and m_ρ are used to set the other two: the interaction mass scale, $\mathcal{G} = 0.59$ GeV, and the current mass for the u/d quark, $m = 0.0183\,\mathcal{G} = 11$ MeV. The fully dressed vertex model is used in these determinations. In practice, we require convergence to 3 significant figures for the masses and this is achieved with a vertex dressed to order $n = 14$. Table 2.1 shows how the vertex dressing influences m_π and m_ρ.

To confirm that our constructed BSE kernel preserves chiral symmetry, we verified that with $m = 0$ and to any order of vertex dressing, the chiral pion is massless to the numerical accuracy considered. The physical m_π is not fixed perfectly by the symmetry but is almost so. The explicit symmetry breaking by the current mass is sufficient to determine m_π for all orders of vertex dressing except for a few

Table 2.1: Effect of quark-gluon vertex dressing to order n upon the masses of the π and ρ mesons (in GeV). The ladder-rainbow (LR) truncation corresponds to $n = 0$, one loop vertex dressing corresponds to $n = 1$, etc, while the full model result (converged to 3 significant figures) is labeled $n = \infty$. Also displayed for m_ρ is the mass error, Δm_ρ, and the relative mass error, $\Delta m_\rho/m_\rho$, of the LR truncation of the present model compared to a previous model [10] based on a limited class of vertex dressing diagrams. The mass scale parameter is $\mathcal{G} = 0.59$ GeV, the current mass of the u/d-quark is $m = 0.0183\,\mathcal{G} = 11$ MeV, and $\mathcal{C} = 0.15$.

Vertex Dressing	m_π	m_ρ	Δm_ρ	$\frac{\Delta m_\rho}{m_\rho}$	$\frac{\Delta m_\rho}{m_\rho}$ [10]
$n = 0$ (LR)	0.140	0.850	+0.074	+0.095	+0.295
$n = 1$ (1-loop)	0.135	0.759	-0.017	-0.022	—
$n = 2$	0.135	0.781	+0.005	+0.006	+0.096
$n = 3$	0.135	0.772	-0.004	-0.005	N/A
$n = 4$	0.135	0.778	+0.002	+0.003	N/A
$n = \infty$ (full model)	0.135	0.776	0.0	0.0	0.0

% error in the ladder-rainbow truncation ($n = 0$). Since the same behavior was observed in earlier work of this nature [9,10], this result is quite model-independent.

The response of m_ρ to increasing order of vertex dressing shows that the ladder-rainbow truncation is missing 74 MeV of attraction compared to the full model result. The magnitude of the error decreases with each added order of vertex dressing. The relative error in the ladder-rainbow mass is 9.5% in the present self-consistent vertex model, compared to 29.5% in the vertex model of Ref. [10]. In the present approach each diagram for the dressed vertex has each of its internal vertices dressed in a self-consistent way. This self-consistency introduces a greater non-linearity into the dependence of the vertex, and BSE kernel, upon the effective strength $(-\mathcal{C}\,\mathcal{G}^2)$ of the relevant integral equation for the vertex. This in turn significantly alters the response of the meson mass calculation to changes in either of these parameters or the order n (maximum number of gluon lines) of the summed vertex.

Some of the attraction due to the corrections to ladder-rainbow truncation in Ref. [10] is offset here by a combination of two effects: a) the presence of the extra diagrams we account for by generating the vertex self-consistently, and b) the resulting smaller values of the strength parameters $\mathcal{C}$ and $\mathcal{G}$ found necessary to fit the lattice vertex data, as well as m_π and m_ρ. Note that in either Ref. [10] or in the present self-consistent scheme for the vertex, diagrams with n gluon lines contain an overall factor $(-\mathcal{C}\,\mathcal{G}^2)^n$. However in the former scheme there is only one diagram of order n, while in the self-consistent scheme, the number is $n(n+1)/2$. With increasing n, this latter effect can quickly alter the balance between positive and negative contributions and can offset the effect of smaller strength for the kernel. In fact calculations of m_ρ for a range of $\mathcal{C}$ values up to 0.5 show that the error of

Table 2.2: Error of the ladder-rainbow truncation for equal quark mass vector mesons in the u/d-, s-, c-, and b-quark regions, according to calculated mass and effective binding energies (in GeV). The ladder-rainbow (LR) truncation corresponds to order $n = 0$ in vertex dressing and the full model result corresponds to vertex dressing to all orders, $n = \infty$, in this model. The mass scale parameter is $\mathcal{G} = 0.59$ GeV, and $\mathcal{C} = 0.15$.

	ladder-rainbow $n = 0$	full model $n = \infty$	LR % error this model	[10]
$m_{u,d} = 0.011$				
m_ρ	0.850	0.776	9.5%	30%
$\mathcal{BE}_\rho$	0.346	0.311	11%	
$m_s = 0.165$				
m_ϕ	1.08	1.02	6.0%	21%
$\mathcal{BE}_\phi$	0.350	0.320	9.0%	
$m_c = 1.35$				
$m_{J/\psi}$	3.11	3.09	0.3%	3.5%
$\mathcal{BE}_{J/\psi}$	0.260	0.260	0%	
$m_b = 4.64$				
m_Υ	9.46	9.46	0%	0%
$\mathcal{BE}_\Upsilon$	0.100	0.100	0%	

the ladder-rainbow truncation is always less in the self-consistent vertex dressing scheme; the converged m_ρ never becomes more than 11% below the ladder-rainbow value. Thus the extra diagrams, or consequent non-linearity of the self-consistent vertex dressing scheme, is the dominant reason for the evident improved accuracy of ladder-rainbow truncation arising from the present simple algebraic model. It is not known whether this finding carries over to a more realistic treatment of QCD dynamics.

2.6.4 Current Quark Mass Dependence

One expects the influence of vertex dressing to decrease with increasing quark mass because of the internal quark propagators in the vertex. Thus the LR truncation should become more accurate for mesons involving heavier quarks. It is useful to quantify this for the following reason. Phenomenological LR kernels [32] are capable of incorporating many realistic features of QCD modeling, and have been developed to provide efficient descriptions of light quark mesons, their elastic and transition form factors, and decay constants. A parameterized LR kernel that reproduces the experimental values of m_π and m_ρ has, by definition, absorbed the effective dressing of the vertex. The present work suggests that this is an amount of vertex attraction worth 9.5% of the vector meson mass. However this phenomeno-

logical representation of the dressing does not have an explicit dependence upon quark mass that would occur if the vertex dressing were to be generated by an explicit Feynman diagram structure. One would expect such a phenomenological LR kernel to be progressively too attractive when applied to mesons with progressively heavier quarks.

The present model provides an opportunity to explore how much of the final meson mass result is attributable to vertex dressing and how this varies with quark mass. In Table 2.2 we display results for the ground state vector mesons in the u/d-, s-, c-, and b-quark regions for both rainbow-ladder truncation and the full model. Again the quark current masses are determined so that the full model reproduces experiment. We see that the amount by which the LR masses are too large decreases steadily with increasing quark mass, as expected. The LR truncation here is missing 6% of attraction for m_ϕ compared to 21% in the restricted class of dressing diagram considerably previously [10]. The LR truncation is quite accurate for the $c\bar{c}$ and $b\bar{b}$ vector states, as expected.

For the larger quark masses, the meson mass is dominated by the sum of the quark masses. We also express the results in a form that has this large mass scale removed. For each state in Table 2.2, we display an effective binding energy defined as $\mathcal{BE} = 2M_q(0) - m_V$, where $M_q(0)$ is the quark mass function obtained from the DSE solution at $p^2 = 0$, and m_V is the meson mass. Thus $M_q(0)$ is being used as a rough measure of the constituent quark mass. The use of a single p^2 point may well be an overestimate of constituent masses. Furthermore, our fitted current quark masses are on the upper edge of what is usually quoted at a renormalization scale of $\mu = 2$ GeV [60]. Such an overestimate would be amplified in the infrared region via a DSE solution for the quark propagator. Nevertheless, a relative comparison should be meaningful. Table 2.2 shows the dependence of $\mathcal{BE}$ upon the current quark mass for the fully dressed model and the ladder-rainbow truncation. On this basis, the relative amount of overbinding of the LR truncation is consistent with its relative lack of attraction with respect to the mass results.

In Table 2.3 we display the full model results for both the vector and pseudoscalar $q\bar{q}$ states. The masses for η_c and η_b are predictions. In the c- and b-quark regions, these results are essentially the same as those of Ref. [10], because the differences in the employed model of vertex dressing become irrelevant when any dressing contribution is suppressed by the large mass of propagators internal to the vertex. The systematics of the mass dependence of hyperfine splitting that spans the c- and b-quark regions, here and in earlier work [10], strongly suggests that the experimental value [60], $m_{\eta_b} = 9.30 \pm 0.03$, is too low.

2.7 Summary

We have taken advantage of an algebraic model to enlarge the class of diagrams for the quark-gluon dressed vertex that can be incorporated into the Bethe-Salpeter kernel, while allowing a practical application to the calculation of meson masses. A given expansion of the vertex in diagrammatic form, produces a diagrammatic

Table 2.3: The masses of the equal quark mass vector and pseudoscalar mesons in the u/d-, s-, c-, and b-quark regions, and the current quark masses required to reproduce the experimental vector meson masses. All are in units of GeV. The values of m_{η_c} and m_{η_b} are predictions. Experimentally [60], $m_{\eta_c} = 2.9797 \pm 0.00015$ and $m_{\eta_b} = 9.30 \pm 0.03$. The fictitious pseudoscalar $0^-_{s\bar{s}}$ is included for comparison with other studies [10].

$m_{u,d} = 0.011$	$m_s = 0.165$	$m_c = 1.35$	$m_b = 4.64$
$m_\rho = 0.776$	$m_\phi = 1.02$	$m_{J/\psi} = 3.09$	$m_{\Upsilon(1S)} = 9.46$
$\mathcal{BE}_\rho = 0.311$	$\mathcal{BE}_\phi = 0.320$	$\mathcal{BE}_{J/\psi} = 0.260$	$\mathcal{BE}_\Upsilon = 0.100$
$m_\pi = 0.135$	$m_{0^-_{s\bar{s}}} = 0.61$	$m_{\eta_c} = 2.97$	$m_{\eta_b} = 9.43$
$\mathcal{BE}_\pi = 0.953$	$\mathcal{BE}_{0^-} = 0.727$	$\mathcal{BE}_{\eta_c} = 0.380$	$\mathcal{BE}_{\eta_b} = 0.130$

expansion of the quark self-energy, which in turn specifies a diagrammatic expansion of the BSE kernel if chiral symmetry is to be respected. This procedure relieves the phenomenology of the task of reproducing Goldstone's theorem whenever parameters are changed. It is always obeyed in this approach and thus phenomenology can address itself to a more constrained task. The constraints are considerable: a realistic ladder-rainbow kernel fitted to $\langle \bar{q}q \rangle^0$ [32] produces m_ρ, m_ϕ and $m_{K^\star}$ to better than 5%. Such a phenomenological LR kernel for light mesons has absorbed vertex dressing but without the explicit m_q dependence associated with an explicit diagrammatic representation of the dressed gluon-quark vertex. In order to gain more information it is necessary to work with a model that can implement a summation of vertex diagrams, turn that into a summation of diagrams for the chiral symmetry preserving BSE kernel, and allow a practical solution of the meson BSE.

To this end we adopted the Munczek-Nemirovsky Ansatz [40] for the interaction kernel. We used an improved model for the quark-gluon dressed vertex wherein each diagram for the dressed vertex has each of its internal vertices dressed in a self-consistent way. This moves considerably beyond the ladder BSE structure [10] for the vertex, in which vertices internal to the dressed vertex of interest are bare. In common with Ref. [10], we also used an effective method, with one parameter ($\mathcal{C} = 0.15$ for this model), to accommodate the important non-Abelian effect of the 3-gluon coupling for the vertex. Quenched lattice-QCD data for the quark propagator and the quark-gluon vertex at zero gluon momentum fixed the parameter $\mathcal{C}$, while m_π and m_ρ fixed the other two parameters via the fully dressed vertex results.

The resulting model provides a laboratory within which the relevance of ladder-rainbow truncation (bare vertex) can be explored over a range of quark masses from u/d-quarks to b-quarks. The influence of the enlarged class of vertex dressing diagrams included in this work is seen to indicate that LR truncation is missing 9.5% of attraction for m_ρ, whereas the previous information from a smaller class of vertex dressing diagrams [10] had LR missing 30% of attraction. We have argued that the

extra diagrams, or consequent non-linearity of the self-consistent vertex dressing scheme, is the dominant reason for the evident improved accuracy of ladder-rainbow truncation arising from the present simple algebraic model. It is not known whether this finding carries over to a more realistic treatment of QCD dynamics. As heavier $q\bar{q}$ mesons are considered, the amount of missing attraction in the LR truncation decreases steadily, as does the influence of vertex dressing which is less than 1% for the J/ψ and Υ.

The influence of the non-Abelian 3-gluon coupling is very significant. No attempt has been made to consider 4-gluon coupling nor to consider non-planar gluon line diagrams (e.g. crossed-box diagrams) for the vertex dressing. On the other hand, a limited class of non-planar gluon line diagrams for the meson BSE kernel, as generated from the planar diagrams of the dressed vertex, are included. Clearly the next step in this analysis is to include all possible diagrams dressed with two-point gluon lines in dressing the quark-gluon vertex and explore the influence of this complete dressing (excluding the 3- and 4-gluon couplings) on the solutions of the GAP equation. Convergence of these solutions with employing the fully dressed vertex will be a strong indicator of the reliability of the predictions made within this framework.

Chapter 3

Fully Dressed Quark-Gluon Vertex

3.1 Introduction

Inspired by the success of the improved vertex dressing scheme explored in the previous chapter, which allowed us to include a generalized class of planar diagrams in the dressing, in this chapter we explore the consequences of completely dressing the vertex with only two-point gluon lines. Here the planar diagrams are defined as those that can be drawn without any two gluon lines crossing each other. In the proposed scheme we will include both planar and non-planar diagrams, where the latter have typically been omitted in the previous models.

3.2 Non-Planar Diagrams and the Correct Large N_c Counting

The lowest-order non-planar diagram, which appears only at order $\mathcal{O}(g^5)$ in dressing the vertex, is shown in Fig. 3.1d. This and all other non-planar diagrams were omitted in the previous models of the vertex dressing, where we assumed that they were small. One of the arguments supporting that conjecture is that non-planar diagrams should have smaller color factors than planar diagrams, as proven by topological arguments in 't Hooft's $1/N_c$ expansion in QCD [11], [13], [14]. On the other hand, the color factors of the diagrams in Fig. 3.1 are easy to calculate explicitly using the properties of the matrices of the fundamental representation of $SU(N)$ group. All the diagrams included in the improved model with a number of internal gluon lines n have the same color factors:

$$\mathrm{Cf}_n^{\mathrm{Imp}} t^a = \left(-\frac{1}{2N_c}\right)^n t_a \tag{3.1}$$

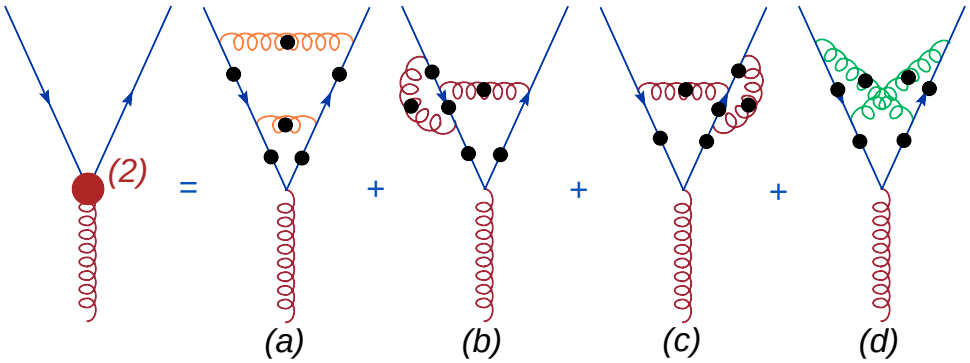

Figure 3.1: Vertex diagrams at $\mathcal{O}(g^5)$. Here the large red circle denotes the 2-nd order dressed quark-gluon vertex function (2 in the parenthesis denotes the number of gluon lines contributing to the vertex) and the small black circles on the propagators denote that the propagators are fully dressed. Previous works included only one or all of the diagrams (a), (b) and (c). Non-planar diagrams included in this work, such as diagram (d), prove to have significantly larger color factors than the planar ones.

Thus $\mathrm{Cf}_2^{\mathrm{Imp}} = 1/4N_c^2$ for diagrams in the Figs. 3.1a-3.1c. The relation (3.1) can be easily proven using the following identity:

$$t^a t^b t^a = (C_{\mathrm{F}} - \frac{C_{\mathrm{A}}}{2})t^b = -\frac{1}{2N_c}t^b \tag{3.2}$$

and remembering the structure of the improved vertex.

The color factor of the diagram (3.1, d) can also be easily calculated

$$\mathrm{Cf}_2^{\mathrm{Npl}} t^a = t^c t^b t^a t^c t^b = \frac{N_c^2+1}{4N_c^2}t^a, \tag{3.3}$$

where we used the following identities

$$\left[t^a, t^b\right] = i f^{abc} t^c, \tag{3.4}$$

$$f^{abc} t^b t^c = \frac{1}{2} i N_c t^a, \tag{3.5}$$

with totally antisymmetric structure constant f^{abc}.

This result seems to be in contradiction with the planarity arguments associated with the $1/N_c$ expansion. The qualitative solution of this puzzle can be easily given if we look more closely at the topological criteria in $1/N_c$. The criteria of planarity can be applied only to color-singlet objects if it is unambiguous. Moreover, the outer edge of the diagram should be a quark loop [14]. The most logical way of constructing a color-singlet object from the vertex diagrams of Fig. 3.1 is by inserting them into the quark self-energy term of the GAP equation and closing

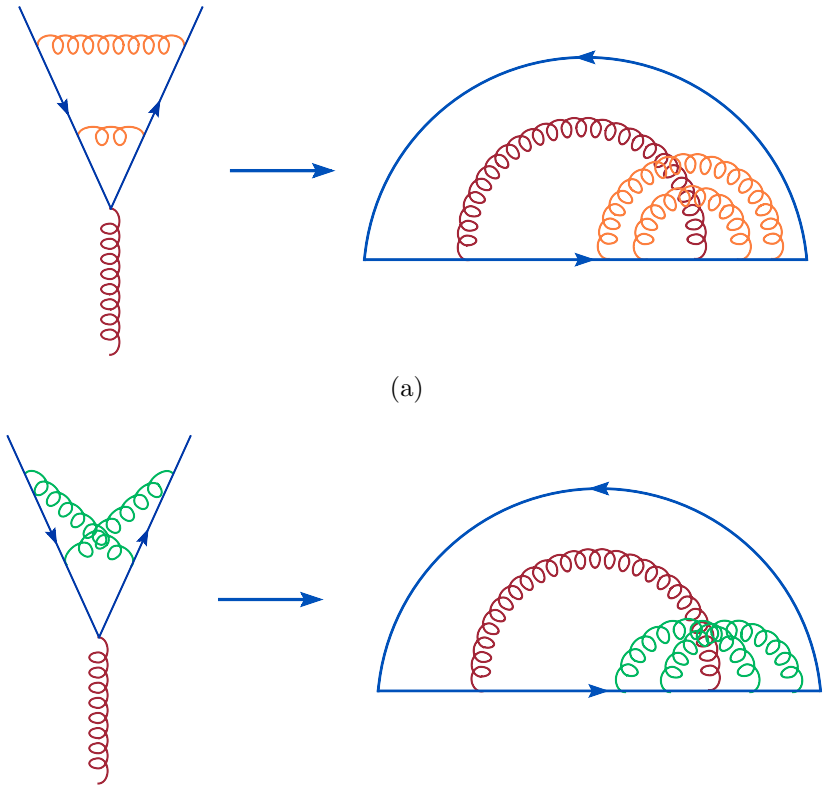

Figure 3.2: The non-planar diagrams obtained from inserting the corresponding vertices into the quark self-energy term and closing the fermion loop to form a color-singlet object. This shows that there is no clear indication as to which diagram is dominant in $1/N_c$ epansion.

the fermion loop in a manner that will leave the quark loop on the outer edge of the diagrams, as demonstrated on the Fig. 3.2 for the diagrams in Fig. 3.1a and 3.1d.

This demonstrates that both vertex diagrams yield non-planar diagrams, which need to be considered in more detail in a $1/N_c$ expansion in order to determine their leading order contribution. We just note here that all the arguments that are true for the diagram in Fig. 3.1a in a $1/N_c$ expansion are also valid for the diagrams in Figs. 3.1b and 3.1c and vice a versa.

3.3 't Hooft's Double-Line Counting Rules and the Undeservingly Discarded $U(1)$ Ghost in $1/N_c$ Expansion

A careful examination of the $1/N_c$ power behavior of the self-energy diagrams requires a short review of the introduction to 't Hooft's model of the $1/N_c$ expansion (also known as large N QCD) [14]. As we mentioned in the previous chapter, QCD in the low energy scale, where most of the hadrons lie, does not have an explicit parameter in which it can be expanded. 't Hooft's proposition was to use $1/N_c$, assuming N_c to be so large that the expansion will be sensible. In the discussion from now on we will drop the c index from the number of colors, writing it simply as N.

The expansion is setup by extending QCD to N colors and N_f flavors of quarks. The underlying local gauge symmetry is the $SU(N)$ in the fundamental representation. Here the color parts of the quark fields are represented by N dimensional vectors and the gauge fields are represented by Hermitian $N \times N$ traceless matrices t^a, $A_\mu \equiv t^a A^a_\mu$, with index $a \in \{1, 2, .., N^2 - 1\}$ in the adjoint representation of $SU(N)$. In the $1/N$ expansion the gauge coupling constant g is taken to be $g = g_0/\sqrt{N}$, which is necessary to keep the theory sensible as $N \to \infty$.

The corresponding Lagrangian density is:

$$\mathcal{L}_{QCD} = \sum_{f=1}^{N_f} \bar{\psi}_f (i\gamma^\mu D_\mu - m)\psi_f - \frac{1}{2} Tr\left[F^{\mu\nu} F_{\mu\nu}\right], \tag{3.6}$$

with the covariant derivative defined via gauge field:

$$D_\mu \equiv \partial_\mu + i\frac{g_0}{\sqrt{N}} A_\mu, \tag{3.7}$$

and the field strength as:

$$F^a_{\mu\nu} \equiv \partial_\mu A^a_\nu - \partial_\nu A^a_\mu + i\frac{g_0}{\sqrt{N}} f_{abc}\left[A^b_\mu, A^c_\nu\right], \tag{3.8}$$

From now on we will ignore the flavor index of the quarks, as it will be irrelevant to our discussion. We want to note that the large N limit can be taken with either N_f or N_f/N fixed.

The counting of the color factors of the Feynman diagrams is necessary in assessing their importance in this counting scheme. 't Hooft proposed a diagrammatic method for counting the color factors of the diagrams, the so-called double-lined notation. The method is easy to understand by considering the color structure of the theory's Green's functions. The quark propagator has the following structure

$$\langle 0 | \psi^i(x) \bar{\psi}^j(y) | 0 \rangle = \delta^{ij} S(x - y), \tag{3.9}$$

where the color indices $i, j \in \{1, 2, ..., N\}$. Thus, the propagator is depicted diagrammatically by an arrowed line with the same color indices on both ends due to δ^{ij}, see Fig. 3.3a.

The gauge field propagator is

$$\left\langle 0 \left| A^a_\mu(x) A^b_\nu(y) \right| 0 \right\rangle = \delta^{ab} D_{\mu\nu}(x - y) \tag{3.10}$$

Using the following $SU(N)$ identity

$$(t^a)^i_j (t^a)^k_l = \frac{1}{2}\delta^i_l \delta^k_j - \frac{1}{2N}\delta^i_j \delta^k_l \tag{3.11}$$

and the normalization condition of the t^a matrices the color indices of the propagator (3.10) can be written explicitly

$$\left\langle 0 \left| \left(A^a_\mu(x)\right)^i_j \left(A^b_\nu(y)\right)^k_l \right| 0 \right\rangle = \left(\frac{1}{2}\delta^i_l \delta^k_j - \frac{1}{2N}\delta^i_j \delta^k_l\right) D_{\mu\nu}(x - y) \tag{3.12}$$

The $U(N)$ identity corresponding to (3.9) has the following form

$$(t^a)^i_j (t^a)^k_l = \frac{1}{2}\delta^i_l \delta^k_j, \tag{3.13}$$

which is usually substituted into the gluon propagator. The gluon propagator is then diagrammatically depicted as a double line, with opposite arrows and the same color indices on both ends of each line, as implied by the Kronecker deltas in (3.13). The second term on the right hand side (RHS) of Eq. (3.11) is dropped, assuming it will be unimportant in the $1/N$ counting, as it is suppressed by a $1/N$ factor.

Here we propose to keep the second term on the RHS of Eq. (3.11), which corresponds to a $U(1)$ ghost field, which is necessary to cancel the extra $U(1)$ gauge boson in relating the $U(N)$ gauge theory to $SU(N)$. We propose to depict the ghost field as a single dotted line with no color indices, as it transfers no color because of the Kronecker deltas that contract the color factors at each end of the line, see Eq. (3.11). The corresponding diagrams are depicted in Fig. 3.3b, where the double-lined object correspond to the $U(N)$ gluon propagator, and the ghost field has a negative sign as one can see from (3.12). In counting the powers of N, each ghost field will enter with a $1/N$ factor also coming from the form of the propagator. This extra penalty of $1/N$ is the reason the ghosts are generally ignored in the literature. We also note that with each double-lined $U(N)$ gluon and $U(1)$ ghost propagator, we have to include a factor of $1/2$ to account for the proper normalization.

In a similar fashion, the quark-gluon vertex can be depicted in the double-lined and dotted notation as shown in Fig. 3.4a. We note here, that in the general literature on the $1/N$ expansion, the ghost contribution is usually ignored as well. For completeness, we also show in Fig. 3.4b and 3.4c the 3 and 4 point gluon vertices in the double-lined notation. We note that there is no 3 or 4 point ghost interaction, nor is there a $U(N)$ gluon-ghost interaction, as these fields are commutative.

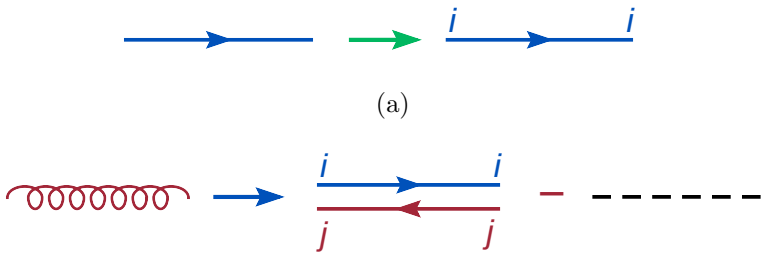

Figure 3.3: The double-lined notation for the low order QCD Green's functions in $1/N_c$ expansion of the vertex diagrams.

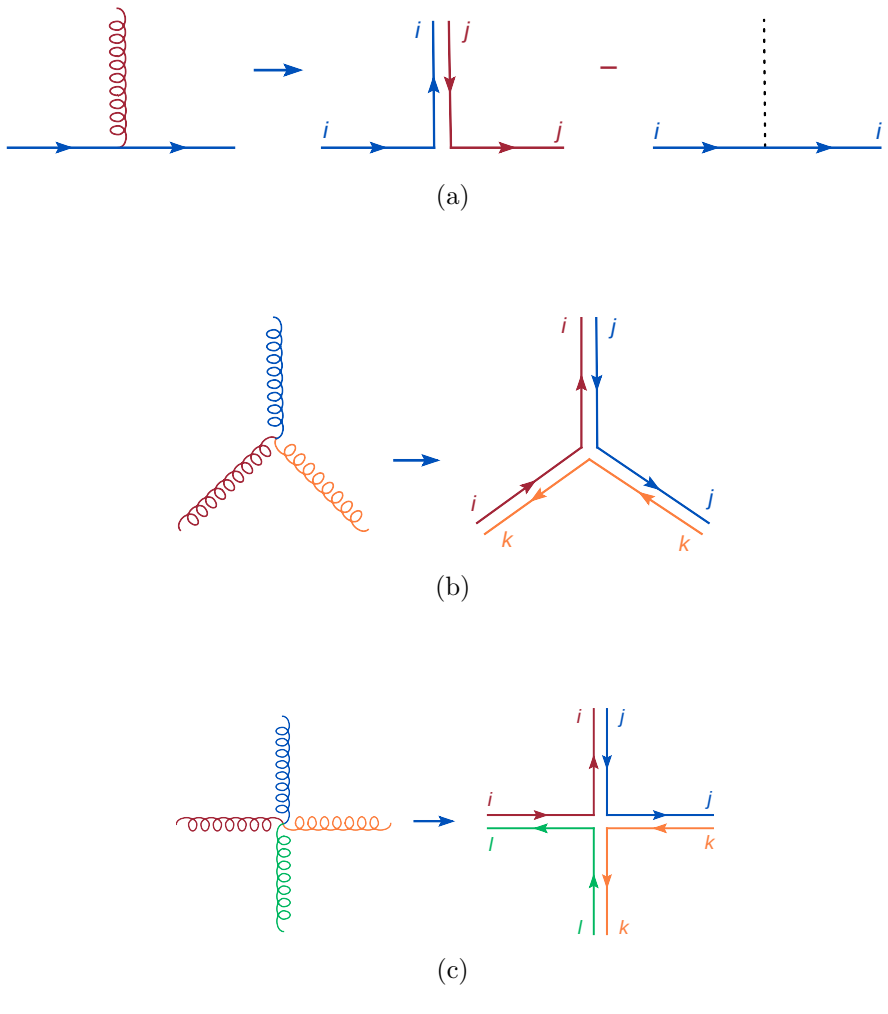

Figure 3.4: The double-lined notation for the low order QCD Green's functions in $1/N_c$ expansion of the vertex diagrams.

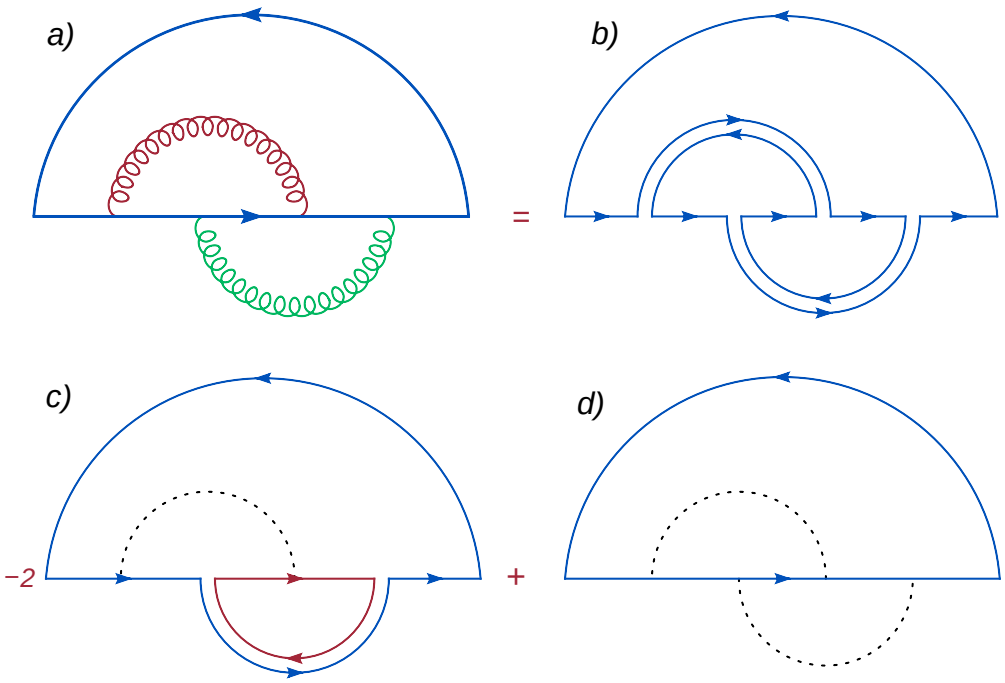

Figure 3.5: The double-lined analysis of the lowest order non-planar diagram with quark loop, where the $U(1)$ ghosts were also included.

With this diagrammatic notation, the color factor of a diagram is counted by replacing the Green's functions with the corresponding 't Hooft line diagrams and counting the number of the closed color index loops, each accounting for a factor of N. The $1/N$ counting is unambiguous only for color-singlet objects, where the corresponding diagram will not have any open color index lines. The overall order of the diagram is then calculated by taking into account the number of $1/\sqrt{N}$ factors from the gauge coupling constant and the $1/N$ factors from the ghost propagators:

$$O = N^{L-C/2-G}, \tag{3.14}$$

where L is the number of the closed color index loops, C is the number of the couplings, g, and G is the number of the ghost propagators in the diagram.

These rules are easy to demonstrate on the simple example depicted in Fig. 3.5.

The color factor and $1/N$ order of the diagram (3.5, a) is easy to calculate

$$\begin{aligned} \mathrm{Cf}_1^{a)} &= Tr[t^a t^b t^a t^b] = -\frac{N^2-1}{4N} \\ O_1^{a)} &= \mathrm{Cf}_1^{a)} \times \left(\frac{1}{\sqrt{N}}\right)^4 = -\frac{N^2-1}{4N^3} \end{aligned} \tag{3.15}$$

The rules described above allow for an easy evaluation of the color factors for the diagrams in Figs. 3.5b-3.5d:

$$\begin{aligned}
\mathrm{Cf}_1^{b)} &= \frac{1}{4}N \qquad (3.16)\\
O_1^{b)} &= \mathrm{Cf}_1^{b)} \times \left(\frac{1}{\sqrt{N}}\right)^4 = \frac{1}{4N}\\
\mathrm{Cf}_1^{c)} &= \frac{1}{4}N^2 \times \frac{1}{N} = \frac{1}{4}N\\
O_1^{c)} &= \mathrm{Cf}_1^{c)} \times \left(\frac{1}{\sqrt{N}}\right)^4 = \frac{1}{4N}\\
\mathrm{Cf}_1^{d)} &= \frac{1}{4}N \times \frac{1}{N^2} = \frac{1}{4N}\\
O_1^{d)} &= \mathrm{Cf}_1^{d)} \times \left(\frac{1}{\sqrt{N}}\right)^4 = \frac{1}{4N^3}
\end{aligned}$$

It is easy to check that

$$\mathrm{Cf}_1^{a)} = \mathrm{Cf}_1^{b)} - 2\mathrm{Cf}_1^{c)} + \mathrm{Cf}_1^{d)}, \qquad (3.17)$$

as depicted in the Fig. 3.5.

Here we see the importance of the ghost fields, where the term $\mathrm{Cf}_1^{c)}$ is equal to $\mathrm{Cf}_1^{b)}$, but is multiplied by a factor of two and has the opposite sign. In the literature this example is demonstrated without the ghost fields, which should yield the wrong sign, but accidentally the right order in the $1/N$ expansion. We want to emphasize that the ghost fields can be discarded in describing the $SU(N)$ theory *only* if we consider the leading order diagrams with the given number of quarks and gluons, that is only for planar diagrams. For planar diagrams, each $U(N)$ gluon forms a new color index loop which cancels the penalty of the $1/N$ induced by two factors of g it carries. On the other hand, a ghost line does not create a color loop and carries an extra $1/N$ penalty for the propagator, thus contributing at $1/N^2$ order compared to the corresponding $U(N)$ gluon. However, for the non-planar diagrams, the $U(N)$ gluon may not create or can even destroy a color index loop, where the ghost stays "invisible" (same old ghostly habits) to the color loops. Thus in some circumstances they become as large as the $U(N)$ gluon contribution.

The $1/N$ analysis for the vertices depicted in Fig. 3.2 is now straightforward. The corresponding double-lined decompositions are depicted in the Figs. 3.6 and 3.7.

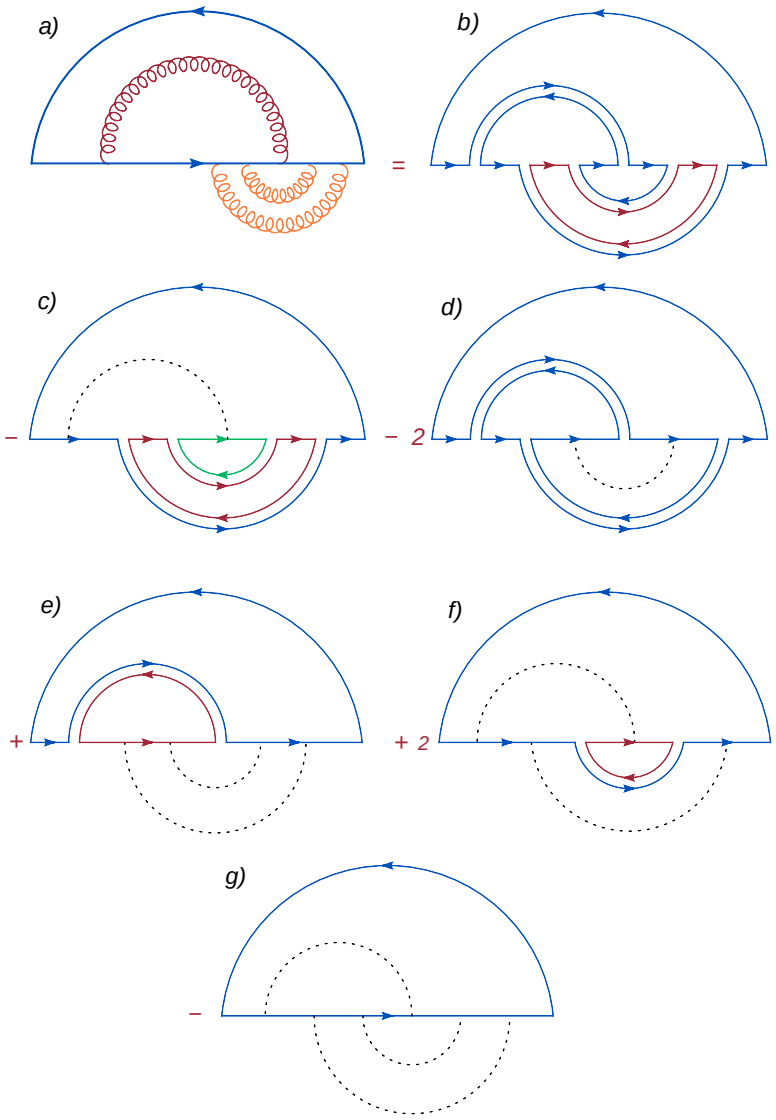

Figure 3.6: The double-lined analysis of the diagam in Fig. 3.2a, where the $U(1)$ ghosts were also included.

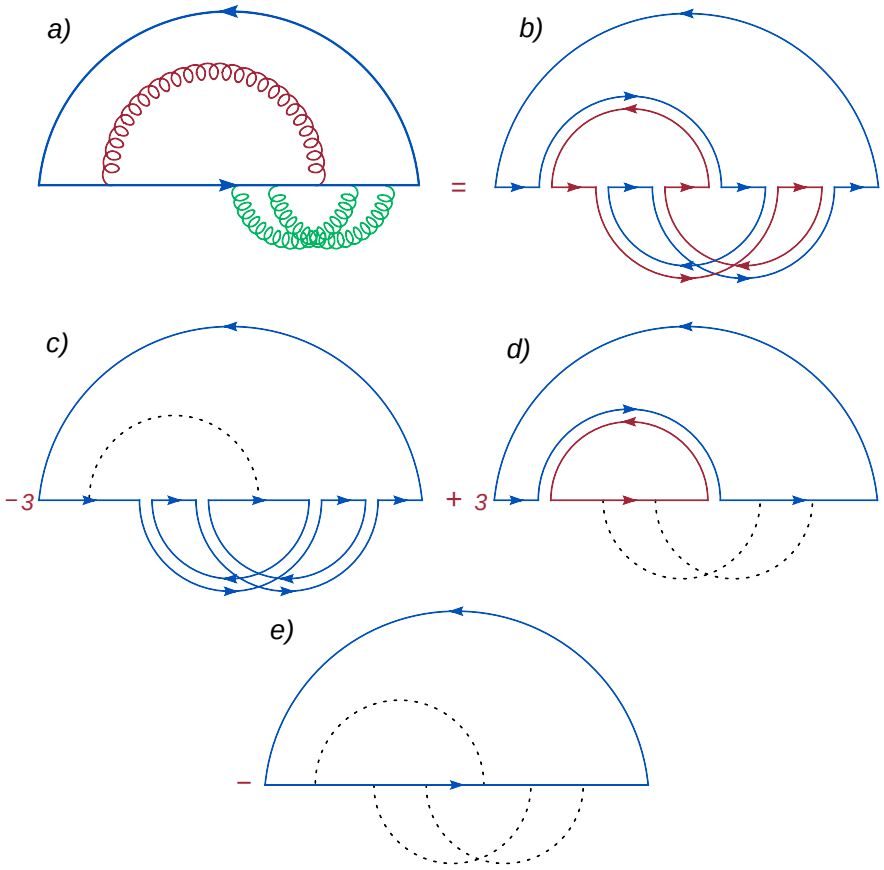

Figure 3.7: The double-lined analysis of the diagam in Fig. 3.2b, where the $U(1)$ ghosts were also included.

We simply write down the corresponding color factors from each diagram

$$\begin{aligned} \mathrm{Cf}_{2a}^{b)} &= \frac{1}{8}N^2 \\ \mathrm{Cf}_{2a}^{c)} &= \frac{1}{8}N^3 \times \frac{1}{N} = \frac{1}{8}N^2 \\ \mathrm{Cf}_{2a}^{d)} &= \frac{1}{8}N \times \frac{1}{N} = \frac{1}{8} \\ \mathrm{Cf}_{2a}^{e)} &= \mathrm{Cf}_{2a}^{f)} = \frac{1}{8}N^2 \times \frac{1}{N^2} = \frac{1}{8} \\ \mathrm{Cf}_{2a}^{g)} &= \frac{1}{8}N \times \frac{1}{N^3} = \frac{1}{8N^2} \end{aligned} \tag{3.18}$$

and

$$\begin{aligned} \mathrm{Cf}_{2b}^{b)} &= \frac{1}{8}N^2 \\ \mathrm{Cf}_{2b}^{c)} &= \frac{1}{8}N \times \frac{1}{N} = \frac{1}{8} \\ \mathrm{Cf}_{2b}^{d)} &= \frac{1}{8}N^2 \times \frac{1}{N^2} = \frac{1}{8} \\ \mathrm{Cf}_{2b}^{e)} &= \frac{1}{8}N \times \frac{1}{N^3} = \frac{1}{8N^2} \end{aligned} \tag{3.19}$$

The $\mathrm{Cf}_{2b}^{a)}$ and $\mathrm{Cf}_{2b}^{b)}$ are easy to calculate using Eqs. (3.1) and (3.3)

$$\mathrm{Cf}_{2a}^{a)} = \mathrm{Cf}_2^{\mathrm{Imp}} Tr\left[t^a t^a\right] = \frac{N^2-1}{8N_c^2}, \tag{3.20}$$

$$\mathrm{Cf}_{2b}^{a)} = \mathrm{Cf}_2^{\mathrm{Npl}} Tr\left[t^a t^a\right] = \frac{N_c^4-1}{8N_c^2}. \tag{3.21}$$

Thus we can again check that

$$\mathrm{Cf}_{2a}^{a)} = \mathrm{Cf}_{2a}^{b)} - \mathrm{Cf}_{2a}^{c)} - 2\mathrm{Cf}_{2a}^{d)} + \mathrm{Cf}_{2a}^{e)} + 2\mathrm{Cf}_{2a}^{f)} - \mathrm{Cf}_{2a}^{g)}, \tag{3.22}$$

$$\mathrm{Cf}_{2b}^{a)} = \mathrm{Cf}_{2b}^{b)} - 3\mathrm{Cf}_{2b}^{c)} + 3\mathrm{Cf}_{2b}^{d)} - \mathrm{Cf}_{2b}^{e)}, \tag{3.23}$$

where we skipped constructing the full $1/N$ ordering of the diagrams, as the factor N^{-3} from gauge coupling g is common for all the diagrams.

Thus the correct $1/N$ analysis of the vertex diagrams completely agrees with the straightforward calculations of the color factors using the properties of the Gell-Mann matrices. It is remarkable that in the diagram of Fig. 3.6 the leading-order contribution from $U(N)$ gluons, Fig. 3.6b, is exactly canceled by a diagram including a ghost line, Fig. 3.6c, so that the leading order contribution is given by diagrams in Figs. 3.6d-3.6f, containing one or more ghost lines.

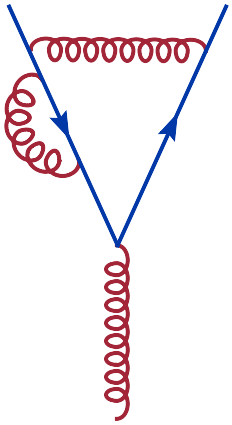

Figure 3.8: Quark self-energy type contribution in dressing the quark-gluon vertex.

3.4 Consequences of Including All Possible Diagrams

The analysis performed in the previous section showed that the previously ignored "non-planar" diagrams are important in dressing the quark-gluon vertex, since they have large color-factors and their numbers grow significantly faster than even the improved vertex diagrams as we include more gluon lines in the dressing. Thus it is crucial to explore the effects of including *all* diagrams dressed with two-point gluon lines in dressing the quark-gluon vertex.

In this section we propose a scheme for dressing the vertex function that includes all possible contributions with two-point gluon lines up to some order n of the gluon lines. We decompose the vertex function into a sum of all contributions with exactly i gluon lines:

$$\Gamma_\mu = \sum_{i=0} \Gamma^i_\mu, \tag{3.24}$$

where $\Gamma^0_\mu = Z_1\,\gamma_\mu$.

We use a recursive algorithm for obtaining all the contributions with exactly i gluon lines, Γ^i_μ , from the diagrams contributing to Γ^{i-1}_μ. We consider each diagram contributing to Γ^{i-1}_μ and consider the diagrams produced by making all possible insertions of a single gluon line into the vertex diagram by attaching its ends to fermion lines, assuring that at least one bare quark-gluon vertex is attached to the fermion line between the endpoints of the new gluon line. This ensures that the produced diagram is not simply a fermion self-energy type correction (see Fig. 3.8). It is then checked whether the resulting diagram was already produced from any previously considered diagrams contributing to Γ^{i-1}_μ to avoid double counting. One can easily see that the algorithm works for constructing the one-loop diagram from the bare vertex diagram and from that the diagrams of Fig. 3.1, as demonstrated on the Fig. 3.9.

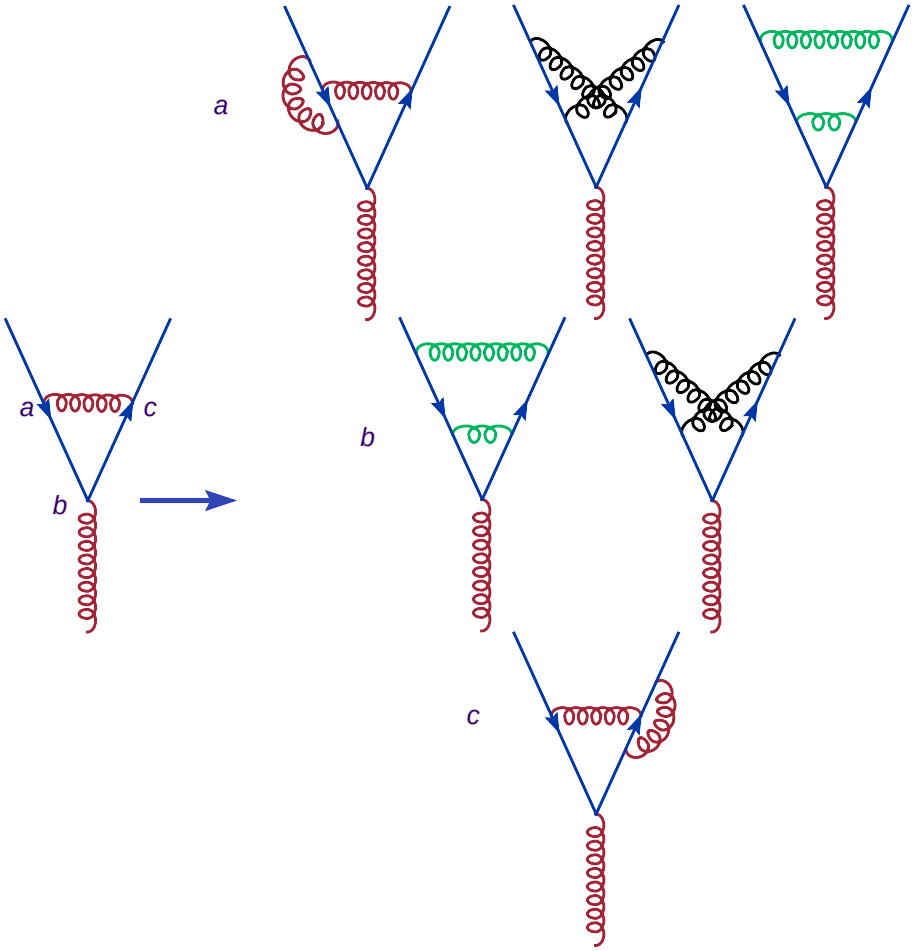

Figure 3.9: Generating all the second order diagrams form the only first order diagram by making all possible insertions of a single gluon line into the first order vertex diagram. The letters indicate the starting point of the inserted line. We note that there are several redundant diagrams generated, which should be removed.

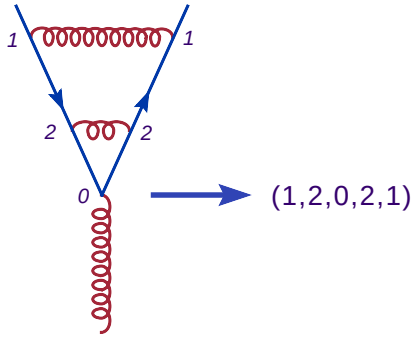

Figure 3.10: Constructing the set of numbers uniquely identifying one of the second order diagrams.

It is trivial to prove, using mathematical induction, that this algorithm produces *all* possible diagrams involving i gluon lines in dressing the vertex for any $i \geq 1$. In the previous paragraph we demonstrated that all the first and second order diagrams are generated using this algorithm. Let's suppose for some $n > 1$ we have all the diagrams with $n-1$ gluon lines, but there is one with n lines that we did not obtain from our insertions. It is easy to see that we can always find one gluon line, which can be removed from the diagram leaving it without quark self-energy type subdiagrams. Then the resulting vertex has $n-1$ gluon lines, thus should be in the set of diagrams we used to construct the vertices with n lines. Since we included all the possible insertions in our construction, we then had to obtain the original diagram as well.

In fact, the gluon line that can be removed is easy to find in a diagram. If the gluon line starting the first on one of the sides of the quark line cannot be removed, then there is a gluon line who's endpoints are separated only by the other end of our gluon. Then we can simply remove that gluon line without generating quark self-energy type subdiagram.

The algorithm described above is easy to implement in practice by constructing a set of numbers uniquely identifying each diagram. We build the set by enumerating the bare quark-gluon vertices in a diagram with $n-1$ gluon lines from 1 to $n-1$ and assigning the same numbers to the vertices attached to the same gluon propagators. We assign 0 to the external gluon vertex. An example of such construction is shown in the Fig. 3.10.

To construct the vertices with n gluon lines, we insert a pair of n into the set described above so that they will not be next to each other, as illustrated in the Fig. 3.11. We relabel the resulting set in the ascending order and check if the final set was already generated.

Algebraic Analysis

In order to solve the GAP equation with our dressed quark-gluon vertex, one needs the gluon 2-point function. As in the previous studies of this kind, we again

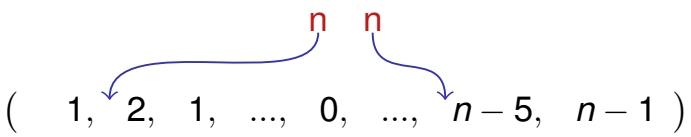

Figure 3.11: The sets for diagrams with exactly n diagrams are obtained from ones corresponding to diagrams with exactly $n-1$ lines by inserting a pair of n into the set and making all possible permutations, so they are never next to each other.

employ the Munczek-Nemirovsky Ansatz [40] for the interaction kernel to reduce the high dimensional integral equations to algebraic ones that make the analysis affordable

$$g^2 D_{\mu\nu}(k) \to \left(\delta_{\mu\nu} - \frac{k_\mu k_\nu}{k^2}\right)(2\pi)^4 \mathcal{G}^2 \delta^4(k), \tag{3.25}$$

where the parameter $\mathcal{G}^2$ is a measure of the integrated kernel strength.

The algebraic form of the GAP equation for the quark propagator corresponding to the gluon propagator (3.25) is

$$S(p)^{-1} = i\not{p} + m_{bm} + \mathcal{G}^2 \gamma_\mu S(p) \Gamma_\mu(p). \tag{3.26}$$

After projection onto the two Dirac amplitudes we have

$$A(p^2) = 1 - \mathcal{G}^2 \frac{i}{4} tr\left[\frac{\not{p}}{p^2}\gamma_\mu S(p)\,\Gamma_\mu(p)\right], \tag{3.27}$$

$$B(p^2) = m_{bm} + \mathcal{G}^2 \frac{1}{4} tr\left[\gamma_\mu\, S(p)\,\Gamma_\mu(p)\right]. \tag{3.28}$$

Equations (3.27) and (3.28) are solved simultaneously with a vertex function calculated at a specified order n of vertex dressing.

The calculations of the Dirac algebra for vertex diagrams was performed using computer-algebraic methods provided by *FeynCalc* package [57] for *Mathematica* [56]. The color factors were calculated by numerical contraction of SU(3) matrices. The number of possible diagrams grows extremely fast with the number of gluon lines included, making it difficult to advance too far with the number of loops. For example, while there are only 4 possible diagrams with exactly 2 internal gluon lines, there are 27 with 3 and 38232 with 6 internal lines. Such a rapid increase in the number of possible contributions forced us to use parallel computing to calculate the invariant amplitude functions for the vertex with exactly 6 gluon lines within a reasonable time frame. The contributions to Γ^7_μ include more than 5×10^5 possible diagrams, which we did not consider feasible to calculate. The comparison of the number of diagrams with the previous dressing schemes is shown in the Table 3.1.

The numerical solutions of the GAP equation constructed with the full vertex function are shown in Figs. 3.12 and 3.13. One can see from the plots that for $n = 3$ and $n = 5$ we obtain the perturbative Wigner-Weyl mode solutions for the quark propagator as $A(s) \to \infty$ and $M(s) \to 0$ when $s \to 0$. This indicates that the

Table 3.1: Comparison of the number of diagrams with exactly n gluon lines included in various dresing schemes.

n	*LRSummed*	*Improved*	*Full*
2	1	3	4
3	1	6	27
6	1	21	38232
7	1	28	$\sim 5 * 10^5$

Abelian part of the vertex dressing is not attractive enough to produce a Nambu-Goldstone mode for the quark propagator, so one necessarily needs at least 3-point gluon functions to account for the non-Abelian part of vertex dressing.

Effect of 3-Point Gluon Function Dressing

Explicit calculations with gluon 3-point functions proved to be extremely difficult, both because of difficulties in reproducing all possible diagrams at some non-trivial order in quark-gluon coupling and from the fact that no suitable, model gluon 2-point function is known to us which would allow for affordable calculations beyond one or two loops. Hence we resort to the method introduced in Ref. [10], which allows effective accounting of 3-point gluon function dressing of the vertex through the introduction of a phenomenological parameter $-1/8 \leq \mathcal{C} \leq 1$ in counting the color factors. We chose to implement the phenomenological color factor counting scheme only for the sub-class of diagrams that were included in the improved dressing scheme from the previous chapter to be unambiguous, since at a given order all of the diagrams included in the improved dressing scheme have the same color factors. The results show that for the range of parameter $\mathcal{C} \in (0.375, 0.8)$ the solutions of the GAP equation are in Nambu-Goldstone mode at every calculated order up to $n = 6$. The solutions for $\mathcal{C} = 0.375$ are presented in Figs. 3.14 and 3.15.

Padé Approximant

One can see from Figs. 3.14 and 3.15 that even though Nambu-Goldstone mode solutions can be obtained using minimal introduction of phenomenological 3-point gluon function, the solutions do not have convincing convergence with respect to the maximum number of gluon lines allowed in the quark-gluon vertex dressing, even in the space-like region. In order to draw any reliable conclusions we employ a Padé approximate to re-sum the perturbative solutions of the GAP equation and yield a solution at $n = \infty$. While the details of this calculations are presented in the Appendix A, the graphs corresponding to the solutions of the GAP equation with Padé approximant used for the quark self-energy contribution are shown in magenta in Figs. 3.14 and 3.15. It is clear from the graph that our results are significantly different from the ones obtained using LR truncation and indicate the severe limitations of that scheme.

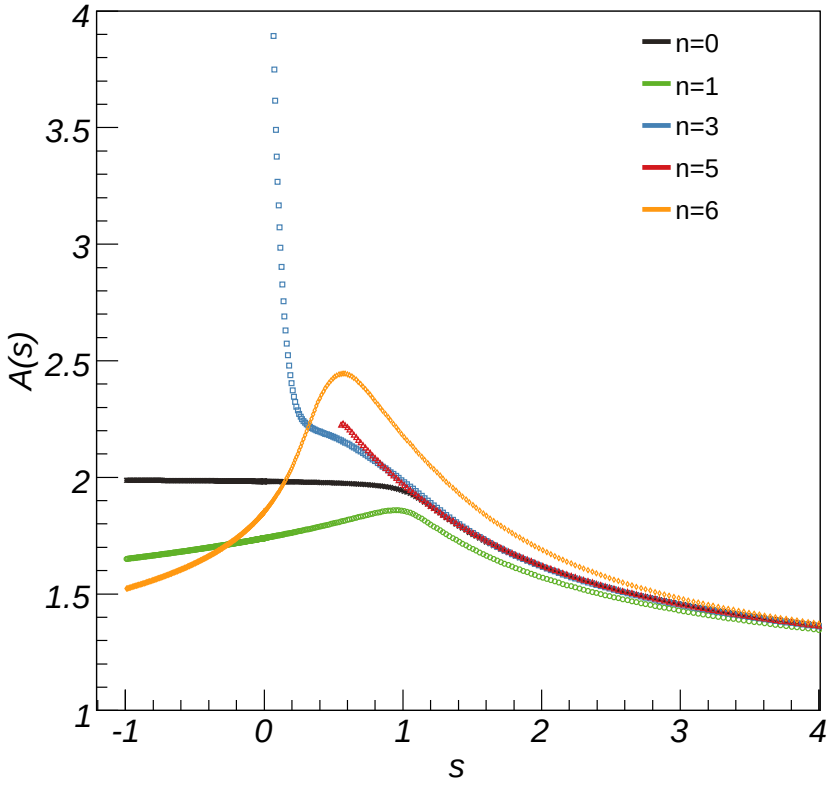

Figure 3.12: Quark propagator amplitude $A(s)$ versus Euclidean $s = p^2$. We use the interaction mass scale $\mathcal{G} = 1$ GeV and the current mass is $m = 0.0175$ $\mathcal{G} = 17.5$ MeV. We show the influence of vertex dressing to order n as described in the text. $n = 0$ yields the black curve and the result is the ladder-rainbow truncation. The other curves are $n = 1$ (green curve, 1-loop vertex), $n = 3$ (blue curve), $n = 5$ (red curve) and $n = 6$ (orange curve) order of dressing of quark gluon vertex.

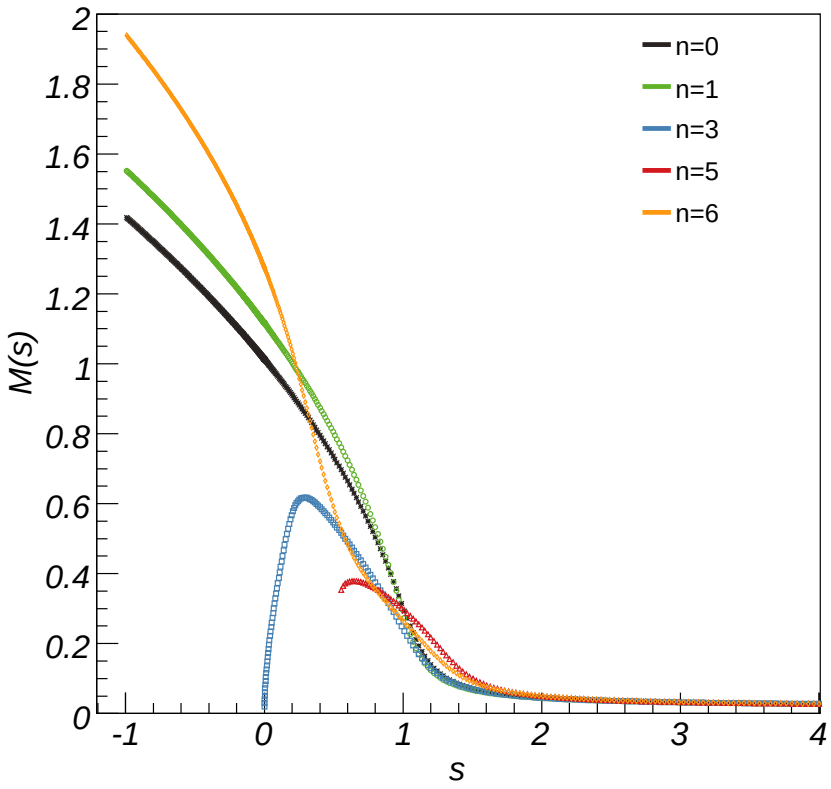

c

Figure 3.13: Quark mass function $M(s)$ versus Euclidean $s = p^2$. We use the interaction mass scale $\mathcal{G} = 1$ GeV and the current mass is $m = 0.0175\ \mathcal{G} = 17.5$ MeV. We show the influence of vertex dressing to order n as described in the text. $n = 0$ yields the black curve and the result is the ladder-rainbow truncation. The other curves are $n = 1$ (green curve, 1-loop vertex), $n = 3$ (blue curve), $n = 5$ (red curve) and $n = 6$ (orange curve) order of dressing of quark gluon vertex.

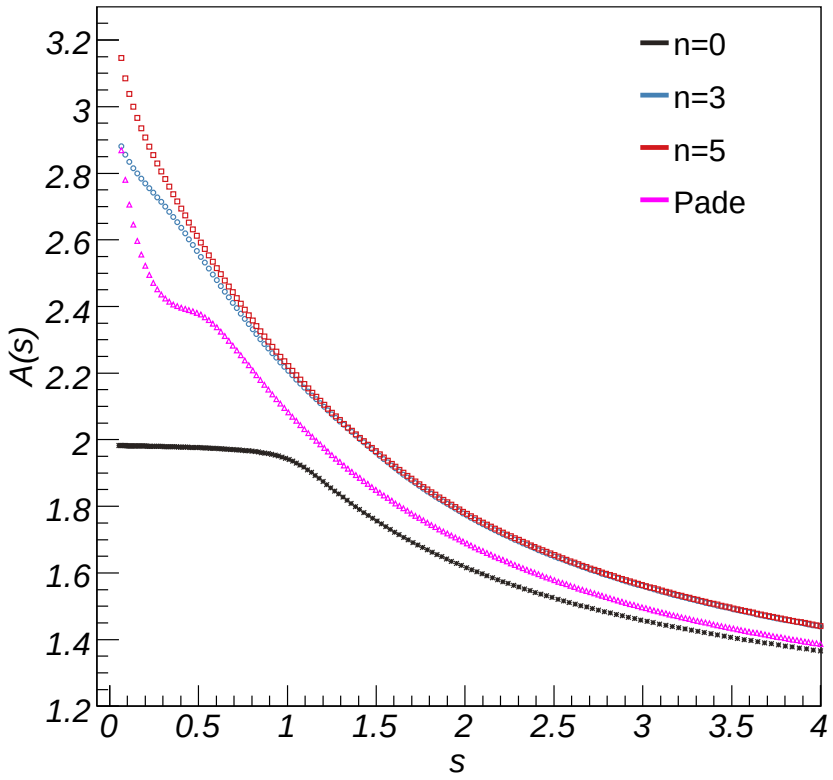

Figure 3.14: Quark propagator amplitude $A(s)$ versus Euclidean $s = p^2$. We use the interaction mass scale $\mathcal{G} = 1$ GeV, the current mass is $m = 0.0175$ $\mathcal{G} = 17.5$ MeV and $\mathcal{C} = 0.375$. We show the solutions in the Nambu-Goldstone mode corresponding to $n = 3$ (blue curve) and $n = 5$ (red curve) order of dressing of quark gluon vertex. The solution obtained using Padé approximation is shown in magenta. The $n = 0$ solution (black curve) corresponding to the ladder-rainbow truncation is shown for reference.

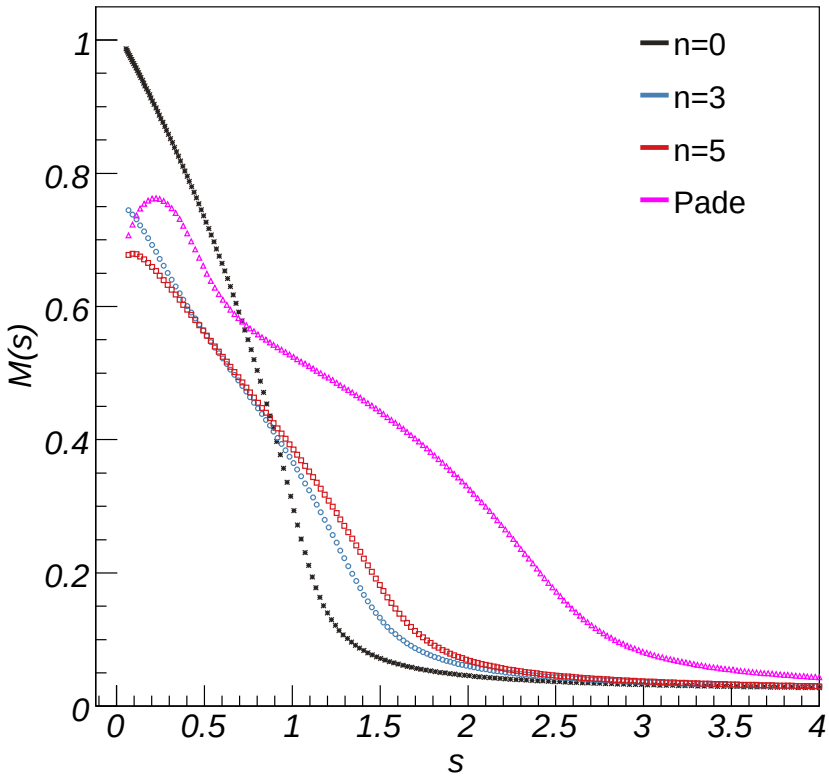

Figure 3.15: Quark mass function $M(s)$ versus Euclidean $s = p^2$. We use the interaction mass scale $\mathcal{G} = 1$ GeV, the current mass is $m = 0.0175\ \mathcal{G} = 17.5$ MeV and $\mathcal{C} = 0.375$. We show the solutions in the Nambu-Goldstone mode corresponding to $n = 3$ (blue curve) and $n = 5$ (red curve) order of dressing of quark gluon vertex. The solution obtained using Padé approximation is shown in magenta. The $n = 0$ solution (black curve) corresponding to the ladder-rainbow truncation is shown for reference.

Unfortunately, the restrictions induced by the model used for the gluon propagator do not allow studies in the time-like region, where the behavior of the propagators have direct impact on the meson masses obtained by solving the corresponding Bethe-Salpeter equations.

3.5 Summary

We explored the consequences of employing the most general quark-gluon vertex dressing scheme with only 2-point gluon functions. We showed that the non-planar vertices have dominant contribution in the diagrams with large numbers of the gluon lines included in the dressing due to their large color factors. A careful application of the $1/N_c$ expansion allowed one to confirm the results for the color factors evaluated in the $SU(3)$ algebra. The inclusion of the $U(1)$ ghost proved to be critical in this evaluation, providing necessary cancellations with $U(N)$ gluons. The discussion of the role of $U(1)$ ghost proved to clear some misconceptions in evaluating the non-planar diagrams, common in all the previous discussions of the $1/N_c$ expansion.

The resulting solutions of the GAP equation with the corresponding vertex calculated up to some finite order showed significant deviation from those calculated previously using ladder-rainbow truncation or its various extensions. Moreover, the resulting solutions with the corresponding vertices dressed to the maximum odd number of gluon lines are in Wigner-Weyl mode for every calculated odd order up to $n = 5$. This indicates that inclusion of only 2-point gluon functions in dressing the quark-gluon vertex omits a significant piece of physics and suggests the importance of the 3- and 4- point gluon function dressing. This also indicates the likely unreliability of the predictions made using the ladder-summed and improved vertex dressing schemes described in the previous chapter. The instability of the solutions shows that the converged solutions in those dressing schemes might be arbitrarily far from the full solution, so they cannot be used as benchmarks for reliability of the ladder-rainbow solutions. Only the solutions explicitly including the 3- and 4- point gluon functions might allow for converged solution close to the full solution. We do not exclude the possibility of this instability being a manifestation of the model gluon artifacts, which made high-order solutions possible in these models.

We used the improved ladder dressed scheme as a phenomenological means of including the effects of 3-point gluon function dressing. This scheme provided enough attraction to produce Nambu-Goldstone mode solutions for the GAP equation, which show significant deviations from the solutions with rainbow truncated vertex.

The solutions of the GAP equation with the full vertex do not indicate convergence with the maximum number of gluon lines included, at least to the order of calculations that we could afford. We employed a Padé approximate for both quark propagator functions to obtain the converged solutions in the space-like region. These solutions can be used for comparison with other models.

Chapter 4

Nucleon Electromagnetic Form Factors from Lattice QCD

4.1 Nucleon Electromagnetic Form Factors and Controversy in Experimental Measurements

The electromagnetic form factors of the nucleon are an invaluable source of information on its structure [1]. For example, observing their fall as Q^2 increases from zero revealed the finite extent of the nucleon, and measuring the Sachs electric form factor of the neutron, G_E^n [61,62], showed that it has a positive core surrounded by a long-range, negative tail [24, 63–67].

In the last few years particular interest has focused on the ratio of the electric and magnetic form factors of the proton, G_E/G_M. The long standing theoretical prediction was that the ratio should be constant in the large Q^2 region (see Refs. [68], [69]), confirmed by numerous measurements using the Rosenbluth separation method for values of $Q^2 \lesssim 6$ GeV^2 [19]- [70]. Recently several experiments at Jefferson Lab which measured the same ratio using the recoil proton polarization method [21,22], [71], have revealed a dramatic decrease with Q^2 – in contrast with earlier work based on the Rosenbluth separation.

While the behavior of G_E/G_M with Q^2 was anticipated in some models (e.g. see Ref. [72], [73–75]), there is no consensus as to which explanation best represents how QCD works. A constant ratio would mean a similar distribution of charge and magnetization throughout proton, while a decreasing ratio with increasing Q^2 would mean that the charge density increases slower than magnetization density towards the center of the proton. Direct guidance from QCD itself would be most valuable and for that purpose lattice QCD represents the one of very few techniques by which one can obtain non-perturbative solutions to QCD.

4.2 Lattice QCD Calculated Data

Lattice QCD (LQCD) is one of very few methods for performing non-perturbative calculations in QCD [16]- [76], [1]. LQCD is formulated in the framework of the Feynman path-integral formalism for QCD, where the expectation values of the field operators corresponding to physical observables are calculated using the path integrals:

$$\langle \mathcal{O} \rangle = \frac{\int \mathcal{D}A_\mu \mathcal{D}\psi \mathcal{D}\bar{\psi} e^{iS(A_\mu,\psi,\bar{\psi})} \mathcal{O}}{\mathcal{Z}}, \tag{4.1}$$

where the normalization is given by the partition function:

$$\mathcal{Z} = \int \mathcal{D}A_\mu \mathcal{D}\psi \mathcal{D}\bar{\psi} e^{iS(A_\mu,\psi,\bar{\psi})}, \tag{4.2}$$

and the fermions are represented through the Grassman variables $\bar{\psi}$,ψ.

Here the QCD action is given as:

$$S(A_\mu, \psi, \bar{\psi}) = \int d^4x \left(-\frac{1}{4} F_c^{\mu\nu} F_{\mu\nu}^c + \bar{\psi} M \psi \right), \tag{4.3}$$

where the Dirac operator M is the quark matrix and c denotes the color index.

The functional integrals of Eqs. (4.1, 4.2) are evaluated in LQCD in several steps. First space-time is discretized on a finite 4-dimensional hyper-cube (the lattice) with some finite lattice spacing a and length L. This allows one to remove the ultraviolet divergences from the theory by introducing a finite cutoff imposed by the smallest possible scale a. One should first note that the results should not depend on the regularization scheme, thus the cutoff should be eliminated from the results before any comparison with experiment is carried out. Analogously, an infrared cutoff is imposed by the finite volume L of the lattice, which is required for any numerical calculation to be possible. This in turn infers that the affordable (to date) calculations should be performed with unphysically high fermion masses to accommodate the bound state hadron inside of the lattice. One should also ensure that the finite volume effects are removed from the final result.

Even with the introduction of the finite space-time lattice, the numerical evaluation of the integrals of Eqs. (4.1, 4.2) is impossible, since the integrands have an oscillatory nature due to the e^{iS} factor and require one to include all possible (infinite) "paths"for the field configurations for evaluation. This conceptual problem is avoided by transformation to the Euclidean space-time via Wick rotation from Minkowski space-time:

$$\begin{aligned} x_0 &\rightarrow -ix_4 \\ p_0 &\rightarrow ip_4 \\ S_{Mink} &\rightarrow iS_{Eucl} \end{aligned} \tag{4.4}$$

While in the Euclidean space, the integrals can be well approximated by a Monte-Carlo integration over a finite number of the field configurations due to the $e^{-S_{Eucl}}$ damping factor, one must make an analytic continuation of the results back to the Minkowski space.

As one can see from Eq. (4.3), the quark fields can be explicitly integrated out in Eqs. (4.1, 4.2):

$$\int \mathcal{D}A_\mu \mathcal{D}\psi \mathcal{D}\bar{\psi} e^{-S} = \int \mathcal{D}A_\mu e^{-(S(A_\mu) - \ln\det M(A_\mu))} \tag{4.5}$$

However, this elimination does not reduce the volume of the calculations, since $\det M$ is a very complicated non-local functional of the gauge field, A_μ, and requires significant computational resources. The quenched approximation in LQCD supposes this determinant to be a constant, effectively neglecting the quark-loop effects and greatly reducing the computational costs. This is a "non-controllable" approximation, since there is no systematic way of improving on it other than completely removing it. While some recent calculations have been able to avoid this approximation, as the computational resources increase, it is still widely employed.

The QCDSF Collaboration recently presented lattice QCD simulations for the form factors of the nucleon over a wide range of values of momentum transfer [18]. These calculations were carried out using quenched, non-perturbatively $O(a)$-improved Wilson fermions (clover fermions), for three different values of the lattice spacing, $a = \{0.47, 0.34, 0.26\}\,\mathrm{GeV}^{-1}$. For each value of a, several sets of pion (or equivalently nucleon) masses were considered. For each mass set, Dirac and Pauli form factors for both the proton and neutron were calculated at several values of Q^2. The typical range for the pion mass used varied from 1.2 GeV to 0.6 GeV, with the corresponding nucleon mass ranging from approximately 2 GeV to 1.5 GeV. The typical range for Q^2 was $0.6\,\mathrm{GeV}^2$ to $2.3\,\mathrm{GeV}^2$. With the smallest lattice spacing being around 0.05 fm ($\beta = 6.4$) and pion mass 580 MeV, these calculations represent the present the state of the art. Therefore one needs to parametrize the form factors as a function of pion mass and extrapolate to the physical value before comparing these lattice results with the experimental data.

At $Q^2 = 0$ there have been a number of studies of the chiral extrapolation of baryon magnetic moments [77–80]. However, there is no model independent way to respect the constraints of chiral symmetry over the range of Q^2 and m_π required by the QCDSF data. Instead, at finite Q^2, one has been led to study various phenomenological parameterizations [81], which have at least ensured the correct leading order non-analytic structure as $m_\pi \to 0$. The purpose of the work here is three-fold. First, the lattice data will be used to investigate whether a particular quark model is capable of describing the properties of the nucleon in this additional dimension of varying m_π - an important test which any respectable quark model should satisfy[1]. Second, having confirmed that the model is consistent

[1]Just as the study of QCD as a function of N_c has proven extremely valuable, so the study of hadron properties as a function of quark mass, using the results of lattice QCD calculations, undoubtedly offers significant insight into QCD, as well as new ways to model it [82].

with the lattice data over the range of m_π noted earlier, the model will be used to extrapolate to large values of Q^2 (for lattice values of m_π). Third, the model will be used to extrapolate to the physical pion mass.

4.3 The Light Front Cloudy Bag Model and Extrapolations

4.3.1 Introduction

The first model which will be considered here is the light front cloudy bag model (LFCBM) [25], where the nucleon is assumed to consist of three bound, relativistically moving constituent quarks, surrounded by a cloud of pions. LFCBM was developed as a means of preserving the successes of the original cloudy bag model [24, 65–67], while ensuring covariance in order to deal unambiguously with modern high energy experiments. The light front constituent quark model, upon which it is built [72], predicted the rapid decrease of G_E/G_M with Q^2 and, as the pion cloud is expected to be relatively unimportant at large Q^2, this success carries over to the LFCBM [25]. Furthermore the LFCBM corresponds to a Lagrangian built upon chiral symmetry, so it can be extended to the limit of low quark mass as well as low and high Q^2.

4.3.2 Review of the LFCBM

The LFCBM is a *relativistic* constituent quark model incorporating the effect of *pion-loops*, key features motivated by chiral symmetry. The light-front dynamics is employed to maintain the Poincaré invariance, and one pion-loop corrections are added to incorporate significant pion cloud effects (particularly in the neutron electric form factor and the magnetic form factors) as well as the leading non-analytic behavior imposed by chiral symmetry. In light-front dynamics the fields are quantized at a fixed "time"$= \tau = x^0 + x^3 \equiv x^+$ (see Refs. [68,83]). The light front time or τ-development operator is then $P^0 - P^3 \equiv P^-$. The canonical spatial variable is $x^- = x^0 - x^3$, with a canonical momentum $P^+ = P^0 + P^3$. The other coordinates are $\mathbf{x}_\perp$ and $\mathbf{P}_\perp$. The relation between the energy and momentum of a free particle is given by $p^- = (p_\perp^2 + m^2)/p^+$, with the quadratic form allowing the separation of center of mass and relative coordinates. The resulting wave functions are frame independent. The light front technique is particularly relevant for calculating form factors because one uses boosts that are independent of interactions.

The Dirac F_1 and Pauli F_2 form factors are defined as the invariant functions in the Dirac decomposition of the nucleon electromagnetic current's matrix element:

$$\langle N, \lambda' p' \left| J^\mu \right| N, \lambda p \rangle = \overline{u}_{\lambda'}(p') \left[F_1(Q^2)\gamma^\mu + \frac{F_2(Q^2)}{2M_N} i\sigma^{\mu\nu}(p'-p)_\nu \right] u_\lambda(p)\,. \qquad (4.6)$$

The momentum transfer is $q^\mu = (\ p' - p)^\mu$, $Q^2 = -q^2$ and J^μ is taken to be the electromagnetic current operator for a free quark. For $Q^2 = 0$ the form factors F_1 and F_2 are, respectively, equal to the charge and the anomalous magnetic moment κ in units of e and $e/(2M_N)$, and the magnetic moment is $\mu = F_1(0) + F_2(0) = 1 + \kappa$.

We are interested in the electric and magnetic Sachs form factors:

$$G_E = F_1 - \frac{Q^2}{4M_N^2} F_2, \qquad\qquad G_M = F_1 + F_2, \tag{4.7}$$

with normalization

$$\begin{aligned} G_E^p(0) &= 1; \\ G_M^p(0) &= \mu_p; \\ G_E^n(0) &= 0; \\ G_M^n(0) &= \mu_n; \end{aligned} \tag{4.8}$$

The evaluation of the form factors is simplified by using the so-called Drell-Yan reference frame in which $q^+ = 0$, so that $Q^2 = q_\perp^2 = q_1^2$. If light-front spinors for the nucleons are used, the form factors can be expressed in terms of matrix elements of the plus component of the current [84]:

$$F_1(Q^2) = \langle N, \uparrow \left| J^+ \right| N, \uparrow \rangle \qquad \text{and} \qquad Q F_2(Q^2) = (-2M_N) \langle N, \uparrow \left| J^+ \right| N, \downarrow \rangle \,. \tag{4.9}$$

The form factors are calculated using the "good" component of the current, J^+, to suppress the effects of quark-pair terms.

The next step is to construct the bare (pionless) nucleon wave function Ψ, which is a symmetric function of the quark momenta, independent of reference frame, and an eigenstate of the canonical spin operator. The commonly used ansatz is:

$$\begin{aligned} \Psi(p_i) &= \Phi(M_0^2) u(p_1) u(p_2) u(p_3) \psi(p_1, p_2, p_3), \\ p_i &= \mathbf{p}_i s_i, \tau_i, \end{aligned} \tag{4.10}$$

where ψ is a spin-isospin color amplitude factor, the p_i are expressed in terms of relative coordinates, the $u(p_i)$ are Dirac spinors and Φ is a momentum distribution wave function. The specific form of ψ is given in Eq. (12) of Ref. [26] and earlier in Ref. [73–75]. This is a relativistic version of the familiar SU(6) wave function, with no configuration mixing included. The notation is that $\mathbf{p}_i = (p_i^+,\ \mathbf{p}_{i\perp})$. The total momentum is $\mathbf{P} = \mathbf{p}_1 + \mathbf{p}_2 + \mathbf{p}_3$, the relative coordinates are $\xi = p_1^+/(p_1^+ + p_2^+)$, $\eta = (p_1^+ + p_2^+)/P^+$, and $\mathbf{k}_\perp = (1-\xi)\mathbf{p}_{1\perp} - \xi \mathbf{p}_{2\perp}$, $\mathbf{K}_\perp = (1-\eta)(\mathbf{p}_{1\perp} + \mathbf{p}_{2\perp}) - \eta \mathbf{p}_{3\perp}$. In computing a form factor, we take quark 3 to be the one struck by the photon. The value of $1-\eta$ is not changed ($q^+ = 0$), so only one relative momentum, $\mathbf{K}_\perp$ is changed: $\mathbf{K}'_\perp = \mathbf{K}_\perp - \eta \mathbf{q}_\perp$. The form of the momentum distribution wave function

is taken from Schlumpf [85]:

$$\Phi(M_0) = N\big(M_0^2 + \beta^2\big)^\gamma\,, \tag{4.11}$$

with M_0^2 the mass-squared operator for a non-interacting system:

$$M_0^2 = \frac{K_\perp^2}{\eta(1-\eta)} + \frac{k_\perp^2 + M^2}{\eta\xi(1-\xi)} + \frac{M^2}{1-\eta}\,. \tag{4.12}$$

Schlumpf's parameters were $\beta = 0.607$ GeV, $\gamma = -3.5$, $M = 0.267$ GeV, where the value of γ was chosen so that $Q^4 G_M(Q^2)$ was approximately constant for $Q^2 > 4$ GeV^2, in accord with experimental data. The parameter β helps govern the values of the transverse momenta allowed by the wave function Φ and is closely related to the rms charge radius. The constituent quark mass, M, was primarily determined by the magnetic moment of the proton. These parameters will be varied to accommodate the inclusion of the pion cloud and to allow for fits to lattice data.

A physical nucleon can sometimes undergo a quantum fluctuation so that it consists of a bare nucleon and a virtual pion. In this case, an incident photon can interact electromagnetically with a bare nucleon, Fig. 4.1a, with a nucleon while a pion is present, Fig. 4.1b, or with a charged pion in flight, Fig. 4.1c. These effects are especially pronounced for the neutron G_E [24,65–67], at small values of Q^2. The tail of the negatively charged pion distribution extends far out into space, causing the mean square charge radius, R_n^2, to be negative. The effects of the pion cloud need to be computed relativistically if one is to confront data taken at large Q^2. This involves evaluating the Feynman diagrams of Fig. 4.1 using photon-bare-nucleon form factors from the relativistic model, and using a relativistic π-nucleon form factor. The resulting model is defined as the light-front cloudy bag model LFCBM [25]. The light-front treatment is implemented by evaluating the integral over the virtual pion four-momentum $k^\pm, \mathbf{k}_\perp$, by first performing the integral over k^- analytically, re-expressing the remaining integrals in terms of relative variables ($\alpha = k^+/p^+$), and shifting the relative $\perp$ variable to $\mathbf{L}_\perp$ to simplify the numerators. Thus the Feynman graphs, Fig. 4.1, are each represented by a single τ-ordered diagram. The use of J^+ and the Yan identity [86] $S_F(p) = \sum_s u(p,s)\overline{u}(p,s)/(p^2 - m^2 + i\epsilon) + \gamma^+/2p^+$ allows one to see that the nucleon current operators appearing in Fig. 4.1b act between on-mass-shell spinors.

The results can be stated as

$$F_{i\alpha}(Q^2) = Z\left[F_{i\alpha}^{(0)}(Q^2) + F_{ib\alpha}(Q^2) + F_{ic\alpha}(Q^2)\right], \tag{4.13}$$

where $i = 1, 2$ denotes the Dirac and Pauli form factors, $\alpha = n, p$ determines the identity of the nucleon, and $F_{i\alpha}^{(0)}(Q^2)$ are the form factors computed in the absence of pionic effects. The wave function renormalization constant, Z, is determined from the condition that the charge of the proton be unity: $F_{1p}(Q^2 = 0) = 1$. For illustration we start with the calculation of the neutron form factors. Then,

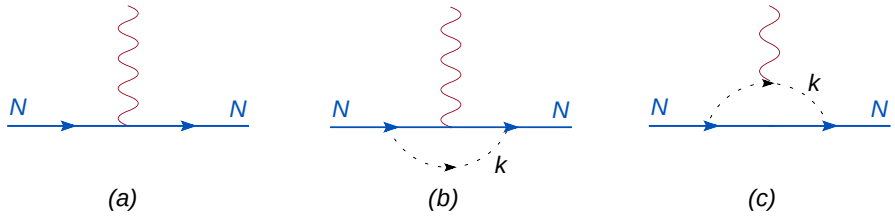

Figure 4.1: Feynman diagrams for bare nucleon (a) and nucleon with a virtual-pion loop (b,c) contributions to the electromagnetic current of the nucleon.

evaluating the graph in Fig. 4.1b gives

$$F_{1bn}(Q^2) = g_0^2 \int_0^1 d\alpha\alpha \int \frac{d^2L}{(2\pi)^3} R_N(\mathbf{L}^{(+)\,2}, \alpha) R_N(\mathbf{L}^{(-)\,2}, \alpha)$$
$$[(F_{1p}^{(0)}(Q^2)+F_{1n}^{(0)}(Q^2)/2)(\alpha^2(M^2-Q^2/4)+L^2)-(F_{2p}^{(0)}(Q^2)+F_{2n}^{(0)}(Q^2)/2))(\alpha^2Q^2/2)], \tag{4.14}$$

$$F_{2bn}(Q^2) = -g_0^2 \int_0^1 d\alpha\alpha \int \frac{d^2L}{(2\pi)^3} R_N(\mathbf{L}^{(+)\,2}, \alpha) R_N(\mathbf{L}^{(-)\,2}, \alpha)$$
$$[(F_{1p}^{(0)}(Q^2) + \frac{1}{2}F_{1n}^{(0)}(Q^2))(2\alpha^2M^2)$$
$$+ (F_{2p}^{(0)}(Q^2) + \frac{1}{2}F_{2n}^{(0)}(Q^2)))(\alpha^2M^2(1-Q^2/4M^2) + (L_x^2 - L_y^2))] \tag{4.15}$$

where g_0 is the bare πN coupling constant, and the renormalized coupling constant $Zg_0^2 = g^2/4\pi = 13.5$, $\mathbf{L}_\perp^{(\pm)} \equiv \mathbf{L}_\perp \pm \alpha\mathbf{q}_\perp/2$, $\alpha \equiv \frac{k^+}{p^+}$, $D_N(k_\perp^2, \alpha) \equiv M^2\alpha^2 + k_\perp^2 + \mu^2(1-\alpha)$, and $R_N(k_\perp^2, \alpha) \equiv \frac{F_{\pi N}^N(k_\perp^2,\alpha)}{D_N(k_\perp^2,\alpha)}$. The πN form factor is taken as [87, 88]

$$F_{\pi N}(k_\perp^2, \alpha) = e^{-(D_N(k_\perp^2,\alpha)/2\alpha(1-\alpha)\Lambda^2)}, \tag{4.16}$$

and maintains charge conservation [89]. The constant Λ is a free parameter, but very large values are excluded by the small flavor asymmetry of the nucleon sea.

From Eqns. (4.14) and (4.15) we see that each term in the nucleon current operator contributes to both F_1 and F_2. The evaluation of graph 4.1c yields

$$F_{1cn}(Q^2) = -g_0^2 F_\pi(Q^2) \int_0^1 d\alpha\alpha \int \frac{d^2K}{(2\pi)^3} R(\mathbf{K}^{(+)\,2}, \alpha) R(\mathbf{K}^{(-)\,2}, \alpha)$$
$$\left[K^2 + M^2\alpha^2 - (1-\alpha)^2\frac{Q^2}{4}\right] \tag{4.17}$$

$$F_{2cn}(Q^2) = -g_0^2(2M^2)F_\pi(Q^2)\int_0^1 d\alpha\alpha^2(1-\alpha)\int\frac{d^2K}{(2\pi)^3}R(\mathbf{K}^{(+)\,2},\alpha)R(\mathbf{K}^{(-)\,2},\alpha) \tag{4.18}$$

where $\mathbf{K}_\perp^{(\pm)} \equiv \mathbf{K}_\perp \pm (1-\alpha)\mathbf{q}_\perp/2$.[2]

The proton form factors can be obtained by simply making the replacements $n \to p$ in Eqs. (4.14,4.15) and $-g_0^2 \to g_0^2$ in Eqs. (4.17,4.18). The change in sign accounts for the feature that the π^- cloud of the neutron becomes a π^+ cloud for the proton. The mean-square isovector radii $\langle r^2\rangle_i^V$, computed using Eqs. (4.13), and then taken to the chiral limit at low-Q^2, have the same singular log terms as those of the relativistic results of Beg and Zepeda [90]. The details of this calculations are presented in Appendix B.

The LFCBM was defined by choosing four free parameters: $m, \beta, \gamma, \Lambda$ so as to best reproduce the four experimentally measured electromagnetic form factors of the nucleon [25]. In the present work, the most relevant of these parameters will be varied to reproduce lattice data, and the resulting dependence on the quark mass and lattice spacing used to extrapolate to the physical region.

4.3.3 Fitting the QCDSF Form Factors and Extrapolating to the Physical Pion Mass

In this section we discuss the fitting procedure used to parametrize the nucleon form factors calculated in lattice QCD. We use data produced by the QCDSF Collaboration [18] and employ the LFCBM to calculate the corresponding form factors, varying the model parameters to find the best-fit to the different sets of lattice data obtained for different values of the current quark mass, m_q. The behavior of the fitting parameters is then represented by a polynomial function of the quark mass m_q. This polynomial fit in m_q, or equivalently in pion mass squared, m_π^2, can then be used to extrapolate the values of the fitting parameters to the physical pion mass. Nucleon form factors for the physical pion mass are then calculated using the extrapolated values for the model parameters. In the following few subsections a more elaborate explanation is given and the results are presented. In section 4.3.3 we describe the available data and the analysis procedure used to extract the quantities necessary for further fits. In sec. 4.3.3 we describe the details of the fitting and extrapolation process and in sec. 4.3.3 we present the nucleon form factors resulting from the extrapolation to the physical pion mass and make comparisons with experiment.

QCDSF Data and its Analysis

The form factor calculations in Ref. [18] were carried out for three different values of the lattice spacing, $a = \{0.47, 0.34, 0.26\}\,\mathrm{GeV}^{-1}$. For each value of a, several sets of pion (or equivalently nucleon) masses were considered. For each mass

[2]These formulae are slightly different from those of Ref. [25], correcting for some very minor typos. This leads to slight changes in the parameters that will be discussed elsewhere.

set, Dirac and Pauli form factors for both the proton and neutron were calculated at several values of Q^2. The typical range for the pion mass used varied from 1.2 GeV to 0.6 GeV, with the corresponding nucleon mass ranging from approximately 2 GeV to 1.5 GeV. The typical range for Q^2 was 0.6 GeV^2 to 2.3 GeV^2.

The LFCBM is basically a relativistic constituent quark model, so we need to relate the model constituent mass of Eq. (4.12) to the masses of the nucleon and pion. To do so we use the approach of Ref. [82], (Eq. (8))

$$M = M_\chi + \frac{cm_q^{phys}}{(m_\pi^{phys})^2} m_\pi^2, \tag{4.19}$$

where M_χ is the constituent quark mass in the chiral limit, m_q^{phys} is the current quark mass and c is of order 1. In the study of octet magnetic moments in the AccessQM model of Ref. [82], the best fit value for M_χ was 0.42 GeV, while for cm_q^{phys} it was 0.0059 GeV.

Lattice Data Fit and Extrapolation

The first step in our extrapolation of the lattice results to the physical quark mass is to fit the lattice results for each quark mass m_q by adjusting the parameters of the LFCBM calculation. For that purpose two fitting parameters were chosen. The first parameter is M_χ in Eq. (4.19), which determines the constituent quark mass. This parameter was varied for each lattice spacing separately, since some dependence upon lattice spacing was anticipated. The second parameter is the internal parameter, γ, in the nucleon wave function Eq. (4.11), which is varied separately for each pion (or equivalently nucleon) mass. For convenience, we express all magnetic form factors G_M in "physical" units of $e/2M_N^{Physical}$. Since the LFCBM uses the mass of the ρ-meson included in the pion electromagnetic form factor, we need the extrapolated value for its mass. We use the simple fitting function from Ref. [91]:

$$m_\rho = c_0 + c_1 m_\pi^2, \tag{4.20}$$

with $c_0 = 0.776\,\mathrm{GeV}$ and $c_1 = 0.427\,\mathrm{GeV}^{-1}$.

A function representing the χ^2 for the deviation between the lattice data and the values calculated using the LFCBM was constructed and minimized by varying the fitting parameters. Changing the value of M_χ causes the calculated form factors to move up or down by an amount approximately independent of Q^2, thereby causing a relatively small change in χ^2. Therefore a simple grid variation for that parameter was employed, with grid boundaries $M_\chi \in [0.15, 0.45]\,\mathrm{GeV}$, and step size of $\delta_{M_\chi} = 0.01\,\mathrm{GeV}$. The variation of χ^2 in γ was much stronger, and the Minuit package of CERN's Root framework [92] was used for the minimization. At first the boundaries for γ were set to keep it in the physical region, but successful boundless runs were also performed in order to confirm the true minimum and error sizes. The pion masses used in the lattice calculation are very large, and the resulting pionic effects are very small. Therefore the value of Λ could not be determined from lattice data

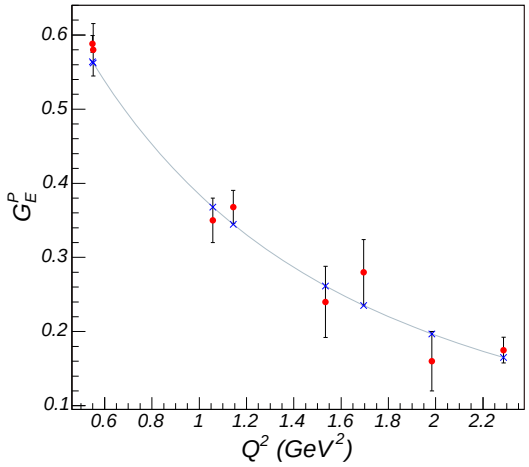

Figure 4.2: LFCBM fit to QCDSF data for $G_E^P(in\ units\ of\ e)$ for a lattice spacing $a = 0.26$ GeV^{-1}, $M_P = 1.80$ GeV and $m_\pi = 0.93$ GeV

and its value was held fixed at $\Lambda = 0.58\,\mathrm{GeV}$ from fits to physical nucleon form factors of Ref. [25]. Similarly, varying β did not change the description of the lattice data, so it was held fixed at $\beta = 0.607\,\mathrm{GeV}/c$ as in Ref. [25]. The resulting fits are in good agreement with data, as one can see in Figs. 4.2, 4.3, 4.4 and 4.5. The best-fit values of the parameters are shown in Table 4.1. The figures show results for the smallest lattice spacing, $a = 0.26\,\mathrm{GeV}^{-1}$, but the reproduction of lattice data is equally successful for larger values of a.

The next step is to extrapolate the fitting parameters to the physical quark mass. This is done using the assumption that the parameters vary smoothly as functions of the quark mass, and the fact that $m_q \sim m_\pi^2$ over the mass range investigated. We limited the extrapolation function to a low order polynomial in m_π^2. The resulting fits for two lattice spacings are presented in Figs. 4.6 and 4.7, from which we see that the fitting function provides a very accurate representation of the values obtained from lattice data.

The fitted values of γ and the extrapolation to the physical value of m_π, with their corresponding errors, are shown in Figs. 4.6 and 4.7.

The fitted values of γ and the extrapolation to the physical value of m_π, with their corresponding errors, are shown in Figs. 4.6 and 4.7.

In our calculations, M_χ has a very weak dependence on the pion mass, but it has a rather strong dependence upon the lattice spacing. As we see in Table 4.1 and Figs. 4.2-4.5, very good fits to the lattice data are obtained even without varying M_χ for each quark mass. In contrast, Fig. 4.8 and Table 4.1 show rather dramatic variation of M_χ for different values of the lattice spacing a. This suggests that the larger values of the lattice spacing are rather far from the continuum limit and (at best) only the results for the smallest lattice spacing should be compared with experimental data. It would clearly be desirable to have new data at even

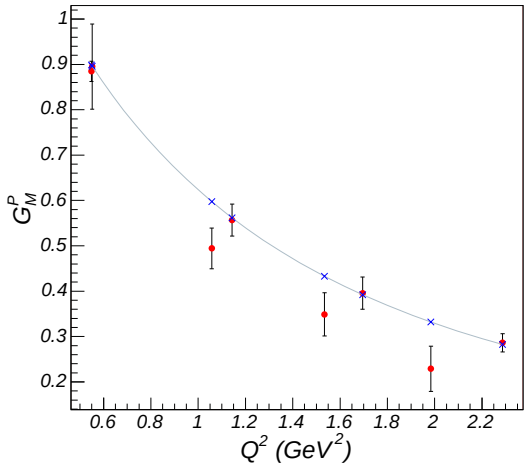

Figure 4.3: LFCBM fit to QCDSF data for $G_M^P(in\ units\ of\ e/(2M_N^{Physical}))$ for a lattice spacing $a = 0.26$ GeV^{-1}, $M_P = 1.80$ GeV and $m_\pi = 0.93$ GeV

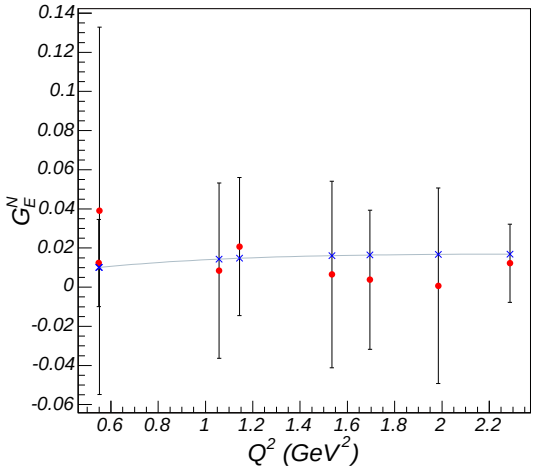

Figure 4.4: LFCBM fit to QCDSF data for $G_E^N(in\ units\ of\ e)$ for a lattice spacing $a = 0.26$ GeV^{-1}, $M_P = 1.80$ GeV and $m_\pi = 0.93$ GeV

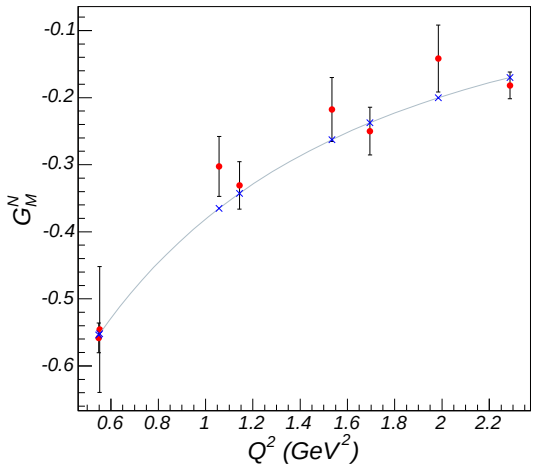

Figure 4.5: LFCBM fit to QCDSF data for $G_M^N(in\ units\ of\ e/(2M_N^{Physical}))$ for a lattice spacing $a = 0.26$ GeV^{-1}, $M_P = 1.80$ GeV and $m_\pi = 0.93$ GeV

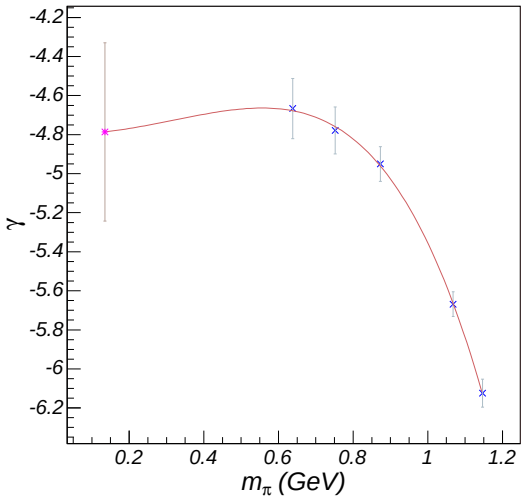

Figure 4.6: Polynomial extrapolation of γ vs. m_π for lattice spacing $a = 0.47\ GeV^{-1}$

Table 4.1: Lattice data and LFCBM fitting parameters. (All expressed in powers of GeV.)

a	m_π	M_N	M_χ	γ
0.47	1.146	2.062	0.390(5)	−6.12(7)
0.47	1.068	1.981	0.390(5)	−5.67(6)
0.47	0.873	1.746	0.390(5)	−4.95(9)
0.47	0.752	1.567	0.390(5)	−4.78(12)
0.47	0.638	1.503	0.390(5)	−4.67(15)
0.47	*0.135*	*0.938*	*0.390(5)*	*−4.79(46)*
0.34	1.201	2.141	0.280(5)	−5.03(6)
0.34	1.035	1.933	0.280(5)	−4.37(5)
0.34	0.881	1.732	0.280(5)	−4.99(5)
0.34	0.706	1.522	0.280(5)	−3.51(6)
0.34	*0.135*	*0.938*	*0.280(5)*	*−2.91(29)*
0.26	1.237	2.202	0.210(5)	−4.78(5)
0.26	1.092	2.028	0.210(5)	−4.14(7)
0.26	0.925	1.802	0.210(5)	−3.69(5)
0.26	0.744	1.600	0.210(5)	−3.09(6)
0.26	0.580	1.379	0.210(5)	−3.01(13)
0.26	*0.135*	*0.938*	*0.210(5)*	*−2.41(22)*

smaller a, or use an improved action, known to provide a good approximation to the continuum limit.

Use of the values of γ and M determined by the lattice data in the LFCBM defines a lattice version of the LFCBM. We may use this new model to compute the form factors at arbitrarily large values of Q^2, thereby extending the kinematic range of the lattice calculations. The results are shown in Figs. 4.9, 4.10, 4.11 and 4.12. In Figs. 4.13 and 4.14 we show the corresponding plots of $\mu_0 G_E/G_M$.

Results at the Physical Pion Mass and Comparison With Experiment

We use the extrapolated values of γ and M (Figs. 4.6-4.8) to calculate the nucleon electric and magnetic form factors using the physical pion and nucleon masses. The resulting plots for G_E, G_M and their ratios vs. Q^2 for both proton and neutron are shown in Figs. 4.15-4.20. Figure 4.21 shows that our results are in more or less good agreement with the experimental data in the low-Q^2 region, but yield a slightly lower value of Q^2 for the zero cross-over point than that extrapolated from experiment [93]. A new analysis that includes an estimate of all of the effects of two photon exchange yields a zero-crossing value that is somewhat closer to ours [94] but future data will resolve this unambiguously.

An alternative method of determining the value of the Q^2 for which G_E/G_M passes through zero at the physical pion mass is to fit the crossover values as a linear

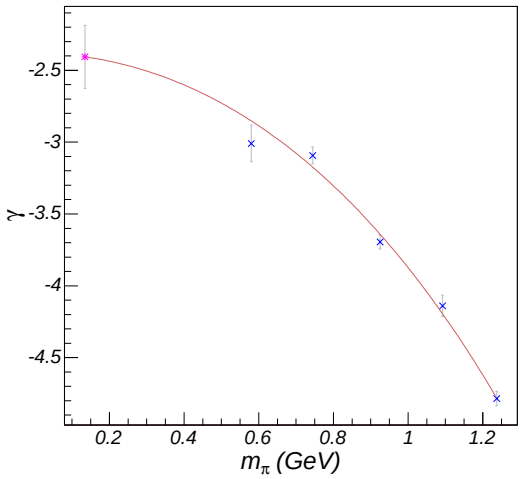

Figure 4.7: Polynomial extrapolation of γ vs. m_π for lattice spacing $a = 0.26\ GeV^{-1}$

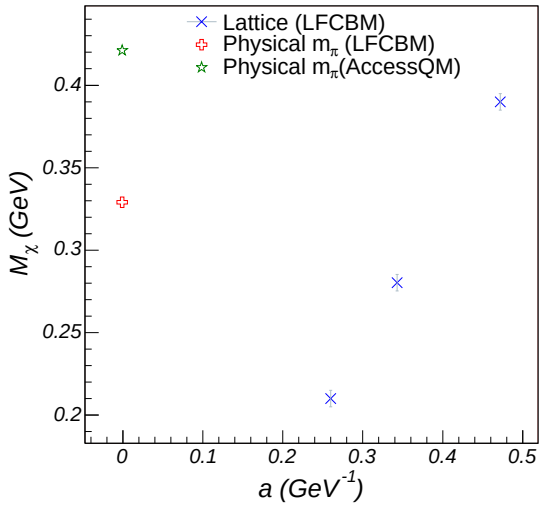

Figure 4.8: Variation of $M_\chi$with lattice spacing a.The best-fit values of M_χ for physical m_π using LFCBM and AcessQM models are presented as well.

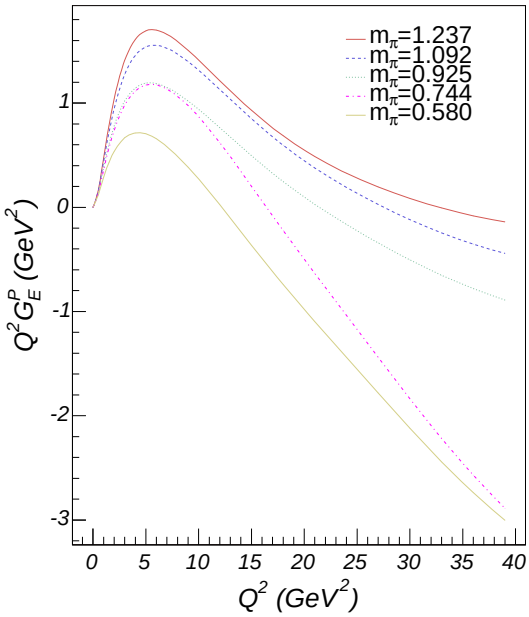

Figure 4.9: LFCBM calculations using parameters (Figs. 4.6, 4.7 and 4.8) obtained by fitting the lattice results for the proton electric form factor, G_E, at lattice spacing $a = 0.26\ GeV^{-1}$.

function of m_π^2 and extrapolate again to the physical pion mass. The resulting plot is shown in Fig. 4.22.

This procedure yields approximately the same cross-over point as found in Fig. 4.17.

4.3.4 Discussion

Our study of the form factors calculated using the LFCBM with parameters determined by lattice data and by extrapolation to the physical pion masses yields very interesting results. The ratio G_E^p/G_M^p passes through zero for all of the calculations, similar to LFCBM prediction for physical proton. The main variation of the position of the crossover between the fitting curves shown in Figs. 4.13 and 4.14 comes from the variation of the nucleon mass, and not the variation of γ. Even though for the physical pion mass, the ratio varies rapidly as a function of γ in the region $\gamma \sim -2$, the function G_E/G_M for the neutron has a turning point at about $\gamma \sim -2.3$. We shall explain these features using the LFCBM.

Let us express the ratio G_E/G_M in terms of Pauli and Dirac form factors, F_1 and F_2, respectively, using Eq. (4.7)

$$\frac{G_E}{G_M} = \frac{F_1 - Q^2/(4M_N^2)F_2}{F_1 + F_2} = 1 - \frac{1 + Q^2/(4M_N^2)}{1 + F_1/F_2} \tag{4.21}$$

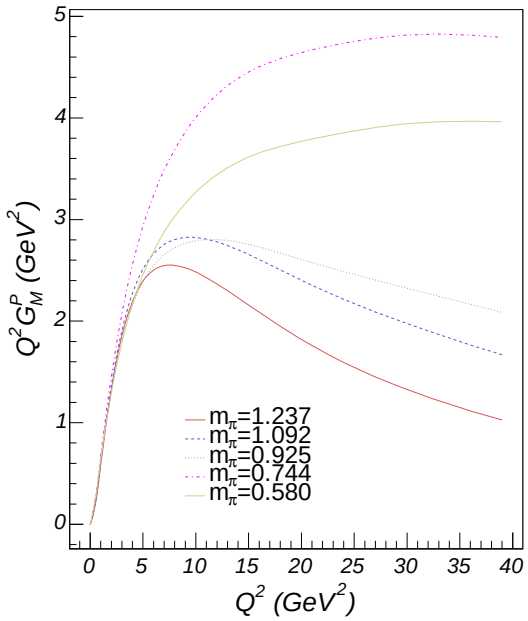

Figure 4.10: LFCBM calculations using parameters (Figs. 4.6, 4.7 and 4.8) obtained by fitting the lattice results for the proton magnetic form factor, G_M, at lattice spacing $a = 0.26\ GeV^{-1}$.

Consider first the values of $Q^2 = (Q^2_{\rm Cross})$ where the ratio G_E/G_M for the proton passes through zero for the set of calculations shown in Fig. 4.13. Equation (4.21) tells us that

$$Q^2_{\rm Cross} = 4M_N^2 \frac{F_1}{F_2} \tag{4.22}$$

Now let us consider the formula for $F_{i\alpha}(Q^2)$, Eq. (4.13). The second and third terms in Eq. (4.13) are only significant in the $low - Q^2$ region for physical pion masses. In the $high - Q^2$ region, or for lattice calculations with high pion mass, these terms are vanishingly small. Indeed the numerical calculations support these statements, so we can neglect their contribution in the rest of the discussion.

The corresponding formulas for $F_1^{(0)}$ and $F_2^{(0)}$ from Ref. [26] are

$$F_1^{(0)}(Q^2) = \int \frac{d^2q_\perp d\xi}{\xi(1-\xi)} \frac{d^2K_\perp d\eta}{\eta(1-\eta)} \tilde{\Phi}^\dagger(M_0')\tilde{\Phi}(M_0) \times \left\langle \chi_0^{rel}(\mathbf{p}_1', \mathbf{p}_2') | \chi_0^{rel}(\mathbf{p}_1, \mathbf{p}_2) \right\rangle \langle \uparrow \mathbf{p}_3' | \uparrow \mathbf{p}_3 \rangle \tag{4.23}$$

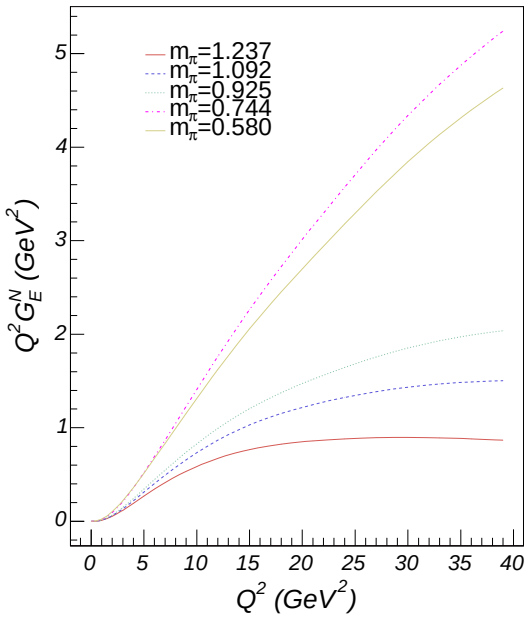

Figure 4.11: LFCBM calculations using parameters (Figs.4.6, 4.7 and 4.8) obtained by fitting the lattice results for the neutron electric form factor, G_E, at lattice spacing $a = 0.26\ GeV^{-1}$.

$$\frac{QF_2^{(0)}(Q^2)}{2M_N} = \int \frac{d^2q_\perp d\xi}{\xi(1-\xi)} \frac{d^2K_\perp d\eta}{\eta(1-\eta)} \tilde{\Phi}^\dagger(M_0')\tilde{\Phi}(M_0) \times \left\langle \chi_0^{rel}(\mathbf{p}_1', \mathbf{p}_2') | \chi_0^{rel}(\mathbf{p}_1, \mathbf{p}_2) \right\rangle \langle \uparrow \mathbf{p}_3' | \downarrow \mathbf{p}_3 \rangle \tag{4.24}$$

The $\tilde{\Phi}(M_0)$ factors are wave functions of the form of Eq. (4.11), but using the lattice values of γ and M shown in Figs. 4.6-4.8. We stress that these two integrals differ only by the last factor, which gives the spin non-flip and spin-flip dependence of $F_1^{(0)}$ and $QF_2^{(0)}/2M_N$, respectively. At high Q^2 these matrix elements are each of order Q, causing the ratio QF_2/F_1 to be approximately constant. So we can express Q^2_{Cross} as

$$Q^2_{Cross} = 4M_N^2 \left(\frac{\int_{\uparrow\uparrow}}{\int_{\uparrow\downarrow}} \right)^2 \tag{4.25}$$

where $\int_{\uparrow\uparrow}$ denotes the integral for $F_1^{(0)}$, and $\int_{\uparrow\downarrow}$ denotes the integral for $F_2^{(0)}$.

In the high-Q^2 region, the ratio in Eq. (4.25) is approximately a constant because the difference comes only from the overlap factors of the spin-dependent parts of the wave functions in the integrals (see Refs. [25], [99]). Therefore the behavior of Q^2_{Cross} is governed primarily by the factor M_N^2. The linear variation of

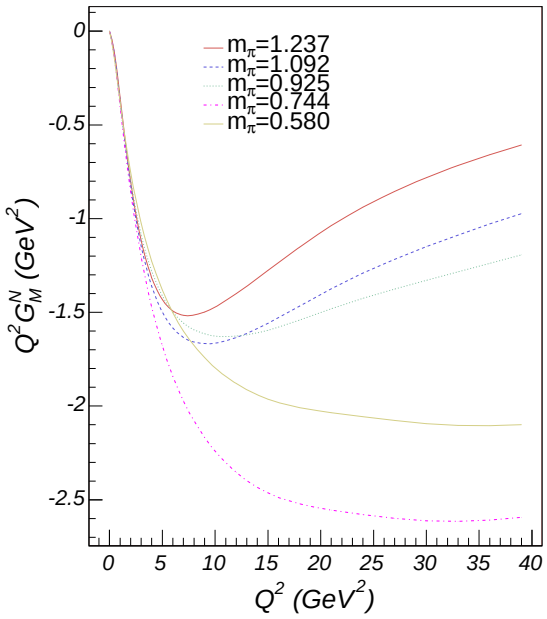

Figure 4.12: LFCBM calculations using parameters (Figs.4.6, 4.7 and 4.8) obtained by fitting the lattice results for the neutron magnetic form factor, G_M, at lattice spacing $a = 0.26\ GeV^{-1}$.

Q^2_{Cross} vs. M^2_N presented in Fig. 4.23 shows the validity of this interpretation.

We can also understand the behavior of G_E/G_M versus γ, by considering its role in the wave function. The factor γ determines the size of the momenta appearing in the integrands of Eqs.(4.23) and (4.24). The corresponding integrands differ by terms that are ratios of second order polynomials of the integration variables. For large absolute values of γ, the high momenta are cut off more strongly, so that the contribution of terms that cause differences between the integrals are not very significant. For small absolute values of γ, the integrals become more sensitive to those terms and we obtain a larger variation of the ratios of the integrals and hence the ratio G_E/G_M.

4.4 VMD

4.4.1 Introduction

Given the considerable interest in the vector meson dominance (VMD) approach, next we consider its suitability as an alternative method of chiral extrapolation. There are many variations of the basic VMD, but we choose the implementation of Lomon [27], because it is phenomenologically extremely successful. We introduce the dependence of the vector meson masses in m_π found in earlier lattice

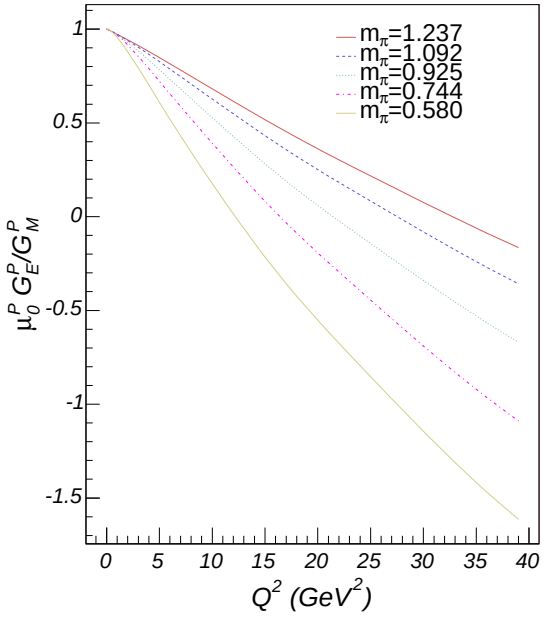

Figure 4.13: LFCBM calculations using parameters (Figs.4.6, 4.7 and 4.8) obtained by reproducing lattice results for the ratio of proton form factors, $\mu_0 G_E/G_M$, at lattice spacing $a = 0.26\ GeV^{-1}$.

studies [77,91] and parametrize the mass dependence of the corresponding couplings in order to best describe the lattice QCD data. The major disappointment is that the functional form is so sensitive to the parameters, that it is meaningless to compare any extrapolation of the form factors to the physical pion mass. This makes the VMD approach unsuitable as a method of chiral extrapolation. On the other hand, by fixing the parameters to the values given in Ref. [27] at the physical mass, it is possible to obtain a fit to all of the lattice QCD data of comparable quality to that found earlier using LFCBM.

4.4.2 Review of the GKex Model

Here we briefly summarize the formulation of the GKex model from Ref. [27]. The extended Gari-Krümpelmann model exhibits the basic properties of a VMD model, and also phenomenologically incorporates the correct high-Q^2 behavior of the nucleon electromagnetic form factors as implied by PQCD. The model was successfully fit to the present experimental data sets available for the nucleon electromagnetic form factors. The particular interest in the model is increased by its ability to describe the fall-off of the proton ratio, G_E/G_M, vs Q^2, as measured recently in Refs. [21, 22].

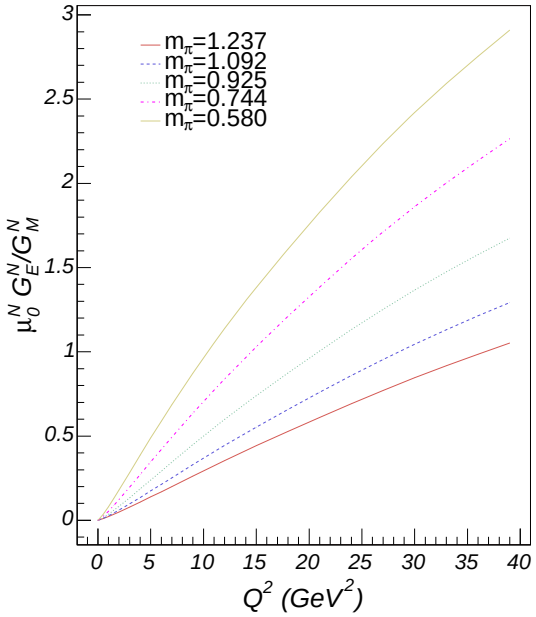

Figure 4.14: LFCBM calculations using parameters (Figs.4.6, 4.7 and 4.8) obtained by reproducing lattice results for the ratio of neutron form factors, $\mu_0 G_E/G_M$, at lattice spacing $a = 0.26\ GeV^{-1}$.

In calculating the nucleon Pauli and Dirac form factors, one can express them in terms of isoscalar and isovector form factors

$$\begin{aligned} 2F_i^p &= F_i^{IS} + F_i^{IV}; \\ 2F_i^n &= F_i^{IS} - F_i^{IV}; \end{aligned} \tag{4.26}$$

where $i = 1, 2$.

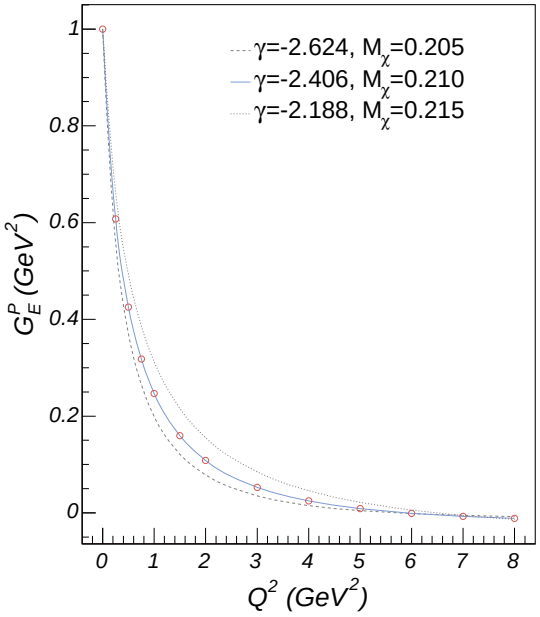

Figure 4.15: Extrapolated calculations for the proton electric form factor, G_E, for lattice spacing $a = 0.26\ GeV^{-1}$. The dashed and dotted curves show the upper and lower limits of variation of the calculated values due to the uncertainties of the parameters γ and M_χ.

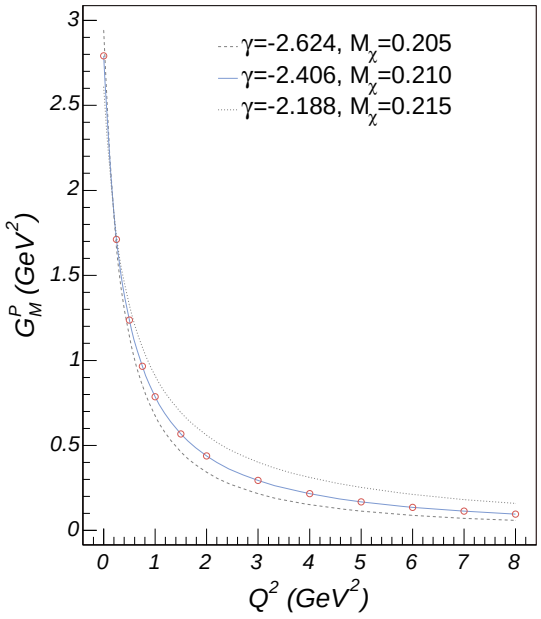

Figure 4.16: Extrapolated calculations for the proton magnetic form factor, G_M, for lattice spacing $a = 0.26\ GeV^{-1}$. The dashed and dotted curves show the upper and lower limits of variation of the calculated values due to the uncertainties of the parameters γ and M_χ.

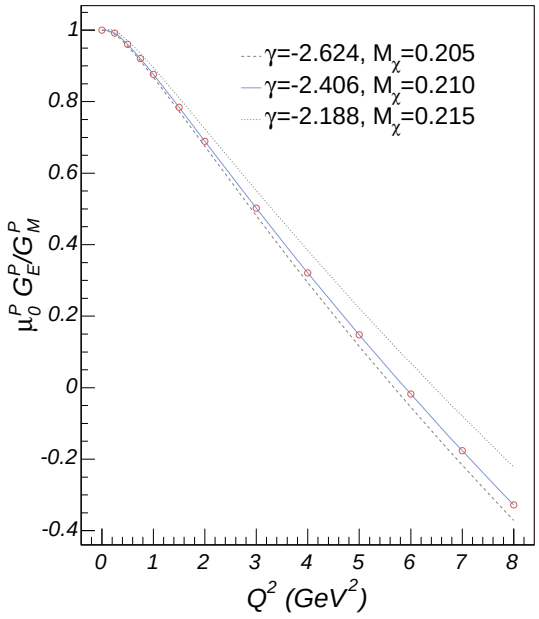

Figure 4.17: Extrapolated calculations for the ratio of proton form factors, $\mu_0 G_E/G_M$, for lattice spacing $a = 0.26\ GeV^{-1}$. The dashed and dotted curves show the upper and lower limits of variation of the calculated values due to the uncertainties of the parameters γ and M_χ.

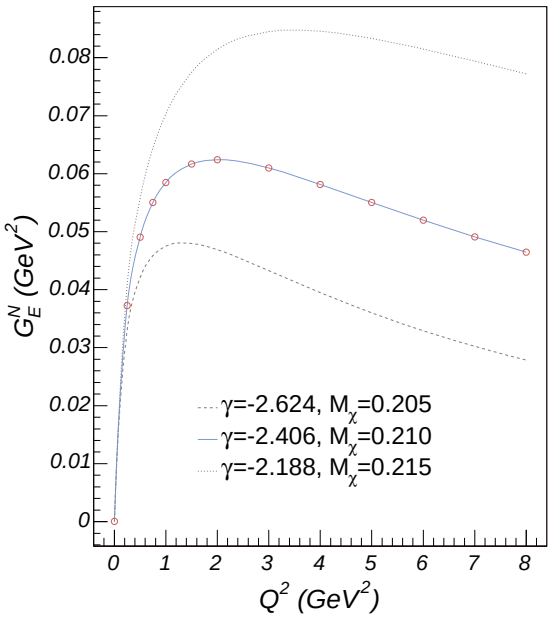

Figure 4.18: Extrapolated calculations for the neutron electric form factor, G_E, for lattice spacing $a = 0.26\ GeV^{-1}$. The dashed and dotted curves show the upper and lower limits of variation of the calculated values due to the uncertainties of the parameters γ and M_χ.

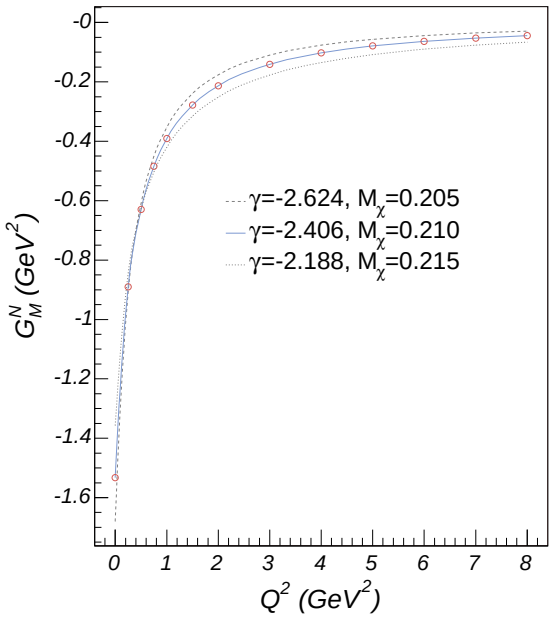

Figure 4.19: Extrapolated calculations for the neutron magnetic form factor, G_M, for lattice spacing $a = 0.26\ GeV^{-1}$. The dashed and dotted curves show the upper and lower limits of variation of the calculated values due to the uncertainties of the parameters γ and M_χ.

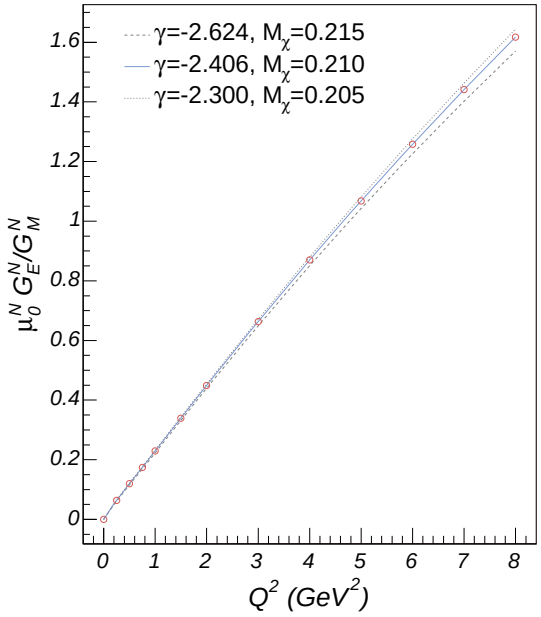

Figure 4.20: Extrapolated calculations for the ratio of neutron form factors, $\mu_0 G_E/G_M$, for lattice spacing $a = 0.26\ GeV^{-1}$. The dashed and dotted curves show the upper and lower limits of variation of the calculated values due to the uncertainties of the parameters γ and M_χ.

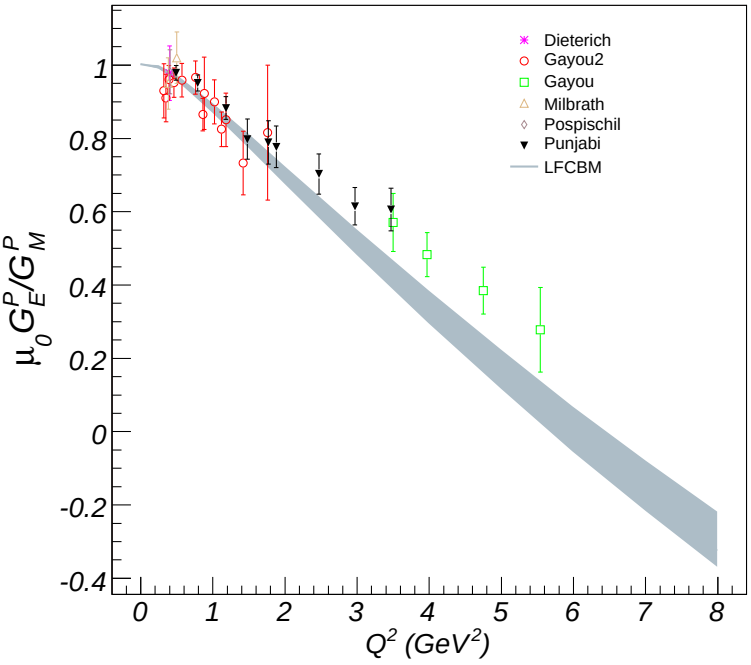

Figure 4.21: Comparison of the extrapolated calculations for the ratio of proton form factors, $\mu_0 G_E/G_M$, for lattice spacing $a = 0.26\ GeV^{-1}$ with the data. The experimental points used are taken from Refs.: Dieterich [95], Gayou2 [96], Gayou [22], Milbrath [97], Pospischil [98] and Punjabi [71]

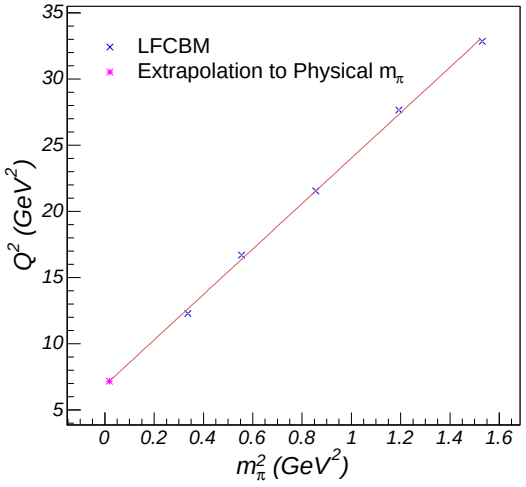

Figure 4.22: Extrapolation of Q^2_{Cross} where G_E/G_M passes through zero for lattice spacing $a = 0.26\ GeV^{-1}$.

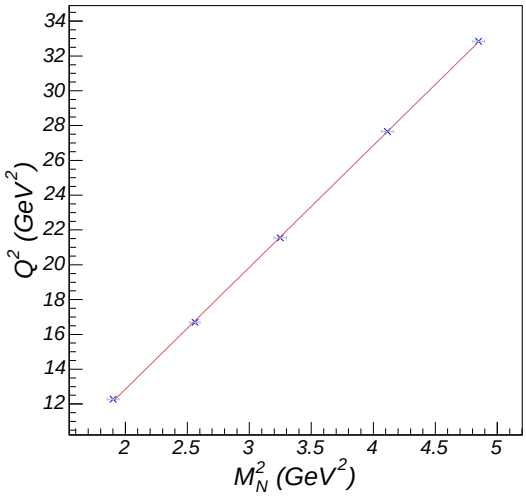

Figure 4.23: Linear fit of Q^2_{Cross} where G_E/G_M passes through zero for lattice spacing $a = 0.26\ GeV^{-1}$.

The isoscalar and isovector form factors were parametrized by Lomon as

$$
\begin{aligned}
F_1^{iv}(Q^2) &= N/2\frac{1.0317 + 0.0875(1+Q^2/0.3176)^{-2}}{(1+Q^2/0.5496)}F_1^{\rho}(Q^2) \\
&\quad + \frac{g_{\rho'}}{f_{\rho'}}\frac{m_{\rho'}^2}{m_{\rho'}^2+Q^2}F_1^{\rho}(Q^2) + \left(1 - 1.1192\,N/2 - \frac{g_{\rho'}}{f_{\rho'}}\right)F_1^{D}(Q^2) \\
F_2^{iv}(Q^2) &= N/2\frac{5.7824 + 0.3907(1+Q^2/0.1422)^{-1}}{(1+Q^2/0.5362)}F_2^{\rho}(Q^2) \\
&\quad + \kappa_{\rho'}\frac{g_{\rho'}}{f_{\rho'}}\frac{m_{\rho'}^2}{m_{\rho'}^2+Q^2}F_2^{\rho}(Q^2) + \left(\kappa_{\nu} - 6.1731\,N/2 - \kappa_{\rho'}\frac{g_{\rho'}}{f_{\rho'}}\right)F_2^{D}(Q^2) \\
F_1^{is}(Q^2) &= \frac{g_{\omega}}{f_{\omega}}\frac{m_{\omega}^2}{m_{\omega}^2+Q^2}F_1^{\omega}(Q^2) + \frac{g_{\omega'}}{f_{\omega'}}\frac{m_{\omega'}^2}{m_{\omega'}^2+Q^2}F_1^{\omega}(Q^2) + \frac{g_{\phi}}{f_{\phi}}\frac{m_{\phi}^2}{m_{\phi}^2+Q^2}F_1^{\phi}(Q^2) \\
&\quad + \left(1 - \frac{g_{\omega}}{f_{\omega}} - \frac{g_{\omega'}}{f_{\omega'}}\right)F_1^{D}(Q^2) \\
F_2^{is}(Q^2) &= \kappa_{\omega}\frac{g_{\omega}}{f_{\omega}}\frac{m_{\omega}^2}{m_{\omega}^2+Q^2}F_2^{\omega}(Q^2) + \kappa_{\omega'}\frac{g_{\omega'}}{f_{\omega'}}\frac{m_{\omega'}^2}{m_{\omega'}^2+Q^2}F_2^{\omega}(Q^2) \\
&\quad + \kappa_{\phi}\frac{g_{\phi}}{f_{\phi}}\frac{m_{\phi}^2}{m_{\phi}^2+Q^2}F_2^{\phi}(Q^2) + \left(\kappa_s - \kappa_{\omega}\frac{g_{\omega}}{f_{\omega}} - \kappa_{\omega'}\frac{g_{\omega'}}{f_{\omega'}} - \kappa_{\phi}\frac{g_{\phi}}{f_{\phi}}\right)F_2^{D}(Q^2)
\end{aligned}
\tag{4.27}
$$

with pole terms of the $\omega(782)$, $\phi(1020)$, $\omega'(1420)$, $\rho(770)$ and $\rho'(1450)$ mesons, and the F_i^D terms ensuring the correct asymptotic behavior as calculated in PQCD. The F_i^{α}, with $\alpha = \rho$, ω, or ϕ, are the meson-nucleon form factors.

The following parametrization of these form factors is chosen for GKex:

$$
\begin{aligned}
F_1^{\alpha,D}(Q^2) &= \frac{\Lambda_{1,D}^2}{\Lambda_{1,D}^2+\tilde{Q}^2}\frac{\Lambda_2^2}{\Lambda_2^2+\tilde{Q}^2}, \\
F_2^{\alpha,D}(Q^2) &= \frac{\Lambda_{1,D}^2}{\Lambda_{1,D}^2+\tilde{Q}^2}\left(\frac{\Lambda_2^2}{\Lambda_2^2+\tilde{Q}^2}\right)^2, \\
F_1^{\phi}(Q^2) &= F_1^{\alpha}\left(\frac{Q^2}{\Lambda_1^2+Q^2}\right)^{1.5}, \quad F_1^{\phi}(0)=0, \\
F_2^{\phi}(Q^2) &= F_2^{\alpha}\left(\frac{\Lambda_1^2}{\mu_\phi^2}\frac{Q^2+\mu_\phi^2}{\Lambda_1^2+Q^2}\right)^{1.5}, \\
\text{with } \tilde{Q}^2 &= Q^2\frac{\ln\left[(\Lambda_D^2+Q^2)/\Lambda_{\rm QCD}^2\right]}{\ln(\Lambda_D^2/\Lambda_{\rm QCD}^2)}\ .
\end{aligned}
\tag{4.28}
$$

With this formulation there are unknown 8 meson coupling constants, 4 cutoff masses, one magnetic moment, and a single normalization constant, all of which should be determined from the fits to the experimental data. Fits to the experimental data points were made using different sets of data, some of which excluded the controversial high G_E^p/G_M^p measured previously by Rosenbluth separation method. The fits with different data sets were labeled GKex(01), GKex(01-), GKex(02S) and GKex(02L). The values of the fitted parameters are listed in the Table I in Ref. [27]. Figure (4.24) shows that the model GKex(02S) describes the fall-off of G_E^p/G_M^p with Q^2, in contrast with GKex(01) and GKex(01-), which stay almost flat in the considered range of the Q^2. In the present work we use all 4 models in our attempt to describe the lattice data.

4.4.3 Lattice Data Fits and Results

We employ the Extended Gari-Krümpelmann Model (GKex) of Lomon Ref. [27] to fit Lattice QCD calculated nucleon electric and magnetic form factors produced by the QCDSF collaboration [18].

Extrapolation of the GKex Model's Parameters

Using the model to reproduce lattice data requires that we make extrapolations of some of the parameters that depend on the mass of the hadron constituents. We start by considering the normalizations of the isovector and isoscalar form factors that depend on the nucleon magnetic moments:

$$
\begin{aligned}
F_2^{IV}(0) &= \kappa_\nu = (\mu_p - 1 - \mu_n)\,; \\
F_2^{IS}(0) &= \kappa_s = (\mu_p - 1 + \mu_n)\,;
\end{aligned}
\tag{4.29}
$$

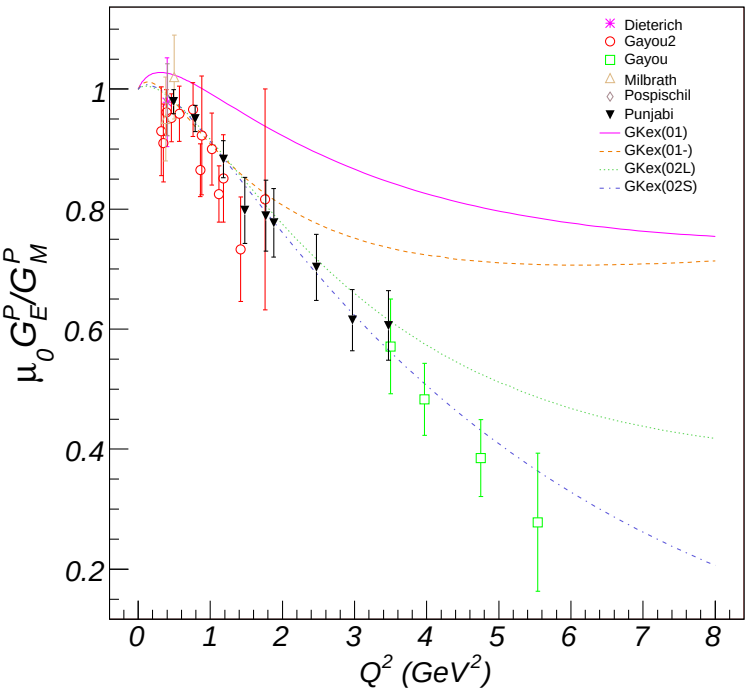

Figure 4.24: R_p, the ratio $\mu_p G_p^E/G_p^M$. Comparison of fits using the GKex model with the data. The experimental points used are taken from Refs.: Dieterich [95], Gayou2 [96], Gayou [22], Milbrath [97], Pospischil [98] and Punjabi [71]

The magnetic moments have non-trivial dependence upon the pion mass as a consequence of chiral symmetry. For example, the leading dependence on the quark mass near the chiral limit is in fact non-analytic (i.e. proportional to $m_\pi \sim m_q^{1/2}$). To extrapolate the nucleon magnetic moments for the mass range accessible in lattice QCD to the physical mass scale, we use the Padé approximant derived in Ref. [77]

$$\begin{aligned} \mu_p\left(m_\pi\right) &= \frac{3.31}{1 + 1.37 \cdot m_\pi + 0.452 \cdot m_\pi^2}, \\ \mu_n\left(m_\pi\right) &= \frac{-2.39}{1 + 1.85 \cdot m_\pi + 0.271 \cdot m_\pi^2}. \end{aligned} \tag{4.30}$$

The dependence of the masses of the vector mesons upon the pion mass was studied in the work by Leinweber et al. [91]. We use a linear extrapolation for the vector meson masses, which was shown in Ref. [91] to provide quite a good approximation to the full mass function including the LNA and NLNA behavior:

$$\begin{aligned} m_v\left(m_\pi\right) &= c_0 + c_1 m_\pi^2; \\ m_v\left(m_\pi\right) &= m_v^{phys} + c_1\left(m_\pi^2 - (m_\pi^{phys})^2\right); \\ c_1 &= 0.4273\,\mathrm{GeV}^{-1}; \end{aligned} \tag{4.31}$$

The vector-meson nucleon effective coupling constants may also depend on the mass of the hadron constituents and to describe that, we choose the following extrapolation forms

$$g_i^\alpha\left(m_\pi^2\right) = g_{i0}^\alpha + a_i^{l_\alpha}\left(m_\pi^2 - (m_\pi^{phys})^2\right) + b_i^{l_\alpha}\left(m_\pi^4 - (m_\pi^{phys})^4\right) \tag{4.32}$$

where $\alpha = \rho'$, ω, ω', ϕ; $l_\alpha = \{IV \text{ for } \alpha = \rho'; IS \text{ for } \alpha = \omega, \omega', \phi\}$; $i = 1, 2$; and $g_{10}^\alpha = \frac{g_\alpha}{f_\alpha}$, $g_{20}^\alpha = \kappa_\omega \frac{g_\alpha}{f_\alpha}$ are the effective coupling constants at the physical m_π. These are taken from the fits to the physical data of Ref. [27].

We choose a similar ansatz for the extrapolation of the cut-off masses

$$\Lambda\left(m_\pi^2\right) = \Lambda_0 + a^\Lambda\left(m_\pi^2 - (m_\pi^{phys})^2\right) + b^\Lambda\left(m_\pi^4 - (m_\pi^{phys})^4\right) \tag{4.33}$$

where $\Lambda = \Lambda_1, \Lambda_2, \Lambda_D, \Lambda_{QCD}$ and μ_ϕ.

Fitting Procedure

Using the extrapolation forms given in Eqs. (4.30-4.33), we can fit the GKex form factors given by Eq. (4.27) to the lattice data by varying the coefficients a, b of relations (4.32) and (4.33). We performed the fits using the 4 different sets of physical GKex parameters reported in Ref. [27].

We fitted the lattice data points for all three lattice spacings available using the Minuit package of CERN's Root framework [92]. The resulting fits for the smallest lattice spacing $a = 0.26$ GeV^{-1} with 120 data points are shown in the Figs. 4.25, 4.26, 4.27 and 4.28, where the corresponding fits using the LFCBM are shown for comparison.

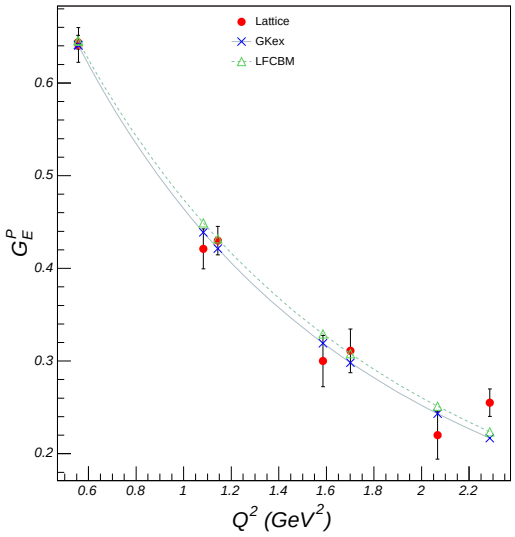

Figure 4.25: GKex(01-) fit[solid] to QCDSF data for $G_E^P(in\ units\ of\ e)$ for a lattice spacing $a = 0.26$ GeV^{-1}, $M_N = 2.20$ GeV and $m_\pi = 1.24$ GeV. LFCBM fits[dashed] are also shown for comparison.

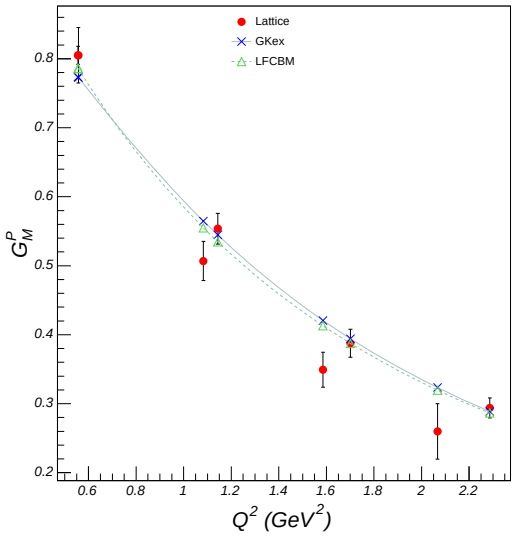

Figure 4.26: GKex(01-) fit[solid] to QCDSF data for $G_M^P(in\ units\ of\ e/(2M_N^{Physical}))$ for a lattice spacing $a = 0.26$ GeV^{-1}, $M_N = 2.20$ GeV and $m_\pi = 1.24$ GeV. LFCBM fits[dashed] are also shown for comparison.

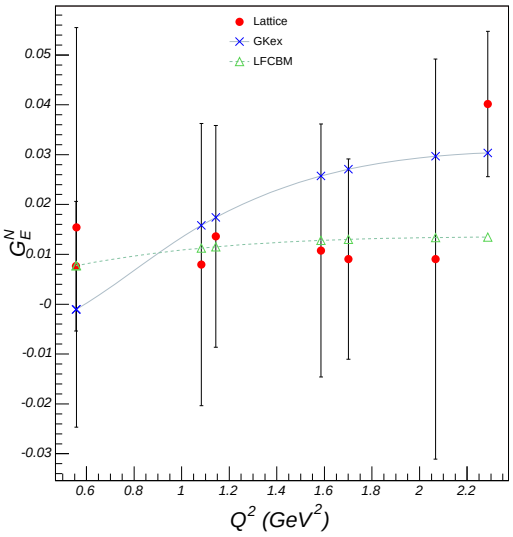

Figure 4.27: GKex(01-) fit[solid] to QCDSF data for $G_E^N(in\ units\ of\ e)$ for a lattice spacing $a = 0.26$ GeV^{-1}, $M_N = 2.20$ GeV and $m_\pi = 1.24$ GeV. LFCBM fits[dashed] are also shown for comparison.

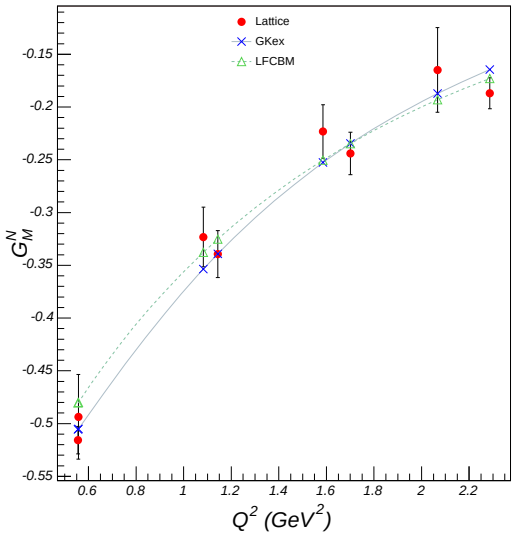

Figure 4.28: GKex(01-) fit[solid] to QCDSF data for $G_M^N(in\ units\ of\ e/(2M_N^{Physical}))$ for a lattice spacing $a = 0.26$ GeV^{-1}, $M_N = 2.20$ GeV and $m_\pi = 1.24$ GeV. LFCBM fits[dashed] are also shown for comparison.

Table 4.2: GKex fitting parameters and χ^2 for lattice spacing $a = 0.26$ GeV^{-1}.

	GKex(01)	GKex(01-)	GKex(02L)	GKex(02S)
χ^2	185	103	671	217
a_1^{IV}	-1.80(16)	-2.35	-1.7(2)	-1.86(17)
b_1^{IV}	0.46(11)	0.81	0.54(14)	0.39(13)
a_2^{IV}	-11.9(5)	-55.2	-1(1)	-10.9(5)
b_2^{IV}	2.98(36)	18	-0.34(76)	2.34(38)
a_1^{IS}	-0.99(18)	-1.61	-0.39(9)	-0.58(1)
b_1^{IS}	-0.21(14)	0.28	0.06(6)	-0.078(73)
a_2^{IS}	8.6(18)	3.1	2.53(58)	-0.32(14)
b_2^{IS}	2.6(14)	-0.44	0.62(41)	0.1(1)
a^{Λ}	0.034(38)	-0.19	0.3(1)	0.035(42)
b^{Λ}	-0.10(3)	0.065(33)	-0.14(6)	-0.12(3)

The resulting χ^2 and the fitting parameters for lattice spacing $a = 0.26$ GeV^{-1} are summarized in Table 4.2. For a comparison, we obtained $\chi^2 = 81$ for the LFCBM fit.

Results

As one can see from Table 4.2, the best fit to the data is obtained using the GKex(01-) model, even though one is inclined to believe that GKex(02S) gives the best description of the nucleon structure since it exhibits the rapid decrease with Q^2 of the experimentally measured ratio, G_E^P/G_M^P. One can see this from our Fig. 4.24 as well as the original work of Ref. [27]. We also note that our attempts to fit the data using only the lowest order polynomial forms in m_π of the coupling constants (4.32), (4.33) did not yield satisfactory results. Indeed we had to include 10 fitting parameters for successful extrapolations.

4.5 Conclusion

We have seen that the LFCBM can produce a very good description of the lattice QCD data for the nucleon form factors over a wide range of quark masses with a smooth, analytic variation of the wave function parameter, γ, and the constituent quark mass, M. The pion cloud plays very little role in the mass range for which the lattice simulations have been made but it rapidly becomes more important as we approach the chiral limit. From the rather strong dependence of the form factors on the lattice spacing, a, it is not yet clear that we have obtained a good approximation to the continuum limit, but the form factors obtained at the smallest value of a are in reasonable agreement with experimental data in the low-Q^2 region for which the lattice simulations were made.

At present the lattice simulations are limited to values of the momentum transfer at or below $2\,\mathrm{GeV}^2$ and it is therefore a very big extrapolation to look at the behavior of the form factors in the region of greatest current interest. Nevertheless, the behavior of G_E/G_M which we find is particularly interesting. The ratio crosses zero for all values of the quark mass but the position where this happens varies over a very wide range of Q^2. This variation can be understood almost entirely in terms of the variation of the corresponding nucleon mass, given that the ratio QF_1/F_2 is approximately Q^2-independent in the model. We obtain the same value of Q^2 for the cross-over whether we extrapolate the position as a function of quark mass or simply evaluate the form factors at the physical pion mass using the fitted dependence of the wave function parameters on pion mass.

Since the VMD approach has been widely used to describe the experimental data at high Q^2 (a region of special phenomenological interest at the present time), we use a modern version of the VMD model, namely the Gari-Krümpelmann model as implemented by Lomon [27], and extend it in a natural way to describe the lattice data in the large mass region. Starting with the existing fit to the experimental data we find that it is possible to describe the lattice simulations quite well. However, it was necessary to allow some 10 parameters to vary smoothly with the pion mass in order to do so. In comparison, the LFCBM produced a fit of similar quality with only two parameters varied. As a result we are led to the conclusion that VMD is not suitable as a method of chiral extrapolation.

In the immediate future it is clearly very important to improve on the lattice data, both by ensuring that we really have a good approximation to the continuum limit (e.g., by using a suitably improved action) and by extending the calculations to higher values of Q^2. It would also be important to remove the need for quenching, even though that may not be such a limitation at large Q^2. From the point of view of developing a deeper understanding of QCD itself, it is important that the LFCBM is able to describe the present lattice data over such a wide range of masses. We would encourage a similar exercise for other models as a novel test of their validity. It remains to be seen whether the LFCBM has indeed been successful in predicting the behavior of the form factors at higher Q^2 and indeed whether it will match future experimental data.

Chapter 5

Quark-Meson Coupling Model: Connecting the Nuclear Forces with the Underlying Degrees Of Freedom

5.1 Introduction

The structure of the atomic nucleus has long been the subject of intensive explorations both for theory and experiment. A large variety of theoretical models have been extremely successful in describing one or more aspects of the structure and properties of nuclei. In most of these models, the basic constituents of the nuclei are the nucleons, bound together by the strong force. The nucleon-nucleon interaction at short distances is governed by the strong interaction, mediated by the quark-gluon content of the nucleons. Thus, contemporary nuclear physics faces the challenge of describing the effective nucleon-nucleon forces in terms of underlying quark-gluon degrees of freedom. This might be too ambitious in the present, since as we have demonstrated in the previous chapters, solving QCD even for one nucleon is an extremely challenging task, calling for novel approaches and requiring enormous computational resources for completion. Thus one can try and include quark-gluon effects at least on the phenomenological level. One way to accomplish this is using a well-established quark model of the nucleon to describe nuclei and nuclear matter, as such models have been very successful in describing the properties of the nucleons, as we demonstrated in the previous chapter. Our work in developing such an approach, namely the Quark-Meson Coupling (QMC) model, was based on describing the nuclear medium as consisting of nucleons, modeled as systems of relativistic, confined quarks, moving in Lorentz scalar and vector mean fields. The quark model description of the nucleons allows for describing the response of the nucleon to the external field, thus manifesting the density dependence of the derived, effective nucleon-nucleon forces. This derived interaction agrees well with popular Skyrme models and reproduces very reasonably the observables for heavy

nuclei. Further, this model was used in the construction of the equation of state for dense nuclear matter, which allowed calculations of properties of slowly rotating neutron starts, such as the radius and the mass of the star corresponding to a given central density, as well as the prediction of the maximum mass of a neutron star. These calculations, while they describe the observational data very well, have also shown a favorable result for the maximum central density of neutron stars of only 6 times the nuclear saturation density, thus giving some confidence in applying the model for the description of the neutron star core.

In this chapter we will describe the key features of the relativistic formulation of the QMC model and elaborate on the derivation of the corresponding Hamiltonian, following the Ref. [100]. We will also present the details of the non-relativistic expansion of the Hamiltonian and the application of the corresponding density functional in calculation of the atomic nuclei properties.

5.2 QMC Model and Hamiltonian

The QMC model is built upon the assumption that bound nucleons generate static, self-consistent scalar and vector fields, which couple directly to up and down constituent quarks. This approximation is well justified for not very light nuclei and cold uniform nuclear matter, the latter having more simplifications due to the uniformity of the fields. As a model for the baryon structure in QMC the MIT bag model is used, where the quarks are confined inside of a nucleon by an impenetrable bag. The bag model gives a good description of the baryon properties and allows for simple algebraic derivations throughout the QMC formulation. While the picture of the impenetrable bag is an over-simplification of the confining mechanism in the nucleon, which looks more like a Y-shaped objects with the quarks confined by a gluon flux tube (see Refs. [101], [102] and also Fig. (5.1)), it allows for a simple formulation and should not be taken as contradictory to the possibility of pion exchange throughout the neighboring bags. Other than being confined into a color-singlet bound state, quarks in the baryons should be able to respond to the external fields. Employment of a more sophisticated model might improve some details of the model, but it would introduce many complications that are premature at this stage. In describing the nuclei here we consider only protons and neutrons, avoiding the complications of including the strange baryons. The formulation of the model with inclusion of the members of the full $SU(3)$ spin 1/2 baryon octet N, Λ, Σ and Ξ, is described in [103] and goes beyond the scope of the current chapter. A covariant version of QMC in application to the European Muon Collaboration (EMC) effect in finite nuclei was formulated in the Ref. [104], where the confining Nambu–Jona-Lasinio model was used for calculations of the nucleon structure functions and quark distributions. This model allowed one to study the nuclear medium modification of these functions and gave a good description of both polarized and unpolarized EMC effect for a range of nuclei.

The essential assumption of QMC is that the nucleons in nuclei can be represented as relativistically moving bags, each confining three constituent quarks. The

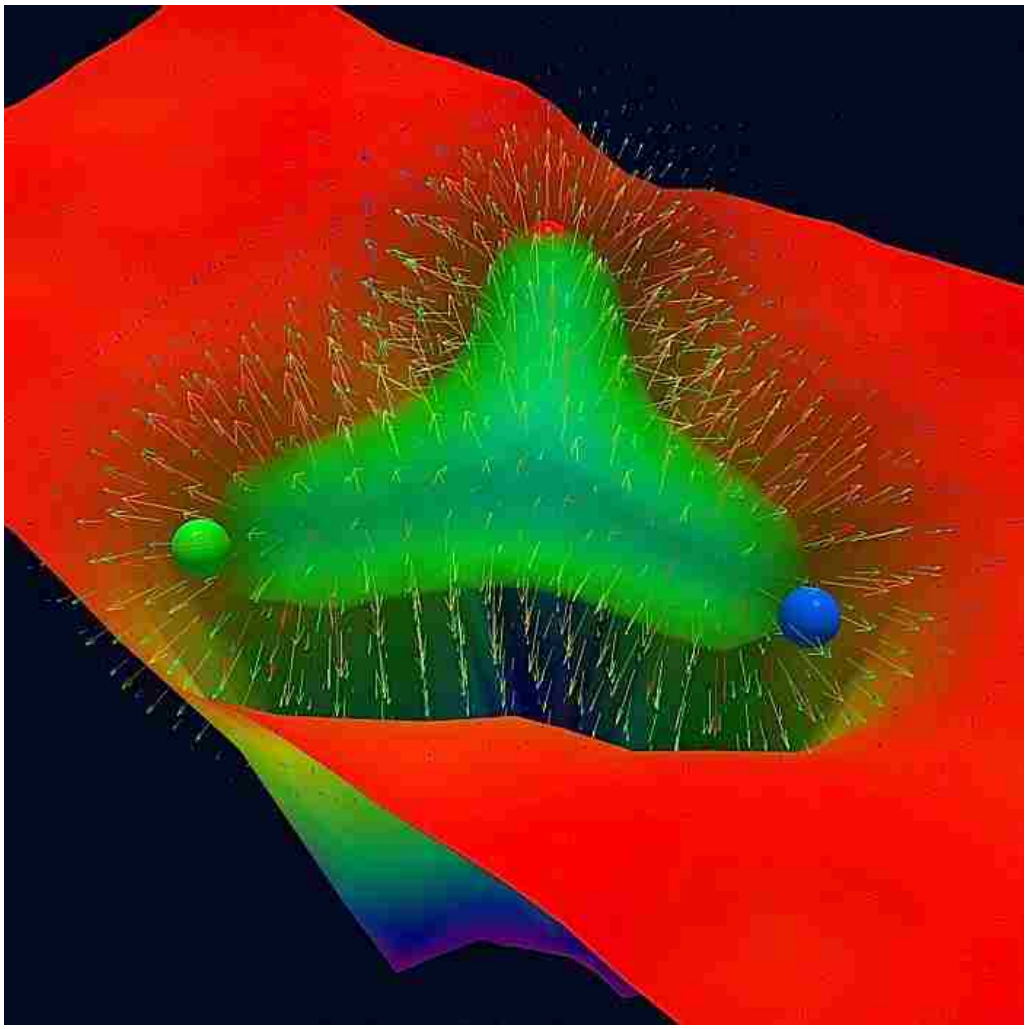

Figure 5.1: The gluon flux tubes in the proton are responsible for creating a confining interaction, as suggested by lattice QCD calculations, giving it a Y-shaped form. The figure is taken form the Ref. [102].

nucleon many body interaction is generated by the self-consistent scalar and vector fields which couple directly to the constituent quarks. In the model we consider only σ, ρ and ω fields to be active, which generate the bulk of the interaction and can absorb the effects generated by the higher lying states by fitting the coupling parameters to the physical observables. The model assumption is that meson fields don't interact with the strange quark, which can be justified by describing the meson fields as correlated multi-pion exchanges.

We assume that at the particle densities considered, the bags don't overlap, so the energy of the $i-$th bag with center of mass momentum P_i can be written as

$$E_i = \sqrt{P_i^2 + M_{eff}(\sigma)^2} + g_\omega \omega + V_{so}, \tag{5.1}$$

where $M_{eff}(\sigma)$ is the effective mass of the bag generated by the interaction with the σ field measured in the center of the bag, g_ω represents the coupling constant with the ω field and V_{so} represents the spin-orbit interaction generated by the variation of the field over the bag. Here we skipped the ρ field, because it enters the equation in exactly the same manner as the ω, except for the isospin dependence.

In order to calculate $M_{eff}(\sigma)$ one needs to solve the bag equations for the relevant value of the σ field. However, we have checked that the quadratic expansion:

$$M_{eff}(\sigma) = M - g_\sigma \sigma + \frac{d}{2} (g_\sigma \sigma)^2 \tag{5.2}$$

is accurate up to values of $g_\sigma \sigma$ as large as 600 MeV, which corresponds to densities far beyond the physical limitations of the model. The parameter d is the scalar polarizability of the nucleon. It depends explicitly on the response of the quark structure to the external scalar field. In the bag model it is well represented as a function of the bag radius, R_B, as

$$d = 0.0044 + 0.211 R_B - 0.0357 R_B^2, \tag{5.3}$$

where both d and R_B are in fm. This does not give exactly the values that were used in Ref. [105], because we have now included the contribution of the spin dependent, "hyperfine" color interaction to the bag energy.

The coupling constant, g_σ, which by definition refers to the nucleon, is related to the σ–quark coupling, g_σ^q, by

$$g_\sigma = 3 g_\sigma^q \int_{Bag} d\vec{r}\, \bar{q} q(\vec{r}), \tag{5.4}$$

where q is the valence quark wavefunction for the free bag. For the vector couplings the relationship is

$$g_\omega = 3 g_\omega^q,\ g_\rho = g_\rho^q. \tag{5.5}$$

The energy of the static meson field has the standard form

$$E_{mesons} = \frac{1}{2}\int d\vec{r}\left[(\nabla\sigma)^2 + m_\sigma^2\sigma^2\right] - \frac{1}{2}\int d\vec{r}\left[(\nabla\omega)^2 + m_\omega^2\omega^2\right], \tag{5.6}$$

with m_σ and m_ω representing the masses of the corresponding mesons.

Thus the total energy of the system is

$$E = \sum_i E_i + E_{mesons}\,. \tag{5.7}$$

We do not quote the expression for the spin orbit interaction here. It was first derived in Ref. [29] and it does not play a crucial role in describing the many body force.

The classical Hamiltonian of the system is constructed using the expression for the total energy of the system, by replacing the variable meson fields with the corresponding solutions of the equations of motion:

$$H(R_i, P_i) = E(R_i, P_i, \sigma \to \sigma_{sol}, \omega \to \omega_{sol}) \tag{5.8}$$

The equation of motion for the meson fields can be obtained by the variational principle:

$$\frac{\delta E}{\delta\sigma} = \frac{\delta E}{\delta\omega} = 0 \tag{5.9}$$

yielding the equations

$$-\nabla^2\sigma + m_\sigma^2\sigma = -\sum_i \delta(\vec{r} - \vec{R}_i)\frac{\partial}{\partial\sigma}\sqrt{P_i^2 + M_{eff}(\sigma)^2}, \tag{5.10}$$

$$-\nabla^2\omega + m_\sigma^2\omega = g_\omega\sum_i \delta(\vec{r} - \vec{R}_i). \tag{5.11}$$

In Eqs. (5.10,5.11) we have neglected the contribution corresponding to the variation of the spin orbit interaction V_{so}. As pointed out in Ref. [105], this results in an error of order V_{so}^2 in the Hamiltonian and it is consistent to neglect it because the spin-orbit interaction in Eq. (5.1) has been derived as a first order perturbation [29]. Since the equation for the ω field is linear, its solution is elementary and poses no new problem with respect to previous work [105]. Its contribution to the energy will be written later and we now concentrate on the field equation for σ.

We assume that we can treat the deviation $\delta\sigma$ of the σ field from its expectation value in the nuclear ground state $\langle\sigma\rangle$ as a small perturbation:

$$\sigma = \langle\sigma\rangle + \delta\sigma, \tag{5.12}$$

where the *C-number* $\langle\sigma\rangle$, also written $\bar{\sigma}$, is defined as[1]

$$\langle\sigma(\vec{r})\rangle = \int d\vec{R}_1 ... d\vec{R}_A \Phi^*(\vec{R}_1 ... \vec{R}_A)\sigma(\vec{r}, \vec{R}_i, \vec{P}_i)\Phi(\vec{R}_1 ... \vec{R}_A). \tag{5.13}$$

Defining

$$K = \sum_i \delta(\vec{r} - \vec{R}_i)\sqrt{P_i^2 + M_{eff}(\sigma)^2} \tag{5.14}$$

we can rewrite the Eq. (5.10) as

$$\left(-\nabla^2 + m_\sigma^2\right)(\bar{\sigma} + \delta\sigma) = -\frac{\partial K}{\partial \sigma} = -\frac{\partial K}{\partial \sigma}(\bar{\sigma}) - \delta\sigma \frac{\partial^2 K}{\partial \sigma^2}(\bar{\sigma}) - \cdots \tag{5.15}$$

By expanding $\frac{\partial K}{\partial \sigma}(\bar{\sigma})$, $\frac{\partial^2 K}{\partial \sigma^2}(\bar{\sigma})$ about their expectation values

$$\begin{aligned} \frac{\partial K}{\partial \sigma}(\bar{\sigma}) &= \left\langle \frac{\partial K}{\partial \sigma}(\bar{\sigma}) \right\rangle + \delta\left[\frac{\partial K}{\partial \sigma}(\bar{\sigma})\right] \\ \frac{\partial^2 K}{\partial \sigma^2}(\bar{\sigma}) &= \left\langle \frac{\partial^2 K}{\partial \sigma^2}(\bar{\sigma}) \right\rangle + \delta\left[\frac{\partial^2 K}{\partial \sigma^2}(\bar{\sigma})\right] \end{aligned} \tag{5.16}$$

and supposing that

$$\delta\sigma,\ \delta\left[\frac{\partial K}{\partial \sigma}(\bar{\sigma})\right],\ \delta\left[\frac{\partial^2 K}{\partial \sigma^2}(\bar{\sigma})\right]$$

are small quantities, we can rewrite the Eq. (5.15) for the terms of the same order:

$$\left(-\nabla^2 + m_\sigma^2\right)\bar{\sigma} = -\left\langle \frac{\partial K}{\partial \sigma}(\bar{\sigma}) \right\rangle \tag{5.17}$$

$$\begin{aligned} \left(-\nabla^2 + m_\sigma^2\right)\delta\sigma &= -\delta\left[\frac{\partial K}{\partial \sigma}(\bar{\sigma})\right] - \delta\sigma\left\langle \frac{\partial^2 K}{\partial \sigma^2}(\bar{\sigma}) \right\rangle \\ &= -\frac{\partial K}{\partial \sigma}(\bar{\sigma}) + \left\langle \frac{\partial K}{\partial \sigma}(\bar{\sigma}) \right\rangle - \delta\sigma\left\langle \frac{\partial^2 K}{\partial \sigma^2}(\bar{\sigma}) \right\rangle \end{aligned} \tag{5.18}$$

As we limit the expansion of the Hamiltonian to order $(\delta\sigma)^2$, it is sufficient to solve the field equation at order $\delta\sigma$, which corresponds to Eqs. (5.17,5.18). Using integration by parts, the Hamiltonian (5.1) may be expanded as

$$\begin{aligned} H = &\int d\vec{r}\, K|_{\bar{\sigma}} + \delta\sigma\frac{\partial K}{\partial \sigma}(\bar{\sigma}) + \frac{1}{2}(\delta\sigma)^2\frac{\partial^2 K}{\partial \sigma^2}(\bar{\sigma}) \\ &+ \frac{1}{2}\bar{\sigma}\left(-\nabla^2 + m_\sigma^2\right)\bar{\sigma} + \delta\sigma\left(-\nabla^2 + m_\sigma^2\right)\bar{\sigma} + \frac{1}{2}\delta\sigma\left(-\nabla^2 + m_\sigma^2\right)\delta\sigma \end{aligned} \tag{5.19}$$

[1]Of course this explicit expression is quite formal as it amounts to having solved the problem.

In the approximation considered, we can substitute the coefficient of the $(\delta\sigma)^2$ term with its expectation value:

$$\frac{\partial^2 K}{\partial\sigma^2}(\bar{\sigma}) \to \left\langle \frac{\partial^2 K}{\partial\sigma^2}(\bar{\sigma}) \right\rangle$$

Using Eqs. (5.17,5.18) we then find:

$$H = \int d\vec{r} \left[K(\bar{\sigma}) - \frac{1}{2}\bar{\sigma} \left\langle \frac{\partial K}{\partial\sigma}(\bar{\sigma}) \right\rangle + \frac{1}{2}\delta\sigma \left(\frac{\partial K}{\partial\sigma}(\bar{\sigma}) - \left\langle \frac{\partial K}{\partial\sigma}(\bar{\sigma}) \right\rangle \right) \right]. \qquad (5.20)$$

Note that the mean field approximation amounts to neglecting $\delta\sigma$ in Eq. (5.20). The Hamiltonian of the Eq. (5.20) can be quantized by writing the quantum form of K and its derivatives. The important simplification is that these are one body operators because they are evaluated at the C-number point $\sigma = \bar{\sigma}$. Thus we can write

$$K(\bar{\sigma}) = \sum_{\alpha\beta} K_{\alpha\beta}(\bar{\sigma}) a^\dagger_\alpha a_\beta,$$

where $a^\dagger_\alpha, a_\alpha$ are the creation and destruction operators for the complete 1-body basis $|\alpha\rangle$. The matrix elements $K_{\alpha\beta}(\bar{\sigma})$ must be chosen so as to reproduce the classical limit, Eq. (5.14). In the momentum space representation, there is a natural choice [2]

$$K(\bar{\sigma}) = \frac{1}{2V} \sum_{\vec{k},\vec{k}'} e^{i(\vec{k}-\vec{k}').\vec{r}} \left(\sqrt{k^2 + M_{eff}[\bar{\sigma}(\vec{r})]^2} + \sqrt{k'^2 + M_{eff}[\bar{\sigma}(\vec{r})]^2} \right) a^\dagger_{\vec{k}} a_{\vec{k}'}, \quad (5.21)$$

where the symmetrization is introduced to ensure hermicity and V is the normalization volume. We also choose

$$\frac{\partial K}{\partial\sigma}(\bar{\sigma}) = \frac{1}{2V} \sum_{\vec{k},\vec{k}'} e^{i(\vec{k}-\vec{k}').\vec{r}} \frac{\partial}{\partial\bar{\sigma}} \left(\sqrt{k^2 + M_{eff}[\bar{\sigma}(\vec{r})]^2} + \sqrt{k'^2 + M_{eff}[\bar{\sigma}(\vec{r})]^2} \right) a^\dagger_{\vec{k}} a_{\vec{k}'} \qquad (5.22)$$

with a similar expression for the second derivative. The ordering ambiguities associated with products of non-commuting operators are fixed by the normal ordering prescription, which amounts to removing that part of the energy which originates from the interaction of one nucleon with its own field.

The Hamiltonian defined in Eq. (5.20) is not a standard many-body problem, since we do not know $\bar{\sigma}$ and $\delta\sigma$ until the ground state nuclear wave function has been specified. Therefore the Hamiltonian must be determined (through $\bar{\sigma}$ and $\delta\sigma$) at each step of the self consistent procedure. This is a significant technical complication. On the other hand, for our purposes it is not necessary to solve this Hamiltonian in the general case. One of the main goals in constructing the model is to obtain the equation of state for very dense nuclear matter, with the goal of applying it to neutron stars [106], but in that case we will only need the uniform

[2] Spin and flavor labels are understood.

matter approximation for which the model is easy to solve. However, we do need to consider finite size effects for ordinary nuclei, a necessary step in order to show that the model is realistic with respect to nuclear phenomenology.

5.2.1 The Non-Relativistic Expansion

In considering the applications of the model in calculations of the properties of finite nuclei, we can make a non-relativistic expansion and build a density functional, $\langle H(\vec{r})\rangle$, using approximations which are standard in low energy nuclear physics, which can then be used in variational calculations. The approximations that we use below involve a non-relativistic expansion and the neglect of those velocity dependent and finite range forces which involve more than 2 bodies, as is the case for conventional effective nuclear forces. This amounts to expanding the terms which involve either the momentum or the gradient of the density in powers of the σ nucleon coupling and stopping at order g_σ^2. To simplify the expressions we omit the spin and flavor indices as long as they are not truly necessary. We first define the number density, $D(\vec{r})$, and kinetic density, $\xi(\vec{r})$, by

$$D(\vec{r}) = \frac{1}{V}\sum_{\vec{k},\vec{k}'} e^{i(\vec{k}-\vec{k}').\vec{r}} a^\dagger_{\vec{k}} a_{\vec{k}'}, \quad \xi(\vec{r}) = \frac{1}{V}\sum_{\vec{k},\vec{k}'} e^{i(\vec{k}-\vec{k}').\vec{r}} \frac{k^2+k'^2}{2} a^\dagger_{\vec{k}} a_{\vec{k}'}. \tag{5.23}$$

Then, following the approximation scheme defined above and using Eq. (5.2) we find the following expression for the operator K and its derivatives

$$\begin{aligned} K|_{\bar\sigma} &= D(\vec{r}) M_{eff}[\bar\sigma(\vec{r})] + \frac{\xi(\vec{r})}{2M}\left(1+\frac{g_\sigma\bar\sigma}{M}\right) \\ \left.\frac{\partial K}{\partial\sigma}\right|_{\bar\sigma} &= D(\vec{r})\frac{\partial M_{eff}}{\partial\bar\sigma} + g_\sigma\frac{\xi(\vec{r})}{2M^2} \\ \left.\frac{\partial^2 K}{\partial\sigma^2}\right|_{\bar\sigma} &= d g_\sigma^2 D(\vec{r}) \end{aligned} \tag{5.24}$$

Substituting the above expressions into Eqs. (5.17,5.18) and using the same approximations, we can solve for $\bar\sigma$ and $\delta\sigma$:

$$g_\sigma\bar\sigma = \frac{G_\sigma\langle D\rangle}{1+dG_\sigma\langle D\rangle} - G_\sigma\frac{\langle\xi\rangle}{2M^2} + G_\sigma\frac{\nabla^2\langle D\rangle}{m_\sigma^2}, \tag{5.25}$$

$$\delta\sigma = \frac{1}{\tilde m_\sigma^2}\left(-\frac{\partial K}{\partial\sigma}(\bar\sigma) + \left\langle\frac{\partial K}{\partial\sigma}(\bar\sigma)\right\rangle\right) + \frac{1}{\tilde m_\sigma^2}\nabla^2\frac{1}{\tilde m_\sigma^2}\left(-\frac{\partial K}{\partial\sigma}(\bar\sigma) + \left\langle\frac{\partial K}{\partial\sigma}(\bar\sigma)\right\rangle\right), \tag{5.26}$$

where we have defined $G_\sigma = g_\sigma^2/m_\sigma^2$ and the (position dependent) effective σ mass

$$\tilde m_\sigma^2 = m_\sigma^2\left(1+G_\sigma d\langle D\rangle\right) \tag{5.27}$$

The model Hamiltonian can be obtained by substituting Eqs. (5.24,5.25,5.26) into Eq. (5.20). In practice we want the corresponding density functional in the

Hartree Fock approximation, so we need to evaluate (note that by definition $\langle \delta\sigma \rangle = 0$)

$$\langle H(\vec{r}) \rangle = \langle K(\bar{\sigma}) \rangle - \frac{1}{2}\bar{\sigma} \left\langle \frac{\partial K}{\partial \sigma}(\bar{\sigma}) \right\rangle + \frac{1}{2} \left\langle \delta\sigma \frac{\partial K}{\partial \sigma}(\bar{\sigma}) \right\rangle, \tag{5.28}$$

where the ground state wave function is a Slater determinant, with Fermi level F, built from the single particle wave functions $\Phi^j(\vec{r}, \sigma, m)$. We now restore the spin flavor dependence but restrict our considerations to nuclei made of protons and neutrons. So the flavor index is just the isospin projection $m = \pm 1/2$. As usual, we define [107]:

$$\rho_m(\vec{r}) = \sum_{i \in F} \sum_{\sigma} \left| \Phi^i(\vec{r}, \sigma, m) \right|^2, \quad \rho(\vec{r}) = \sum_m \rho_m(\vec{r}) \tag{5.29}$$

$$\tau_m(\vec{r}) = \sum_{i \in F} \sum_{\sigma} \left| \vec{\nabla} \Phi^{i*}(\vec{r}, \sigma, m) \right|^2, \quad \tau(\vec{r}) = \sum_m \tau_m(\vec{r}) \tag{5.30}$$

$$\vec{J}_m(\vec{r}) = i \sum_{i \in F} \sum_{\sigma\sigma'} \vec{\sigma}_{\sigma'\sigma} \times \left[\vec{\nabla} \Phi^i(\vec{r}, \sigma, m) \right] \Phi^{i*}(\vec{r}, \sigma', m), \quad \vec{J}(\vec{r}) = \sum_m \vec{J}_m(\vec{r}) \tag{5.31}$$

The density functional then can be expressed using the above notation. While the lengthy details of the calculations are shown in the Appendix C, here we simply write down the results:

$$\begin{aligned} \langle H(\vec{r}) \rangle = \rho M &+ \frac{\tau}{2M} \\ &+ \frac{G_\sigma}{2M^2} \left(\rho\tau + \frac{1}{8} \sum_m \rho_m \nabla^2 \rho_m \right) \\ &- \left(\frac{G_\sigma}{2m_\sigma^2} + \frac{G_\sigma}{4M^2} \right) \left(\rho \nabla^2 \rho - \sum_m \left(\frac{1}{4} \rho_m \nabla^2 \rho_m - \rho_m \tau_m \right) \right) \\ &- \frac{1}{2} \frac{G_\sigma}{1 + dG_\sigma \rho} \left(\rho^2 - \frac{1}{2(1 + dG_\sigma \rho)^2} \sum_m \rho_m^2 \right) \end{aligned} \tag{5.32}$$

For completeness, we give the ω, ρ and spin orbit contributions (labelled IS for isoscalar and IV for isovector):

$$\left\langle : \mathcal{H}_{so}^{IS}(\vec{r}) : \right\rangle = -\frac{1}{4M^2}\left[G_\sigma + \left(2\frac{\mu_{IS}}{\mu_N} - 1\right)G_\omega\right]\sum_{mm'}\left[\left(1 + \frac{1}{2}\delta_{mm'}\right)\rho_{m'}\vec{\nabla}.\vec{J}_{m'}\right], \tag{5.33}$$

$$\left\langle : \mathcal{H}_{so}^{IV}(\vec{r}) : \right\rangle = -\frac{G_\rho}{4M^2}\left[2\frac{\mu_{IV}}{\mu_N} - 1\right]\sum_{mm'}\left[\left(mm' + \frac{1}{2}C_{mm'}\right)\rho_{m'}\vec{\nabla}.\vec{J}_m\right], \tag{5.34}$$

$$\begin{aligned}\left\langle : \mathcal{H}_\omega(\vec{r}) : \right\rangle = \frac{G_\omega}{2}\sum_{mm'}\Bigg[&\left(1 - \frac{1}{2}\delta_{mm'}\right)\rho_m\rho_{m'} \\ &+\frac{1}{m_\omega^2}\left(\rho_m\nabla^2\rho_{m'} - \frac{1}{4}\delta_{mm'}\left(\rho_m\nabla^2\rho_m - 4\rho_m\tau_m\right)\right)\Bigg],\end{aligned} \tag{5.35}$$

$$\begin{aligned}\left\langle : \mathcal{H}_\rho(\vec{r}) : \right\rangle = \frac{G_\rho}{2}\sum_{mm'}\Bigg\{&\left(mm' - \frac{1}{2}C_{mm'}\right)\rho_m\rho_{m'} \\ &+\frac{1}{m_\rho^2}\left(mm' - \frac{1}{4}C_{mm'}\right)\rho_m\nabla^2\rho_{m'} + \frac{1}{m_\rho^2}C_{mm'}\rho_m\tau_{m'}\Bigg\},\end{aligned} \tag{5.36}$$

where: $C_{mm'} = \delta_{mm'}m^2 + (\delta_{m,m'+1} + \delta_{m',m+1})/2$ and $G_\omega = g_\omega^2/m_\omega^2, G_\rho = g_\rho^2/m_\rho^2$. The isoscalar and isovector magnetic moments which appear in the spin orbit interaction have the values

$$\mu_{IS} = \mu_p + \mu_n = 0.88,\ \mu_{IV} = \mu_p - \mu_n = 4.7. \tag{5.37}$$

We note that all terms which involve the square of the spin density, $\vec{J}$, have been neglected. This is common practice and, since it amounts to treating the spin orbit interaction as a first order perturbation, it is consistent with our derivation of the expression for the effective mass, Eq. (5.1).

We have determined the couplings G_σ, G_ω, G_ρ by fixing the saturation density and binding energy of normal nuclear matter to be $\rho_0 = 0.16$ fm^3 and $E_B = -15.85$ MeV, as well as the asymmetry energy of nuclear matter as $a_4 = 30$ MeV. Apart from a small readjustment of the couplings, we found no significant sensitivity to the bag radius. We therefore display our results for only one value, $R_B = 0.8$ fm, which is quite realistic [64]. The ω and ρ masses are set at their experimental values. The last parameter, which is not well fixed by experiment, is the σ mass. We shall use $m_\sigma = 600, 650, 700, 750$ MeV. The corresponding results are given in Table 5.1. We see that the incompressibility, K_N, is a little high with respect to the currently preferred range, but we point out that this calculation has not yet taken into account the single pion exchange interaction. We know [105] that the pion Fock term alone reduces K_N by as much as 10% and it is likely that this is amplified by other correlations.

Table 5.1: The best-fit values of the couplings G_σ, G_ω and G_ρ and the corresponfing value for the nuclear incompressibility for different values of the scalar meson mass, m_σ.

m_σ(MeV)	G_σ(fm^2)	G_ω(fm^2)	G_ρ(fm^2)	K_N(MeV)
600	12.652	9.838	9.67	346
650	12.428	9.308	8.583	346
700	12.254	8.899	7.724	346
750	12.116	8.575	7.048	346

5.2.2 Description of the Finite Nuclei.

Starting from the QMC energy functional one can easily derive the corresponding Hartree-Fock (HF) equations. They have a form similar to the Skyrme-HF equations, apart from the rearrangement term and the one-body spin-orbit interaction, which have a different density and isospin dependence. The HF equations were solved in coordinate space, following the method described in Ref. [107] and the Coulomb interaction was treated in a standard way – i.e., the contribution of its exchange part was calculated in the Slater approximation. The calculations were performed for the doubly magic nuclei ^{16}O, ^{40}Ca, ^{48}Ca and ^{208}Pb. For definiteness, the σ meson mass has been set to $m_\sigma = 700$ MeV, as suggested by the comparison with the SkM* interaction. At this point we recall that the QMC model is essentially classical because both the position and velocity of the bag are assumed known in the energy expression (5.2). The quantization then leaves some arbitrariness in the ordering of the momentum dependent pieces of the interaction. As pointed out in previous work [105], in the non-relativistic approximation the difference between the orderings is equivalent to a change of about 10% in m_σ. In this chapter the ordering is fixed by the relativistic expression chosen for the operator K, Eq. (5.21). The non-relativistic reduction then leads to an ordering which is not the same as in Ref. [105]. This is why the σ meson mass that we use here is somewhat higher. Note that this ordering ambiguity is only of concern in the case of finite nuclei. In uniform matter, which is the relevant approximation for neutron stars, the problem does not exist.

The results for the binding energies and charge radii are shown in Table 5.2. The charge densities are calculated with the proton form factor usually employed in the Skyrme-HF calculations [107]. From Table 5.2 one can see that QMC-HF gives results which are in reasonable agreement with the experimental values. The agreement is not quite as good as that given by the recent Skyrme or RMF models, but one should keep in mind that in these models the experimental values for the binding energies and radii are included in the fitting procedure (which involves many additional parameters), which is not the case for the QMC functional.

In Figs. 5.2, 5.3 we show the proton and neutron densities calculated with the QMC model and with the Sly4 Skyrme force [108]. In the proton case we also show the experimental values [109]. Once again the two models give rather similar results, with the largest differences noticed for the neutron skin of ^{208}Pb. More precisely, for

Table 5.2: Comparison of the QMC Hartree-Fock calculated binding energies and charge radii of several nuclei with the measured experimental values.

	E_B(MeV, exp)	E_B(MeV, QMC)	r_c(fm, exp)	r_c(fm, QMC)
^{16}O	7.976	7.618	2.73	2.702
^{40}Ca	8.551	8.213	3.485	3.415
^{48}Ca	8.666	8.343	3.484	3.468
^{208}Pb	7.867	7.515	5.5	5.42

this nucleus the neutron skin (i.e., the difference between the neutron and proton rms radii) is equal to 0.12 fm for QMC, compared to 0.16 fm for the Skyrme force. With respect to experiment the QMC model tends to overestimate the density in the central region, but the overall agreement is quite good given that the model has no parameter adjusted to fit the properties of finite nuclei.

5.3 Conclusion

We have explored the possibility of including the effects of the nucleon structure in describing the nucleon many body interaction in finite nuclei and nuclear matter. Employment of the MIT bag model to describe the quark content of the nucleon and the quark meson exchange hypothesis for the nucleon-nucleon interaction allowed for a fully relativistic formulation of the problem and a derivation of the Hamiltonian for the system which yields density-dependent many body force of nucleon-nucleon interaction. A nonrelativistic expansion of the Hamiltonian allowed for a good description of the finite nuclei in the Hartree-Fock approximation, as well as a favorable comparison with a well-established phenomenological Skyrme-type interaction. The further application of this formulation to the cold uniform nuclear matter, which includes the full $SU(3)$ strange baryon octet, described in the Ref. [103], allows the derivation of an equation of state for nuclear matter. This equation of state was applied to the calculation of the maximum masses and radii of the neutron stars close to most recent observations, yielding a maximum density of the nuclear matter in the neutron star of only six times the nuclear saturation density, favoring it over more traditional models, which give higher central densities and raise questions of the applicability of the models in the domain of high densities, where the relativistic effects are important and nucleons might start to merge into quark-gluon matter.

While this model does not provide a true "*ab-initio* description" of the nuclear many body interaction in terms of their quark-gluon content, it allows for arguably the most realistic approach to the problem, at least in the foreseeable future. While the development of the effective field theories (EFTs) in describing the nuclear many body interactions, guided by the fundamental symmetries of QCD, have been very successful, (for example, Weinberg's power counting scheme [110], allowed for calculation to date of 2-, 3- and 4-nucleon forces up to next-to-next-to-next-to-leading order [111], [112], [113], [114]), the EFT approach has severe limitations in its

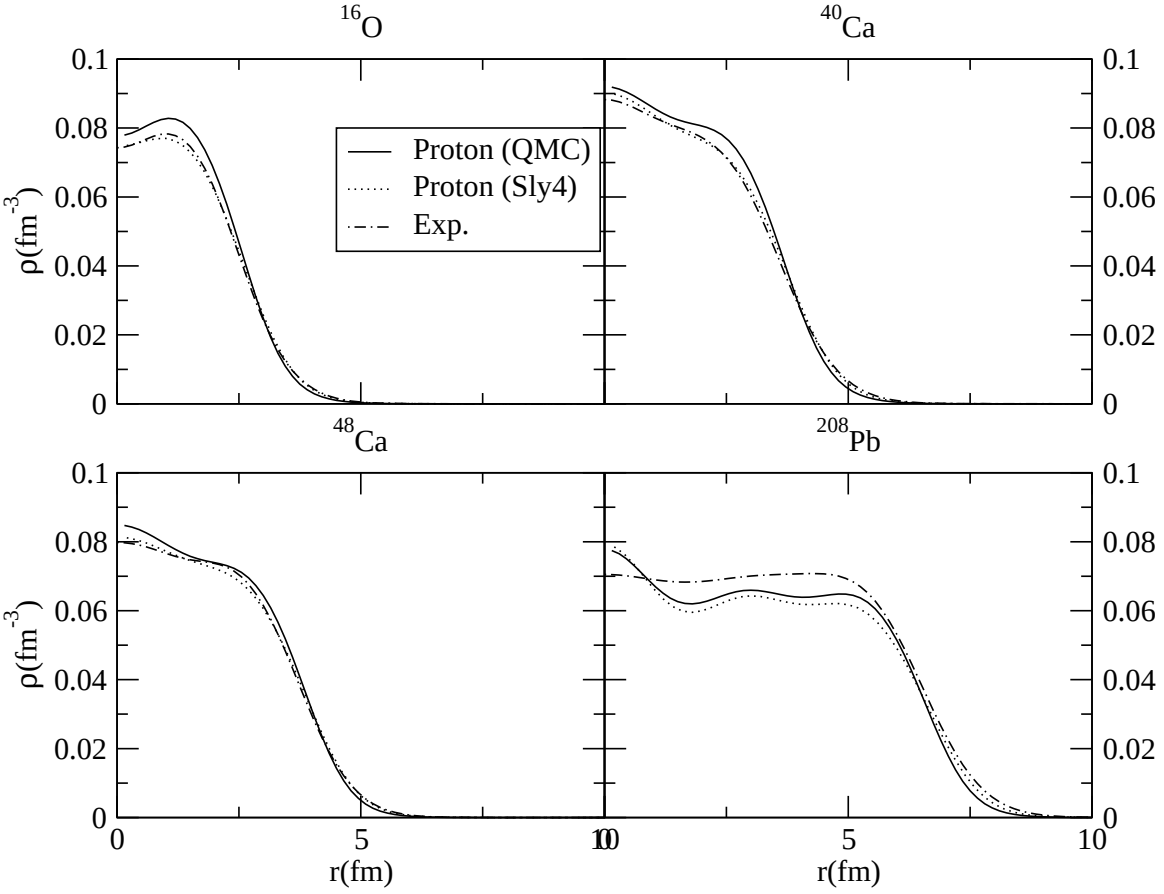

Figure 5.2: Comparison of the QMC calculated proton densities in selected, closed shell nuclei with the experimental measurements. The Skyrme Sly4 results are also shown for comparison.

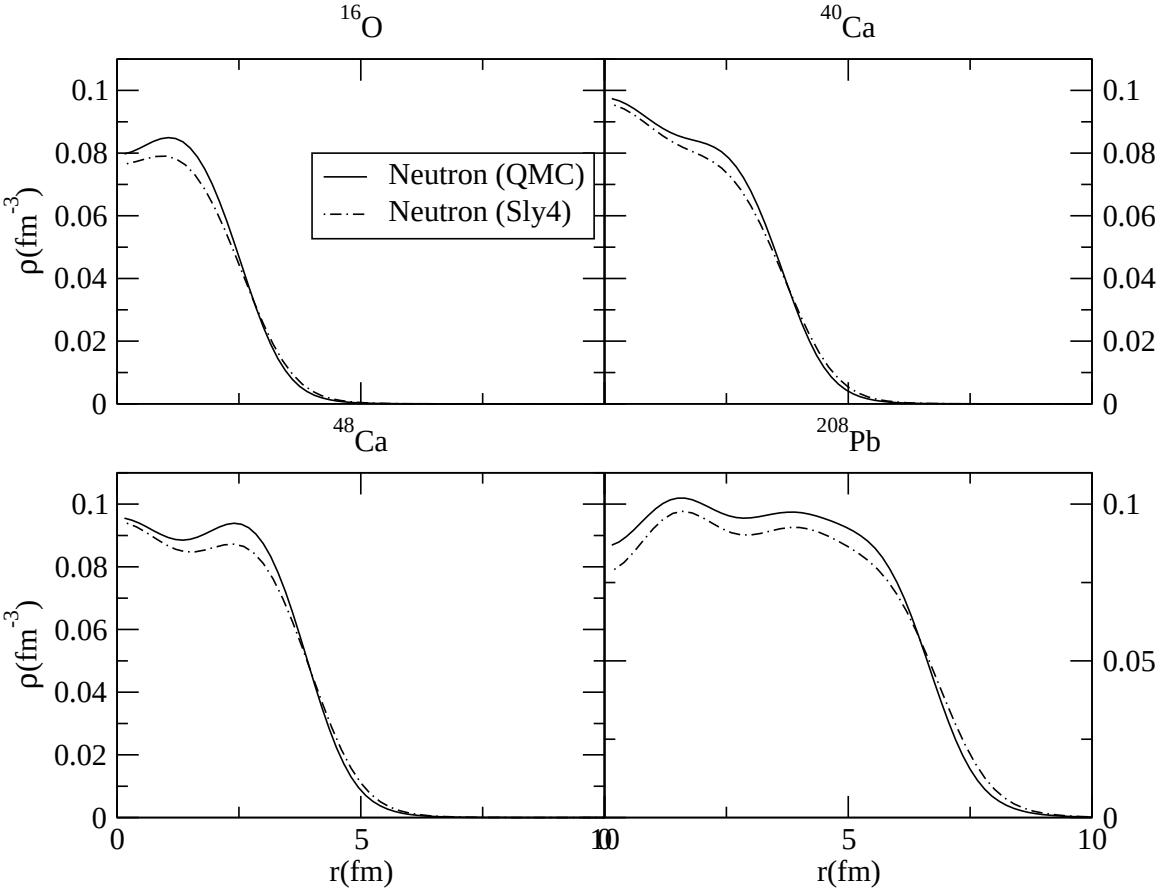

Figure 5.3: Comparison of the QMC calculated neutron densities in selected, closed shell nuclei with the experimental measurements. The Skyrme Sly4 results are also shown for comparison.

range of applicability. EFTs rely on the existence of a small and a large parameter, for example, in the case of nuclear many body interactions, the low energy transfer in comparison with the typical hadronic mass scale, which allows one to apply order-by-order perturbation theory in this small parameter and number of interacting nucleons. It is clear that for high-density nuclear matter, where the energy transfer in the interaction can become large, one needs to sum over *all orders* in perturbation theory, including all possible many-body interactions. Another attractive initiative is to calculate the nucleon-nucleon interaction using lattice QCD, as proposed by the NPLQCD collaboration [115], [116]. While this approach is very attractive, since it amounts to solving the problem directly from QCD in the limit of infinitely large and fine lattices, the current limitations on computational power and several theoretical and technical obstacles will probably delay the calculations for any sizable nuclei into the far future. Thus, phenomenological models like QMC will provide important information on the role of the baryon structure in describing the atomic nuclei and dense nuclear matter.

Chapter 6

Concluding Remarks

In this work we have outlined a path for constructing models to link the properties of the nuclear force to the underlying quark-gluon structure of the nucleons and the theory (QCD) widely believed to govern the interaction of these constituents. While a straight forward approach to solving this problem is far beyond our understanding at present, we tried to build a phenomenological approach and justify these models by comparing some key quantities calculated from these models to those obtained by "first principle" approaches to solving QCD, as well as to experiment.

First, we explored the consequences of improving the model of dressing the quark-gluon vertex function on the calculated masses and binding energies of the ground-state pseudo-scalar and vector mesons in the framework of the Dyson-Schwinger equations. At first, we improved the ladder-dressed approximation by making the dressing model self-consistent and constructing the chiral symmetry preserving Bethe-Salpeter quark-antiquark scattering kernel. The model was then solved for quark propagator functions and the masses of the bound states. This showed that the ladder-rainbow truncation, widely employed in this framework for calculating various physical observables, yields very close results to our model calculations, as compared to previous studies with more limited models for the vertex. This result encouraged further exploration of the quark-gluon vertex dressing, which is a key ingredient in describing the low-energy phenomena in QCD. We further included all possible 2-point gluon lines in the model vertex function, which yielded surprising results. The solutions of the corresponding equations for the quark GAP equation showed large variations from the solutions corresponding the ladder-rainbow truncation, yielding solutions in Wigner-Weyl mode at some orders of calculation, thus strongly indicating the importance of the omitted 3- and 4-point gluon functions in dressing the vertex and in describing the dynamics of QCD at the infrared momentum scale.

Simulated by these calculations, we reviewed 't Hooft's proposed $1/N_c$ counting scheme in QCD and found an insufficient description of the expansion and some "classic" examples being wrongfully treated in the further review articles of this expansion. This review allowed us to formulate a complete set of Feynman rules for this expansion, which, unlike in the previous case is valid beyond the leading order of the $1/N_c$ expansion. These new rules were applied to correctly describe

$1/N_c$ expansion of the quark-gluon vertex dressing diagrams included in our work, as well as the next-to-leading order diagram in a closed quark loop system, widely described in the literature with a wrong sign. This work allowed us not only to further develop a rigorous approach of solving QCD to obtain properties of the bound systems in the low-energy region, but to also gain some insight into dynamical aspects of the theory. In particular, dynamical quark mass generation through the contributions of the self-energy type diagrams as entailed by the GAP equation, yielded a quark mass at low momentum transfer of about 300 MeV, close to the mass of the constituent quarks employed in phenomenological models of baryon structure. In these phenomenological models the effects of the strong dressing of the current quarks of the baryons are approximated by introducing slowly moving quasi-particles, namely the constituent quarks, with masses fixed by fitting the calculated physical observables to the experiment.

Next we turned our attention to alternative methods for describing the baryons in terms of QCD. The Lattice QCD calculated nucleon electromagnetic form factors allow us to describe the structure of the nucleons from the first principle calculations in the limit of large and very fine lattices, as well as high computing capabilities. We have explored the possibility of describing these calculations with well-established models for the nucleon structure, like the Light Front Cloudy Bag Model (LFCBM) and one of the most advanced variations of the Vector Meson Dominance (VMD) models. This allowed us to first test these models against a first principle QCD calculation, to try to test how experimental data-dependent they are and if they will be able to describe the QCD predictions at some other mass scale without dramatic modifications. After we have established that one of the models applied, LFCBM, was able to successfully describe the Lattice QCD calculations with parameters of the model varying very smoothly with the mass scale, we were able to extrapolate the Lattice calculations to the physical mass region, where we found a surprising overlap with the current experimental measurements of the ratio of the electric to magnetic form factors of the proton. We also presented predictions that will be tested by the planned experiments at Jefferson Lab and elsewhere. This allowed us to ensure the viability of these phenomenological models in describing the key features of nucleon structure, while having sufficiently simple structure for real-world applications.

The exploration of hadron structure and the development of different approaches for describing it gave us unique and clear understanding of its importance in considering atomic nuclei and nuclear matter. This gave us a great opportunity to participate in the development of a model for the nuclear interaction, where the quark-gluon structure of the nucleons was explicitly included, even at the level of the phenomenological modeling. The Quark-Meson Coupling (QMC) model, first formulated almost two decades ago, presently allows for a self-consistent, relativistic description of nuclear matter with active quark degrees of freedom. The nuclear many-body interaction is modeled by a self-consistent mean field mediated by exchange of scalar and vector mesons and the nucleon structure is described by the MIT bag model. The new formalism we have developed in the last chapter avoids the strict approximations, where the mean scalar field variations are small and allows

for the derivation of a density-dependent nuclear many-body force that provides a good description of a wide range of nuclei and some well-measured properties of the nuclear matter. The new formulation is also easily adaptable for describing dense nuclear matter, including the induced strangeness at higher densities as an important mechanism for "softening" the equation of the state of the matter. As shown in our work in Ref. [103], this model allows for a very plausible description of nuclear stars, with low central density and a range of maximum mass and radius in a good agreement with observational data.

In conclusion we think that the path of directly linking the nuclear forces to the QCD origin, lies through inclusion of the hadron structure by means of proven and effective models that would allow for reasonable quantitative calculations. Advances in our understanding of hadrons and the structure of the low-energy QCD will result in a deeper derivation and development of these models, while clearer understanding of the features of the QCD like dynamical mass generation will help us to justify and adjust these models. For example, the efforts towards solving the puzzle of confinement in the DSE framework will help us to better understand the behavior of the QCD Green's functions in the infrared region, which will have direct impact on the concept of the constituent quarks, leading towards hadron models that will have an even closer resemblance to QCD solutions than the present models. This in turn will allow us to construct better models for nuclear many body interactions and a better description of the nuclear force.

This approach might seem too model dependent, but this might be one of the very limited options for positive progress at present. Improvements in these models with a better understanding of hadronic structure will help us to formulate a clear and unambiguous theory of the nuclear interactions starting from the quark-gluon degrees of freedom and fundamental symmetries of QCD.

The perspectives for immediate advances following our work are the following. In exploring the models of the quark-gluon vertex function the first step in improving them will be to consider a more realistic, momentum-dependent, gluon 2-point function in dressing the quark-gluon vertex and the corresponding DSEs and BSEs. An order-by order approach in this case will be limited to very low orders of calculation, since the momentum loop integrals are difficult to evaluate beyond two or three loops. An interesting way of including the diagrams at all orders is by writing a model DSE for the vertex for the class of the diagrams considered. This procedure usually involves only a single loop integral, thus making it affordable for calculations. The further developments will necessarily need to explicitly include the 3- and 4- point gluon functions in dressing. While it will be very interesting to employ more realistic gluon propagators in solving the quark GAP equation, the main goal should be to solve the coupled quark-gluon-ghost 2-point function DSEs with model higher n-point functions involved in the equations. This will give us a better understanding of the infrared behavior of the QCD Green's functions and probably resolve the inconsistency of the calculations for some of the meson masses in comparison with experiment. This should establish the DSE approach more firmly as a framework for treating hadronic physics.

Advanced lattice calculations of the nucleon electromagnetic form factors are currently in progress by several LQCD collaborations, where improved lattice actions and state-of-the-art computational facilities help to reduce the systematic errors and remove the quenching approximation while decreasing the statistical errors and reducing the masses closer to the physical scale. These results, when available, will become a more stringent test for models of nuclear structure as high precision data will help to rule out the inconsistent models. Furthermore, the models successfully tested for consistency will be used to extrapolate the LQCD calculations to the physical mass scale and over a wide range of momentum transfer to compare with the experiment at very small statistical and extrapolation errors. While several experiments at Jefferson Lab are set to measure the form factors of both the proton and neutron, it is critical to make accurate theoretical predictions ahead of the completion of those experiments to prove the reliability of both the models and LQCD calculations.

The development of the QMC approach will necessarily involve the employment of a more sophisticated model for the nucleon structure than the MIT bag model. A favorable candidate for us is the LFCBM, which might improve the description of the nuclear observables like the nuclear incompressibility and give a more detailed description of the nuclear spectrum. A more detailed overview of the density limit where the nuclear matter starts to fuse into quark-gluon matter will also be very interesting in determining the physical limit of the QMC model in applications to the description of dense nuclear matter and neutron stars.

Bibliography

[1] Anthony W. Thomas and Wolfram Weise. *The Structure of the Nucleon.* Wiley-VCH, Berlin, Germany, 1st, edition, 2001.

[2] Michael E. Peskin and D. V. Schroeder. *An Introduction to quantum field theory.* Addison-Wesley, Reading, USA, 1995.

[3] Derek B. Leinweber. URL http://www.physics.adelaide.edu.au/theory/staff/leinweber/VisualQCD/Nobel/, 2004.

[4] Reinhard Alkofer. Qcd green functions and their application to hadron physics. *arXiv:hep-ph/0611090*, 2006.

[5] Reinhard Alkofer and Lorenz von Smekal. The infrared behavior of qcd green's functions: Confinement, dynamical symmetry breaking, and hadrons as relativistic bound states. *Phys. Rept.*, 353:281, 2001.

[6] Pieter Maris and Craig D. Roberts. Dyson-schwinger equations: A tool for hadron physics. *Int. J. Mod. Phys.*, E12:297–365, 2003.

[7] Craig D. Roberts and Anthony G. Williams. Dyson-schwinger equations and their application to hadronic physics. *Prog. Part. Nucl. Phys.*, 33:477–575, 1994.

[8] A. Bender, C. D. Roberts, and L. Von Smekal. Goldstone theorem and diquark confinement beyond rainbow- ladder approximation. *Phys. Lett.*, B380:7–12, 1996.

[9] A. Bender, W. Detmold, C. D. Roberts, and A. W. Thomas. Bethe-salpeter equation and a nonperturbative quark gluon vertex. *Phys. Rev.*, C65:065203, 2002.

[10] M. S. Bhagwat, A. Holl, A. Krassnigg, C. D. Roberts, and P. C. Tandy. Aspects and consequences of a dressed-quark-gluon vertex. *Phys. Rev.*, C70:035205, 2004.

[11] Gerard 't Hooft. A planar diagram theory for strong interactions. *Nucl. Phys.*, B72:461, 1974.

[12] Gerard 't Hooft. A two-dimensional model for mesons. *Nucl. Phys.*, B75:461, 1974.

[13] Edward Witten. Baryons in the 1/n expansion. *Nucl. Phys.*, B160:57, 1979.

[14] Aneesh V. Manohar. Large n qcd. *arXiv:hep-ph/9802419*, 1998.

[15] Thomas A. DeGrand. Lattice qcd at the end of 2003. *Int. J. Mod. Phys.*, A19:1337–1394, 2004.

[16] Rajan Gupta. Introduction to lattice qcd. *arXiv:hep-lat/9807028*, 1997.

[17] Olivier Pene. An introduction to lattice qcd. *arXiv:hep-ph/9504271*, 1995.

[18] M. Gockeler et al. Nucleon electromagnetic form factors on the lattice and in chiral effective field theory. *Phys. Rev.*, D71:034508, 2005.

[19] R. C. Walker et al. Measurements of the proton elastic form-factors for 1-gev/c**2 ¡= q**2 ¡= 3-gev/c**2 at slac. *Phys. Rev.*, D49:5671–5689, 1994.

[20] Stanley J. Brodsky and Glennys R. Farrar. Scaling laws for large momentum transfer processes. *Phys. Rev.*, D11:1309, 1975.

[21] M. K. Jones et al. G(e(p))/g(m(p)) ratio by polarization transfer in $e(pol.)p-->ep(pol.)$. *Phys. Rev. Lett.*, 84:1398–1402, 2000.

[22] O. Gayou et al. Measurement of g(e(p))/g(m(p)) in e(pol.) p –¿ e p(pol.) to q**2 = 5.6-gev**2. *Phys. Rev. Lett.*, 88:092301, 2002.

[23] P. G. Blunden, W. Melnitchouk, and J. A. Tjon. Two-photon exchange in elastic electron nucleon scattering. *Phys. Rev.*, C72:034612, 2005.

[24] Anthony W. Thomas, S. Theberge, and Gerald A. Miller. The cloudy bag model of the nucleon. *Phys. Rev.*, D24:216, 1981.

[25] Gerald A. Miller. Light front cloudy bag model: Nucleon electromagnetic form factors. *Phys. Rev.*, C66:032201, 2002.

[26] Gerald A. Miller and Michael R. Frank. Q**2 independence of qf(2)/f(1), poincare invariance and the non-conservation of helicity. *Phys. Rev.*, C65:065205, 2002.

[27] Earle L. Lomon. Effect of recent r(p) and r(n) measurements on extended gari-kruempelmann model fits to nucleon electromagnetic form factors. *Phys. Rev.*, C66:045501, 2002.

[28] P. A. M. Guichon. A possible quark mechanism for the saturation of nuclear matter. *Phys. Lett.*, B200:235, 1988.

[29] Pierre A. M. Guichon, Koichi Saito, Evgenii N. Rodionov, and Anthony W. Thomas. The role of nucleon structure in finite nuclei. *Nucl. Phys.*, A601:349–379, 1996.

[30] Anthony W. Thomas, Pierre A. M. Guichon, Derek B. Leinweber, and Ross D. Young. Towards a connection between nuclear structure and qcd. *Prog. Theor. Phys. Suppl.*, 156:124–136, 2004.

[31] J. Volmer et al. New results for the charged pion electromagnetic form- factor. *Phys. Rev. Lett.*, 86:1713, 2001.

[32] Pieter Maris and Peter C. Tandy. The pi, k+, and k0 electromagnetic form factors. *Phys. Rev.*, C62:055204, 2000.

[33] R. Alkofer, A. Holl, M. Kloker, A. Krassnigg, and C. D. Roberts. On nucleon electromagnetic form factors. *Few Body Syst.*, 37:1–31, 2005.

[34] Dennis Jarecke, Pieter Maris, and Peter C. Tandy. Strong decays of light vector mesons. *Phys. Rev.*, C67:035202, 2003.

[35] Pieter Maris and Craig D. Roberts. pi and k meson bethe-salpeter amplitudes. *Phys. Rev.*, C56:3369–3383, 1997.

[36] Pieter Maris, Craig D. Roberts, and Peter C. Tandy. Pion mass and decay constant. *Phys. Lett.*, B420:267–273, 1998.

[37] Craig D. Roberts and Sebastian M. Schmidt. Dyson-schwinger equations: Density, temperature and continuum strong qcd. *Prog. Part. Nucl. Phys.*, 45S1:1–103, 2000.

[38] H. J. Munczek. Dynamical chiral symmetry breaking, goldstone's theorem and the consistency of the schwinger-dyson and bethe-salpeter equations. *Phys. Rev.*, D52:4736–4740, 1995.

[39] P. Watson, W. Cassing, and P. C. Tandy. Bethe-salpeter meson masses beyond ladder approximation. *Few Body Syst.*, 35:129–153, 2004.

[40] H. J. Munczek and A. M. Nemirovsky. The ground state q anti-q mass spectrum in qcd. *Phys. Rev.*, D28:181, 1983.

[41] Taco Nieuwenhuis and J. A. Tjon. Nonperturbative study of generalized ladder graphs in a phi**2 chi theory. *Phys. Rev. Lett.*, 77:814–817, 1996.

[42] Cetin Savkli, Franz Gross, and John Tjon. The role of interaction vertices in bound state calculations. *Phys. Lett.*, B531:161–166, 2002.

[43] Christian S. Fischer and Reinhard Alkofer. Non-perturbative propagators, running coupling and dynamical quark mass of landau gauge qcd. *Phys. Rev.*, D67:094020, 2003.

[44] James S. Ball and Ting-Wai Chiu. Analytic properties of the vertex function in gauge theories. 1. *Phys. Rev.*, D22:2542, 1980.

[45] D. C. Curtis and M. R. Pennington. Truncating the schwinger-dyson equations: How multiplicative renormalizability and the ward identity restrict the three point vertex in qed. *Phys. Rev.*, D42:4165–4169, 1990.

[46] William J. Marciano and Heinz Pagels. Quantum chromodynamics: A review. *Phys. Rept.*, 36:137, 1978.

[47] Jonivar I. Skullerud, Patrick O. Bowman, Ayse Kızılersü, Derek B. Leinweber, and Anthony G. Williams. Nonperturbative structure of the quark gluon vertex. *JHEP*, 04:047, 2003.

[48] Jon-Ivar Skullerud, Patrick O. Bowman, Ayse Kizilersu, Derek B. Leinweber, and Anthony G. Williams. Quark-gluon vertex in arbitrary kinematics. *Nucl. Phys. Proc. Suppl.*, 141:244–249, 2005.

[49] M. S. Bhagwat and P. C. Tandy. Quark-gluon vertex model and lattice-qcd data. *Phys. Rev.*, D70:094039, 2004.

[50] Pieter Maris and Peter C. Tandy. The quark photon vertex and the pion charge radius. *Phys. Rev.*, C61:045202, 2000.

[51] P. Maris. Dyson-schwinger studies of meson masses and decay constants. *Nucl. Phys.*, A663:621–624, 2000.

[52] P. Maris and P. C. Tandy. The quark photon vertex and meson electromagnetic form factors. *Nucl. Phys.*, A663:401–404, 2000.

[53] A. Krassnigg and P. Maris. Pseudoscalar and vector mesons as q anti-q bound states. *J. Phys. Conf. Ser.*, 9:153–160, 2005.

[54] Andrei I. Davydychev, P. Osland, and L. Saks. Quark gluon vertex in arbitrary gauge and dimension. *Phys. Rev.*, D63:014022, 2001.

[55] John M. Cornwall, R. Jackiw, and E. Tomboulis. Effective action for composite operators. *Phys. Rev.*, D10:2428–2445, 1974.

[56] Wolfram. Mathematica 5.2. URL http://www.wolfram.com, 2005.

[57] R. Mertig, M. Bohm, and A. Denner. Feyn calc: Computer algebraic calculation of feynman amplitudes. *Comput. Phys. Commun.*, 64:345–359, 1991.

[58] Patrick O. Bowman, Urs M. Heller, Derek B. Leinweber, and Anthony G. Williams. Modelling the quark propagator. *Nucl. Phys. Proc. Suppl.*, 119:323–325, 2003.

[59] Pieter Maris and Peter C. Tandy. Bethe-salpeter study of vector meson masses and decay constants. *Phys. Rev.*, C60:055214, 1999.

[60] S. Eidelman et al. Review of particle physics. *Phys. Lett.*, B592:1, 2004.

[61] T. Reichelt et al. Measurement of the neutron electric form factor via recoil polarimetry. *Eur. Phys. J.*, A18:181–183, 2003.

[62] D. I. Glazier et al. Measurement of the electric form factor of the neutron at $q^2 = 0.3 - 0.8(gev/c)^2$. *Eur. Phys. J.*, A24:101–109, 2005.

[63] J. Friedrich and T. Walcher. A coherent interpretation of the form factors of the nucleon in terms of a pion cloud and constituent quarks. *Eur. Phys. J.*, A17:607–623, 2003.

[64] Anthony W. Thomas. Chiral symmetry and the bag model: A new starting point for nuclear physics. *Adv. Nucl. Phys.*, 13:1–137, 1984.

[65] S. Theberge, Anthony W. Thomas, and Gerald A. Miller. The cloudy bag model. 1. the (3,3) resonance. *Phys. Rev.*, D22:2838, 1980.

[66] Serge Theberge, Gerald A. Miller, and Anthony W. Thomas. The cloudy bag model. 4. higher order corrections to the nucleon properties. *Can. J. Phys.*, 60:59, 1982.

[67] G. A. Miller, Anthony W. Thomas, and S. Theberge. Pion - nucleon scattering in the cloudy bag model. *Phys. Lett.*, B91:192, 1980.

[68] G. Peter Lepage and Stanley J. Brodsky. Exclusive processes in perturbative quantum chromodynamics. *Phys. Rev.*, D22:2157, 1980.

[69] V. L. Chernyak and A. R. Zhitnitsky. Asymptotics of hadronic form-factors in the quantum chromodynamics. (in russian). *Sov. J. Nucl. Phys.*, 31:544–552, 1980.

[70] J. Arrington. New measurement of g(e)/g(m) for the proton. *arXiv:nucl-ex/0312017*, 2003.

[71] V. Punjabi et al. Proton elastic form factor ratios to q**2 = 3.5-gev**2 by polarization transfer. *Phys. Rev.*, C71:055202, 2005.

[72] M. R. Frank, B. K. Jennings, and G. A. Miller. The role of color neutrality in nuclear physics– modifications of nucleonic wave functions. *Phys. Rev.*, C54:920–935, 1996.

[73] P. L. Chung and F. Coester. Relativistic constituent quark model of nucleon form- factors. *Phys. Rev.*, D44:229–241, 1991.

[74] Fabio Cardarelli and Silvano Simula. Su(6) breaking effects in the nucleon elastic electromagnetic form factors. *Phys. Rev.*, C62:065201, 2000.

[75] R. F. Wagenbrunn, S. Boffi, W. Klink, W. Plessas, and M. Radici. Covariant nucleon electromagnetic form factors from the goldstone-boson exchange quark model. *Phys. Lett.*, B511:33–39, 2001.

[76] Massimo Di Pierro. From monte carlo integration to lattice quantum chromodynamics: An introduction. *arXiv:hep-lat/0009001*, 2000.

[77] Derek B. Leinweber, Ding Hui Lu, and Anthony W. Thomas. Nucleon magnetic moments beyond the perturbative chiral regime. *Phys. Rev.*, D60:034014, 1999.

[78] Emily J. Hackett-Jones, D. B. Leinweber, and Anthony W. Thomas. Incorporating chiral symmetry in extrapolations of octet baryon magnetic moments. *Phys. Lett.*, B489:143–147, 2000.

[79] Thomas R. Hemmert and Wolfram Weise. Chiral magnetism of the nucleon. *Eur. Phys. J.*, A15:487–504, 2002.

[80] R. D. Young, D. B. Leinweber, and A. W. Thomas. Leading quenching effects in the proton magnetic moment. *Phys. Rev.*, D71:014001, 2005.

[81] J. D. Ashley, D. B. Leinweber, Anthony W. Thomas, and R. D. Young. Nucleon electromagnetic form factors from lattice qcd. *Eur. Phys. J.*, A19:9–14, 2004.

[82] I. C. Cloet, D. B. Leinweber, and Anthony W. Thomas. Simple quark model with chiral phenomenology. *Phys. Rev.*, C65:062201, 2002.

[83] Gerald A. Miller. Light front quantization: A technique for relativistic and realistic nuclear physics. *Prog. Part. Nucl. Phys.*, 45:83–155, 2000.

[84] Stanley J. Brodsky and S. D. Drell. The anomalous magnetic moment and limits on fermion substructure. *Phys. Rev.*, D22:2236, 1980.

[85] Felix Schlumpf. Relativistic constituent quark model for baryons. *arXiv:hep-ph/9211255*, 1992.

[86] Shau-Jin Chang and Tung-Mow Yan. Quantum field theories in the infinite momentum frame. 2. scattering matrices of scalar and dirac fields. *Phys. Rev.*, D7:1147–1161, 1973.

[87] V. R. Zoller. Peripheral structure of nucleon in probing with high q**2 photons. *Z. Phys.*, C53:443–452, 1992.

[88] H. Holtmann, A. Szczurek, and J. Speth. Flavour and spin of the proton and the meson cloud. *Nucl. Phys.*, A596:631–669, 1996.

[89] J. Speth and Anthony W. Thomas. Mesonic contributions to the spin and flavor structure of the nucleon. *Adv. Nucl. Phys.*, 24:83–149, 1997.

[90] M. A. B. Beg and A. Zepeda. Pion radius and isovector nucleon radii in the limit of small pion mass. *Phys. Rev.*, D6:2912–2918, 1972.

[91] D. B. Leinweber, Anthony W. Thomas, K. Tsushima, and S. V. Wright. Chiral behaviour of the rho meson in lattice qcd. *Phys. Rev.*, D64:094502, 2001.

[92] R. Brun and F. Rademakers. Root: An object oriented data analysis framework. *Nucl. Instrum. Meth.*, A389:81–86, 1997.

[93] P. G. Blunden, W. Melnitchouk, and J. A. Tjon. Two-photon exchange and elastic electron proton scattering. *Phys. Rev. Lett.*, 91:142304, 2003.

[94] J. Arrington. How well do we know the electromagnetic form factors of the proton? *Phys. Rev.*, C68:034325, 2003.

[95] S. Dieterich et al. Polarization transfer in the he-4(e(pol.),e' p(pol.)h-3 reaction. *Phys. Lett.*, B500:47–52, 2001.

[96] O. Gayou et al. Measurements of the elastic electromagnetic form factor ratio mu pgep/gmp via polarization transfer. *Phys. Rev.*, C64:038202, 2001.

[97] B. D. Milbrath et al. A comparison of polarization observables in electron scattering from the proton and deuteron. *Phys. Rev. Lett.*, 80:452–455, 1998.

[98] T. Pospischil et al. Measurement of g(e(p))/g(m(p)) via polarization transfer at q**2 = 0.4-gev/c**2. *Eur. Phys. J.*, A12:125–127, 2001.

[99] Gerald A. Miller. Shapes of the proton. *Phys. Rev.*, C68:022201, 2003.

[100] P. A. M. Guichon, H. H. Matevosyan, N. Sandulescu, and A. W. Thomas. Physical origin of density dependent force of the skyrme type within the quark meson coupling model. *Nucl. Phys.*, A772:1–19, 2006.

[101] C. Alexandrou, P. de Forcrand, and Oliver Jahn. The ground state of three quarks. *Nucl. Phys. Proc. Suppl.*, 119:667–669, 2003.

[102] F. Bissey et al. Gluon field distribution in baryons. *Nucl. Phys. Proc. Suppl.*, 141:22–25, 2005.

[103] J. Rikovska-Stone, P. A. M. Guichon, H. H. Matevosyan, and A. W. Thomas. Cold uniform matter and neutron stars in the quark-meson- coupling model. *arXiv:nucl-th/0611030*, 2006.

[104] I. C. Cloet, W. Bentz, and A. W. Thomas. Emc and polarized emc effects in nuclei. *Phys. Lett.*, B642:210–217, 2006.

[105] P. A. M. Guichon and A. W. Thomas. Quark structure and nuclear effective forces. *Phys. Rev. Lett.*, 93:132502, 2004.

[106] S. Lawley, W. Bentz, and A. W. Thomas. Nucleons, nuclear matter and quark matter: A unified njl approach. *J. Phys.*, G32:667–680, 2006.

[107] D. Vautherin and D. M. Brink. Hartree-fock calculations with skyrme's interaction. 1. spherical nuclei. *Phys. Rev.*, C5:626–647, 1972.

[108] E. Chabanat, P. Bonche, P. Haensel, J. Meyer, and R. Schaeffer. A skyrme parametrization from subnuclear to neutron star densities. 2. nuclei far from stablities. *Nucl. Phys.*, A635:231–256, 1998.

[109] C. W. De Jager, H. De Vries, and C. De Vries. Nuclear charge and magnetization density distribution parameters from elastic electron scattering. *Atom. Data Nucl. Data Tabl.*, 36:495–536, 1987.

[110] Steven Weinberg. Nuclear forces from chiral lagrangians. *Phys. Lett.*, B251:288–292, 1990.

[111] E. Epelbaum et al. Three-nucleon forces from chiral effective field theory. *Phys. Rev.*, C66:064001, 2002.

[112] D. R. Entem and R. Machleidt. Accurate charge-dependent nucleon-nucleon potential at fourth order of chiral perturbation theory. *Phys. Rev.*, C68:041001, 2003.

[113] E. Epelbaum, W. Glockle, and Ulf-G. Meissner. The two-nucleon system at next-to-next-to-next-to-leading order. *Nucl. Phys.*, A747:362–424, 2005.

[114] E. Epelbaum. Four-nucleon force in chiral effective field theory. *Phys. Lett.*, B639:456–461, 2006.

[115] S. R. Beane, P. F. Bedaque, A. Parreno, and M. J. Savage. Two nucleons on a lattice. *Phys. Lett.*, B585:106–114, 2004.

[116] S. R. Beane, P. F. Bedaque, K. Orginos, and M. J. Savage. Nucleon nucleon scattering from fully-dynamical lattice qcd. *Phys. Rev. Lett.*, 97:012001, 2006.

Appendix A

Padé Approximant for the Quark Self-Energy Term

The solutions of the GAP equation (2.35) for the quark propagator amplitudes $A(s)$ and $B(s)$ depend on the number n of the included gluon lines in the calculations through the Dirac projections of the quark self-energy term with appropriately dressed quark-gluon vertex function on the RHS of Eqs.(2.36) and (2.37) (the terms under the tr). We re-summed the perturbative solutions of the GAP equation and obtained a solution at $n = \infty$ by employing a Padé approximant in n for these self-energy terms.

In order to construct a Padé approximant for each of these terms we established their dependence on n by introducing a fictitious coefficient, ω, to the bare quark-gluon vertex coupling g in dressing the vertex function and constructing the projections of the self-energy term in Eqs. (2.36) and (2.37). In each case a Padé approximant of the following form

$$f(\lambda) = \frac{a_0 + a_1\lambda + a_2\lambda^2}{1 + b_1\lambda + b_2\lambda^2}, \tag{A.1}$$

where $\lambda = \omega^2$, was used to match the appropriate self-energy projection term by solving for the coefficients a_i and b_i. We considered the self-energy projection terms with the quark-gluon vertex dressed to order $n = 3$ in the number of gluon loops to determine all the parameters in (A.1).

After determining the coefficients a_i and b_i, the parameter ω was set to 1 and the corresponding coupled equations for $A(s)$ and $B(s)$ were solved. For the case $\mathcal{C} = 0.375$, the solutions obtained with the approximant self-energy projection terms are finite and continuous in the space-like region.

Appendix B

The Leading Order Non-Analytic Chiral Behavior of the Nucleon Charge Radius Square from the LFCBM Form Factors

In this appendix we will follow the original work by G. Miller to demonstrate that the leading non-analytic behavior as $m_\pi \to 0$ of the nucleon isovector charge radius square from the LFCBM form factors agrees in the leading order of Q^2 with the relativistic calculations of Ref. [90] :

$$\left\langle r_1^2 \right\rangle^v \to \left(\frac{g^2}{4\pi} \frac{3}{\pi M^2} + \frac{1}{8\pi^2} \frac{1 - g_A^2}{f_\pi^2} \right) \ln\left(\frac{M}{\mu} \right) \tag{B.1}$$

$$\kappa_v \left\langle r_2^2 \right\rangle^v \to \left(\frac{g^2}{4\pi} \frac{1}{2M^2} \right) \frac{M}{\mu} + \left(\frac{g^2}{4\pi} \frac{6}{\pi M^2} \right) \ln\left(\frac{M}{\mu} \right) \tag{B.2}$$

Here $\mu \equiv m_\pi$ is the pion mass, f_π is the pion decay constant and $\kappa_v = \kappa_p - \kappa_n$ is the nucleon isovector anomalous magnetic moment.

The LFCBM form factors are defined in Eqs. (4.13-4.18) with the quark core contribution for the proton shown in Eqs. (4.23, 4.24). The nucleon charge radius is related to the appropriate form factor via full derivative with respect to Q^2. Thus the first step is to take the chiral limit of the LFCBM form factors at low Q^2. We expand the expressions for the form factors and keep only the terms up to Q^2, and then take the chiral limit $m_\pi \to 0$ considering only the singular terms with respect to m_π. The quark-core contribution doesn't contain any non-analytic terms in the limit $\mu \to 0$, so we need to consider only the pion-loop terms.

For a simplification we first examine the integral

$$\int_N \equiv \frac{g^2}{2(2\pi)^3}\int d^2L_\perp \frac{d\alpha}{\alpha}\frac{\alpha^2}{M^2\alpha^2+(\mathbf{L}_\perp+\alpha/2\mathbf{q}_\perp)^2+\mu^2(1-\alpha)} \frac{1}{M^2\alpha^2+(\mathbf{L}_\perp-\alpha/2\mathbf{q}_\perp)^2+\mu^2(1-\alpha)} \quad \text{(B.3)}$$

It is useful to define

$$D_0 \equiv M^2\alpha^2+\mathbf{L}_\perp^2+\mu^2(1-\alpha) \quad \text{(B.4)}$$

Then the integral (B.3) can be expressed as:

$$\begin{aligned}\int_N &= \frac{g_0^2}{2(2\pi)^3}\int d^2L_\perp \frac{d\alpha}{\alpha}\frac{\alpha^2}{D_0^2}\frac{1}{1+(\mathbf{L}_\perp\cdot\mathbf{q}_\perp\alpha/D_0)+(\alpha\mathbf{q}_\perp/2)^2/D_0} \quad \text{(B.5)}\\ &\quad \frac{1}{1-(\mathbf{L}_\perp\cdot\mathbf{q}_\perp\alpha/D_0)+(\alpha\mathbf{q}_\perp/2)^2/D_0}\\ &= \frac{g_0^2}{2(2\pi)^3}\int d^2L_\perp\frac{d\alpha}{\alpha}\alpha^2\frac{1}{D_0^2}[\frac{1}{1-(\mathbf{L}_\perp\cdot\mathbf{q}_\perp\alpha/D_0)^2+2(\alpha\mathbf{q}_\perp/2)^2/D_0}]\\ &= \frac{g_0^2}{2(2\pi)^3}\int d^2L_\perp\frac{d\alpha}{\alpha}\alpha^2\frac{1}{D_0^2}[1+(\mathbf{L}_\perp\cdot\mathbf{q}_\perp\alpha/D_0)^2\ -(\alpha\mathbf{q}_\perp)^2/(2D_0)]\\ &= \frac{g_0^2}{2(2\pi)^3}\int d^2L_\perp\frac{d\alpha}{\alpha}\alpha^2\frac{1}{D_0^2}[1+\alpha^2L_\perp^2Q^2/(2D_0^2)\ -\alpha^2Q^2/(2D_0)]\\ &= \frac{g_0^2}{2(2\pi)^3}\int d^2L_\perp\alpha\frac{d\alpha}{D_0^2}[1+\alpha^2Q^2/(2D_0)(L_\perp^2/D_0-1)]\end{aligned}$$

We note that

$$L_\perp^2 = D_0-M^2\alpha^2-\mu^2(1-\alpha),\ L_\perp^2/D_0-1 = -\frac{(M^2\alpha^2+\mu^2(1-\alpha))}{D_0} \quad \text{(B.6)}$$

then $\int_N$ can be expressed as:

$$\int_N = \frac{g_0^2}{2(2\pi)^3}\int d^2L_\perp\alpha\frac{d\alpha}{D_0^2}[1-\alpha^2Q^2\frac{(M^2\alpha^2+\mu^2(1-\alpha))}{2D_0^2}] \quad \text{(B.7)}$$

The following integrals will be needed in the calculations:

$$I_n \equiv \int d^2L_\perp\frac{1}{D_0^n} \quad \text{(B.8)}$$

The integral for the non-convergent case of $i = 1$ is regularized using a cutoff on $L_\perp$ at some $\Delta \sim M$:

$$
\begin{aligned}
I_1 &= \pi \ln \frac{\Delta^2 + M^2\alpha^2 + \mu^2(1-\alpha)}{M^2\alpha^2 + \mu^2(1-\alpha)} \\
I_2 &= \pi \frac{1}{M^2\alpha^2 + \mu^2(1-\alpha)} \\
I_3 &= \frac{\pi}{2} \frac{\pi}{(M^2\alpha^2 + \mu^2(1-\alpha))^2} \\
I_4 &= \frac{\pi}{3} \frac{1}{(M^2\alpha^2 + \mu^2(1-\alpha))^3}
\end{aligned}
\tag{B.9}
$$

Using the relations (B.7) and (B.9) the F_{1bn} then can be transformed to:

$$
\begin{aligned}
&F_{1bn}(Q^2) = \\
&\quad \frac{g_0^2}{(2\pi)^3}(2M^2)\left(F_\pi(Q^2) \to 1\right) \int_0^1 d\alpha\alpha \int d^2L_\perp R_N(\mathbf{L}^{(+)^2}, \alpha) R_N(\mathbf{L}^{(-)^2}, \alpha) \\
&\qquad \left[\left(\alpha^2\left(M^2 - \frac{Q^2}{4}\right) + L^2\right) - \left(F_{2p}^{(0)}(Q^2) + \frac{F_{2n}^{(0)}(Q^2)}{2}\right)\frac{\alpha^2 Q^2}{2}\right]
\end{aligned}
$$

$$
\begin{aligned}
&= \frac{g_0^2}{(2\pi)^3}(2M^2) \int_0^1 d\alpha\alpha \int \frac{d^2L_\perp}{D_0^2} \\
&\qquad \left[\left\{\left(D_0 - \mu^2(1-\alpha)\right)\left(1 - \alpha^2 Q^2 \frac{M^2\alpha^2 + \mu^2(1-\alpha)}{2D_0^2}\right)\right.\right. \\
&\qquad\qquad \left.\left. -\frac{\alpha^2 Q^2}{4}\right\} - \left(F_{2p}^{(0)}(Q^2) + \frac{F_{2n}^{(0)}(Q^2)}{2}\right)\frac{\alpha^2 Q^2}{2}\right]
\end{aligned}
$$

$$
\begin{aligned}
&= \frac{g_0^2}{(2\pi)^3}(2M^2) \int_0^1 d\alpha\alpha \left[I_1 - \mu^2(1-\alpha) I_2\right. \\
&\qquad - (I_3 - \mu^2(1-\alpha) I_4)\alpha^2 Q^2 \frac{M^2\alpha^2 + \mu^2(1-\alpha)}{2} \\
&\qquad\qquad \left. -\frac{\alpha^2 Q^2}{4} I_2 - \left(F_{2p}^{(0)}(Q^2) + \frac{F_{2n}^{(0)}(Q^2)}{2}\right)\frac{\alpha^2 Q^2}{2} I_2\right]
\end{aligned}
$$

We note that

$$
\begin{aligned}
\lim_{\mu\to 0} \int_0^1 d\alpha\alpha I_1 &= \pi \lim_{\mu\to 0} \int_0^1 d\alpha\alpha \ln \frac{\Delta^2 + M^2\alpha^2 + \mu^2(1-\alpha)}{M^2\alpha^2 + \mu^2(1-\alpha)} \\
&= \pi \int_0^1 d\alpha\alpha \left[\ln\left(\Delta^2 + M^2\alpha^2\right) - \ln\left(M^2\alpha^2\right)\right] = finite
\end{aligned}
\tag{B.10}
$$

$$\lim_{\mu\to 0}\int_0^1 d\alpha\alpha\mu^2 I_2 = \lim_{\mu\to 0}\int_0^1 d\alpha\alpha\mu^2\pi\frac{1}{M^2\alpha^2+\mu^2(1-\alpha)} = finite \tag{B.11}$$

$$\lim_{\mu\to 0}\int_0^1 d\alpha\alpha^2\mu^2 I_2 = finite \tag{B.12}$$

$$\lim_{\mu\to 0}\int_0^1 d\alpha\alpha^3 I_2 = finite \tag{B.13}$$

$$\begin{aligned}\lim_{\mu\to 0}\int_0^1 d\alpha\alpha(I_3-\mu^2(1-\alpha)I_4)\alpha^2Q^2\frac{M^2\alpha^2+\mu^2(1-\alpha)}{2} \\ \to Q^2\lim_{\mu\to 0}\int_0^1 d\alpha\alpha^3(I_2-\mu^2(1-\alpha)I_3) = finite\end{aligned} \tag{B.14}$$

Thus it follows:

$$\lim_{\mu\to 0} F_{1bn}(Q^2) = finite \tag{B.15}$$

The F_{1bn} is finite and it does not contribute to the non-analytic behavior of the charge radius square.

Analogous calculations can be performed for the F_{2bn}

$$\begin{aligned}F_{2bn}(Q^2) = -\frac{g_0^2}{(2\pi)^3}\int_0^1 d\alpha\alpha\int\frac{d^2L_\perp}{D_0^2}\left[\left(1-\alpha^2Q^2\frac{(M^2\alpha^2+\mu^2(1-\alpha))}{2D_0^2}\right)\right. \\ \left((2\alpha^2M^2)+(F_{2p}^{(0)}(Q^2)+\frac{1}{2}F_{2n}^{(0)}(Q^2))\alpha^2M^2(1-Q^2/4M^2)\right) \\ \left.+(F_{2p}^{(0)}(Q^2)+\frac{1}{2}F_{2n}^{(0)}(Q^2))\left((L_x^2-L_y^2)\to finite\right)\right] \\ \to\int_0^1 d\alpha\alpha\left[I_2-\alpha^2Q^2\frac{(M^2\alpha^2+\mu^2(1-\alpha))}{2}I_4\right] \\ \left((2\alpha^2M^2)+(F_{2p}^{(0)}(Q^2)+\frac{1}{2}F_{2n}^{(0)}(Q^2))\alpha^2M^2(1-Q^2/4M^2)\right) \\ \to finite\end{aligned} \tag{B.16}$$

From the above expression shows that F_{2bn} does not contribute to the charge radius square's non-analytic behavior.

Next we treat the expression for F_{1cn}:

$$\begin{aligned}F_{1cn}(Q^2) = -g_0^2F_\pi(Q^2)\int_0^1 d\alpha\alpha\int\frac{d^2K_\perp}{(2\pi)^3}R(\mathbf{K}_\perp^{(+)^2},\alpha)R(\mathbf{K}_\perp^{(-)^2},\alpha) \\ \left[\mathbf{K}_\perp^2+M^2\alpha^2-(1-\alpha)^2\frac{Q^2}{4}\right]\end{aligned}$$

$$\to \frac{-g_0^2}{(2\pi)^3}\int_0^1 d\alpha\alpha \int \frac{d^2K_\perp}{D_0^2}$$
$$\left\{\left[D_0^2-\mu^2(1-\alpha)\right]\left[1-\frac{(1-\alpha)^2Q^2(M^2\alpha^2+\mu^2(1-\alpha))}{2D_0^2}\right]-(1-\alpha)^2\frac{Q^2}{4}\right\}$$

$$= \frac{-g_0^2}{(2\pi)^3}\int_0^1 d\alpha\alpha\left\{I_1-\mu^2(1-\alpha)I_2\text{-}\frac{(1-\alpha)^2Q^2(M^2\alpha^2+\mu^2(1-\alpha))}{2}I_3\right.$$
$$\left.+\frac{\mu^2(1-\alpha)^3Q^2(M^2\alpha^2+\mu^2(1-\alpha))}{2}I_4-\frac{(1-\alpha)^2Q^2}{4}I_2\right\}$$

$$\to \frac{-\pi g_0^2}{(2\pi)^3}\int_0^1 d\alpha\alpha\left\{\ln\frac{\Delta^2+M^2\alpha^2+\mu^2(1-\alpha)}{M^2\alpha^2+\mu^2(1-\alpha)}-\frac{\mu^2(1-\alpha)}{M^2\alpha^2+\mu^2(1-\alpha)}\right.$$
$$-\frac{(1-\alpha)^2Q^2}{4(M^2\alpha^2+\mu^2(1-\alpha))}+\frac{\mu^2(1-\alpha)^3Q^2}{6(M^2\alpha^2+\mu^2(1-\alpha))^2}$$
$$\left.-\frac{(1-\alpha)^2Q^2}{4}\frac{1}{M^2\alpha^2+\mu^2(1-\alpha)}\right\}$$

$$\to \frac{-\pi g_0^2}{(2\pi)^3}\int_0^1 d\alpha\left\{\left(\alpha\ln\frac{\Delta^2+M^2\alpha^2+\mu^2(1-\alpha)}{M^2\alpha^2+\mu^2(1-\alpha)}\longrightarrow 0\right)\right.$$
$$-\left(\frac{\alpha(1-\alpha)\mu^2}{M^2\alpha^2+\mu^2(1-\alpha)}\longrightarrow 0\right)-\frac{\alpha(1-\alpha)^2Q}{2(M^2\alpha^2+\mu^2(1-\alpha))}$$
$$\left.+\left(\frac{\alpha(1-\alpha)^3\mu^2Q^2}{6(M^2\alpha^2+\mu^2(1-\alpha))^2}\longrightarrow finite\right)\right\}$$

$$\to \frac{g_0^2}{8\pi^2}\frac{Q^2}{2M^2}\ln\left(\frac{M}{\mu}\right) \tag{B.17}$$

The non-analytic behavior of the Dirac isovector form factor is then determined by the F_{1cn}, since

$$F_1^v = F_1^p - F_1^n \to -2F_{1cn} \tag{B.18}$$

It is easy to extract the leading non-analytic term for the isovector charge radius 1 square:

$$\left\langle r_1^2\right\rangle^v = -6\frac{d}{dQ^2}F_1^v(Q^2) \to \frac{g_0^2}{8\pi^2}\frac{6}{M^2}\ln\left(\frac{M}{\mu}\right) \tag{B.19}$$

Substituting $g_A/f_\pi = g/M$ we arrive at the final expression:

$$\left\langle r_1^2\right\rangle^v \to \frac{6g_A^2}{8\pi^2 f_\pi^2}\ln\left(\frac{M}{\mu}\right) \tag{B.20}$$

Analogous manipulations with F_{2cn} yield:

$$F_{2cn}(Q^2) = -g_0^2(2M^2)F_\pi(Q^2)\int_0^1 d\alpha\alpha^2(1-\alpha)\int\frac{d^2K_\perp}{(2\pi)^3}R(\mathbf{K}_\perp^{(+)^2},\alpha)R(\mathbf{K}_\perp^{(-)^2},\alpha) \tag{B.21}$$

$$= -g_0^2(2M^2)(F_\pi(Q^2)\to 1)\int_0^1 d\alpha\alpha^2(1-\alpha)$$
$$\int\frac{d^2K_\perp}{(2\pi)^3}\frac{F_{\pi N}(\mathbf{K}_\perp^{(+)^2},\alpha)\to 1}{M^2\alpha^2+\mu^2(1-\alpha)+\mathbf{K}_\perp^{(+)^2}}\frac{F_{\pi N}(\mathbf{K}_\perp^{(-)^2},\alpha)\to 1}{M^2\alpha^2+\mu^2(1-\alpha)+\mathbf{K}_\perp^{(-)^2}}$$

$$= \frac{-2g_0^2M^2}{(2\pi)^3}\int_0^1 d\alpha\alpha^2(1-\alpha)\left\{I_2-(1-\alpha)^2Q^2\frac{M^2\alpha^2+\mu^2(1-\alpha)}{2}I_4\right\}$$
$$= \frac{-2g_0^2M^2\pi}{(2\pi)^3}\int_0^1 d\alpha\alpha^2(1-\alpha)\left\{\frac{1}{M^2\alpha^2+\mu^2(1-\alpha)}\right.$$
$$\left.-\frac{1}{3}\frac{(1-\alpha)^2Q^2}{2}\frac{1}{\left(M^2\alpha^2+\mu^2(1-\alpha)\right)^2}\right\}$$
$$\to 2\frac{\pi g_0^2}{6(2\pi)^3}\frac{Q^2}{M^2}\left\{\frac{\pi M}{4\mu}+\frac{3}{2}\ln\left(\frac{\mu^2}{M^2}\right)\right\}$$

The isovector Pauli form factor is then expressed as:

$$F_2^v = F_2^p - F_2^n \to -2F_{2cn} \tag{B.22}$$

The leading non-analytical term of the isovector charge radius 2 is:

$$\kappa_v\left\langle r_2^2\right\rangle^v = -6\frac{d}{dQ^2}F_2^v(Q^2)\to\frac{4\pi}{(2\pi)^3}\frac{g_0^2}{M^2}\left\{\frac{\pi}{4}\frac{M}{\mu}+\frac{3}{2}\ln\left(\frac{\mu^2}{M^2}\right)\right\} \tag{B.23}$$

Finally by substituting $g_A/f_\pi = g/M$ we obtain:

$$\kappa_v\left\langle r_2^2\right\rangle^v \to \frac{g_A^2}{8\pi f_\pi^2}\frac{M}{\mu}-12\frac{g_A^2}{8\pi f_\pi^2}\ln\left(\frac{M}{\mu}\right) \tag{B.24}$$

The results (B.20) and (B.24) agree with (B.1) and (B.2) of Ref. [90] in the leading order of Q^2, given that $g_A/f_\pi = g/M$ and $g_A \sim 1$.

Appendix C

Derivation of the QMC Density Functional

C.1 General Concepts

Our goal is to express the QMC density functional

$$\langle H(\vec{r})\rangle = \langle K(\bar{\sigma})\rangle - \frac{1}{2}\bar{\sigma}\left\langle \frac{\partial K}{\partial \sigma}(\bar{\sigma})\right\rangle + \frac{1}{2}\left\langle \delta\sigma\frac{\partial K}{\partial \sigma}(\bar{\sigma})\right\rangle, \tag{C.1}$$

in terms of the C number densities defined as

$$\rho_m(\vec{r}) = \sum_{i\in F}\sum_{\sigma}\left|\Phi^i(\vec{r},\sigma,m)\right|^2, \quad \rho(\vec{r}) = \sum_m \rho_m(\vec{r}) \tag{C.2}$$

$$\tau_m(\vec{r}) = \sum_{i\in F}\sum_{\sigma}\left|\vec{\nabla}\Phi^{i*}(\vec{r},\sigma,m)\right|^2, \quad \tau(\vec{r}) = \sum_m \tau_m(\vec{r}) \tag{C.3}$$

$$\vec{J}_m(\vec{r}) = i\sum_{i\in F}\sum_{\sigma\sigma'}\vec{\sigma}_{\sigma'\sigma}\times\left[\vec{\nabla}\Phi^i(\vec{r},\sigma,m)\right]\Phi^{i*}(\vec{r},\sigma',m), \quad \vec{J}(\vec{r}) = \sum_m \vec{J}_m(\vec{r}) \tag{C.4}$$

in the Hartree Fock approximation work frame.

Here we simply rewrite the expressions needed for our derivations from the Chapter 5:

$$K|_{\bar{\sigma}} = D(\vec{r})M_{eff}[\bar{\sigma}(\vec{r})] + \frac{\xi(\vec{r})}{2M}\left(1+\frac{g_\sigma\bar{\sigma}}{M}\right) \tag{C.5}$$

$$\left.\frac{\partial K}{\partial \sigma}\right|_{\bar{\sigma}} = D(\vec{r})\frac{\partial M_{eff}}{\partial\bar{\sigma}} + g_\sigma\frac{\xi(\vec{r})}{2M^2} \tag{C.6}$$

$$\left.\frac{\partial^2 K}{\partial \sigma^2}\right|_{\bar{\sigma}} = dg_\sigma^2 D(\vec{r}) \tag{C.7}$$

$$g_\sigma\bar{\sigma} = \frac{G_\sigma\langle D\rangle}{1+dG_\sigma\langle D\rangle} - G_\sigma\frac{\langle\xi\rangle}{2M^2} + G_\sigma\frac{\nabla^2\langle D\rangle}{m_\sigma^2}, \tag{C.8}$$

$$\delta\sigma = \frac{1}{\tilde{m}_\sigma^2}\left(-\frac{\partial K}{\partial\sigma}(\bar{\sigma}) + \left\langle\frac{\partial K}{\partial\sigma}(\bar{\sigma})\right\rangle\right) + \frac{1}{\tilde{m}_\sigma^2}\nabla^2\frac{1}{\tilde{m}_\sigma^2}\left(-\frac{\partial K}{\partial\sigma}(\bar{\sigma}) + \left\langle\frac{\partial K}{\partial\sigma}(\bar{\sigma})\right\rangle\right), \quad \text{(C.9)}$$

Here we want to also write down the meson Hamiltonian and derive the corresponding density functional

$$H_{\omega,\rho} = \frac{G_\omega}{2}\int d\vec{r}\, D\left(D + \frac{\nabla^2}{m_\omega^2}D\right) + \frac{G_\rho}{2}\int d\vec{r}\,\vec{D}_{IV}\cdot\left(\vec{D}_{IV} + \frac{\nabla^2}{m_\rho^2}\vec{D}_{IV}\right), \quad \text{(C.10)}$$

where

$$G_\omega = \frac{g_\omega^2}{m_\omega^2},\ \ G_\rho = \frac{g_\rho^2}{m_\rho^2} \quad \text{(C.11)}$$

and the isovector operator density is defined as

$$\vec{D}_{IV}(\vec{r}) = \sum_{i,j}\sum_{\sigma}\sum_{mm'}\Phi^{i*}(\vec{r},\sigma,m)\vec{I}^t_{mm'}\Phi^j(\vec{r},\sigma,m')\,a_i^\dagger a_j = \sum_{i,j}\vec{D}_{IV,ij}(\vec{r})\,a_i^\dagger a_j, \quad \text{(C.12)}$$

with m, m' representing isospin projection indices and $\vec{I}^t_{mm'}$ is the isospin matrix, with $t = 1/2$ for the nucleons.

We assume that the variational state has the form

$$|F\rangle = \left(a^\dagger_{i_1 f_1}a^\dagger_{i_2 f_1}...a^\dagger_{i_N f_1}\right)\left(a^\dagger_{i_1 f_2}a^\dagger_{i_2 f_2}...a^\dagger_{i_N f_2}\right)etc...\,|vacuum\rangle \quad \text{(C.13)}$$

that is a product of states with given flavour.

In our model the Hamiltonian density involves the product of one body operators:

$$H = \mathcal{H}(\vec{r}) = \int d\vec{r}\ :AB...Z: \quad \text{(C.14)}$$

with

$$A = \sum_{i,j}A_{ij}a_i^\dagger a_j,\ \ B = ... \quad \text{(C.15)}$$

As shown in the next section, the expectation values

$$\langle F|:AB...Z:|F\rangle \quad \text{(C.16)}$$

are conveniently written in terms of the Fermi traces $\widetilde{Tr}$ defined as

$$\widetilde{Tr}[AB...Z] = \sum_{i,jk...m\in F}A_{ij}B_{jk}...Z_{mi}. \quad \text{(C.17)}$$

In particular, for a two body operator one has

$$\langle F|:AB:|F\rangle = \widetilde{Tr}[A]\widetilde{Tr}[B] - \widetilde{Tr}[AB] \quad \text{(C.18)}$$

We note, that the Hartree approximation would correspond to

$$\langle F|:AB...Z:|F\rangle|_{Hartree} \to \widetilde{Tr}[A]\widetilde{Tr}[B]...\widetilde{Tr}[Z] \quad \text{(C.19)}$$

Thus our task boils down to expressing the expectation values of the products of one body operators in terms of the corresponding Fermi traces and evaluating the Fermi traces of various combinations of the operators.

A quick examination of the relations for the density functional Eq. (C.1) and Eqs. (C.2-C.8) shows that we need to evaluate the following quantities:

$$\langle D^n \rangle\,,\ \langle D^n \xi \rangle\,,\ \left\langle D^n \vec{\nabla} D \right\rangle,\ \left\langle D^n \left(\vec{\nabla} D\right)^2 \right\rangle\ \langle D^n \nabla^2 D \rangle\,,\ \left\langle (\vec{D}_{IV})^2 \right\rangle, \qquad \text{(C.20)}$$
$$\left\langle \vec{D}_{IV} \cdot \nabla^2 \vec{D}_{IV} \right\rangle, \quad n \leq 2,$$

where the common position argument $\vec{r}$ is dropped for simplicity.

In the next section we will discuss the relations of the expectation values of the one body operators and the Fermi traces. In section C.4 we will derive expressions for various traces that will be used in the expression for the density functional.

C.2 Many Body Operators and the Fermi Traces

Let A be a one body operator

$$A = \sum_{i,j} A_{ij} a_i^\dagger a_j, \qquad \text{(C.21)}$$

and consider

$$\left\langle A^N \right\rangle \equiv \langle F| : A^N : |F\rangle \qquad \text{(C.22)}$$

where

$$|F\rangle = a_{i_1}^\dagger a_{i_2}^\dagger .... |0\rangle$$

and : : stands for the normal ordering with respect to $|0\rangle$. Then the following recurrence relation holds:

$$\left\langle A^N \right\rangle = \left\langle A^{N-1} \right\rangle \widetilde{Tr}[A] + \sum_{k=1}^{N-1} (-1)^k (N-1)(N-2)...(N-k) \left\langle A^{N-k-1} \right\rangle \widetilde{Tr}[A^{k+1}] \qquad \text{(C.23)}$$

where $\langle A^0 \rangle = 1$ and the Fermi trace symbol $\widetilde{Tr}$ is defined by:

$$\widetilde{Tr}[A] = \sum_{i \in F} A_{ii}, \qquad \text{(C.24)}$$

$$\widetilde{Tr}[A^2] = \sum_{i \in F} \sum_{j \in F} A_{ij} A_{ji} \qquad \text{(C.25)}$$

The proof is obvious using Wick's theorem, simply noting, that

$$\langle F| : a_i^\dagger a_j : |F\rangle = \delta_{i,j} \Theta(i \in F), \qquad \text{(C.26)}$$

$$\langle F| : a_i a_j^\dagger : |F\rangle = -\delta_{i,j} \Theta(i \in F) \qquad \text{(C.27)}$$

and using relation (C.21).

Now let $\{A_1, A_2, ...A_N\}$ be a product of one body operators which need not be all different. Then

$$\langle F| : A_1 A_2 ... A_N : |F\rangle = \frac{1}{N!} \frac{\partial^N}{\partial x_1 \partial x_2 ... \partial x_N} \left[\langle F| : \left(\sum_{i=1,N} x_i A_i \right)^N : |F\rangle \right]_{x_1 = x_2 = ... = x_N = 0} \tag{C.28}$$

and we can use Eq. (C.23) for further simplifications.

For convenience we present here the formulas for the expectation values of 2, 3 and 4 one-body operator products, which could be easily obtained using Eqs. (C.23, C.28):

$$\langle : AB : \rangle = \widetilde{Tr}[A]\widetilde{Tr}[B] - \widetilde{Tr}[AB] \tag{C.29}$$

$$\begin{aligned} \langle : A_1 A_2 A_3 : \rangle = \widetilde{Tr}\left[A_1\right]\widetilde{Tr}\left[A_2\right]\widetilde{Tr}\left[A_3\right] - \widetilde{Tr}\left[A_1\right]\widetilde{Tr}\left[A_2 A_3\right] \\ -\widetilde{Tr}\left[A_2\right]\widetilde{Tr}\left[A_1 A_3\right] - \widetilde{Tr}\left[A_3\right]\widetilde{Tr}\left[A_1 A_2\right] \\ +\widetilde{Tr}\left[A_1 A_2 A_3\right] + \widetilde{Tr}\left[A_3 A_2 A_1\right] \end{aligned} \tag{C.30}$$

$$\begin{aligned} \langle : A_1 A_2 A_3 A_4 : \rangle = \widetilde{Tr}\left[A_1\right]\widetilde{Tr}\left[A_2\right]\widetilde{Tr}\left[A_3\right]\widetilde{Tr}\left[A_4\right] \\ - \sum_{i<j;k<l=1}^{4} \widetilde{Tr}\left[A_i\right]\widetilde{Tr}\left[A_j\right]\widetilde{Tr}\left[A_k A_l\right] + \sum_{i<j,k;k<l=1}^{4} \widetilde{Tr}\left[A_i A_j\right]\widetilde{Tr}\left[A_k A_l\right] \\ + \sum_{i;j<k,l=1}^{4} \widetilde{Tr}\left[A_i\right]\widetilde{Tr}\left[A_j A_k A_l\right] - \sum_{i<j,k,l=1}^{4} \widetilde{Tr}\left[A_i A_j A_k A_l\right] \end{aligned} \tag{C.31}$$

C.3 Some Properties of the Densities

First, the condition of no flavour mixing in the HF state implies:

$$\sum_{i \in F} \Phi^i(\vec{r}, \sigma, f)\Phi^{i*}(\vec{r}', \sigma', f') = \delta(f, f') \sum_{i \in F} \Phi^i(\vec{r}, \sigma, f)\Phi^{i*}(\vec{r}', \sigma', f), \tag{C.32}$$

where f describes the flavor, which in our case is the isospin projection index m. In the rest of this section the flavour index is implied.

If the HF state satisfies the time reversal condition then one has:

$$\vec{J}^* = \vec{J} \tag{C.33}$$

$$\sum_{i\in F}\Phi^i(\vec{r},\sigma,f)\Phi^{i*}(\vec{r},\sigma',f)=\frac{1}{2}\delta_{\sigma\sigma'}\rho_f(\vec{r}) \tag{C.34}$$

$$\sum_{i\in F}\sum_{\sigma}\Phi^i(\vec{r},\sigma,f)\vec{\nabla}\Phi^{i*}(\vec{r},\sigma,f)=\sum_{i\in F}\sum_{\sigma}\vec{\nabla}\Phi^i(\vec{r},\sigma,f)\Phi^{i*}(\vec{r},\sigma,f)=\frac{1}{2}\vec{\nabla}\rho_f \tag{C.35}$$

Equation (C.34) is easy to prove, since the sum can be decomposed as

$$\sum_{i\in F}\Phi^i(r,\sigma)\Phi^{i*}(r,\sigma')=a\delta_{\sigma\sigma'}+\vec{b}\cdot\vec{\sigma}_{\sigma\sigma'}, \tag{C.36}$$

where

$$a=\frac{1}{2}\sum_{\sigma}\sum_{i\in F}\Phi^i(r,\sigma)\Phi^{i*}(r,\sigma)=\frac{\rho}{2} \tag{C.37}$$

and, using time reversal, that is

$$\sum_{i\in F}\Phi^i(r,\sigma)\Phi^{i*}(r,\sigma')=\sum_{i\in F}\Phi^{i*}(r,-\sigma)\Phi^i(r,-\sigma')(-1)^{1+\sigma+\sigma'} \tag{C.38}$$

and using $(-1)^{1-\sigma-\sigma'}\vec{\sigma}_{-\sigma'-\sigma}=-\vec{\sigma}_{\sigma\sigma'}$, we have

$$\begin{aligned}2\vec{b}&=\sum_{\sigma,\sigma'}\sum_{i\in F}\Phi^i(r,\sigma)\Phi^{i*}(r,\sigma')\vec{\sigma}_{\sigma\sigma'}=\sum_{\sigma,\sigma'}\sum_{i\in F}\Phi^{i*}(r,-\sigma)\Phi^i(r,-\sigma')(-1)^{1+\sigma+\sigma'}\vec{\sigma}_{\sigma\sigma'}\\&=\sum_{\sigma\sigma'}\sum_{i\in F}\Phi^i(r,\sigma)\Phi^{i*}(r,\sigma')(-1)^{1-\sigma-\sigma'}\vec{\sigma}_{-\sigma'-\sigma}=-2\vec{b}\end{aligned} \tag{C.39}$$

Thus, $\vec{b}=0$ and we arrive at Eq. (C.34). The proof of relations (C.33, C.35) go along the same lines.

If, moreover, one assumes that the HF state is a closed j shell (i.e. it is axially symmetric), then

$$\sum_{i\in F}\Phi^i(\vec{r},\sigma,f)\vec{\nabla}\Phi^{i*}(\vec{r},\sigma',f)=\frac{1}{4}\left[\vec{\nabla}\rho_f\delta_{\sigma\sigma'}+i\vec{J}_f\times\vec{\sigma}_{\sigma\sigma'}\right] \tag{C.40}$$

$$\sum_{i\in F}\vec{\nabla}\Phi^i(\vec{r},\sigma,f)\Phi^{i*}(\vec{r},\sigma',f)=\frac{1}{4}\left[\vec{\nabla}\rho_f\delta_{\sigma\sigma'}+i\vec{\sigma}_{\sigma\sigma'}\times\vec{J}_f\right] \tag{C.41}$$

The above relations can be proven by expressing the sum as

$$\sum_{i\in F}\Phi^i(\vec{r},\sigma)\nabla^\alpha\Phi^{i*}(\vec{r},\sigma')=a^\alpha\delta_{\sigma\sigma'}+b^{\alpha\beta}\sigma^\beta_{\sigma\sigma'}, \tag{C.42}$$

where, using (C.35), the first term is

$$\vec{a} = \frac{1}{2}\sum_{i\in F}\sum_{\sigma}\Phi^{i}(\vec{r},\sigma)\vec{\nabla}\Phi^{i*}(\vec{r},\sigma) = \frac{\vec{\nabla}\rho}{4} \tag{C.43}$$

and

$$b^{\alpha\beta} = \frac{1}{2}\sum_{i\in F}\sum_{\sigma,\sigma'}\Phi^{i}(\vec{r},\sigma)\nabla^{\alpha}\Phi^{i*}(\vec{r},\sigma')\sigma^{\beta}_{\sigma'\sigma} \tag{C.44}$$

Using the identity

$$\nabla^{\alpha}\sigma^{\beta} = \frac{\nabla^{\alpha}\sigma^{\beta} + \nabla^{\beta}\sigma^{\alpha}}{2} + \frac{1}{2}\varepsilon^{\alpha\beta\gamma}\left[\vec{\nabla}\times\vec{\sigma}\right]^{\gamma} \tag{C.45}$$

and that the symmetric part of the tensor does not contribute if the HF state has axial symmetry, we have

$$b^{\alpha\beta} = \frac{\varepsilon^{\alpha\beta\gamma}}{4}\sum_{i\in F}\sum_{\sigma,\sigma'}\Phi^{i}(\vec{r},\sigma)\left[\vec{\nabla}\times\vec{\sigma}_{\sigma'\sigma}\right]^{\gamma}\Phi^{i*}(\vec{r},\sigma') = -i\frac{\varepsilon^{\alpha\beta\gamma}J^{\gamma}}{4}, \tag{C.46}$$

which leads to relations (C.40, C.41).

C.4 Fermi Traces of Density Operators

The evaluation of the quantities listed in (C.20) requires the following quantities, as we can obviously see from the relations (C.29-C.31):

$$\widetilde{Tr}[D^{n}(f)],\ \widetilde{Tr}[D^{n}\xi],\ \widetilde{Tr}[D^{n}\nabla^{2}D],\ \widetilde{Tr}\left[D^{n}\left(\vec{\nabla}D\right)^{2}\right],\ \widetilde{Tr}\left[\vec{D}_{IV}\right],\ \widetilde{Tr}\left[(\vec{D}_{IV})^{2}\right],$$
$$\widetilde{Tr}\left[\vec{D}_{IV}\cdot\nabla^{2}\vec{D}_{IV}\right] \tag{C.47}$$

They always involve a single flavor since, due to the non flavour mixing, one can use

$$\widetilde{Tr}[D[(f_1)D(f_2)D(f_3)....] = \delta_{f_1f_2}\delta_{f_2f_3}...Tr[D^{n}(f_1)]$$

and the same for the other cases. To simplify the notations, the fixed flavor, f, as well as the position argument, $\vec{r}$, in $D(\vec{r},f)$ are omitted in this section. The sums over $i,j,...$ are understood to be over occupied levels.

C.4.1 $\widetilde{Tr}[D^{n+1}]$

By definition,

$$\widetilde{Tr}[D^{n+1}] = \tag{C.48}$$
$$\sum_{i_1,i_2,...i_{n+1}} \sum_{\sigma^1,\sigma^2,...\sigma^{n+1}} \Phi^{i_1*}(\sigma^1)\Phi^{i_2}(\sigma^1)\Phi^{i_2*}(\sigma^2)\Phi^{i_3}(\sigma^2)...\Phi^{i_{n+1}*}(\sigma^{n+1})\Phi^{i_1}(\sigma^{n+1}),$$

We note that here we have n factors of the form

$$\sum_i \Phi^i(\sigma)\Phi^{i*}(\sigma') = \delta_{\sigma\sigma'}\frac{\rho}{2}, \tag{C.49}$$

according to Eq.(C.34).

Therefore

$$\widetilde{Tr}[D^{n+1}] = \left(\frac{\rho}{2}\right)^n \sum_{i_1} \sum_{\sigma^1=1}^{2} \Phi^{i_1*}(\sigma^1)\Phi^{i_1}(\sigma^1) = 2\left(\frac{\rho}{2}\right)^{n+1}. \tag{C.50}$$

C.4.2 $\widetilde{Tr}[D^n\xi]$

For $n = 0$ we simply have

$$\widetilde{Tr}[\xi] = \sum_i \sum_\sigma \vec{\nabla}\Phi^{i*}(\sigma)\cdot\vec{\nabla}\Phi^i(\sigma) = \tau. \tag{C.51}$$

For $n > 0$

$$\widetilde{Tr}[D^n\xi] = \tag{C.52}$$
$$\sum_{i_1,...i_{n+1}} \sum_{\sigma^1,...\sigma^{n+1}} \Phi^{i_1*}(\sigma^1)\Phi^{i_2}(\sigma^1)\Phi^{i_2*}(\sigma^2)...\Phi^{i_{n+1}}(\sigma^n)\vec{\nabla}\Phi^{i_{n+1}*}(\sigma^{n+1})\cdot\vec{\nabla}\Phi^{i_1}(\sigma^{n+1}) \tag{C.53}$$

Again there are $n-1$ factors of the form $\delta_{\sigma\sigma'}\rho/2$, which gives

$$\widetilde{Tr}[D^n\xi] = \left(\frac{\rho}{2}\right)^{n-1} \sum_{i_1,i_{n+1}} \sum_{\sigma^1,\sigma^{n+1}} \Phi^{i_1*}(\sigma^1)\Phi^{i_{n+1}}(\sigma^1)\vec{\nabla}\Phi^{i_{n+1}*}(\sigma^{n+1})\cdot\vec{\nabla}\Phi^{i_1}(\sigma^{n+1}) \tag{C.54}$$

$$= \left(\frac{\rho}{2}\right)^{n-1} \sum_{\sigma^1,\sigma^{n+1}} \frac{1}{16}\left[\delta_{\sigma^1\sigma^{n+1}}\vec{\nabla}\rho + i\vec{J}\times\vec{\sigma}_{\sigma^1\sigma^{n+1}}\right]\cdot\left[\delta_{\sigma^{n+1}\sigma^1}\vec{\nabla}\rho + i\vec{\sigma}_{\sigma^{n+1}\sigma^1}\times\vec{J}\right]$$

$$= \left(\frac{\rho}{2}\right)^{n-1}\left[\frac{1}{8}\left(\vec{\nabla}\rho\right)^2 + \frac{1}{4}\vec{J}^2\right],$$

where we used Eqs. (C.40, C.41).

In summary:

$$\widetilde{Tr}[D^n\xi] = \delta_{n,0}\tau + (1-\delta_{n,0})\frac{1}{8}\left(\frac{\rho}{2}\right)^{n-1}\left[\left(\vec{\nabla}\rho\right)^2 + 2\vec{J}^2\right] \tag{C.55}$$

C.4.3 $\widetilde{Tr}[D^n\nabla^2 D]$

For $n = 0$ we simply have

$$\widetilde{Tr}[\nabla^2 D] = \nabla^2\widetilde{Tr}[D] = \nabla^2\rho. \tag{C.56}$$

For $n > 0$, we have

$$\widetilde{Tr}[D^n\nabla^2 D] = \tag{C.57}$$
$$\sum_{i_1,\dots i_{n+1}}\sum_{\sigma^1,\dots\sigma^{n+1}} \Phi^{i_1*}(\sigma^1)\Phi^{i_2}(\sigma^1)\Phi^{i_2*}(\sigma^2)\dots\Phi^{i_{n+1}}(\sigma^n)\nabla^2\left[\Phi^{i_{n+1}*}(\sigma^{n+1})\Phi^{i_1}(\sigma^{n+1})\right]$$
$$= \left(\frac{\rho}{2}\right)^{n-1}\sum_{i_1,i_{n+1}}\sum_{\sigma^1,\sigma^{n+1}} \Phi^{i_1*}(\sigma^1)\Phi^{i_{n+1}}(\sigma^1)\nabla^2\left[\Phi^{i_{n+1}*}(\sigma^{n+1})\Phi^{i_1}(\sigma^{n+1})\right]$$

This can be written as

$$\widetilde{Tr}[D^n\nabla^2 D] = \tag{C.58}$$
$$\left(\frac{\rho}{2}\right)^{n-1}\vec{\nabla}\cdot\left[\sum_{i_1,i_{n+1}}\sum_{\sigma^1,\sigma^{n+1}} \Phi^{i_1*}(\sigma^1)\Phi^{i_{n+1}}(\sigma^1)\vec{\nabla}\left[\Phi^{i_{n+1}*}(\sigma^{n+1})\Phi^{i_1}(\sigma^{n+1})\right]\right]$$
$$-\left(\frac{\rho}{2}\right)^{n-1}\sum_{i_1,i_{n+1}}\sum_{\sigma^1,\sigma^{n+1}} \vec{\nabla}\left[\Phi^{i_1*}(\sigma^1)\Phi^{i_{n+1}}(\sigma^1)\right]\cdot\vec{\nabla}\left[\Phi^{i_{n+1}*}(\sigma^{n+1})\Phi^{i_1}(\sigma^{n+1})\right]$$

We can apply the rule of the derivatives and use the already familiar expressions (C.33-C.41) to derive

$$\sum_{i_1,i_{n+1}}\sum_{\sigma^1,\sigma^{n+1}} \Phi^{i_1*}(\sigma^1)\Phi^{i_{n+1}}(\sigma^1)\vec{\nabla}\left[\Phi^{i_{n+1}*}(\sigma^{n+1})\Phi^{i_1}(\sigma^{n+1})\right] \tag{C.59}$$
$$= \sum_{i_1,i_{n+1}}\sum_{\sigma^1,\sigma^{n+1}} \Phi^{i_1}(\sigma^{n+1})\Phi^{i_1*}(\sigma^1)\Phi^{i_{n+1}}(\sigma^1)\vec{\nabla}\left[\Phi^{i_{n+1}*}(\sigma^{n+1})\right]$$
$$+ \sum_{i_1,i_{n+1}}\sum_{\sigma^1,\sigma^{n+1}} \Phi^{i_{n+1}}(\sigma^1)\Phi^{i_{n+1}*}(\sigma^{n+1})\vec{\nabla}\left[\Phi^{i_1}(\sigma^{n+1})\right]\Phi^{i_1*}(\sigma^1)$$
$$= \frac{1}{2}\rho\vec{\nabla}\rho$$

and

$$\sum_{i_1,i_{n+1}}\sum_{\sigma^1,\sigma^{n+1}}\vec{\nabla}\left[\Phi^{i_1*}(\sigma^1)\Phi^{i_{n+1}}(\sigma^1)\right]\cdot\vec{\nabla}\left[\Phi^{i_{n+1}*}(\sigma^{n+1})\Phi^{i_1}(\sigma^{n+1})\right] \tag{C.60}$$

$$\begin{aligned}
&= \sum_{i_1,i_{n+1}}\sum_{\sigma^1,\sigma^{n+1}}\Phi^{i_1}(\sigma^1)\Phi^{i_1*}(\sigma^{n+1})\vec{\nabla}\left[\Phi^{i_n}(\sigma^1)\right]\cdot\vec{\nabla}\Phi^{i_n*}(\sigma^{n+1})\\
&+ \sum_{i_1,i_{n+1}}\sum_{\sigma^1,\sigma^{n+1}}\Phi^{i_n}(\sigma^1)\Phi^{i_n*}(\sigma^{n+1})\vec{\nabla}\left[\Phi^{i_1}(\sigma^1)\right]\cdot\vec{\nabla}\Phi^{i_1*}(\sigma^{n+1})\\
&+ \sum_{i_1,i_{n+1}}\sum_{\sigma^1,\sigma^{n+1}}\Phi^{i_n}(\sigma^1)\vec{\nabla}\left[\Phi^{i_n*}(\sigma^{n+1})\right]\Phi^{i_1}(\sigma^{n+1})\cdot\vec{\nabla}\left[\Phi^{i_1*}(\sigma^1)\right]\\
&+ \sum_{i_1,i_{n+1}}\sum_{\sigma^1,\sigma^{n+1}}\vec{\nabla}\left[\Phi^{i_n}(\sigma^1)\right]\Phi^{i_n*}(\sigma^{n+1})\cdot\vec{\nabla}\left[\Phi^{i_1}(\sigma^{n+1})\right]\Phi^{i_1*}(\sigma^1)\\
&= \rho\tau+\frac{1}{16}\sum_{\sigma^1,\sigma^{n+1}}\left[\delta_{\sigma^1\sigma^{n+1}}\vec{\nabla}\rho+i\vec{J}\times\vec{\sigma}_{\sigma^1\sigma^{n+1}}\right]\cdot\left[\delta_{\sigma^{n+1}\sigma^1}\vec{\nabla}\rho+i\vec{J}\times\vec{\sigma}_{\sigma^{n+1}\sigma^1}\right]\\
&+\frac{1}{16}\sum_{\sigma^1,\sigma^{n+1}}\left[\delta_{\sigma^1\sigma^{n+1}}\vec{\nabla}\rho+i\vec{\sigma}_{\sigma^1\sigma^{n+1}}\times\vec{J}\right]\cdot\left[\delta_{\sigma^{n+1}\sigma^1}\vec{\nabla}\rho+i\vec{\sigma}_{\sigma^{n+1}\sigma^1}\times\vec{J}\right]\\
&= \rho\tau+\frac{1}{4}\left[\left(\vec{\nabla}\rho\right)^2-2\vec{J}^2\right]
\end{aligned}$$

Thus, for $n>0$ we have:

$$\begin{aligned}
\widetilde{Tr}[D^n\nabla^2 D] &= \left(\frac{\rho}{2}\right)^{n-1}\vec{\nabla}\cdot\left[\frac{\rho}{2}\vec{\nabla}\rho\right]-\left(\frac{\rho}{2}\right)^{n-1}\left(\rho\tau+\frac{1}{4}\left[\left(\vec{\nabla}\rho\right)^2-2\vec{J}^2\right]\right) \qquad \text{(C.61)}\\
&= \left(\frac{\rho}{2}\right)^{n}\nabla^2\rho+\frac{1}{4}\left(\frac{\rho}{2}\right)^{n-1}\left[\left(\vec{\nabla}\rho\right)^2+2\vec{J}^2-4\rho\tau\right]
\end{aligned}$$

$$\widetilde{Tr}[D^n\nabla^2 D] = \left(\frac{\rho}{2}\right)^{n}\nabla^2\rho+(1-\delta_{n,0})\frac{1}{4}\left(\frac{\rho}{2}\right)^{n-1}\left[\left(\vec{\nabla}\rho\right)^2+2\vec{J}^2-4\rho\tau\right] \tag{C.62}$$

where $n\geq 1$.

C.4.4 $\widetilde{Tr}[D^n\vec{\nabla}D]$

For $n=0$ we simply have

$$\widetilde{Tr}[\vec{\nabla}D] = \vec{\nabla}\widetilde{Tr}[D] = \frac{\vec{\nabla}\rho}{2} \tag{C.63}$$

For $n > 0$ we can write

$$\widetilde{Tr}[D^n\vec{\nabla}D] = \left(\frac{\rho}{2}\right)^{n-1}\sum_{i,j}\sum_{\sigma,\sigma'}\Phi^{i*}(\sigma)\Phi^{j}(\sigma)\vec{\nabla}\left[\Phi^{j*}(\sigma')\Phi^{i}(\sigma')\right] \tag{C.64}$$
$$= \left(\frac{\rho}{2}\right)^{n-1}\frac{\rho}{2}2\sum_{\sigma}\Phi^{j}(\sigma)\vec{\nabla}\Phi^{j*}(\sigma') = \left(\frac{\rho}{2}\right)^{n}\vec{\nabla}\rho$$

where we skipped the intermediate step.

C.4.5 $\widetilde{Tr}\left[D^n(\vec{\nabla}D)^2\right]$

For $n = 0$ we recall the expression from the section C.4.3:

$$\widetilde{Tr}\left[(\vec{\nabla}D)^2\right] = \sum_{i,j}\sum_{\sigma,\sigma'}\vec{\nabla}\left[\Phi^{i*}(\sigma)\Phi^{j}(\sigma)\right]\cdot\vec{\nabla}\left[\Phi^{j*}(\sigma')\Phi^{i}(\sigma')\right] = \rho\tau + \frac{1}{4}\left[\left(\vec{\nabla}\rho\right)^2 - 2\vec{J}^2\right] \tag{C.65}$$

For $n > 0$ we can write

$$\widetilde{Tr}\left[D^n(f)(\vec{\nabla}D)^2\right] = \tag{C.66}$$
$$\sum_{i_1,\dots i_{n+2}}\sum_{\sigma^1,\dots\sigma^{n+2}}\Phi^{i_1*}(\sigma)\Phi^{i_2}(\sigma)\Phi^{i_2*}(\sigma')\dots\Phi^{i_{n+1}}(\sigma^n)\vec{\nabla}\left[\Phi^{i_{n+1}*}(\sigma^{n+1})\Phi^{i_{n+2}}(\sigma^{n+1})\right]$$
$$\cdot\vec{\nabla}\left[\Phi^{i_{n+2}*}(\sigma^{n+2})\Phi^{i_1}(\sigma^{n+2})\right]$$
$$= \left(\frac{\rho}{2}\right)^{n-1}\sum_{i_1,i_{n+1},i_{n+2}}\sum_{\sigma^1,\sigma^{n+1},\sigma^{n+2}}\Phi^{i_1*}(\sigma)\Phi^{i_{n+1}}(\sigma)\vec{\nabla}\left[\Phi^{i_{n+1}*}(\sigma^{n+1})\Phi^{i_{n+2}}(\sigma^{n+1})\right]$$
$$\cdot\vec{\nabla}\left[\Phi^{i_{n+2}*}(\sigma^{n+2})\Phi^{i_1}(\sigma^{n+2})\right]$$
$$= \left(\frac{\rho}{2}\right)^{n}\left[\frac{\rho\tau}{2}\right]$$
$$+\frac{1}{16}\left(\frac{\rho}{2}\right)^{n}\left(\sum_{\sigma^1,\sigma^{n+1}}(\delta_{\sigma^1\sigma^{n+1}}\vec{\nabla}\rho + i\vec{J}\times\vec{\sigma}_{\sigma^1\sigma^{n+1}})\cdot(\delta_{\sigma^{n+1}\sigma^1}\vec{\nabla}\rho + i\vec{J}\times\vec{\sigma}_{\sigma^{n+1}\sigma^1})\right.$$
$$+\sum_{\sigma^1,\sigma^{n+2}}(\delta_{\sigma^1\sigma^{n+2}}\vec{\nabla}\rho + i\vec{J}\times\vec{\sigma}_{\sigma^1\sigma^{n+2}})\cdot(\delta_{\sigma^{n+2}\sigma^1}\vec{\nabla}\rho + i\vec{J}\times\vec{\sigma}_{\sigma^{n+2}\sigma^1})$$
$$\left.+\sum_{\sigma^{n+1},\sigma^{n+2}}(\delta_{\sigma^{n+1}\sigma^{n+2}}\vec{\nabla}\rho + i\vec{J}\times\vec{\sigma}_{\sigma^{n+1}\sigma^{n+2}})\cdot(\delta_{\sigma^{n+2}\sigma^{n+1}}\vec{\nabla}\rho + i\vec{J}\times\vec{\sigma}_{\sigma^{n+2}\sigma^{n+1}})\right)$$
$$= \left(\frac{\rho}{2}\right)^{n}\left[\frac{\rho\tau}{2} + \frac{3}{8}\left(\vec{\nabla}\rho\right)^2 - \frac{1}{4}\vec{J}^2\right] = \frac{1}{8}\left(\frac{\rho}{2}\right)^{n}\left[4\rho\tau + 3\left(\vec{\nabla}\rho\right)^2 - 2\vec{J}^2\right].$$

Thus, the general formula is

$$\widetilde{Tr}\left[D^n(\vec{\nabla}D)^2\right] = \frac{\delta_{n0}}{4}\left[4\rho\tau + \left(\vec{\nabla}\rho\right)^2 - 2\vec{J}^2\right] + \frac{1-\delta_{n0}}{8}\left(\frac{\rho}{2}\right)^n\left[4\rho\tau + 3\left(\vec{\nabla}\rho\right)^2 - 2\vec{J}^2\right] \tag{C.67}$$

C.4.6 $\widetilde{Tr}[D\nabla_\alpha[D]\,D\nabla_\alpha D]$

We can write the above expression as

$$\widetilde{Tr}[D\vec{\nabla}[D]\,D\cdot\vec{\nabla}D] = \tag{C.68}$$

$$= \sum_{i_1,...i_4}\sum_{\sigma^1,...\sigma^4}\Phi^{i_1*}(\sigma^1)\Phi^{i_2}(\sigma^1)\vec{\nabla}\left[\Phi^{i_2*}(\sigma^2)\Phi^{i_3}(\sigma^2)\right]\Phi^{i_3*}(\sigma^3)\Phi^{i_4}(\sigma^3)$$

$$\cdot\vec{\nabla}\left[\Phi^{i_4*}(\sigma^4)\Phi^{i_1}(\sigma^4)\right]$$

$$= \left(\frac{\rho}{2}\right)^2\sum_{i,j}\sum_{\sigma,\sigma'}\Big(\Phi^i(\sigma)\vec{\nabla}\left[\Phi^{i*}(\sigma')\right]\Phi^j(\sigma')\cdot\vec{\nabla}\left[\Phi^{j*}(\sigma)\right] + \Phi^i(\sigma)\vec{\nabla}\left[\Phi^{i*}(\sigma')\right]$$

$$\cdot\vec{\nabla}\left[\Phi^j(\sigma')\right]\Phi^{j*}(\sigma)$$

$$+\vec{\nabla}\left[\Phi^i(\sigma)\right]\Phi^{i*}(\sigma')\Phi^j(\sigma')\cdot\vec{\nabla}\left[\Phi^{j*}(\sigma)\right] + \vec{\nabla}\left[\Phi^i(\sigma)\right]\Phi^{i*}(\sigma')\cdot\vec{\nabla}\left[\Phi^j(\sigma')\right]\Phi^{j*}(\sigma)\Big)$$

$$= \frac{1}{8}\rho^2\left(\vec{\nabla}\rho\right)^2,$$

where in the first step we relabeled the remaining indices from $i_1, ...i_4$ into i, j and $\sigma^1, ...\sigma^4$ into σ, σ' after opening the derivatives and summing up the $\Phi^{i*}(\sigma)\Phi^i(\sigma')$ type terms.

C.4.7 $\widetilde{Tr}[\vec{D}_{IV}]$

To evaluate $\widetilde{Tr}[\vec{D}_{IV}]$ we must write the flavour labels explicitly. Using

$$\sum_i \Phi^i(\sigma,m)\Phi^{i*}(\sigma',m') = \frac{\rho_m}{2}\delta_{\sigma\sigma'}\delta_{mm'} \tag{C.69}$$

we get:

$$\widetilde{Tr}[\vec{D}_{IV}] = \sum_i\sum_\sigma\sum_{mm'}\Phi^{i*}(\sigma,m)\vec{I}^t_{mm'}\Phi^i(\sigma,m') = \sum_m \rho_m\vec{I}^t_{mm} \tag{C.70}$$

$$= \vec{e}(3)\sum_m m\rho_m = \vec{e}(3)\frac{1}{2}\left(\rho_p - \rho_n\right),$$

where $\vec{e}(3)$ is the the regular Cartesian unit vector pointing in the third direction.

C.4.8 $\widetilde{Tr}[\vec{D}_{IV} \cdot \vec{D}_{IV}]$

For $\widetilde{Tr}[\vec{D}_{IV} \cdot \vec{D}_{IV}]$ we have

$$\widetilde{Tr}[\vec{D}_{IV} \cdot \vec{D}_{IV}] = \sum_{i,j} \sum_{\sigma\sigma'} \sum_{mm'} \Phi^{i*}(\sigma, m) \vec{I}^t_{mm'} \Phi^j(\sigma, m') \cdot \Phi^{j*}(\sigma', m') \vec{I}^t_{m'm} \Phi^i(\sigma', m)$$
$$= \frac{1}{2} \sum_{mm'} \rho_m \rho_{m'} \vec{I}^t_{mm'} \cdot \vec{I}^t_{m'm} = \frac{1}{2} \sum_m \left(m^2 \rho_m^2 + \frac{1}{2} \rho_m \rho_{(m\pm1)} \right) \quad \text{(C.71)}$$

C.4.9 $\widetilde{Tr}[\nabla^2 \vec{D}_{IV}]$

For $\widetilde{Tr}[\nabla^2 \vec{D}_{IV}]$ we have

$$\widetilde{Tr}[\nabla^2 \vec{D}_{IV}] = \vec{e}(3) \nabla^2 \sum_m m \rho_m \quad \text{(C.72)}$$

C.4.10 $\widetilde{Tr}[\vec{D}_{IV} \cdot \nabla^2 \vec{D}_{IV}]$

For $\widetilde{Tr}[\vec{D}_{IV} \cdot \nabla^2 \vec{D}_{IV}]$ by the definition we have:

$$\widetilde{Tr}[\vec{D}_{IV} \cdot \nabla^2 \vec{D}_{IV}] = \quad \text{(C.73)}$$
$$= \sum_{m,m'} \vec{I}^t_{mm'} . \vec{I}^t_{m'm} \sum_{i,j} \sum_{\sigma\sigma'} \Phi^{i*}(\sigma, m) \Phi^j(\sigma, m') \nabla^2 \left[\Phi^{j*}(\sigma', m') \Phi^i(\sigma', m) \right]$$

We can express the sums on the RHS as:

$$\sum_{i,j} \sum_{\sigma\sigma'} \Phi^{i*}(\sigma, m) \Phi^j(\sigma, m') \nabla^2 \left[\Phi^{j*}(\sigma', m') \Phi^i(\sigma', m) \right] =$$
$$= \vec{\nabla} \cdot \left[\sum_{ik} \sum_{\sigma\sigma'} \Phi^{i*}(\sigma, m) \Phi^k(\sigma, m') \vec{\nabla} \left[\Phi^{k*}(\sigma', m') \Phi^i(\sigma', m) \right] \right]$$
$$- \sum_{ik} \sum_{\sigma\sigma'} \vec{\nabla} \left[\Phi^{i*}(\sigma, m) \Phi^k(\sigma, m') \right] \cdot \vec{\nabla} \left[\Phi^{k*}(\sigma', m') \Phi^i(\sigma', m) \right] \quad \text{(C.74)}$$

We first evaluate the factor under the nabla:

$$\sum_{ik} \sum_{\sigma\sigma'} \Phi^{i*}(\sigma, m) \Phi^k(\sigma, m') \vec{\nabla} \left[\Phi^{k*}(\sigma', m') \Phi^i(\sigma', m) \right] =$$
$$= \sum_{ik} \sum_{\sigma\sigma'} \Phi^k(\sigma, m') \Phi^{k*}(\sigma', m') \vec{\nabla} \left[\Phi^i(\sigma', m) \right] \Phi^{i*}(\sigma, m)$$
$$+ \sum_{ik} \sum_{\sigma\sigma'} \Phi^i(\sigma', m) \Phi^{i*}(\sigma, m) \Phi^k(\sigma, m') \vec{\nabla} \left[\Phi^{k*}(\sigma', m') \right] = \frac{1}{4} \rho_{m'} \vec{\nabla} \rho_m + \frac{1}{4} \rho_m \vec{\nabla} \rho_{m'} \quad \text{(C.75)}$$

The second term is

$$\sum_{ik}\sum_{\sigma\sigma'}\vec{\nabla}\left[\Phi^{i*}(\sigma,m)\Phi^{k}(\sigma,m')\right]\cdot\vec{\nabla}\left[\Phi^{k*}(\sigma',m')\Phi^{i}(\sigma',m)\right]=$$
$$=\sum_{ik}\sum_{\sigma\sigma'}\Phi^{i}(\sigma,m)\Phi^{i*}(\sigma',m)\vec{\nabla}\left[\Phi^{k}(\sigma,m')\right]\cdot\vec{\nabla}\Phi^{k*}(\sigma',m')$$
$$+\sum_{ik}\sum_{\sigma\sigma'}\Phi^{k}(\sigma,m')\Phi^{k*}(\sigma',m')\vec{\nabla}\left[\Phi^{i}(\sigma,m)\right]\cdot\vec{\nabla}\Phi^{i*}(\sigma',m)$$
$$+\sum_{ik}\sum_{\sigma\sigma'}\Phi^{k}(\sigma,m')\vec{\nabla}\left[\Phi^{k*}(\sigma',m')\right]\Phi^{i}(\sigma',m)\cdot\vec{\nabla}\left[\Phi^{i*}(\sigma,m)\right]$$
$$+\sum_{ik}\sum_{\sigma\sigma'}\vec{\nabla}\left[\Phi^{k}(\sigma,m')\right]\Phi^{k*}(\sigma',m')\cdot\vec{\nabla}\left[\Phi^{i}(\sigma',m)\right]\Phi^{i*}(\sigma,m)$$
$$=\frac{1}{2}\rho_m\tau_{m'}+\frac{1}{2}\rho_{m'}\tau_m+\frac{1}{16}\sum_{\sigma\sigma'}\left[\delta_{\sigma\sigma'}\vec{\nabla}\rho_{m'}+i\vec{J}_{m'}\times\vec{\sigma}_{\sigma\sigma'}\right]\cdot\left[\delta_{\sigma'\sigma}\vec{\nabla}\rho_m+i\vec{J}_m\times\vec{\sigma}_{\sigma'\sigma}\right]$$
$$+\frac{1}{16}\sum_{\sigma\sigma'}\left[\delta_{\sigma\sigma'}\vec{\nabla}\rho_{m'}+i\vec{\sigma}_{\sigma\sigma'}\times\vec{J}_{m'}\right]\cdot\left[\delta_{\sigma'\sigma}\vec{\nabla}\rho_m+i\vec{\sigma}_{\sigma'\sigma}\times\vec{J}_m\right]$$
$$=\frac{1}{2}(\rho_m\tau_{m'}+\rho_{m'}\tau_m)+\frac{1}{4}\left[\vec{\nabla}\rho_m\cdot\vec{\nabla}\rho_{m'}-2\vec{J}_m\cdot\vec{J}_{m'}\right],\qquad\text{(C.76)}$$

so we get

$$\sum_{i,j}\sum_{\sigma\sigma'}\Phi^{i*}(\sigma,m)\Phi^{j}(\sigma,m')\nabla^2\left[\Phi^{j*}(\sigma',m')\Phi^{i}(\sigma',m)\right]=\qquad\text{(C.77)}$$
$$=\frac{1}{4}\vec{\nabla}\cdot\left[\rho_m\vec{\nabla}\rho_{m'}+\rho_{m'}\vec{\nabla}\rho_m\right]-\frac{1}{2}(\rho_m\tau_{m'}+\rho_{m'}\tau_m)-\frac{1}{4}\left[\vec{\nabla}\rho_m\cdot\vec{\nabla}\rho_{m'}-2\vec{J}_m\cdot\vec{J}_{m'}\right]$$
$$=\frac{1}{4}\left[\rho_m\nabla^2\rho_{m'}+\rho_{m'}\nabla^2\rho_m+\vec{\nabla}\rho_m\cdot\vec{\nabla}\rho_{m'}+2\vec{J}_m\cdot\vec{J}_{m'}-2(\rho_m\tau_{m'}+\rho_{m'}\tau_m)\right]$$

Restoring the full indices and using the symmetry of $\vec{I}^t_{mm'}\cdot\vec{I}^t_{m'm}$ with respect to the exchange of m,m', we get

$$\widetilde{Tr}[\vec{D}_{IV}\cdot\nabla^2\vec{D}_{IV}]$$
$$=\frac{1}{4}\sum_{m,m'}\vec{I}^t_{mm'}.\vec{I}^t_{m'm}\left[2\rho_m\nabla^2\rho_{m'}+\vec{\nabla}\rho_m\cdot\vec{\nabla}\rho_{m'}+2\vec{J}_m\cdot\vec{J}_{m'}-4\rho_m\tau_{m'}\right]\qquad\text{(C.78)}$$
$$=\frac{1}{4}\sum_m m^2\left[2\rho_m\nabla^2\rho_m+\left(\vec{\nabla}\rho_m\right)^2+2\vec{J}_m^2-4\rho_m\tau_m\right]$$
$$+\frac{1}{8}\sum_m\left[2\rho_m\nabla^2\rho_{(m\pm1)}+\vec{\nabla}\rho_m\cdot\vec{\nabla}\rho_{(m\pm1)}+2\vec{J}_m\cdot\vec{J}_{(m\pm1)}-4\rho_m\tau_{(m\pm1)}\right]$$

Since the isovector density is only 2-body, a total derivative $\vec{\nabla}\cdot(\rho_a\cdot\vec{\nabla}\rho_b)$ will give zero after integration over the volume $\vec{r}$, so we can replace $\vec{\nabla}\rho_a\cdot\vec{\nabla}\rho_b\rightarrow-\rho_a\nabla^2\rho_b$,

which gives

$$\widetilde{Tr}[\vec{D}_{IV}\cdot\nabla^2\vec{D}_{IV}] = \frac{1}{4}\sum_m m^2\left[\rho_m\nabla^2\rho_m + 2\vec{J}_m^2 - 4\rho_m\tau_m\right]$$
$$+\frac{1}{8}\sum_m\left[\rho_m\nabla^2\rho_{(m\pm1)} + 2\vec{J}_m\cdot\vec{J}_{(m\pm1)} - 4\rho_m\tau_{(m\pm1)}\right] \quad \text{(C.79)}$$

C.5 Expectation Values of Operator Densities.

After evaluating all of the necessary Fermi traces, we can proceed with the evaluation of the expectation values of the operator densities listed in (C.20), assuming we have $N = N_f$ flavors of baryons (in our case of protons and neutrons $N_f = 2$).

To evaluate the expectation values of the operator densities that involve sums over all flavors, we can use the multinomial expansion. Let us consider an operator of the following form

$$\langle : A^n : \rangle = \left\langle : \left(\sum_{f=1,N} a(f)A(\vec{r},f)\right)^n : \right\rangle, \quad \text{(C.80)}$$

where the weights $a(f)$ are C numbers and $A(\vec{r},f)$ are one body operators diagonal in flavor. From here on we will drop the position argument $\vec{r}$ for simplicity. To expand the RHS of the above equation, we employ the multinomial formulae:

$$\left(\sum_{f=1,N} x_i\right)^n = \sum_{n_1,n_2,...n_N\geq 0} C^n_{n_1n_2...n_N} x_1^{n_1}x_2^{n_2}...x_N^{n_N}, \quad \text{(C.81)}$$

where the multinomial coefficient is

$$C^n_{n_1n_2...n_N} = \frac{n!}{n_1!n_2!....n_N!}\delta(n_1+n_2+..+n_N-n). \quad \text{(C.82)}$$

We shall use the compact notation $\{n\}$ for the family $\{n_1,n_2,...n_N\}$, including the condition that $n_i \geq 0$. Due to the normal ordering we don't need to worry about the order of the operators and we can write

$$\left\langle : \left(\sum_{f=1,N} a(f)A(f)\right)^n : \right\rangle =$$
$$\sum_{\{n\}} C^n_{\{n\}} a(1)^{n_1}a(2)^{n_2}...a(N)^{n_N}\left\langle : A(1)^{n_1}A(2)^{n_2}...A(N)^{n_N} : \right\rangle. \quad \text{(C.83)}$$

Due to the assumed flavour structure of the HF state, the expectation value of a product of different flavor operators is factorizable:

$$\langle : A(1)^{n_1} A(2)^{n_2} ... A(N)^{n_N} : \rangle = \langle : A(1)^{n_1} : \rangle \langle : A(2)^{n_2} : \rangle ... \langle : A(N)^{n_N} : \rangle \tag{C.84}$$

Thus we arrive at the master formula:

$$\left\langle : \left(\sum_{f=1,N} a(f) A(f) \right)^n : \right\rangle = \sum_{\{n\}} C^n_{\{n\}} \prod_{f=1,N} a(f)^{n_f} \langle : A(f)^{n_f} : \rangle . \tag{C.85}$$

Let us point out that in our case, $N = 2$, we can simplify the notation of the above equation using the usual binomial formula:

$$\langle : \left(a\left(1\right) A(1) + a(2) A(2) \right)^n : \rangle = \sum_{i=0}^{n} \frac{n!}{i!(n-i)!} a(1)^i a(2)^{n-i} \left\langle : A(1)^i : \right\rangle \left\langle : A(2)^{n-i} : \right\rangle . \tag{C.86}$$

C.5.1 $\langle : D^n : \rangle$

We can easily apply the above procedure to evaluate $\langle : D^n : \rangle$, which can be expressed as

$$\langle : D^n : \rangle = \left\langle : \left(\sum_{f=1,N} D(f) \right)^n : \right\rangle = \sum_{\{n\}} C^n_{\{n\}} \prod_{f=1,N} \langle : D(f)^{n_f} : \rangle . \tag{C.87}$$

We need to evaluate $\langle : D(f)^n : \rangle$ in the cases $n = 0, 1, 2$. Using Eq. (C.29) and the trace formulas from the previous section, we have

$$\left\langle : D(f)^0 : \right\rangle = 1, \tag{C.88}$$

$$\langle : D(f) : \rangle = \rho_f,$$

$$\left\langle : D(f)^2 : \right\rangle = \widetilde{Tr}[D(f)]^2 - \widetilde{Tr}[D(f)^2] = \frac{\rho_f^2}{2}, \tag{C.89}$$

$$\langle : D(f)^n : \rangle = 0 \;\; n > 2, \tag{C.90}$$

which can be written as

$$\langle : D(f)^n : \rangle = \Theta(2-n) \rho_f^n \left(1 - \frac{n(n-1)}{4} \right), \tag{C.91}$$

where $\Theta(x)$ is the usual Heaviside unit step function.

It is useful to define

$$\Delta(n) = \Theta(2-n) \left(1 - \frac{n(n-1)}{4} \right), \tag{C.92}$$

and the final result is

$$\langle : D(f)^{n_f} : \rangle = \Delta(n)\rho_f^{n_f}. \tag{C.93}$$

Thus we have for the full density operator D

$$\langle D \rangle = \sum_f \rho_f = \rho \tag{C.94}$$

$$\left\langle D^2 \right\rangle = \sum_{f=1}^{N} \left\langle D(f)^2 \right\rangle + 2\prod_{f=1}^{N} \langle D(f) \rangle = \sum_f \frac{\rho_f^2}{2} + 2\prod_{f=1}^{N} \rho_f \equiv \sum_{f,f'=1}^{N} (1-\delta_{ff'})\,\rho_f \rho_{f'} \tag{C.95}$$

Similarly, for evaluating the other terms in the density functional, we will need the following expectation values from (C.20), which we will evaluate one by one.

C.5.2 $\langle : D(f)^n \xi(f) : \rangle$

we need to evaluate $\langle : D(f)^n \xi(f) : \rangle$ with $n = 0, 1, 2$.

$$\langle : \xi(f) : \rangle = \tau_f \tag{C.96}$$

$$\begin{aligned} \langle : D(f)\xi(f) : \rangle &= \widetilde{Tr}[D(f)]\widetilde{Tr}[K(f)] - \widetilde{Tr}[D(f)K(f)] \\ &= \rho_f \tau_f - \frac{1}{8}\left[\left(\vec{\nabla}\rho_f\right)^2 + 2\vec{J}_f^2\right] \end{aligned} \tag{C.97}$$

$$\begin{aligned} \left\langle : D(f)^2 \xi(f) : \right\rangle &= \widetilde{Tr}[D(f)]^2 \widetilde{Tr}[K(f)] - \widetilde{Tr}[D(f)^2]\widetilde{Tr}[K(f)] \\ &\quad -2\widetilde{Tr}[D(f)]\widetilde{Tr}[D(f)K(f)] + 2\widetilde{Tr}[D^2 K(f)] \\ &= \frac{\rho_f^2}{2}\tau_f - \frac{\rho_f}{8}\left[\left(\vec{\nabla}\rho_f\right)^2 + 2\vec{J}_f^2\right] \end{aligned} \tag{C.98}$$

which can be summarized as

$$\Theta(2-n)\,\langle : D(f)^n \xi(f) : \rangle = \Delta(n)\rho_f^{n-1}\left[\tau_f \rho_f - \frac{k}{8}\left(\left(\vec{\nabla}\rho_f\right)^2 + 2\vec{J}_f^2\right)\right] \tag{C.99}$$

where $\Delta(k)$ has been defined in (C.92).

C.5.3 $\left\langle : D(f)^n \vec{\nabla} D(f) : \right\rangle$

For $\langle : D(f)^n \nabla_\alpha D(f) : \rangle\,,\ n = 0, 1, 2$ we have

$$\langle : \nabla_\alpha D(f) : \rangle = \nabla_\alpha \rho_f, \tag{C.100}$$

$$\langle : D(f)\nabla_\alpha D(f) : \rangle = \widetilde{Tr}[D(f)]\widetilde{Tr}[\nabla_\alpha D(f)] - \widetilde{Tr}[D(f)\nabla_\alpha D(f)] \tag{C.101}$$
$$= \rho_f \nabla_\alpha \rho_f - \frac{1}{2}\rho_f \nabla_\alpha \rho_f = \frac{1}{2}\rho_f \nabla_\alpha \rho_f,$$

$$\left\langle : D(f)^2 \nabla_\alpha D(f) : \right\rangle = \left(\widetilde{Tr}[D(f)]\right)^2 \widetilde{Tr}[\nabla_\alpha D(f)] - 2\widetilde{Tr}[D(f)]\widetilde{Tr}[D(f)\nabla_\alpha D(f)] \tag{C.102}$$
$$-\widetilde{Tr}\left[D(f)^2\right]\widetilde{Tr}[\nabla_\alpha D(f)] + 2\widetilde{Tr}\left[D(f)^2\nabla_\alpha D(f)\right]$$
$$= \rho_f^2 \nabla_\alpha \rho_f - 2\frac{\rho_f^2 \nabla_\alpha \rho_f}{2} - \frac{\rho_f^2 \nabla_\alpha \rho_f}{2} + 2\frac{\rho_f^2 \nabla_\alpha \rho_f}{4}$$
$$= 0,$$

where we used Eq. (C.30) for the last formula.

This is summarized by

$$\Theta(2-n) <: D(f)^n \nabla_\alpha D(f) :>= \Theta(2-n)\frac{2-n}{2}\rho_f^n \nabla_\alpha \rho_f \tag{C.103}$$

C.5.4 $\left\langle : D(f)^n \left(\vec{\nabla} D(f)\right)^2 : \right\rangle$

For $\left\langle : D(f)^n \left(\vec{\nabla} D(f)\right)^2 : \right\rangle$, $n = 0, 1, 2$ we have

$$\left\langle : \left(\vec{\nabla} D(f)\right)^2 : \right\rangle = \widetilde{Tr}[\nabla_\alpha D(f)]\widetilde{Tr}[\nabla_\alpha D(f)] - \widetilde{Tr}[\nabla_\alpha D(f)\nabla_\alpha D(f)] \tag{C.104}$$
$$= \frac{1}{4}\left[-4\rho_f \tau_f + 3\left(\vec{\nabla}\rho_f\right)^2 + 2\vec{J}_f^{\,2}\right]$$

$$\left\langle : D(f)\left(\vec{\nabla} D(f)\right)^2 : \right\rangle = \tag{C.105}$$
$$= \widetilde{Tr}[D(f)]\left(\widetilde{Tr}[\nabla_\alpha D(f)]\right)^2 - 2\widetilde{Tr}[\nabla_\alpha D(f)]\widetilde{Tr}[D(f)\nabla_\alpha D(f)]$$
$$-\widetilde{Tr}[D(f)]\widetilde{Tr}[(\nabla_\alpha D(f))^2] + 2\widetilde{Tr}[D(f)\,(\nabla_\alpha D(f))^2]$$
$$= \frac{\rho_f}{8}\left[-4\rho_f \tau_f + \left(\vec{\nabla}\rho_f\right)^2 + 2\vec{J}_f^{\,2}\right]$$

$$\left\langle : D(f)^2 \left(\vec{\nabla} D(f)\right)^2 : \right\rangle = \tag{C.106}$$
$$= \left(\widetilde{Tr}[D(f)]\right)^2 \left(\widetilde{Tr}[\vec{\nabla} D(f)]\right)^2 - \left(\widetilde{Tr}[D(f)]\right)^2 \widetilde{Tr}\left[\left(\vec{\nabla} D(f)\right)^2\right] -$$
$$-\widetilde{Tr}\left[D(f)^2\right]\left(\widetilde{Tr}[\vec{\nabla} D(f)]\right)^2 - 4\widetilde{Tr}[D(f)]\widetilde{Tr}[\vec{\nabla} D(f)]\widetilde{Tr}[D(f)\vec{\nabla} D(f)]$$
$$+\widetilde{Tr}\left[D(f)^2\right]\widetilde{Tr}\left[\left(\vec{\nabla} D(f)\right)^2\right] + 2\left(\widetilde{Tr}[D(f)\vec{\nabla} D(f)]\right)^2$$
$$+4\widetilde{Tr}[D(f)]\widetilde{Tr}\left[D(f)\left(\vec{\nabla} D(f)\right)^2\right] + 4\widetilde{Tr}[\vec{\nabla} D(f)]\widetilde{Tr}\left[D(f)^2\vec{\nabla} D(f)\right]$$
$$-4\widetilde{Tr}[D(f)]\widetilde{Tr}\left[D(f)\left(\vec{\nabla} D(f)\right)^2\right] - 2\widetilde{Tr}\left[\left(D(f)\vec{\nabla} D(f)\right)^2\right]$$
$$= \rho_f^2\left(\vec{\nabla}\rho_f\right)^2 - \frac{1}{4}\rho_f^2\left\{\left(\vec{\nabla}\rho_f\right)^2 + z\right\} - \frac{1}{2}\rho_f^2\left(\vec{\nabla}\rho_f\right)^2$$
$$-\frac{4}{2}\rho_f^2\left(\vec{\nabla}\rho_f\right)^2 + \frac{1}{8}\rho_f^2\left\{\left(\vec{\nabla}\rho_f\right)^2 + z\right\} + \frac{2}{4}\rho_f^2\left(\vec{\nabla}\rho_f\right)^2$$
$$+\frac{4}{16}\rho_f^2\left\{3\left(\vec{\nabla}\rho_f\right)^2 + z\right\} + \frac{4}{4}\rho_f^2\left(\vec{\nabla}\rho_f\right)^2$$
$$-\frac{4}{32}\rho_f^2\left\{3\left(\vec{\nabla}\rho_f\right)^2 + z\right\} - \frac{2}{8}\rho_f^2\left(\vec{\nabla}\rho_f\right)^2$$
$$= 0,$$

where $z \equiv 4\rho_f\tau_f - 2\vec{J}_f^{\,2}$ and we used Eq. (C.31) for the last formula.

We can rewrite the formula above as:

$$\Theta(2-n)\left\langle : D(f)^n \left(\vec{\nabla} D(f)\right)^2 : \right\rangle =$$
$$= \Theta(2-n)\frac{2-n}{2}\frac{\rho_f^n}{4}\left[-4\rho_f\tau_f + (3-2n)\left(\vec{\nabla}\rho_f\right)^2 + 2\vec{J}_f^{\,2}\right] \tag{C.107}$$

C.5.5 $\left\langle : D(f)^n\nabla^2 D(f) : \right\rangle$

For $\langle : D(f)^n\nabla^2 D(f) : \rangle$, $n = 0, 1, 2$ we have:

$$\left\langle : \nabla^2 D(f) : \right\rangle = \nabla^2\rho_f \tag{C.108}$$

$$\left\langle : D(f)\nabla^2 D(f) : \right\rangle = \tilde{Tr}[D(f)]\tilde{Tr}[\nabla^2 D(f)] - \tilde{Tr}[D(f)\nabla^2 D(f)] \tag{C.109}$$
$$= \rho_f\nabla^2\rho_f - \left(\frac{\rho_f}{2}\nabla^2\rho_f + \frac{1}{4}\left(\left(\vec{\nabla}\rho_f\right)^2 + 2\vec{J}_f^2 - 4\rho_f\tau_f\right)\right)$$
$$= \frac{1}{2}\rho_f\nabla^2\rho_f - \frac{1}{4}\left(\left(\vec{\nabla}\rho_f\right)^2 + 2\vec{J}_f^2 - 4\rho_f\tau_f\right)$$

$$\left\langle : D(f)^2\nabla^2 D(f) : \right\rangle = \tilde{Tr}[D(f)]^2\tilde{Tr}[\nabla^2 D(f)] - \tilde{Tr}[D(f)^2]\tilde{Tr}[\nabla^2 D(f)] \quad \text{(C.110)}$$
$$-2\tilde{Tr}[D(f)]\tilde{Tr}[D(f)\nabla^2 D(f)] + 2Tr[D(f)^2\nabla^2 D(f)]$$
$$= \rho_f^2\nabla^2\rho_f - \frac{\rho_f^2}{2}\nabla^2\rho_f - 2\rho_f\left(\frac{\rho_f}{2}\nabla^2\rho_f + \frac{1}{4}\left(\left(\vec{\nabla}\rho_f\right)^2 + 2\vec{J}_f^2 - 4\rho_f\tau_f\right)\right)$$
$$+2\left(\frac{\rho_f^2}{4}\nabla^2\rho_f + \frac{1}{4}\frac{\rho_f}{2}\left(\left(\vec{\nabla}\rho_f\right)^2 + 2\vec{J}_f^2 - 4\rho_f\tau_f\right)\right)$$
$$= -\frac{\rho_f}{4}\left(\left(\vec{\nabla}\rho_f\right)^2 + 2\vec{J}_f^2 - 4\rho_f\tau_f\right)$$

which is equivalent to

$$\left\langle : D(f)^n\nabla^2 D(f) : \right\rangle =$$
$$= \Theta(2-n)\left[\frac{2-n}{2}\rho_f^n\nabla^2\rho_n - \frac{n(3-n)}{8}\rho_f^{n-1}\left(\left(\vec{\nabla}\rho_f\right)^2 + 2\vec{J}_f^2 - 4\rho_f\tau_f\right)\right] \quad \text{(C.111)}$$

C.5.6 $\left\langle : \vec{D}_{IV}^2 : \right\rangle$

For $\left\langle : \vec{D}_{IV}^2) : \right\rangle$ we have:

$$\left\langle : \vec{D}_{IV}\cdot\vec{D}_{IV} : \right\rangle = \quad \text{(C.112)}$$
$$= \widetilde{Tr}[\vec{D}_{IV}]^2 - \widetilde{Tr}[\vec{D}_{IV}{}^2] = \left(\sum_m m\rho_m\right)^2 - \frac{1}{2}\sum_m\left(m^2\rho_m^2 + \frac{1}{2}\rho_m\rho_{(m\pm1)}\right)$$
$$= \sum_{m,m'=-1/2}^{1/2}\left(mm' - \frac{1}{2}C_{mm\prime}\right)\rho_m\rho_{m'},$$

where

$$C_{mm\prime} = \delta_{m,m'}m^2 + \frac{1}{2}\left(\delta_{m,m'+1} + \delta_{m',m+1}\right) \quad \text{(C.113)}$$

C.5.7 $\left\langle : \vec{D}_{IV} \cdot \nabla^2 \vec{D}_{IV} : \right\rangle$

For $\left\langle : \vec{D}_{IV} \cdot \nabla^2 \vec{D}_{IV} : \right\rangle$ we have:

$$\begin{aligned}\left\langle : \vec{D}_{IV} \cdot \nabla^2 \vec{D}_{IV} : \right\rangle &= \widetilde{Tr}[\vec{D}_{IV}] \cdot \widetilde{Tr}[\nabla^2 \vec{D}_{IV}] - \widetilde{Tr}[\vec{D}_{IV} \cdot \nabla^2 \vec{D}_{IV}] \\ &= \sum_m m\rho_m \nabla^2 \sum_m m\rho_m \\ &\quad -\frac{1}{4}\sum_m m^2 \left[\rho_m \nabla^2 \rho_m + 2\vec{J}_m^2 - 4\rho_m \tau_m\right] \\ &\quad -\frac{1}{8}\sum_m \left[\rho_m \nabla^2 \rho_{(m\pm1)} + 2\vec{J}_m \cdot \vec{J}_{(m\pm1)} - 4\rho_m \tau_{(m\pm1)}\right] \\ &= \sum_{m,m'=-1/2}^{1/2} \left\{\left(mm' - \frac{1}{4}C_{mm\prime}\right)\rho_m \nabla^2 \rho_{m'} + C_{mm\prime}\rho_m \tau_{m'}\right\},\end{aligned} \tag{C.114}$$

where in the last step we ignored the terms quadratic in the spin density $\vec{J}$. This amounts to treating the spin orbit interaction as a first order perturbation.

C.6 Results

Using the expectation values of the density operator products derived above and the multinomial expansion for flavor decomposition we can easily write down the density functional of the (C.1) as

$$\begin{aligned}\langle H(\vec{r})\rangle &= \rho M + \frac{\tau}{2M} + \frac{G_\sigma}{2M^2}\left(\rho\tau + \frac{1}{8}\sum_m \rho_m \nabla^2 \rho_m\right) \\ &\quad -\left(\frac{G_\sigma}{2m_\sigma^2} + \frac{G_\sigma}{4M^2}\right)\left(\rho\nabla^2\rho - \sum_m\left(\frac{1}{4}\rho_m\nabla^2\rho_m - \rho_m\tau_m\right)\right) \\ &\quad -\frac{1}{2}\frac{G_\sigma}{1+dG_\sigma\rho}\left(\rho^2 - \frac{1}{2(1+dG_\sigma\rho)^2}\sum_m \rho_m^2\right)\end{aligned} \tag{C.115}$$

The result for the meson part is also very easy to write down

$$\begin{aligned}\langle : \mathcal{H}_\omega(\vec{r}) : \rangle &= \frac{G_\omega}{2}\sum_{mm'}\left[\left(1 - \frac{1}{2}\delta_{mm'}\right)\rho_m\rho_{m'}\right. \\ &\quad \left.+\frac{1}{m_\omega^2}\left(\rho_m\nabla^2\rho_{m'} - \frac{1}{4}\delta_{mm'}\left(\rho_m\nabla^2\rho_m - 4\rho_m\tau_m\right)\right)\right],\end{aligned} \tag{C.116}$$

$$\langle : \mathcal{H}_\rho(\vec{r}) : \rangle = \frac{G_\rho}{2} \sum_{mm'} \left\{ \left(mm' - \frac{1}{2} C_{mm'} \right) \rho_m \rho_{m'} \right. \tag{C.117}$$
$$\left. + \frac{1}{m_\rho^2} \left(mm' - \frac{1}{4} C_{mm'} \right) \rho_m \nabla^2 \rho_{m'} + \frac{1}{m_\rho^2} C_{mm'} \rho_m \tau_{m'} \right\},$$

where we straight forwardly used the results of section C.5.

The treatment of the remaining spin-orbit part of the Hamiltonian goes along the same lines and does not pose any difficulty.

Vita

Hrayr Hamlet Matevosyan was born on September 17, 1980, in Yerevan, Armenia (Armenian Soviet Socialist Republic at the time). He attended Artashes Shahinyan's Special Phys-Math School in Yerevan, where he graduated with a gold medal award in May of 1997. In September of 1997 he entered the Department of Physics of Yerevan State University, where he received his Bachelor of Science degree with honors in theoretical physics in June of 2001. He attended the masteral program of the same department by correspondence and was awarded Master of Science degree in theoretical physics in June of 2003. He was admitted to the doctoral program of the Department of Physics and Astronomy of Louisiana State University in August of 2001, where his degree of Doctor of Philosophy in physics is expected to be awarded in August of 2007.